Fluxes of Atmospheric Methane Using Novel Instruments, Field Measurements, and Inverse Modeling

Fluxes of atmospheric methane using novel instruments, field measurements, and inverse modeling

A dissertation presented

by

Gregory Winn Santoni

to

The *Department of Earth and Planetary Sciences*

in partial fulfillment of the requirements

for the degree of

Doctor of Philosophy

in the subject of

Earth and Planetary Sciences

Harvard University

Cambridge, Massachusetts

May 2013

Dissertation Advisor: Professor Steven C. Wofsy Gregory Winn Santoni

Fluxes of atmospheric methane using novel instruments, field measurements, and inverse modeling

Abstract

The atmospheric concentration of methane (CH_4) – the most significant non-CO_2 anthropogenic long-lived greenhouse gas – stabilized between 1999 and 2006 and then began to rise again. Explanations for this behavior differ but studies agree that more measurements and better modeling are needed to reliably explain the model-data discrepancies and predict future change. This dissertation focuses on measurements of CH_4 and inverse modeling of atmospheric CH_4 fluxes using field measurements at a variety of spatial scales.

We first present a new fast-response instrument to measure the isotopic composition of CH_4 in ambient air. The instrument was used to characterize mass fluxes and isofluxes (a isotopically-weighted mass flux) from a well-studied research fen in New Hampshire. Eddy-covariance and automatic chamber techniques produced consistent estimates of both the CH_4 fluxes and their isotopic composition at sub-hourly resolution. We then characterize fluxes of CH_4 from aircraft engines using measurements made with the same instrument during the Alternative Aviation Fuel Experiment (AAFEX), a study that aimed to determine the atmospheric impacts of alternative fuel use in the growing aviation industry. Emissions of CO_2, CH_4, and N_2O from different synthetic fuels were statistically indistinguishable from those of the widely used JP-8 jet fuel.

We then present airborne observations of the long-lived greenhouse gas suite – CO_2, CH_4, N_2O, and CO – during two aircraft campaigns, HIPPO and CalNex, made using a similar instrument built specifically for the NCAR HIAPER GV aircraft. These measurements are

compared to data from other onboard sensors and show excellent agreement. We discuss the details of the end-to-end calibration procedures and the data quality-assurance and quality-control (QA/QC). Lastly, we quantify a top-down estimate of California's CH_4 emission inventory using the CalNex CH_4 observations. Observed CH_4 enhancements above background concentrations are simulated using a lagrangian transport model driven by validated meteorology. *A priori* source-specific emission inventories are optimized in a Bayesian inversion framework to show that California's CH_4 budget is 1.6 ± 0.34 times larger than the current estimate of California's Air Resources Board (CARB), the body charged with enforcing the California Global Solutions Act and tracking emission changes over time. Findings highlight large underestimates of emissions from cattle and natural gas infrastructure.

Acknowledgments

Many people have contributed to this work and I am extremely grateful for their advice and support. Steve Wofsy has been a wonderful advisor and mentor over the years. He helped hone my critical thinking skills by teaching me to ask the right questions, sparked my interest in the field, and pushed me to grow as a scientist.

I have been fortunate to spend many hours with Ben Lee, Eric Kort, VY Chow, and Marcos Longo in graduate school discussing science and life. Bruce Daube has been a tremendous mentor and it has been a pleasure to spend so much time with him. Mark Zahniser, David Nelson, and Barry McManus of Aerodyne Research Inc. have been incredible sources of wisdom and motivation. Scott Herndon and Ezra Wood showed me how to get fieldwork done efficiently under pressure. Bill Munger, Elaine Gottlieb, Jasna Pittman, Sunyoung Park, Rodrigo Jimenez, Scott Saleska, Ruth Varner, and Patrick Crill have been a pleasure to work with, and they all contributed to making these measurements possible. I was lucky to share offices with Eric Kort and John Budney and thank them for all the conversations. The Atmospheric and Earth and Planetary Sciences communities at Harvard were incredibly stimulating and exciting environments to be a part of and I am grateful to everyone who contributed to this culture. I also thank the numerous collaborators at NOAA and NCAR who made the CalNex and HIPPO field deployments a success and offered incredibly helpful feedback on subsequent analysis.

Finally, I thank my parents, family, and friends for all their love and support. I couldn't have done this without them.

Table of Contents

List of Figures

Chapter 2

wind speed (black) and u* (grey) where the dashed grey line is the u* threshold of 0.1 m/s used as a filter, (b) wind direction, (c, left) air temperature, (c, right) relative humidity shown calculated using the Licor H_2O measurement (grey) and using the QCLS H_2O measurement (thin black), (d) mean mixing ratios of CH_4 (black) and CO_2 (grey), and (e) mean $\delta^{13}C_{CH_4}$ where the dashed black line in represents -47 ‰, the mean isotopic composition of ambient CH_4 in the free troposphere.

Figure 2.9: Time series of EC half-hourly (a) sensible and latent heat fluxes, (b) CO_2 fluxes, where the thin dashed black line denotes the transition from positive to negative NEE and light grey circles represent fluxes not used in the analysis because they correspond to half-hour intervals with u* < 0.1 m/s, (c) CH_4 fluxes where the thick dashed black line denotes the average over the two days, and (d) CH_4 isofluxes. For (c) and (d), two different scales are used on the left and right axes. The time series of the resulting source isotopic composition of CH_4 derived from the measurements, $\delta^{13}C_{CH_{4source}}$ is shown in (e) for n = 90 (grey triangles), n = 55 (thin black pluses) and n = 32 (solid black circles) of the 96 half-hour intervals corresponding to the different filters discussed, along with a thin dashed line at -47 ‰, the mean isotopic composition of ambient CH_4 in the free troposphere, and a thick dashed line at -71 ‰, the mean isotopic composition for n=90 (grey triangles).

Figure 2.10: (left) Examples of QCLS autochamber subsampling intervals for linear (top), ebullitive (middle), and random (bottom) fluxes calculated with Equation 2.9 and the blue regression. Missing data corresponds to background zero-air, low-span, or high-span calibration tank additions. (right) Corresponding Keeling plots for the three time series where $\delta^{13}C_{CH_4}$ is shown color-coded by elapsed time to relate the left plots to the right. The isotopic composition of background atmospheric CH_4 is shown at -47 ‰ (dotted black) and the Keeling regression slope is shown in red. An additional Keeling regression for an ebullition event (middle) is shown in green, where the grey (triangles) represent the ebullitive subset of the data used in the analysis.

Figure 2.11: Log-log relationship of 1σ error on Keeling intercept as a function of CH_4 flux (shown with two separate but equivalent scales). The slope and intercept give predicted Keeling plot 1σ errors on the regression. The 1σ errors on the regression for linear, bubble, and random chamber buildups are 1.3 ‰, 1.1 ‰, and 2.5 ‰, respectively. The variance is smaller on autochamber closings containing ebullitive events because excursions of CH_4 above ambient conditions are generally larger.

Figure 2.12: (left) Histogram of the $\delta^{13}C_{CH_{4source}}$ composition using autochamber Keeling plot methods. (right) Histogram of the half-hourly $\delta^{13}C_{CH_{4source}}$ composition calculated using EC isoflux methods. Of the 96 half-hour intervals, the 90 with isotopic composition within 3σ of the mean are shown in white and have a mean composition of -71 ‰. Filtering by u* >0.1 m/s, CH_4 flux > 1 nmol/mol-m/s, and stability parameter $z/L \in (-5,0)$ result in different mean isotopic composition of -79 ‰, -78 ‰, and -82 ‰. The 1σ of the distributions is 33 ‰ for all of the filters, similar to the isoflux measurement error derived from the cross covariance far from true

lag-time. The grey vertical dashed line in both histograms represents the isotopic composition of atmospheric CH_4.

Figure 2.13: Supplementary Figure 1: The 96 half-hour interval CH_4 fluxes plotted against their corresponding u* values. Vertical grey lines denote u* = 0.07 m/s and u* = 0.1 m/s and the black trace shows the mean CH_4 flux in bins of u* with spacing 0.02 m/s, showing the leveling off of CH_4 fluxes at the u* = 0.1 threshold chosen for this study.

Chapter 3

Figure 3.1: (left) Time series (January 26th, 2009, 2pm local time) of the enhancement above background values (ΔCH_4, ΔN_2O, ΔCO_2) of ambient plume AAFEX data illustrating positive correlation between CH_4 and CO_2 at idle conditions (before minute 20), and negative correlation at higher thrusts (after minute 20). N_2O is positively correlated with CO_2 at all thrust conditions. (right) Two examples of emission ratio (ER) regressions at 4% (idle) and 30% (approach) maximum rated thrust using CH_4 and CO_2 data from the left panel.

Figure 3.2: CH_4 emission indices (top), N_2O emission indices (middle), and CO_2 concentration at the Engine Exhaust Plane (bottom, courtesy of Changlie Wey) binned by fuel and percent maximum rated engine thrust. The latter is used to calculate plume dilution of canister samples taken from the 1-m probe which are shown superimposed on the CH_4 EI plot (**top**). Black bars represent the median, boxes extend from the first to the third quartile, and whiskers represent 1.5 inter-quartile ranges. Outliers are shown as black circles.

Figure 3.3: Mean engine exhaust concentrations of CH_4 and N_2O for various aircraft emission studies compared to the present AAFEX study. Atmospheric mixing ratios of CH_4 and N_2O are shown as dashed lines for reference.

Chapter 4

Figure 4.1: The absorption spectra for the 3 quantum cascade lasers. QCL1 (a) is a differential measurement of $^{12}CO_2$ and therefore appears inverted because this sample has a lower concentration of CO_2 than the reference gas. QCL2 (b) shows the spectrum for CH_4 and N_2O and QCL3 (c) shows the spectrum for CO.

Figure 4.2: Time series for the 4 QCLS species during 20 minutes of in-flight sampling over the Pacific during HIPPO II (top) and the Allan variance as a function of averaging time for the data shown (bottom). Table 4.1 summarizes these data and also provides corresponding values for sampling from a calibration cylinder in the laboratory.

Figure 4.3: Schematic of the QCLS-CO2 sampling system.

Figure 4.4: The sampling sequence used to calibrate a secondary cylinder (Table 4.2b) using 3 primary cylinders (Table 4.2a). Zero air (red) is sampled for 5 minutes, the primary cylinders are then each sampled for 3 minutes (green) in order of increasing concentration and then the target

secondary cylinder (pink) is sampled for 3 minutes. The pink points are interpolated to the two primaries that bracket the secondary concentration and that data is shown in Figure 4.5.

Figure 4.5: The concatenated target secondary cylinder interpolated values (i.e. the pink points in Figure 4.4). The three panels represent a calibration of the secondary cylinder CC89589 in 2010, 2011, and 2012, that was used to fill the gas deck for HIPPO III, IV, and V, illustrating the stability of the tank over time. Also plotted in blue is the quadratic fit to all3 primary cylinders used in the calibration of this tank.

Figure 4.6: Calibration sequence of in-flight measurements. The reference gas (QCLS-CO2) and zero gas (QCLS-DUAL) are sampled every 15 minutes, a low-span and a high span every 30 minutes, and a check-span every two hours. The sample data (green) are interpolated to the mean values of each group of the calibration spans (red).

Figure 4.7: A series of square-wave tests, alternatively sampling from a check-span secondary tank with ambient concentration and a zero-air tank every 5 minutes, superimposed upon one-another to illustrate the slow sample equilibration time for N_2O. A decrease in the surface area of PFA or Dekaron™ results in a faster equilibration time. Both CH_4 and CO do not exhibit this behavior.

Figure 4.8: The gas-deck in-flight calibration addition stability over the course of one flight on HIPPO V. Each point represents the average of the group of red points in Figure 4.6 and the axes for each QCLS species are equivalent in range. The lines represent the Akima spline interpolations to the different spans and are used to relate the spectroscopically-calibrated mixing ratios to the NOAA scale. QCLS-CO2 and QCLS-DUAL use different interpolation techniques as discussed in the text. The HIMIL inlet pressure is also shown in grey.

Figure 4.9: An estimate of the calibration linearity (top) and uncertainty (bottom) for the 4 QCLS species. For QCLS-CO2, the quadratic interpolation function for each research flight in CalNex (which is more variable that in the HIPPO) is shown. The standard deviation across the 21 flights as a function of calibrated mixing ratio is shown in the bottom panel, reaching a minimum at the value of the reference gas deck calibration cylinder. The histograms of the CalNex (blue) and HIPPO (data) are shown and the 10% and 90% quantiles are plotted as vertical lines for each, indicating that the variability in the quadratic interpolation function typically contributes no more than 0.1 ppm. For QCLS-DUAL, the 1:1 correspondence of the spectroscopically-calibrated QCLS mixing ratio is plotted against 4 known primary cylinders and regressions are calculated using the error uncertainties from the primary cylinders shown in Table 4.2a. The bottom plot shows the standard deviation of the residual uncertainty, where we exclude the very low CH_4 primary (~500 ppb) and the very high CO (~1000 ppb) from the uncertainty estimate.

Figure 4.10: The 1 Hz HIPPO I-V data comparison for QCLS-CO2 with OMS (left) and AO2 (middle) as well as the QCLS-DUAL CO comparison with the RAF VUV-CO.

Figure 4.11: QCLS-DUAL comparisons to the onboard gas chromatographs PANTHER (top) and UCATS (bottom) for CH_4 (A), N_2O (B), and CO (C).

Figure 4.12: QCLS comparisons to NOAA flask data during HIPPO I-V for CO_2 (A), CH_4 (B), N_2O (C), and CO (D). With the exception of N_2O which has a much tighter correlation with the flask measurements, the axes are all scaled to the same ranges as Figure 4.11. The biases for each fit are reported in Table 4.4.

Figure 4.13: The 1 Hz CalNex data comparison for QCLS with the NOAA/Picarro CRDS for CO_2 (left) and CH_4 (middle) as well as the comparison with the NOAA VUV sensor for CO (right).

Chapter 5

Figure 5.1: Flight paths for the 6 Central Valley (CV) flights along with the mean coordinates of vertical profile locations with ranges > 1300 m and the corresponding CH_4 profiles (with a 150 m smoothing window) at those locations averaged over each day.

Figure 5.2: Flight paths for the 5 South Coast Air Basin (SoCAB) flights along with the mean coordinates of vertical profile locations with ranges > 1300 m and the corresponding CH_4 profiles (with a 150 m smoothing window) at those locations and averaged over each day.

Figure 5.3: Spatial distributions of the surface logarithmic CH_4 emission prior estimates from EDGAR and CalGEM at 0.1° x 0.1° resolution. The two color-scales are the same for all plots, with the left scale in units of log(ppb) and the right scale in units of (ppb).

Figure 5.4: Cumulative footprints for the CV (left) and SoCAB (right) receptors.

Figure 5.5: Time series of CH_4 for the CV (a) and SoCAB (b) flights along with the altitude trace. Modeled concentrations are shown in colors pre and post inversions. Only the NOAA curtain boundary condition based inversions are shown, but the GEOS-Chem boundary condition is shown (dotted red) to compare to the NOAA curtain boundary condition (dotted blue). The EDGAR-substituted inversions are not shown but represent a hybrid between the EDGAR and CalGEM inversions. GEOS-Chem modeled CH_4 concentrations at the receptors are shown in green and the locations of flight profiling have grey backing and correspond to the locations of the X's in Figures 1 and 2.

Figure 5.6: Mean vertical profiles for the CV (a) and SoCAB (b) flights using the same data from Figure 5.5. Error bars represent 2 standard deviations for the observations and the 95% confidence interval for the inversions.

Figure 5.7: Optimized California CH_4 emissions for the CV and SoCAB using the CalGEM inventory. Corresponding total emissions are shown in Table 2c.

Figure 5.8: Measured and modeled concentrations for the CV (a) and SoCAB (b) flights pre (left) and post (right) optimization using the CalGEM emission inventories

Appendix

Figure S1: WRF nested domains.

Figure S2: Comparisons of boundary conditions with HIPPO data.

Figure S3: WRF PBLH comparisons with P-3 *in situ* profiling.

Figure S4: WRF PBLH comparisons with HSRL data.

Figure S5: Inversion scaling factors as a function of regularization parameter as well as the L-curve and its curvature.

Figure S6: CalGEM inversion results for different uncertainties assigned to the *a priori* emissions.

Figure S7: Inversion time series for the EDGAR and EDGAR-Substituted inversions.

Figure S8: Inversion profiles for the EDGAR and EDGAR-Substituted inversions.

Figure S9: Seasonality of rice emissions in the CalGEM inventory.

List of Tables

Chapter 3

Chapter 4

Chapter 5

Citations to Previously Published Work

Chapters 2 and 3 have appeared in the following publications:

Santoni, G. W., B. H. Lee, J. P. Goodrich, R. K. Varner, P. M. Crill, J. B. McManus, D. D. Nelson, M. S. Zahniser, and S. C. Wofsy (2012), Mass fluxes and isofluxes of methane (CH_4) at a New Hampshire fen measured by a continuous wave quantum cascade laser spectrometer, *J. Geophys. Res.,* 117, D10301, doi:10.1029/2011JD016960.

Santoni, G. W., B. H. Lee, E. C. Wood, S. C. Herndon, R. C. Miake-Lye, S. C. Wofsy, J. Barry McManus, D. D. Nelson, M. S. Zahniser (2011), *Environ. Sci. & Technol.*, **45**, 7075-7082, doi:10.1021/es200897h.

Chapter 4 will be submitted as:

Santoni, G. W., B. C. Daube, E. A. Kort, R. Jimenez, S. Park, J. V. Pittman, E. Gottlieb, B. Xiang, M. S. Zahniser, D. D. Nelson, J. B. McManus, J. Peischl, T. B. Ryerson, J. Holloway, A. E. Andrews, C. Sweeney, B. Hall, E. Hintsa, F. Moore, J. Elkins, B. Stephens, and S. C. Wofsy (2013) Intercomparison of the Airborne Quantum Cascade Laser Spectrometer (QCLS) Measurements of the Greenhouse Gas suite – CO_2, CH_4, N_2O, and CO – during the CalNex and HIPPO campaigns, to be submitted to *Atmospheric Measurement Techniques*.

Chapter 5 has been submitted as:

Santoni, G. W., B. Xiang, E. A. Kort, B. C. Daube, A. E. Andrews, C. Sweeney, K. J. Wecht, J. Peischl, T. B. Ryerson, W. M. Angevine, M. Trainer, T. Nehrkorn, J. Eluszkiewicz, S. Jeong, M. L. Fischer, R. A. Ferrare, S. C. Wofsy (2013) California's Methane Budget derived from CalNex P-3 Aircraft Observations and a Lagrangian Transport Model, *Journal of Geophysical Reasearch*, submitted.

Chapter 1:

Introduction

Atmospheric growth rates of methane (CH_4) leveled off between 1999 and 2006, stabilizing concentrations at ~1.8 μmol/mol, but subsequent data demonstrated renewed growth. Forward modeling efforts based on emission inventories, reaction rates, hydroxyl radical (OH) distributions, and other source and sink parameters have shown limited success in recreating observed spatial distributions over time. Some studies have attributed the slowdown to a decrease in microbial Northern Hemisphere emissions [Kai et al. 2011] while others suggest that reduced fossil fuel emissions can account for 30-70% of the decrease [Simpson et al. 2012]. Much of the analysis, however, is limited by poor spatiotemporal resolution of the measurements and modeling efforts.

This thesis presents work done to address current limitations in the measurement and modeling of atmospheric CH_4 with the overall goal of more accurately quantifying CH_4 fluxes at various spatiotemporal scales. Chapter 2 presents the development of a field-deployable quantum cascade laser spectrometer that continuously measures the $^{12}CH_4$ and $^{13}CH_4$ absorption lines and achieves an RMS Allan $\delta^{13}C_{CH_4}$ precision of 1.5 ‰ $Hz^{-1/2}$ and 0.2 ‰ $Hz^{-1/2}$ at 1-sec and 10^2-sec, respectively. We deployed the instrument at a well-studied research peatland in New Hampshire during the 2010 growing season to make proof-of-concept mass flux and isoflux measurements of CH_4 from both automated chambers and an eddy-covariance tower.

Chapter 3 presents aircraft emission indices of CH_4, nitrous oxide (N_2O), and carbon dioxide (CO_2) calculated during the Alternative Aviation Fuel Experiment in January of 2009 in

Palmdale, CA, using the same spectrometer from Chapter 2. We discuss the implications of changes in aviation fuel on atmospheric distributions of CH_4 and N_2O.

A different quantum cascade laser spectrometer (QCLS) developed for airborne observations of the long-lived greenhouse gas suite – CO_2, CH_4, N_2O and CO – is then discussed in Chapter 4. This chapter focuses on the sample conditioning, calibration and traceability, isotopic effects, and measurement intercomparisons with other airborne sensors. We demonstrate that the QCLS Allan precisions in-flight are nearly as good as Allan precisions during laboratory testing, amounting to 1-sec RMS precisions of 20 ppb, 0.5 ppb, 0.09 ppb, and 0.15 ppb for CO_2, CH_4, N_2O and CO, respectively. Intercomparisons are presented for two airborne measurement campaigns: the California Nexus of Air Quality and Climate Change Experiment (CalNex 2010) and the HIaper Pole-to-Pole Observations (HIPPO) campaign (2009–2011).

Using the measurements from these campaigns, we estimate California's CH_4 budget to be a factor of 1.6 ± 0.36 too low and present the modeling efforts used to produce this result in Chapter 5. Our Bayesian inversion framework is based on a Lagrangian particle dispersion model (STILT, the Stochastic Time-Inverted Lagrangian Transport model) driven by Weather Research and Forecasting (WRF) meteorology at 4 km by 4 km horizontal resolution. The modeling explores the influence of 1) boundary condition biases using the HIPPO dataset, 2) meteorological inaccuracies using airborne LIDaR measurements of planetary boundary layer height (PBLH), and 3) spatial distributions of *a priori* emission inventories at 0.1° x 0.1° resolution, on the optimized emission estimates. We perform inversions that scale different source sectors independently, estimating that annual emissions from livestock, landfills, rice, natural gas infrastructure, and wastewater represent 175%, 110%, 315%, 211%, and 147% (weighted mean = 160%) of the California Air Resources Board's (CARB) current CH_4 budget

of 1.52 $TgCH_4$/yr. In order to fulfill the goals set forth in California's Assembly Bill 32 (the Global Warming Solutions Act of 2006), better emission *a priori* estimates with accurate spatial distributions of CH_4 sources and their seasonality need to be put forth and tracked by CARB. We demonstrate the need for aircraft measurements, which are influenced by surface emissions from large regional scales and are able to constrain boundary conditions inaccuracies.

References

Kai, F. M., S. C. Tyler, J. T. Randerson, and D. R. Blake (2011), Reduced methane growth rate explained by decreased Northern Hemispher microbial sources, *Nature*, 476, 194-197.

Simpson, I. J., M. P. S. Andersen, S. Meinardi, L. Bruhwiler, N. J. Blake, D. Helmig, F. S. Rowland, D. R. Blake (2012), Long-term decline of global atmospheric ethane concentrations and implications for methane, *Nature*, 488, 490-494.

Chapter 2:

Mass Fluxes and Isofluxes of Methane (CH_4) at a New Hampshire Fen Measured by a Continuous Wave Quantum Cascade Laser Spectrometer[1]

Abstract

We have developed a mid-infrared continuous-wave Quantum Cascade Laser direct-absorption Spectrometer (QCLS) capable of high frequency (≥1 Hz) measurements of $^{12}CH_4$ and $^{13}CH_4$ isotopologues of methane (CH_4) with *in-situ* 1-sec RMS $\delta^{13}C_{CH_4}$ precision of 1.5 ‰ and Allan-minimum precision of 0.2 ‰. We deployed this QCLS in a well-studied New Hampshire fen to compare measurements of CH_4 isoflux by eddy covariance (EC) to Keeling regressions of data from automated flux chamber sampling. Mean CH_4 fluxes of 6.5 ± 0.7 mg CH_4 m^{-2} hr^{-1} over two days of EC sampling in July, 2009 were indistinguishable from mean autochamber CH_4 fluxes (6.6 ± 0.8 mgCH_4 m^{-2} hr^{-1}) over the same period. Mean $\delta^{13}C_{CH_4}$ composition of emitted CH_4 calculated using EC isoflux methods was -71 ± 8 ‰ (95% C.I.) while Keeling regressions of 332 chamber closing events over 8 days yielded a corresponding value of -64.5 ± 0.8 ‰. Ebullitive fluxes, representing ~10% of total CH_4 fluxes at this site, were on average 1.2 ‰ enriched in ^{13}C compared to diffusive fluxes. CH_4 isoflux time series have the potential to improve process-based understanding of methanogenesis, fully characterize source isotopic distributions, and serve as additional constraints for both regional and global CH_4 modeling analysis.

[1] Santoni, G. W., B. H. Lee, J. P. Goodrich, R. K. Varner, P. M. Crill, J. B. McManus, D. D. Nelson, M. S. Zahniser, and S. C. Wofsy (2012), Mass fluxes and isofluxes of methane (CH4) at a New Hampshire fen measured by a continuous wave quantum cascade laser spectrometer, *J. Geophys. Res.*, 117, D10301, doi:10.1029/2011JD016960.

2.1. Introduction

Methane (CH_4) is roughly 25 times more effective than carbon dioxide (CO_2) in terms of its integrated greenhouse effect at hundred year timescales [*Lelieveld et al*., 1998]. After nearly a century of increasing atmospheric mixing ratios, growth rates of atmospheric CH_4 leveled off between 1999 and 2006, stabilizing atmospheric concentrations at ~1.8 μmol/mol [*Lassey et al*., 2007; *Dlugokencky et al*., 2009]. Subsequent data, however, suggested renewed growth [*Rigby et al*., 2008; *Bousquet et al*., 2011]. These changes in CH_4 concentrations and trends were not predicted [*Montzka et al*., 2011]. Forward modeling based on emission inventories, reaction rates, OH distributions, and other source and sink parameters have shown limited success in recreating observed spatial distributions over time [*Dlugokencky et al*., 2003; *Bousquet et al*. *2006*].

Isotopic measurements of CH_4 can help constrain source and sink uncertainties because processes related to methanogensis and methanotropy fractionate differently. Isotopic composition, commonly expressed in units of per mil (‰), represents a ratio of two stable isotopes in a sample to that of a standard according to:

$$\delta^{13}C_{sample} = \left(\frac{^{13}C_{sample}}{^{12}C_{sample}} \Big/ \frac{^{13}C_{vpdb}}{^{12}C_{vpdb}} - 1 \right) \cdot 1000 \qquad (2.1)$$

where Vienna Pee Dee Belemnite (VPDB) is the international standard for carbon isotopes. Different emission sources have distinguishing isotopic composition. The global mean $\delta^{13}C_{CH_4}$ of tropospheric CH_4 is -47.3 ‰, with interhemispheric differences on the order of 0.2 – 0.6 ‰ and seasonal variations ranging between 0.1 ‰ and 0.6 ‰ depending on site proximity to CH_4 sources with large seasonal changes in CH_4 flux [*Quay et al*., 1999; *Miller et al*., 2002], representing the sum of the flux weighted average of individual CH_4 source isotopic

compositions and the mean sink fractionation [*Gierczak et al*., 1997; *Lassey et al*. 2000; *Saueressig et al*., 2001].

The utility of isotopic characterization is limited by cumbersome measurement methods. $\delta^{13}C_{CH_4}$ measurements typically involve taking flask samples in the field and returning the flasks to a facility for analysis. Isotopic composition is determined by using a gas chromatograph (GC) to separate out CH_4, a combustor (C) to fully oxidize CH_4 to CO_2 and an Isotope Ratio Mass Spectrometer (IRMS) to measure the $^{13}C_{sample}$ /$^{12}C_{sample}$ ratio of that CO_2. High accuracy can be achieved: GC-C-IRMS has reported precision of ~0.1 ‰ with 0.2 L of air [*Miller et al*., 2002] and even better precisions of <~0.05 ‰ for larger volumes of air (order ~10 L) are achieved with 'off-line' techniques [*Lowe et al*., 1991]. Samples, however, are cumbersome to obtain, expensive to analyze, and require large masses of CH_4 and consequently large sample volumes for atmospheric measurements. Long-term continuous measurements in remote areas are impractical, and consistent monitoring of source composition is costly and labor intensive.

Significant research has focused on the development of laser-based absorption spectrometers to measure the isotopic composition of various tracers such as H_2O [*Dawson et al*., 2002; *Gupta et al*., 2009], CO_2 [*Crosson et al*., 2002; *Bowling et al*., 2003; *Griffis et al*., 2008; *McManus et al*., 2005, 2010], CH_4 [*Kosterev et al*., 1999; *Zahniser et al*., 2009; *Witinski et al*., 2010] and N_2O [*Waechter et al*., 2008; *Mohn et al*., 2010]. This technique generates continuous high frequency data and is readily usable at long-term monitoring sites. Such instrumentation has inspired the concept of CO_2 isofluxes – isotopically weighted CO_2 fluxes derived from isotopic mass balance – using eddy covariance (EC) techniques, useful in partitioning between respiration and photosynthesis and determining source isotopic composition of CO_2 [*Baldocchi and Bowling*, 2003; *Knohl and Buchmann*, 2005; *Saleska et al*., 2006; *Griffis et al*., 2008].

We present the first *in-situ* ambient CH_4 isoflux measurements by EC sampling using a tunable Quantum Cascade Laser direct-absorption Spectrometer (QCLS) at Sallie's Fen, a research fen in New Hampshire. We divide the isoflux measurements of CH_4 by the mass flux measurements of CH_4 to derive the isotopic composition of CH_4 emitted from the fen. Using the QCLS to subsample an established automatic flux chamber network (autochambers) distributed throughout the fen, we compare Keeling plot regressions of the autochamber data to derived $\delta^{13}C_{CH_{4_{source}}}$ values from EC isoflux methods in order to further characterize the isotopic source composition of CH_4 emissions from the fen. Potential improvements to instrumentation, sample conditioning, calibration, and data post-processing are discussed.

2.2. Site Description

Sallie's Fen is a *Sphagnum*-dominated peatland located in southeastern New Hampshire near the University of New Hampshire (43° 12.5' N, 71° 03.5' W). It is a mineral poor 1.7 ha fen with a peat depth range of 2 – 4.5 m. Ten automated Lexan flux chambers (autochambers) were interspersed in various plant communities in the fen and have been in operation since 2000. The chamber system and fen characterization are described in more detail by *Bubier et al*. [2003]. Figure 2.1 shows the distribution of the chambers in the fen, the boundary between the fen and surrounding forested lands and farms, the location of the EC tower sampling location, and the location of the QCLS during sampling. Ongoing measurements since 1989 have characterized gas exchange [*Carroll and Crill*, 1997; *Bubier et al*., 2003], seasonality [*Melloh and Crill*, 1996; *Treat et al*., 2007], vegetation [*Frolking and Crill*, 1994], and isotopic composition of carbon in CO_2 [*Shoemaker and Schrag*, 2011]. Year-long autochamber measurements from 2009 have used a Los Gatos Reseach (LGR) Integrated Cavity Output Spectrometer (ICOS) to record both CH_4 and CO_2 fluxes from the autochambers [*Goodrich et al*., 2011].

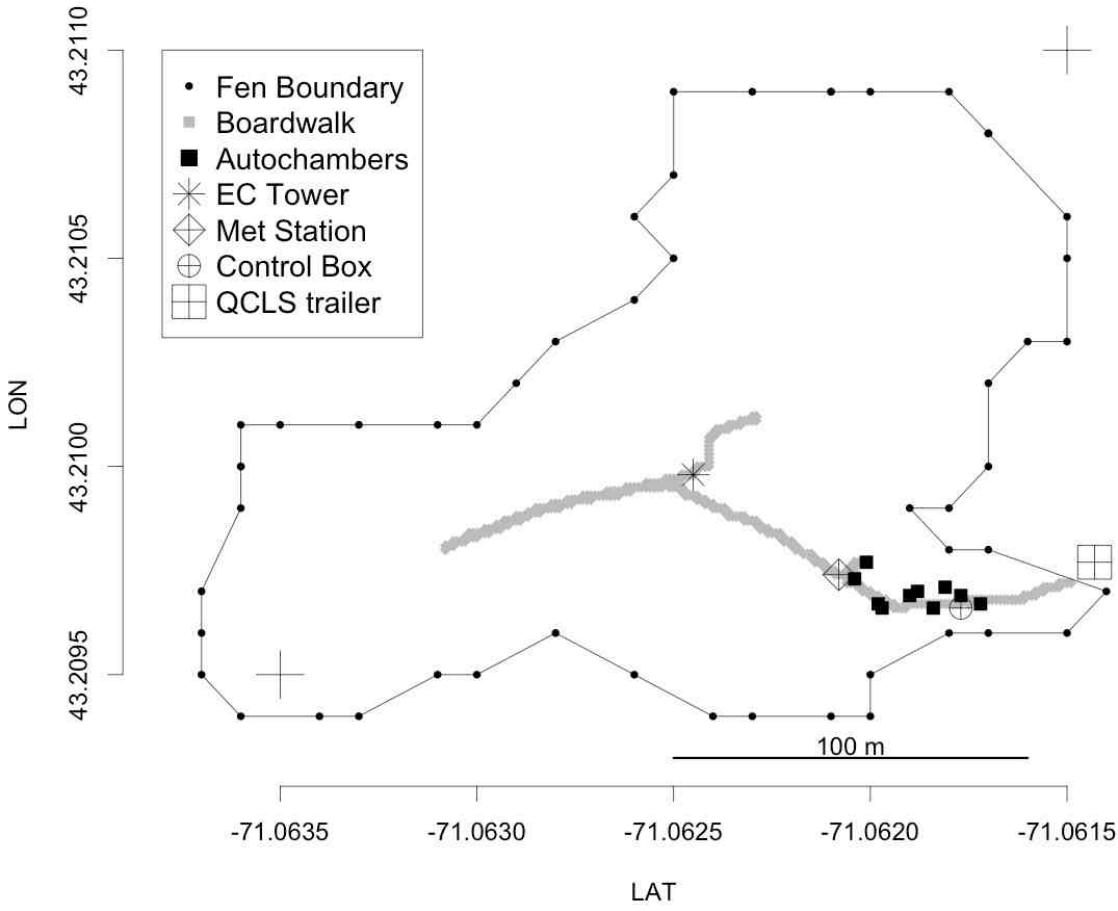

Figure 2.1: Location of the QCLS relative to the EC tower and autochambers at Sallie's Fen. Waypoints for the edge of the fen are shown in black. Land surrounding the fen is largely forested with Red Maple. The two hatches show the lower-left and upper-right points corresponding to the axis hash marks.

2.3. Instrumentation

2.3.1. Quantum Cascade Laser Spectrometer (QCLS)

Infrared absorption spectroscopy is a widely used technique based on the Beer-Lambert law to quantify trace gas concentrations using frequency-specific light absorption by individual molecules associated with ro-vibrational transitions. Advances in laser sources [*Faist et al*., 1994], detectors [*Nelson et al*., 2004], and multi-pass cells [*McManus et al*., 1995] have allowed for increased sensitivity [*Tuzson et al*., 2008; *McManus et al*., 2010] and high frequency measurements [*Zahniser et al*., 1995] of chemical species, and their stable isotopes, with low ambient concentrations.

In our sensor, a room-temperature, mid-infrared, continuous-wave Quantum Cascade Laser (QCL, Alpes Lasers) was housed in a hermetically sealed box, and its temperature (-14°C) and output frequency were controlled by a Peltier element in the box coupled to a recirculating chiller. Output power of the QCL was ~ 30 mW. The output frequency was coarsely maintained by controlling the laser temperature while fine adjustments to the output frequency were made by modulating the current with a high-compliance source (ILX Lightwave 3232). Current to the QCL was linearly ramped, scanning the laser frequency across 480 channels at a rate of 909 kHz. The scan included absorption lines for $^{12}CH_4$, $^{13}CH_4$, N_2O, and H_2O in the 1294.1 to 1294.4 cm^{-1} region. The current supplied to the laser dropped below lasing threshold for an additional 40 channels during each scan so that a background 'zero-light-level' (detector output) was measured. This ramped current and shutoff pulse sequence was controlled by TDL Wintel ® software. A total scan of 520 channels took $5.72 \cdot 10^{-4}$ seconds. Because the laser frequency did not respond linearly to the ramped current supplied to the laser, the laser frequency tuning rate was determined by fitting the spectrum of the system with a Germanium etalon in the beam path.

The instrumental half-width at half-maximum (HWHM) line width for the laser was <0.001 cm^{-1}, negligible compared to the molecular absorption line width.

Light from the QCL was directed into an astigmatic multi-pass sampling cell operated at low pressure (< 7 kPa) and detected by a thermoelectrically cooled detector. A long effective path length (210 m) was required to achieve sufficient precision on the $^{13}CH_4$ line and achieved using 238 passes between mirrors spaced 88.23 cm apart. During EC measurements, a TriScroll 600 l/min pump (Varian TriScroll600) generated a flow rate of ~11 slpm through the 5 L sample cell at 4.0 kPa, corresponding to a cell time constant of 1.08 seconds.

Mixing ratios were derived by TDL Wintel ® at ~1 sec intervals using a Levenberg-Marquardt least squares fit to each sample spectrum. The fitting procedure treated each spectral line as a Voigt profile taking into account the line strength, line location, air broadening coefficient, pressure, and temperature. A sample ~1 second spectrum representing the average of 1748 scans across the 480 channels is shown in Figure 2.2 along with the fit to the spectrum and a simulation using HITRAN line parameters and measured temperature, pressure, and mixing ratios. The baseline level (I_o in the Beer-Lambert law) was modeled as a low-order polynomial. The fitting algorithm took ~115 ms, making ~8 Hz measurements possible, but not independent on account of the cell time constant.

Removal of absorbance in the external path and baseline flattening was achieved by background subtraction using CH_4-free air as determined with the QCLS spectra. Middlesex Gases 0.0001 Ultra Zero Air was passed through the sample cell and an average background spectrum was acquired over 20 seconds. Sample spectra were normalized by dividing by the mean of bracketing background spectra [*Nelson et al.*, 2004].

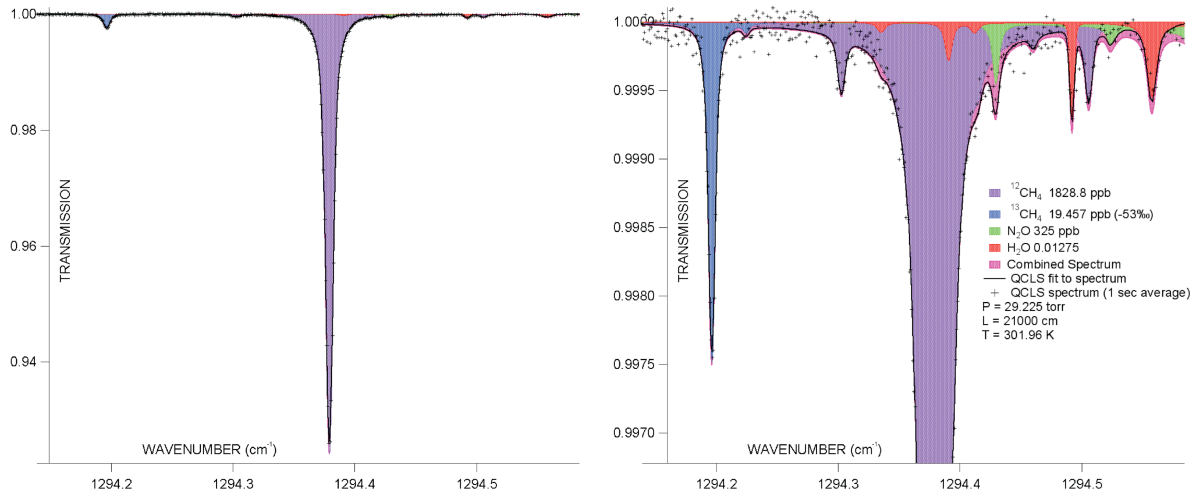

Figure 2.2: (left) A 1-second QCLS spectrum (pluses) of the 520 channels tuned across with the QCL along with the TDLWintel fit to the spectrum (black line), and a simulated HITRAN spectrum using the measured pressure, temperature, absorbing species (colors), and an instrumental linewidth of 0.001 cm^{-1}. **(right)** Close-up of the spectrum focusing on the $^{13}CH_4$ line.

Figure 2.3 shows an in-field time series of $^{12}CH_4$, $^{13}CH_4$, and their ratio expressed as $\delta^{13}C_{CH_4}$ for 30 minutes of sampling from a calibration tank. The $^{12}CH_4$ and $^{13}CH_4$ axes are each scaled by their relative abundance according to HITRAN, 0.0111031 and 0.988274, respectively, to illustrate the factor of ~6 greater noise on the $^{13}CH_4$ absorption line. Precision as a function of integration time gives a 1-sec RMS $\delta^{13}C_{CH_4}$ precision of 1.5 ‰ $Hz^{-1/2}$. The Allan minimum reaches <0.2 ‰ $Hz^{-1/2}$ at order 10^2 seconds, approaching the precision of GCC-IRMS methods. In order to compare instruments measuring different tracers, it is useful to express performance as absorption precisions, which relate measurement precisions to line strengths and ambient mixing ratios [*Nelson et al.*, 2002]. The absorption precisions for $^{13}CH_4$ and $^{12}CH_4$ are $4.5 \cdot 10^{-6}$ $Hz^{-1/2}$ and $1.5 \cdot 10^{-5}$ $Hz^{-1/2}$, respectively, determined using the corresponding line center absorbances of 0.25 % and 8 % calculated in the spectral simulation (Figure 2.2) and the 1 Hz Allan precisions at atmospheric abundance. Absorption precision on the major isotopologue ($^{12}CH_4$) is worse than for $^{13}CH_4$ because the measurement of the $^{12}CH_4$ is limited by noise proportional to its peak absorbance, a factor of 36 times greater than that of the $^{13}CH_4$.

Density fluctuations associated with water vapor fluxes are a concern for gas sampling systems because of the potential need for Webb-Pearlman-Leuning (WPL) corrections [*Webb et al.*, 1980]. Because of the fast flow rates and large sample volumes during EC measurements, drying the sample was impractical. Instead, the QCLS scan was expanded to include an additional 40 channels to measure water content using a nearby absorption line seen in Figure 2.2. Tuzcon et al. [2010] used a similar instrument to show that in addition to density corrections, line broadening effects due to water vapor accounted for an additional correction of 16% of the total WPL correction. This additional correction is non-negligible in certain applications such as EC observations above areas of low CH_4 flux. Tests using calibrated cylinder air run through a

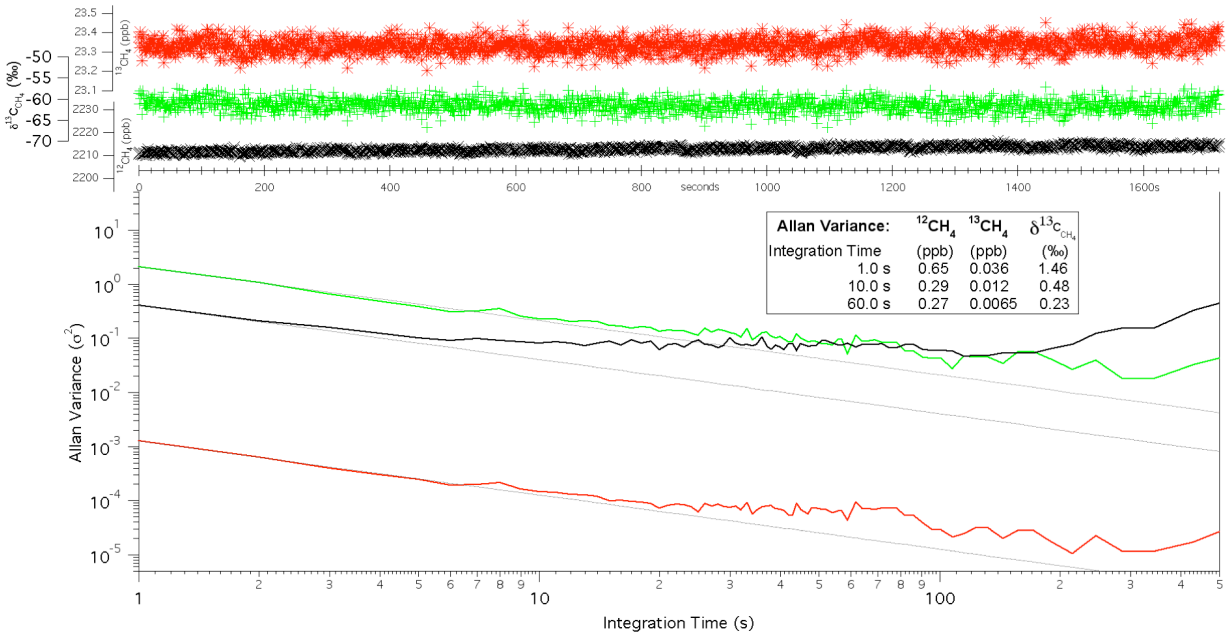

Figure 2.3: Time series and Allan variance plot of $^{12}CH_4$ (black), $^{13}CH_4$ (red), and $\delta^{13}C_{CH_4}$ (green). Data were taken over 45 minutes with 45 second background ultra-zero air spectra taken every 3 minutes. The axes for $^{12}CH_4$ and $^{13}CH_4$ each represent 40 ppb once scaled by the HITRAN isotopic abundances, 0.0111031 and 0.988274, respectively [De Bievre et al. 1984]. This illustrates the factor of ~6 larger noise on the $^{13}CH_4$ absorption line. The Allan variance for each time series is plotted along with the white-noise variance, showing that the $\delta^{13}C_{CH_4}$ measurement precision at minute-long timescales, 0.23 ‰, approaches the precision of GC-C-IRMS methods.

water-bubbler to generate air with varying H_2O mixing ratios showed that H_2O content did not modify the isotopic measurements since the line broadening effects were close to identical for both isotopologues.

2.3.2. Autochamber and Eddy Covariance Measurements

The QCLS, calibration tanks, and other peripherals were located in an enclosed 6' by 8' trailer at the edge of the fen, approximately 40 m from the autochambers. The autochambers consisted of 10 chambers with closed loops of 3/8" OD Synflex (Dekaron) tubing and total loop lengths ranging from 10 – 30 m depending on the chamber location relative to the valve manifold control box (Figure 2.1, 2.4). A two-stage diaphragm pump drew ~10 slpm of air through the autochambers in a closed loop via the valve manifold, spending 18 minutes on each individual chamber for a total autochamber sampling cycle of 180 minutes. Individual autochambers were automatically closed and opened at minutes 6 and 12, respectively, during which time a flux was calculated. Minutes 0-6 and 12-18 of a given 18 minute cycle flushed the system with ambient air while the autochamber lid was open to the atmosphere. Measurements of CO_2 and CH_4 at 12 second intervals were obtained using the LGR-ICOS which subsampled ~2 slpm from the main ~10 slpm draw [*Goodrich et al.*, 2011]. During autochamber subsampling, a second closed loop of 80 m using 1/4" OD Synflex tubing brought air to the QCLS from the main ~10 slpm autochamber flow (Figure 2.4). A 4-stage low pressure pump (Vaccubrand MD-4) was used to achieve a 2.5 slpm flow through the 5 L QCLS sampling cell volume at 5.3 kPa. A Licor (LI-7000) was positioned upstream in series of the QCLS and recorded CO_2 and H_2O at 1 Hz using a CO_2-calibrated dry tank as the reference. Calibration additions were done upstream of the Licor and involved an additional solenoid valve to control return flow from the pump to the main autochamber draw so as not to return tank air to the main autochamber draw.

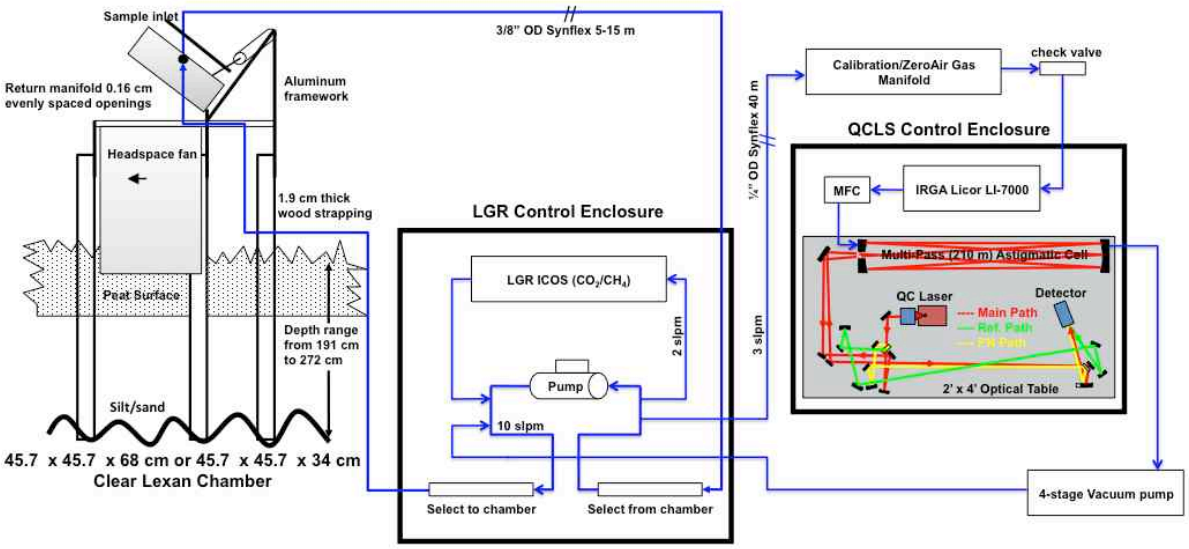

Figure 2.4: Autochamber system depicted by *Bubier et al*. [2003] showing the sample flow (blue arrows) for both QCLS and LGR subsampling from the main autochamber loop. The subsamples for both the LGR and QCLS are returned to the main autochamber loop downstream of the main autochamber pump (middle) and individual chambers are selected sequentially on an 18-minute-per-chamber cycle.

The EC sampling location was positioned in the center of the fen, approximately 100 m from the QCLS. A sonic anemometer (Campbell CSAT-3) was mounted on a 3 m tower such that the sonic head was 2.0 m above the peat surface and oriented facing into the predominant wind-direction (N-NE). A sample inlet consisting of two 1-micron filters connected in parallel (to minimize the pressure drop across the filter and decrease the likelihood of blockage) was located 2.0 m above the peat surface and 0.2 m downwind from the CSAT head. The vegetation canopy was roughly 0.3 m above the peat surface. To minimize the pressure drop associated with a 100 m long sampling line, 1/2" OD synflex tubing was used, requiring a 26 slpm flow to maintain fully turbulent conditions (R_e ~ 4000), and resulting in a pressure drop of only 3.3 kPa from the EC sampling inlet to the QCLS.

To avoid wasting calibration gases associated with high flows during EC sampling, tank air was introduced upstream of the QCLS through a manifold equipped with a diaphragm check valve to reduce excess regulator pressure down to atmospheric pressure. During tank air additions the mass flow controller maintained instantaneous cell pressure fluctuations to within ~100 Pa of sampling pressure, which stabilized within 2 seconds of switching from sample to calibration gas. A second two-head diaphragm pump (KNF Neuberger Model UA0026.1) pulled ~13 slpm through the Licor measuring H_2O and CO_2 at 5 Hz. The cell volume of the Licor is 10.86 cm^3, resulting in a sample cell time constant of .086 seconds. The ~11 slpm QCLS draw (Section 3.1), the ~13 slpm Licor draw, and a third draw of ~7 slpm were connected in parallel for a total flow of ~ 31 slpm through the main 100 m sampling line. This configuration, shown in Figure 2.5, minimized tank air consumption, ensured a ~1 sec response time, and maintained turbulence at the inlet even during tank-air additions to the QCLS.

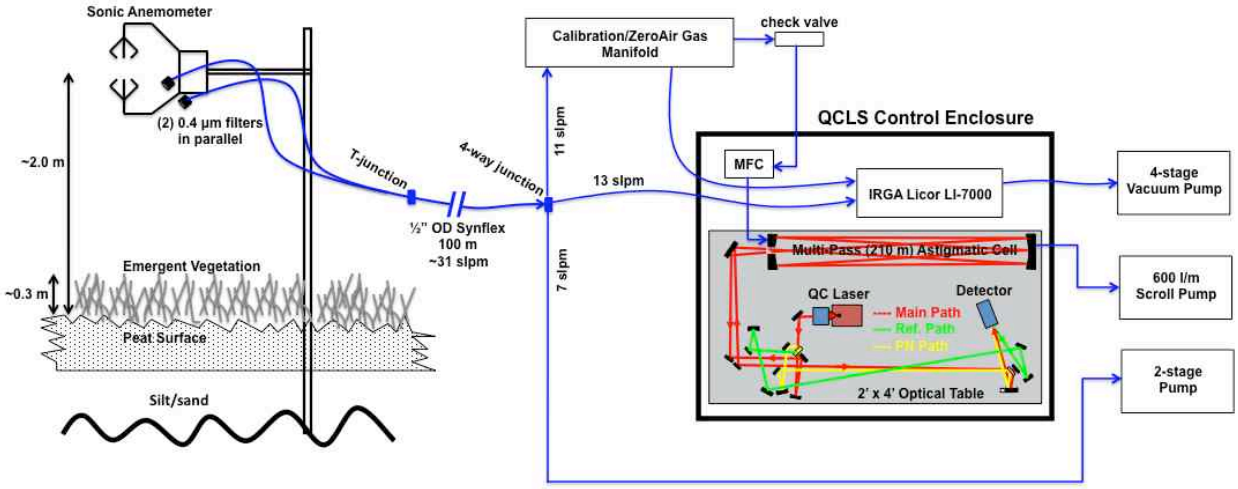

Figure 2.5: Eddy Covariance setup and flow diagram during QCLS isoflux measurements. Sample flow is shown in blue arrows, originating by the EC tower in the middle of the fen. Three pumps (right) draw through various instruments to maintain fully turbulent conditions throughout the sampling system.

A datalogger (Cambell CR-10 with new PROM for CSAT-3 sonic commands) located at the base of EC tower recorded wind velocities and sonic temperatures from the sonic anemometer at 8 Hz as well as air and water temperatures from two thermistors at 1 Hz. A PC in the instrument enclosure periodically collected data from the datalogger via a short-haul modem (Campbell RAD-5). Unfortunately, data transfers every 3 minutes resulted in corruption of the CSAT data with spurious time-stamps. Exclusion of these artifacts resulted in the loss of 34% of the sonic data over the EC measurement period. The PC logging the CR-10 data also serially recorded the Licor data and was networked and time-synchronized to the QCLS computer.

2.4. Methods

2.4.1. QCLS Calibrations

QCLS accuracy depended largely on the calibration procedure and the stability of the background laser spectrum in the absence of absorbing species. Ultra-zero air was introduced to the sampling cell every 10 minutes (background subtraction) in order to capture the influence on the baseline of small temperature and pressure variations that occurred over diurnal timescales. Calibrations were done using pairs of tanks that spanned the observed atmospheric range of CH_4 above the fen, notably ~1.8 to ~10 μmol/mol, the latter of which was regularly observed during summer/fall nighttime inversions. During EC measurements, a low-span (LS, ~1.8 μmol/mol) tank was sampled every 10 minutes and a high-span (HS, ~10 μmol/mol) tank every 3 hours. This was done because the LS tank was closer to ambient concentration and therefore had a greater influence on the calibration interpolation applied to the data. During autochamber measurements, when fluxes inside a closed chamber induced consistently higher mixing ratios, HS and LS tanks were alternately sampled every 18 minutes, coincident with the autochamber cycle. A cubic spline was interpolated to the $^{12}CH_4$ and $^{13}CH_4$ mixing ratios for both the HS and

LS tanks. Each isotopologue of CH_4 was treated as an independent measurement, separately calibrated. The range of variation of mixing ratios of CH_4 obtained from spectral parameters only for one particular calibration tank over the course of a day, normalized by the atmospheric abundance of each, was roughly 30 ppb or 1.6%. The cubic spline interpolations versus time for $^{12}CH_4$ and $^{13}CH_4$ tracked each other well, largely because diurnal temperature variations affected each line similarly. The LS and HS tanks were calibrated to the VPDB scale by means of duplicate subsampled flasks of all calibration cylinders which were analyzed offline by means of GC-C-IRMS at Woods Hole Oceanographic Institute. Calibrated tank values for χ_{CH_4} were given by Scott Specialty Gases at 1% accuracy (i.e. ±18 nmol/mol for a ~1.8 μmol/mol LS tank and ±100 nmol/mol for a ~10 μmol/mol HS tank) and confirmed using the QCLS and spectroscopic parameters (linestrength, pressure, temperature, broadening coefficients, etc.). QCLS mixing ratios of total CH_4, $^{12}CH_4$, and $^{13}CH_4$ acquired by spectral fitting were then linearly interpolated to the cubic spline calibration interpolations, putting them on the VPDB scale. The interpolation was calculated as:

(2.2)

$$\chi_{^{12}CH_4} = \left(\frac{\chi_{^{12}CH_{4,QCLS}} - \chi_{^{12}CH_{4,LS,spl}}}{\chi_{^{12}CH_{4,HS,spl}} - \chi_{^{12}CH_{4,LS,spl}}} \right) \cdot \left(\chi_{^{12}CH_{4,HS,cal}} - \chi_{^{12}CH_{4,LS,cal}} \right) + \chi_{^{12}CH_{4,LS,cal}} = \chi_{CH_4} \cdot A_{HITRAN_{^{12}CH_4}}$$

$$\frac{\chi_{^{13}CH_4}}{\left({}^{13}C_{vpdb} / {}^{12}C_{vpdb} \right)} = \left(\frac{\chi_{^{13}CH_{4,QCLS}} - \chi_{^{13}CH_{4,LS,spl}}}{\chi_{^{13}CH_{4,HS,spl}} - \chi_{^{13}CH_{4,LS,spl}}} \right) \cdot \left[\chi_{^{12}CH_{4,HS,cal}} \cdot \left(1 + \frac{\delta^{13}C_{CH_{4,HS,vpdb}}}{1000} \right) - \chi_{^{12}CH_{4,LS,cal}} \cdot \left(1 + \frac{\delta^{13}C_{CH_{4,LS,vpdb}}}{1000} \right) \right] + \chi_{^{12}CH_{4,LS,cal}} \cdot \left(1 + \frac{\delta^{13}C_{CH_{4,LS,vpdb}}}{1000} \right)$$

(2.3)

where $\chi_{^{12}CH_4,QCLS}$ and $\chi_{^{13}CH_4,QCLS}$ represent the 1 Hz dry air mixing ratios calculated by TDL Wintel ®, $\chi_{^{12}CH_4,HS,spl}$ and $\chi_{^{13}CH_4,HS,spl}$ the high-span spline interpolations to the $^{12}CH_4$ and $^{13}CH_4$ mixing ratios calculated by TDL Wintel ® from retrieved absorbance during the calibration tank additions, $\chi_{^{12}CH_4,LS,cal}$ and $\chi_{^{12}CH_4,HS,cal}$ the calibrated mole fraction values for the LS and HS tanks respectively, and $\delta^{13}C_{CH_4,LS,vpdb}$ and $\delta^{13}C_{CH_4,HS,vpdb}$ the GC-C-IRMS calibrated isotopic composition of the LS and HS tanks, respectively. The ratio of $\chi_{^{13}CH_4}$ to $\chi_{^{12}CH_4}$ computed using Equations 2.3 and 2, respectively, represents the quantity $\frac{^{13}C_{sample}}{^{12}C_{sample}}$ and can be expressed in ‰ notation according to Equation 2.1. The total mole fraction of CH_4, χ_{CH_4}, is determined using Equation 2.2 and the HITRAN isotopic abundances for the dominant isotopologue of CH_4, $A_{HITRAN_{^{12}CH_4}}$ [*De Bievre et al*., 1984].

4.2. Eddy Covariance Data Processing

Continuous EC data were obtained on 18-19 July 2009. The CH_4 flux was calculated from the covariance of χ_{CH_4}' and w', the fluctuating parts of the CH_4 mixing ratio and vertical wind velocity, respectively. Adopting the notation of *Saleska et al*. [2006], we define the CH_4 flux as:

$$F_{CH_4} = \rho\overline{w'\chi_{CH_4}'} \tag{2.4}$$

where ρ represents the density of the sample, the overline represents the covariance of the two quantities, and the primes in the covariance term are fluctuations from the mean using Reynolds decomposition. Derivation of the isoflux has been presented by *Saleska et al*. [2006] and *Griffis et al*. [2008] who both focus on isofluxes of CO_2 as a means of partitioning photosynthesis and respiration. The analog of Equation 2.4 for isofluxes of CH_4 is:

$$\delta^{13}C_{CH_{4_{source}}} \cdot F_{CH_4} = \rho \overline{w' \left(\delta^{13}C_{CH_4} \cdot \chi_{CH_4} \right)'} \quad (2.5)$$

where $\left(\delta^{13}C_{CH_4} \cdot \chi_{CH_4} \right)'$ is the fluctuating part of the Reynolds decomposition of the product of $\delta^{13}C_{CH_4}$, calculated from Equations 2.1–3, and χ_{CH_4}, the calibration corrected mixing ratio from Equation 2.2. We estimate the isotopic source composition of CH_4 from the fen, $\delta^{13}C_{CH_{4_{source}}}$, by dividing Equation 2.5 by Equation 2.4. Isotopic data from the autochambers do not exist for these two days, but comparisons to Keeling plots were made with QCLS autochamber data later in the summer.

Non-sonic scalars were measured ~100 m from the EC tower at the QCLS trailer. Lag-times were determined by maximizing the covariance of each scalar (χ_{CH_4}', χ_{CO_2}', χ_{H_2O}', etc.) with w' as a function of Δt over 100 second intervals. 42 of the 96 half-hour intervals with u* >0.1 m/s and a clearly identifiable maximum/minimum covariance in the lagged covariance plot were linearly interpolated to determine the sampling lag time (typically ~ 6-8 seconds) through the tubing for each half-hour time segment. The standard deviation of the covariances of the first and last 20 seconds of the 100 second interval is reported as measurement error, a method often used for closed-path sensors [*Wienhold et al*., 1994; *Kormann et al*., 2001; *Smeets et al*., 2009]. Other relevant quantities calculated have been summarized elsewhere: *Kormann et al*. [2001] provide a detailed overview of the important quantities, *Smeets et al*. [2009] discuss CH_4–specific EC calculations, and both *Webb et al*. [1980] and *Ibrom et al*. [2007a] discuss WPL corrections.

We performed two coordinate rotations to force the mean horizontal and vertical winds to zero. Rotation of the vertical axis resulted in a mean angle of rotation for the 96 half-hourly segments of 0.56° with a 95% CI of 1.1°. EC averaging time was set to be 30 minutes, long

enough to capture the fast and slow eddies up to the spectral gap beyond which diurnal and synoptic variability influenced the power spectrum of winds, momentum, and heat flux. Spectral analysis showed that the ogives – the cumulative power densities of the cospectra – of our flux data asymptote well before frequencies associated with 30 minutes [*Lee et al.*, 2004]. Because of the gaps in the data every 3 and 10 minutes associated with datalogger transfers and calibrations, respectively, Lomb-Scargle methods were used instead of traditional spectral analysis to compute cospectra [*Press et al.*, 1992].

The frequency spectrum of w' for 57 of the 96 half-hour intervals over the two days, each having a friction velocity (u*) greater than 0.1 m/s is shown in Figure 2.6. Relevant cospectra calculated by Lomb-Scargle methods are shown in Figure 2.7 and represent half-hour averages with power averaged into exponentially increasing frequency bins. The spectra are approximated by the model [*Lee et al.*, 2004]:

$$f \cdot S(f) = \frac{A \cdot \left(f / f_x \right)}{\left[1 + m \left(f / f_x \right)^{2\mu} \right] \frac{1}{2\mu} \left(\frac{m}{m+1} \right)} \tag{2.6}$$

where A is a normalization parameter, f_x is the frequency at which the frequency-weighted power co/spectrum reaches a maximum (here 0.09 Hz for w' and $w'T'$, and 0.064 Hz for $w'\chi_{CH_4}'$), μ is a broadness parameter (here 2/3, consistent with a slightly unstable atmosphere), and m is set to 3/2 for spectra and 3/4 for cospectra to describe the -5/3 and -7/3 power laws in the inertial subrange, respectively. Peak power was well predicted by the Kaimal curve for the spectra using a measurement height of 2.0 m, a vegetation height of 0.3 m, and a mean horizontal wind velocity of 0.45 m/s [*Kaimal and Finnigan*, 1994]. Cospectra in Figure 2.7, approximated from

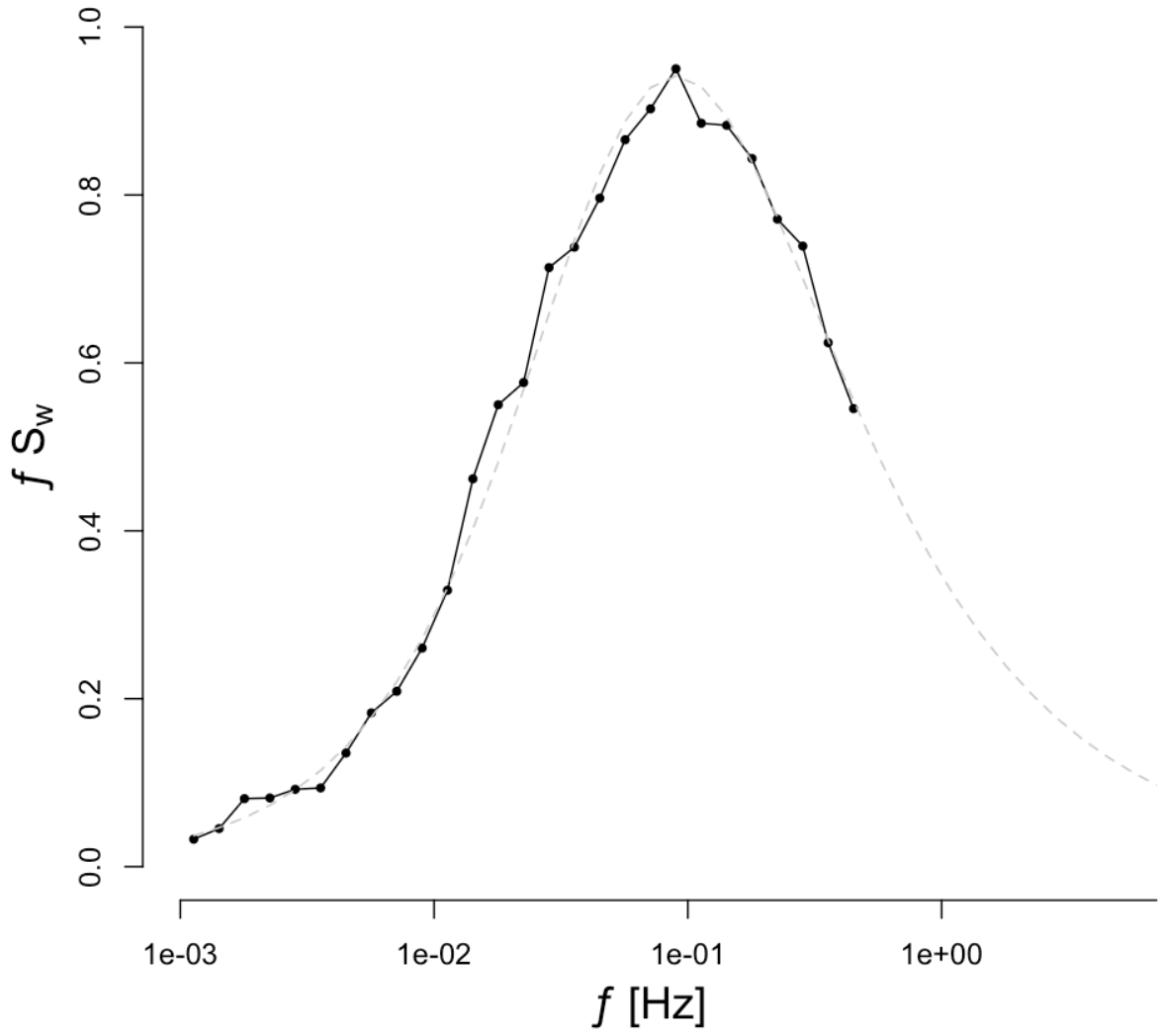

Figure 2.6: The vertical wind velocity (w') spectrum from the 2m tower using the power spectrum of 57 of the 96 half-hour intervals (two days) calculated by Lomb-Scargle methods (black) and the predicted Kaimal curve (grey) [*Kaimal and Finnigan*, 1994; *Lee et al*., 2004] for a slightly unstable atmosphere.

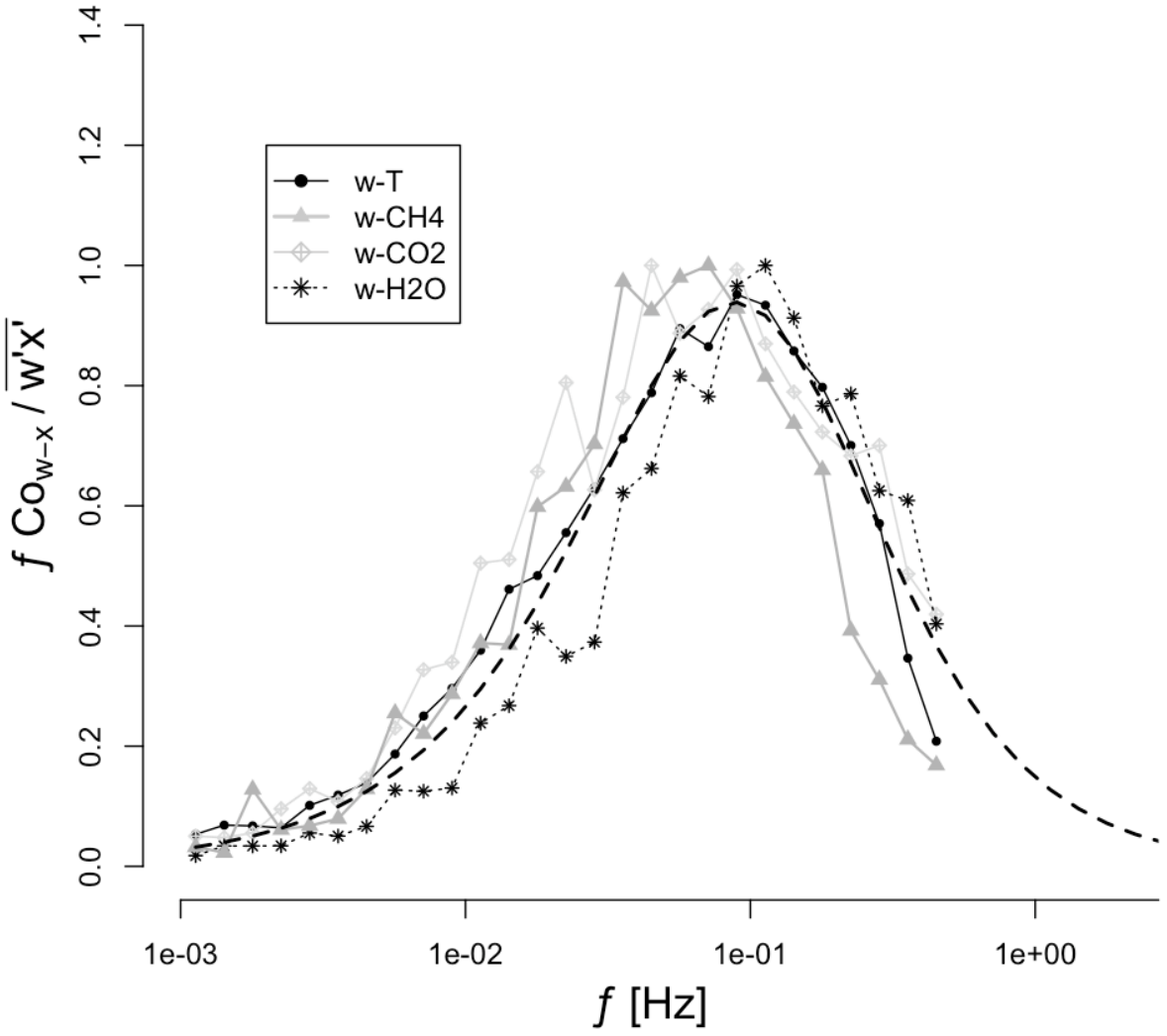

Figure 2.7: Various cospectra calculated from Lomb-Scargle methods. Cospectra are multiplied by the frequency and normalized by the half-hourly covariance and represent the mean of the 57 half-hour intervals with u* >0.1 m/s. The predicted cospectrum for $w'T'$ is shown as a smooth black dashed line [*Lee et al*., 2004].

Equation 2.6 with m = 3/4, show some evidence of differential spectral attenuation and illustrate the different eddy lengthscales responsible for the fluxes of the different scalars.

We calculated CH_4 fluxes and isofluxes from Equations 2.4 and 2.5 using two methods: WPL corrected fluxes and dry-mole fraction fluxes. The first used the water vapor measurement of the Licor and applied WPL corrections to the wet-mole fraction CH_4 fluxes. The second used the QCLS water measurement to correct the $^{12}CH_4$ and $^{13}CH_4$ mixing ratios to dry-mole fraction. The two methods produced statistically indistinguishable results at the p = 0.05 level and the latter method is presented in the results. Because measurements such as χ_{CH_4}' and χ_{CO_2}' did not occur at frequencies as high as that of the sonic anemometer, degradation of the $\overline{w'T_v'}$ cospectrum (vertical wind velocity and sonic virtual temperature) from 8 Hz 'raw' data to 5 Hz Licor and 1 Hz QCLS data was used to calculate the correction factor for high-frequency loss [*Ibrom et al*., 2007b] according to:

$$F_1 = \frac{\overline{w'T_{v_{raw}}'}}{\overline{w'T_{v_{sample}}'}} \tag{2.7}$$

For Licor sampling at 5 Hz, the mean F_1 was 100.05 ± 0.85 (95% C.I.) % showing that the high-frequency loss due to degradation of an 8 Hz signal into a 5 Hz was negligible. Correction factors for high frequency loss of CO_2 and H_2O fluxes were therefore not applied to the data. The corresponding high frequency correction factor for the 1 Hz QCLS data was 92.87 ± 6.59 % indicating a loss of ~7 % of the covariance at high frequency. We corrected for this loss using Equation 2.7, substituting CH_4 for T_v and rearranging, to solve for the true covariance as [*Ibrom et al*., 2007b; *Kroon et al*., 2007]:

$$\overline{w'\chi_{CH_4}'} = \frac{1}{F_1} \cdot \left(\overline{w'\chi_{CH_{4@1Hz}}'} \right) \tag{2.8}$$

Horst [1996] calculate F_1 using spectral transfer function analysis according to $F_1 = 1 + (2\pi f_m \tau_c)^{\alpha}$ where f_m represents the peak of the logarithmic cospectrum (0.064 Hz for χ_{CH_4}), τ_c represents the time constant of the sensor (1.08 seconds for the QCLS), and $\alpha = 7/8$ for neutral and unstable stratification within the surface-flux layer, giving a high frequency attenuation correction factor of 1.48, much larger than the correction factor derived from Equation 2.7.

2.4.3. Autochamber Data Processing

Eighty autochamber closures per day were observed by the QCLS data over eight days (12-13, 28-31 August 2009, 1-2 September 2009). Each chamber closing was treated as an independent measurement of a) the CH_4 flux, calculated from chamber ground temperature (T_{ground}), volume ($V_{chamber}$), surface area ($A_{chamber}$), and a regression of the CH_4 time series using a Type I simple linear regression (SLR, e.g. blue lines on the left of Figure 2.10) according to:

$$F_{CH_4} = \frac{\Delta \chi_{CH_4}}{\Delta t} \cdot \left(\frac{M_{CH_4} P_{ground} V_{chamber}}{R T_{ground} A_{chamber}} \right), \tag{2.9}$$

where R is the ideal gas constant, and M_{CH_4} is the molecular mass of CH_4, and b) isotopic source composition for that chamber, $\delta^{13}C_{CH_{4_{source}}}$, derived from the y-intercept of a Keeling plot (e.g. x = 0 on the right side of Figure 2.10) in which $\delta^{13}C_{CH_4}$ is plotted against $1/\chi_{CH_4}$. The regression is a mixing line assuming two end members: CH_4 from the fen and atmospheric CH_4. In this case, Type II regressions which use independent error constraints on ordinate and abscissa variables were indistinguishable from Type I regression because the measurement error on $1/\chi_{CH_4}$ was negligible compared to the measurement error of $\delta^{13}C_{CH_4}$.

Of the 640 chamber closings observed with the QCLS, 585 were used to calculate fluxes and isotopic composition; 217, 139, and 229 of which were categorized as linear, ebullitive, and random fluxes, respectively. Linear buildups were defined as having residual variances on the flux regression <0.05 nmol/mol/s. CH_4 fluxes both by diffusion from the water surface and by plant mediated transport exhibited linear buildups of CH_4 in chambers whereas ebullitive fluxes showed sudden jumps, categorized by a CH_4 flux regression >8 nmol/mol/s that were between 10 and 120 seconds in duration as defined in *Goodrich et al*. [2011]. In order to differentiate the isotopic composition of ebullitive fluxes in the autochambers, Keeling regressions using the ebullitive events were compared to the Keeling regression of the entire flux interval using 83 definitive ebullitive events which lasted between 10 and 60 seconds. Random buildups showed oscillations in the CH_4 time series having amplitudes >50 nmol/mol, a result of improper sealing of the chamber due to emergent vegetation and/or inadequate mixing of the chamber headspace.

2.5. Results

Figure 2.8 shows the mean mixing ratios of CH_4, CO_2, and $\delta^{13}C_{CH_4}$ along with relative humidity, temperature, u*, wind speed, and wind direction. Half hour mean CH_4 and CO_2 mixing ratios were correlated, showing a diurnal pattern consistent with nighttime inversion of the Planetary Boundary Layer (PBL). These inversions typically involve stable atmospheric conditions, u* < 0.1 m/s and low mean wind speeds. Wind direction averaged -35 degrees N-NW over the two days. Mean half-hourly $\delta^{13}C_{CH_4}$ values approached the free tropospheric northern hemisphere value of -47 ‰ during the periods of highest wind speed. During periods of lower mean wind speeds, the influence of the fen on the mean $\delta^{13}C_{CH_4}$ was apparent with deviations towards more ^{13}C depleted CH_4 values, consistent with a biogenic CH_4 source.

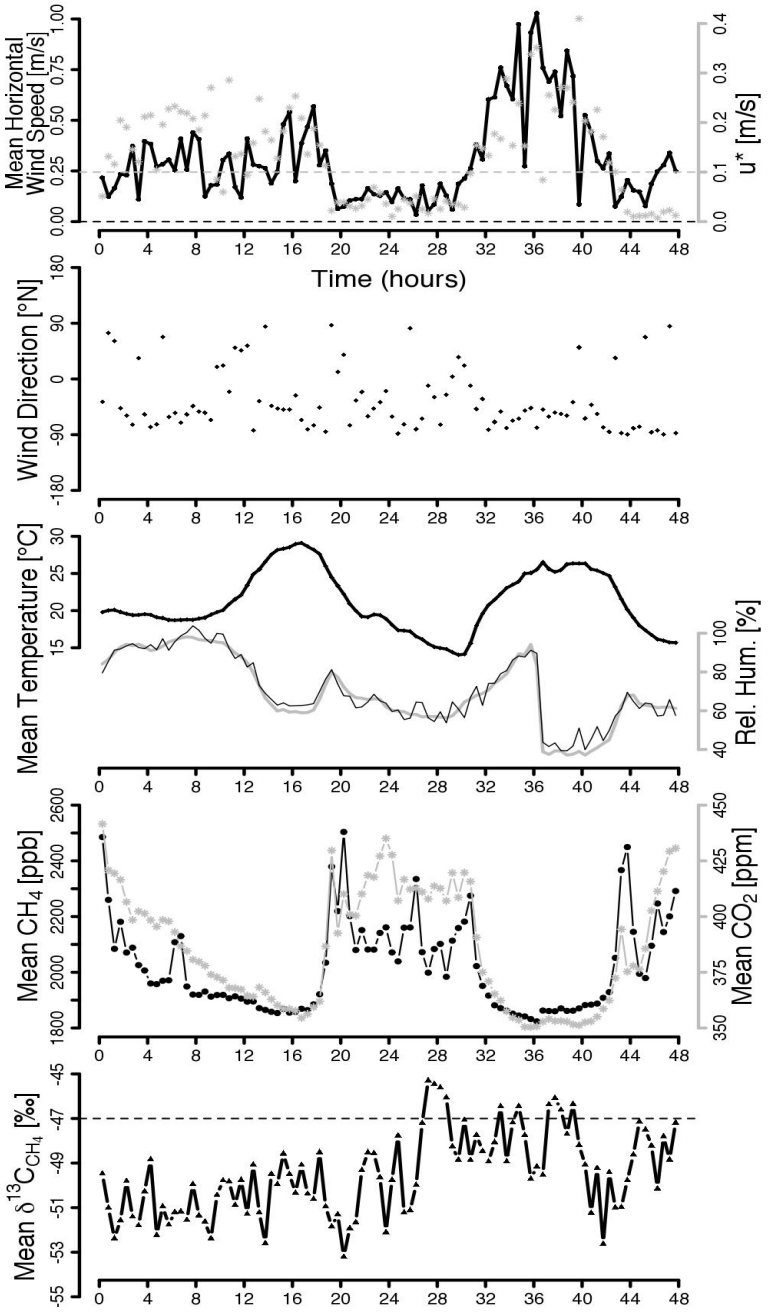

Figure 2.8: Time series of EC half-hourly averages over 18-19 July 2009 of (a) mean horizontal wind speed (black) and u* (grey) where the dashed grey line is the u* threshold of 0.1 m/s used as a filter, (b) wind direction, (c, left) air temperature, (c, right) relative humidity shown calculated using the Licor H_2O measurement (grey) and using the QCLS H_2O measurement (thin black), (d) mean mixing ratios of CH_4 (black) and CO_2 (grey), and (e) mean $\delta^{13}C_{CH_4}$ where the dashed black line in represents -47 ‰, the mean isotopic composition of ambient CH_4 in the free troposphere.

The flux time series is shown in Figure 2.9 where solid dots represent fluxes calculated during periods in which u* exceeded 0.1 m/s (fluxes for periods with u*<0.1 m/s are artifacts not used in our analysis but are shown as open grey circles). The mean CH_4 flux for the two days using only data with u* >0.1 m/s (solid dots) was 6.5 ± 0.7 (95% C.I.) mg CH_4 m^{-2} hr^{-1}, in excellent agreement with the mean autochamber CH_4 flux of 6.6 ± 0.8 (95% C.I.) mg CH_4 m^{-2} hr^{-1}. Mean CH_4 isofluxes were -518 ± 73 (95% C.I.) ‰ mg CH_4 m^{-2} hr^{-1} and the resulting distribution of inferred $\delta^{13}C_{CH_{4_{source}}}$ had a mean of -79 ± 9 (95% C.I.) ‰.

Figure 2.10 shows examples of chamber closing cycles illustrating the buildup of CH_4 following chamber closing at minute 1 and the abrupt return to near-ambient concentrations after minute 7 when the chamber opens (the lag is residual high CH_4 data from the closed QCLS loop not sampled during QCLS calibration). The linear regression to minutes 2-6 used to calculate the flux is shown in blue. High concentrations of CH_4 during the chamber closure intervals correspond to $\delta^{13}C_{CH_4}$ depletions, consistent with a biogenic CH_4 source. Keeling analysis is well suited to chamber data, as large enhancements from ambient concentrations of CH_4 that accumulate during a chamber closure improve regression statistics for extrapolation to infinite concentrations ($1/\chi_{CH_4} \rightarrow 0$) [*Pataki et al.*, 2003]. The linear increase in χ_{CH_4} shown in Figure 2.10 corresponds to a flux that is half the mean August fluxes yet still shows enhancements of ~1 μmol/mol above ambient CH_4 concentrations. The regression shown has a standard deviation on the intercept of 0.9 ‰, representing the error estimate of the isotopic source composition, $\delta^{13}C_{CH_{4_{source}}}$. Uncertainties in the Keeling intercept decrease with increasing CH_4 enhancements, as shown in Figure 2.11. The 25, 50, and 75 quartiles of CH_4 fluxes have associated 1σ

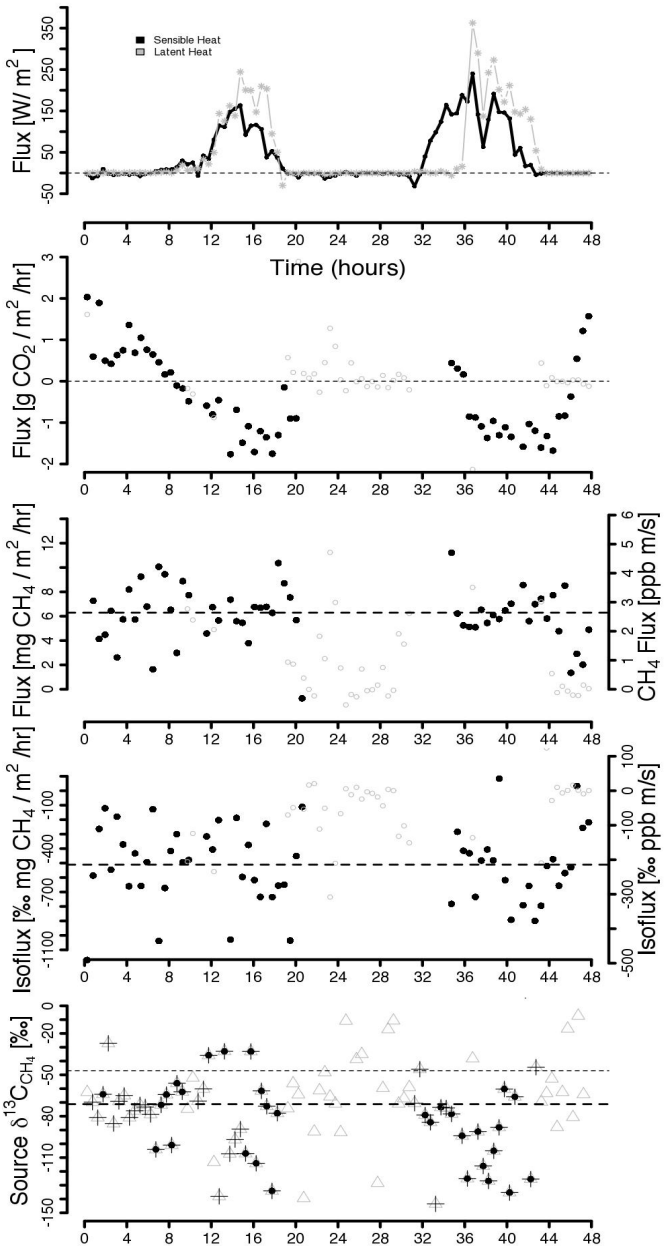

Figure 2.9: Time series of EC half-hourly (a) sensible and latent heat fluxes, (b) CO_2 fluxes, where the thin dashed black line denotes the transition from positive to negative NEE and light grey circles represent fluxes not used in the analysis because they correspond to half-hour intervals with u* < 0.1 m/s, (c) CH_4 fluxes where the thick dashed black line denotes the average over the two days, and (d) CH_4 isofluxes. For (c) and (d), two different scales are used on the left and right axes. The time series of the resulting source isotopic composition of CH_4 derived from the measurements, $\delta^{13}C_{CH_{4_{source}}}$ is shown in (e) for n = 90 (grey triangles), n = 55 (thin black pluses) and n = 32 (solid black circles) of the 96 half-hour intervals corresponding to the different filters discussed, along with a thin dashed line at -47 ‰, the mean isotopic composition of ambient CH_4 in the free troposphere, and a thick dashed line at -71 ‰, the mean isotopic composition for n = 90 (grey triangles).

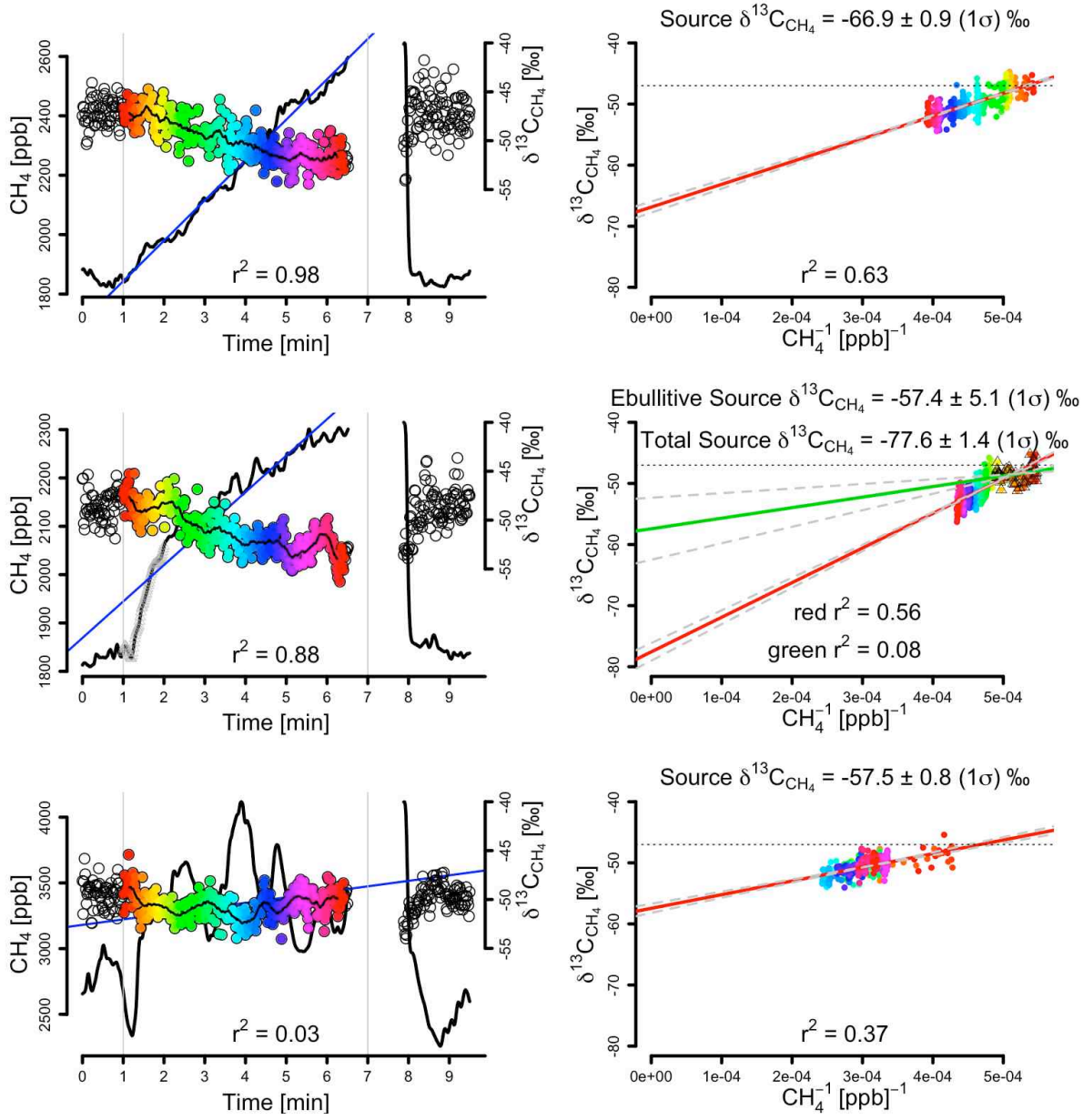

Figure 2.10: (left) Examples of QCLS autochamber subsampling intervals for linear (**top**), ebullitive (**middle**), and random (**bottom**) fluxes calculated with Equation 2.9 and the blue regression. Missing data corresponds to background zero-air, low-span, or high-span calibration tank additions. **(right)** Corresponding Keeling plots for the three time series where $\delta^{13}C_{CH_4}$ is shown color-coded by elapsed time to relate the left plots to the right. The isotopic composition of background atmospheric CH_4 is shown at -47 ‰ (dotted black) and the Keeling regression slope is shown in red. An additional Keeling regression for an ebullition event (middle) is shown in green, where the grey (triangles) represent the ebullitive subset of the data used in the analysis.

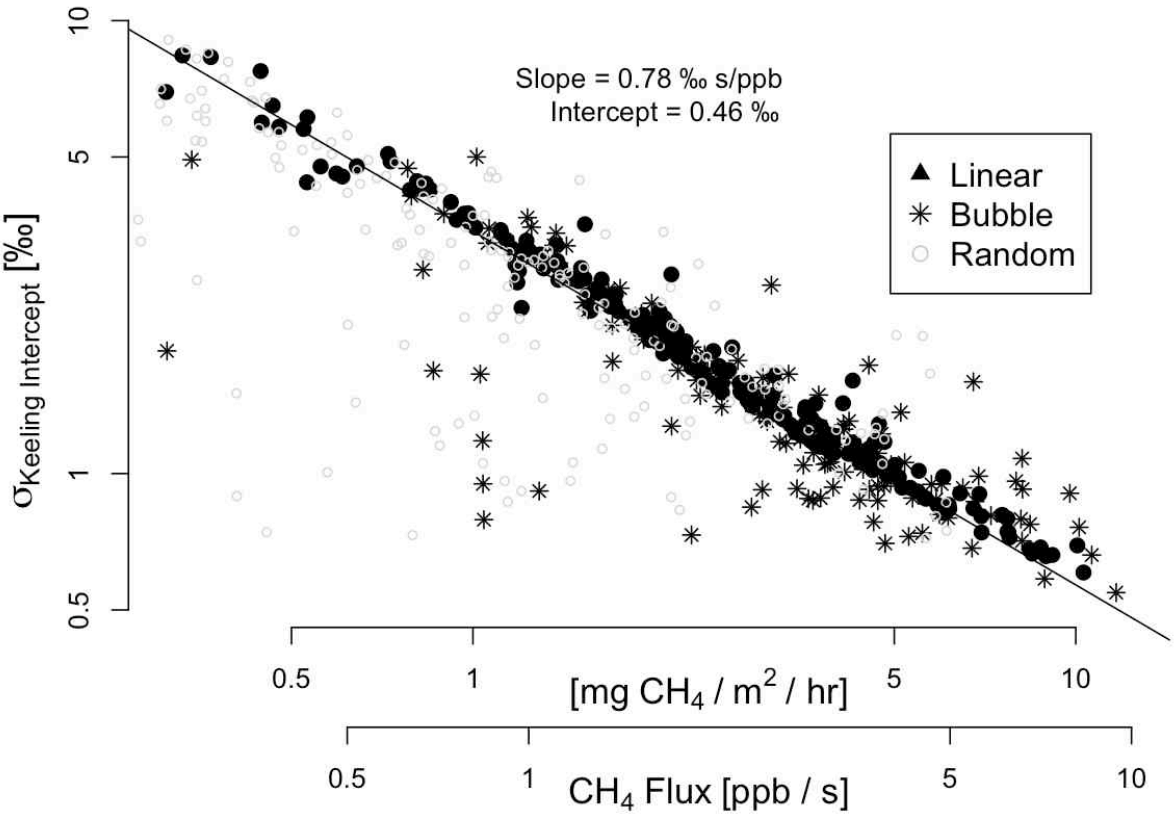

Figure 2.11: Log-log relationship of 1σ error on Keeling intercept as a function of CH_4 flux (shown with two separate but equivalent scales). The slope and intercept give predicted Keeling plot 1σ errors on the regression. The 1σ errors on the regression for linear, bubble, and random chamber buildups are 1.3 ‰, 1.1 ‰, and 2.5 ‰, respectively. The variance is smaller on autochamber closings containing ebullitive events because excursions of CH_4 above ambient conditions are generally larger.

uncertainties on the isotopic source of 2.3 ‰, 1.6 ‰, and 1.1 ‰, with minimum uncertainties of <0.6 ‰ associated with the largest fluxes.

Variability in Keeling intercepts largely represent real differences in the isotopic composition of CH_4 from the fen in the individual chambers. The distributions of $\delta^{13}C_{CH_{4_{source}}}$ derived from EC isoflux methods and autochamber Keeling analysis are compared in Figure 2.12. Mean $\delta^{13}C_{CH_{4_{source}}}$ from Keeling regressions (n = 332 chamber closings of linear and ebullitive fluxes with q-statistic >0.5) was -64.5 ± 0.8 (95% C.I.) ‰, statistically indistinguishable (at p = 0.05) from -71 ± 8 (95% C.I.) ‰ for EC isoflux methods. Neither CH_4 fluxes nor $\delta^{13}C_{CH_{4_{source}}}$ exhibited a significant diurnal pattern. Mean CH_4 fluxes for each of the individual 10 chambers highlighted the heterogeneity of the fen. Chambers with large percentages of *Carex* plants, for instance, had larger fluxes because plant mediated transport occurred faster than diffusion through surface water. The distributions of $\delta^{13}C_{CH_{4_{source}}}$ by chamber, however, were statistically indistinguishable at p = 0.05.

2.6. Discussion

2.6.1. Error Estimates

The precision of $^{12}CH_4$ and $^{13}CH_4$ compare well to other reported instrument precisions [*Hendriks et al.*, 2008; *Kroon et al.*, 2007; *Lee et al.*, 2009; *Nelson et al.*, 2004]. The selection of spectral sampling features between 1294.1 and 1294.5 cm^{-1} combined with CW operation of a 30 mW QCL light source, a high D* thermoelectrically-cooled 8 μm detector, and a 210 m effective path length resulted in a $\delta^{13}C_{CH_4}$ precision <0.2 ‰ at order 10^2 s averaging times. Reductions in isoflux error could be achieved with higher sampling rates accompanied by shorter sample cell residence times, and a more complete micrometeorological dataset. We attribute 20% of our

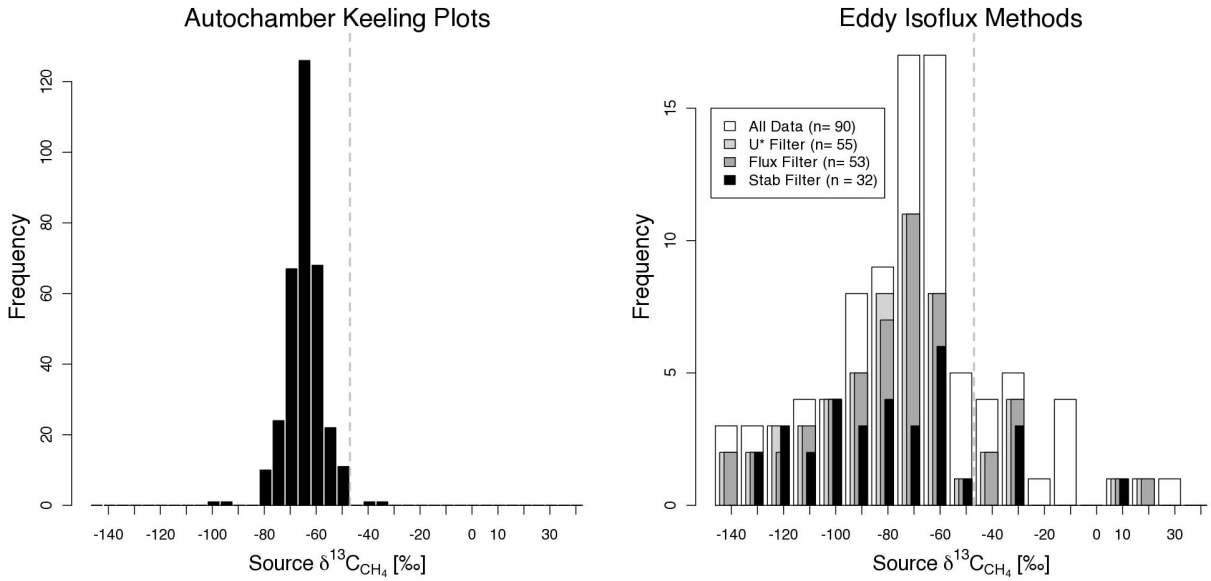

Figure 2.12: (left) Histogram of the $\delta^{13}C_{CH_{4_{source}}}$ composition using autochamber Keeling plot methods. **(right)** Histogram of the half-hourly $\delta^{13}C_{CH_{4_{source}}}$ composition calculated using EC isoflux methods. Of the 96 half-hour intervals, the 90 with isotopic composition within 3σ of the mean are shown in white and have a mean composition of -71 ‰. Filtering by u* >0.1 m/s, CH_4 flux > 1 nmol/mol-m/s, and stability parameter z/L∈ (-5,0) result in different mean isotopic composition of -79 ‰, -78 ‰, and -82 ‰. The 1σ of the distributions is 33 ‰ for all of the filters, similar to the isoflux measurement error derived from the cross covariance far from true lag-time. The grey vertical dashed line in both histograms represents the isotopic composition of atmospheric CH_4.

isoflux error to incomplete micrometeorological data, and estimate an upper limit on an improvement factor of ~2.2 (√5) for 5 Hz sampling. Recent improvements in cell design have resulted in a 2.1 L sampling cell volume with effective path lengths of up to 260 m using 554 passes between mirrors spaced ~47 cm apart where losses from mirror reflectivity due to higher pass numbers are mitigated by using wavelength specific mirror coatings [*McManus et al.*, 2011]. This reduced sampling volume would allow for independent sampling at ≥ 2 Hz and would decrease F_1, the high-frequency loss term of our EC measurements. It is hard to predict actual isoflux error improvements because 5 Hz measurement noise will also be ~ 2.2 (√5) times higher than that of 1 Hz sampling due to the acquisition of fewer spectra over a given sampling interval. The upper limit improvement with faster sampling could decrease the standard deviation of the $\delta^{13}C_{CH_4}$ measurement distribution, $1\sigma_{\delta^{13}C_{CH_4}}$, from 25 ‰ to 9 ‰, approaching the real variability of the fen depicted in Figure 2.12 with the autochamber QCLS data.

For comparison, the 1σ error estimate on F_{CH_4} was 0.97 mg CH_4 m^{-2} hr^{-1}, as calculated from the standard deviation of $\overline{w'\chi_{CH_4}'}$ for the first and last 20 seconds of a 100 second lag-time interval. This corresponded to a signal to noise (S/N) ratio of ~7. Smaller by a factor of two, the S/N of the isoflux was ~3.5 with a corresponding 1σ error estimate of 158 ‰ mg CH_4 m^{-2} hr^{-1} (or in alternate units, 66.4 ‰·nmol/mol·m/s). We characterized the error on the resultant $\delta^{13}C_{CH_{4_{source}}}$ by dividing the isoflux error estimate by the range of mean CH_4 fluxes observed giving a mean 1 $\sigma_{\delta^{13}C_{CH_4}}$ of 25 ‰. This error is the same order as the deviation between the isotopic composition of CH_4 from the free troposphere (-47 ‰) and CH_4 from biogenic sources (-60 to -70 ‰) and illustrates how a decrease in the $1\sigma_{\delta^{13}C_{CH_4}}$ to 9 ‰ from a smaller sampling volume would improve the retrieved EC isoflux calculations.

2.6.2. CH_4 Fluxes

Filtering of EC data by friction velocity is critical for EC systems [*Hendriks et al*., 2008; *Kormann et al*., 2001; *Wille et al*., 2008]. Plotting CH_4 flux versus friction velocity shows that a drop in CH_4 flux occurs below u* values of 0.07 m/s at Sallie's Fen (Figure 2.13). Other studies have used similar thresholds, notably 0.1 m/s [*Kormann et al*., 2001] and 0.09 [*Hendriks et al*., 2008]. We use 0.1 m/s as the threshold and note that only 6 half-hour points lie in the 0.07 to 0.1 range.

Similar to *Hendriks et al*. [2008], we observed that mean CH_4 fluxes derived using vegetation-type-by-surface-area weighted fluxes of chamber data were statistically indistinguishable (at the $p = 0.05$ level) from EC measurements over the same period. Autochambers were distributed to be representative of the fen [*Bubier et al*., 2003], and it is reassuring that the two methods produce similar CH_4 flux estimates. *Schuepp et al*. [1990] define a footprint function for fluxes in terms of local meteorological conditions and sampling height that predict a maximum surface sensitivity of the EC observations ~10 m upwind from the EC tower at Sallie's Fen, roughly 4 times smaller than the nearest edge of the fen. We estimate that 90% of the cumulative footprint lies within the area of the fen [*Kormann and Meixner*, 2000].

Although we have only 10 days of measurements using the QCLS, year-long autochamber measurements using the LGR show that seasonal trends in CH_4 emissions agree with those of similar fens [*Goodrich et al*., 2011; *Rinne et al*., 2007]. Flux magnitudes, in contrast to seasonality, are more site-dependent. Our mean CH_4 flux of 6.5 mg $CH_4\,m^{-2}\,hr^{-1}$ lie within the range of summertime fluxes observed at similar fens by *Hendriks et al*. [2008], *Rinne et al*. [2007], *Kormann et al*. [2001], and *Verma et al*. [1992] who report mean summertime emissions

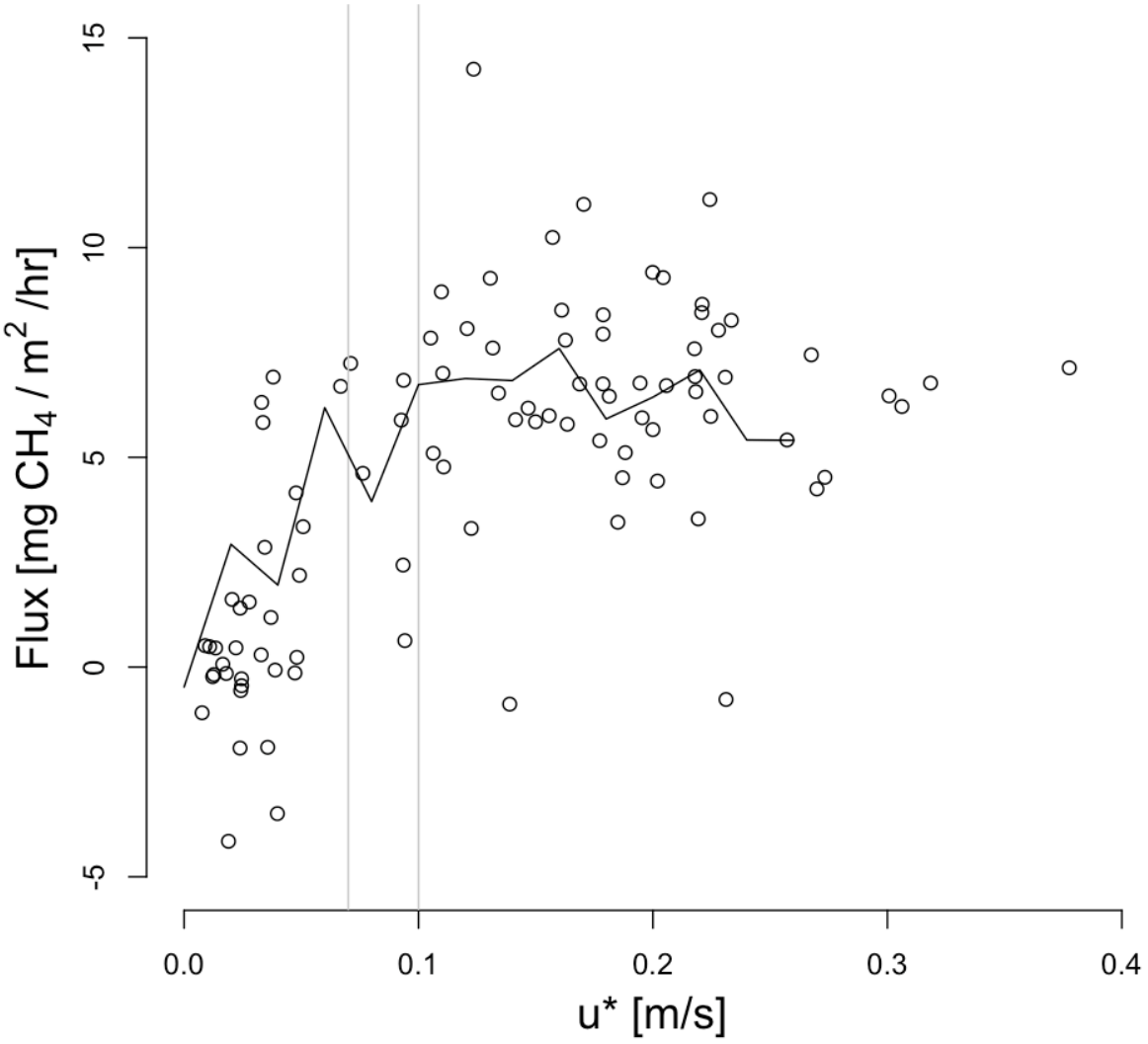

Figure 2.13: The 96 half-hour interval CH_4 fluxes plotted against their corresponding u* values. Vertical grey lines denote u* = 0.07 m/s and u* = 0.1 m/s and the black trace shows the mean CH_4 flux in bins of u* with spacing 0.02 m/s, showing the leveling off of CH_4 fluxes at the u* = 0.1 threshold chosen for this study.

of 1.7, 3.5, 5.4, and 7.4 mg CH_4 m^{-2} hr^{-1}, respectively. With the exception of *Hendriks et al.* [2008] who report emission maximums during daytime, most studies do not observe diurnal patterns of CH_4 flux, suggesting that passive diffusion via plant vascular tissue is the dominant CH_4 transport mechanism to the atmosphere [*Chasar et al.*, 2000; *Popp et al.*, 1999; *Shannon et al.*, 1996].

Differential attenuation of scalar measurements such as H_2O and CO_2 by closed-path EC systems must be accounted for when using WPL corrections [*Ibrom et al.*, 2007b]. Attenuation is particularly of concern for stable isotope measurements where there is potential for fractionation due to sampling. *Griffis et al.* [2008] characterize this sampling effect with a CO_2 isotope spectrometer and find attenuation <0.5 ‰ for both $\delta^{13}C_{CO_2}$ and $\delta^{18}O_{CO_2}$. We maintained fully turbulent conditions throughout our sampling system as fractionation has been demonstrated insignificant in turbulent conditions [*Griffis et al.*, 2008].

2.6.3. Isofluxes and $\delta^{13}C_{CH_{4_{source}}}$

CH_4 from anaerobic environments is released to the atmosphere largely by three different processes: diffusion through peatland pore water, plant mediated transport, and ebullition. Depth profiles of pore water CH_4 show that CO_2 reduction to CH_4 is the dominant pathway of methanogenesis at depth while acetate fermentation is more prevalent closer to the surface [*Popp et al.*, 1999, 2000]. At the oxic-anoxic interface, CH_4 oxidation results in ^{13}C enrichment because methanotrophs preferentially oxidize $^{12}CH_4$ by roughly 5-20 ‰ [*King et al.*, 1989, *Whiticar*, 1999]. Of the three transport pathways, ebullition is perhaps the most poorly quantified and least understood. *Goodrich et al.* [2011] estimated that ebullition accounted for up to 12 % of CH_4 fluxes at Sallie's Fen by separating linear fluxes (pore water diffusion and plant-mediated fluxes) from ebullitive fluxes using the same methods described in section 4.3.

Ebullition exhibited a diurnal cycle at Sallie's Fen, with more ebullitive events occurring at night [*Goodrich et al*., 2011]. Keeling intercepts of ebullitive fluxes measured during the 8 days of QCLS subsampling were on average 1.2 ± 0.7 ‰ (95% C.I., 1σ = ± 3.2 ‰) enriched in ^{13}C compared to the Keeling intercept using the entire chamber subset. We hypothesize that bubbles which can form and grow on plant vascular tissue are more likely to encounter more oxic conditions due to plant pathways that facilitate oxygen exchange. CH_4 oxidation to CO_2 leaves residual CH_4 in the bubble enriched in ^{13}C which can later outgas via ebullition. A complementary effect proposed by *Chanton et al*. [1997] is that plants relying on passive gas transport act as restrictive pipes that discriminate against ^{13}C. In rice paddies, this effect, combined with a fraction of total CH_4 being oxidized, produced what they refer to as 'bubble CH_4' enriched in ^{13}C by roughly 5 ‰ [*Chanton et al*., 1997]. This diffusional fractionation, theoretically a 19.5 ‰ effect in air but a smaller effect in water, could also explain the observed difference as ebullitive fluxes originating from depth would tend to bypass diffusional fractionation in the water column [*Popp et al*., 1999; *Cerling et al*., 1991].

The mean $\delta^{13}C_{CH_{4_{source}}}$ calculated by bootstrapping using resampled data (1000 times, with replacement) to construct a population distribution of the Keeling plot autochamber analysis was -64.5 ± 0.8 (95% C.I.) ‰. This agrees with the isotopic content of CH_4 from similar ecosystems as presented by *Popp et al*., [1999, 2000] and *Whiticar* [1999]. Bootstrapped mean $\delta^{13}C_{CH_{4_{source}}}$ by EC isoflux techniques were -71 ± 8 (95% C.I.) ‰, -79 ± 9 ‰, and -82 ± 12 ‰ using subsets of the total 96 half-hour intervals, representing n = 90 intervals with $\delta^{13}C_{CH_{4_{source}}}$ within 3σ of the mean calculated $\delta^{13}C_{CH_{4_{source}}}$, n = 55 intervals with u* > 0.1 m/s, and n = 32 intervals with the stability parameter z/L < 0 (see *Kormann et al*. [2001]), respectively (Figure 2.12). Because the

covariance terms in Equations 2.4 and 2.5 contain the same scalar measurements (w' and χ_{CH_4}'), dividing the two equations to calculate $\delta^{13}C_{CH_{4source}}$ results in error cancellation such that the retrieved $\delta^{13}C_{CH_{4source}}$ distribution by EC is statistically indistinguishable (at p=0.05) from the autochamber Keeling plot derived $\delta^{13}C_{CH_{4source}}$ distribution when all the data (n = 90) are used. When filters typically applied to EC data are used (e.g. n = 55 or n = 32 subsets), the retrieved $\delta^{13}C_{CH_{4source}}$ is distinguishable (at p = 0.05) from the Keeling plot derived $\delta^{13}C_{CH_{4source}}$, though we note that these filters preferentially remove nighttime data, thereby biasing the distribution towards depleted ^{13}C values by partially removing the influence of ^{13}C enriched nighttime ebullitive fluxes. In the present study, Keeling plots provide a more robust constraint on the real distribution of $\delta^{13}C_{CH_{4source}}$ from the fen as our EC isoflux sample size is limited and the isoflux error is similar in magnitude to the variability of the $\delta^{13}C_{CH_{4source}}$ distribution from 332 Keeling plot intercepts.

2.7. Conclusion

We presented measurements using a QCLS capable of *in-situ* $\delta^{13}C_{CH_4}$ precisions of 1.5 ‰ and <0.2 ‰ at 1 second and 10^2 second averaging times, respectively, demonstrating that both EC isoflux methods and autochamber Keeling analysis achieve consistent characterization of $\delta^{13}C_{CH_{4source}}$, producing statistically indistinguishable CH_4 flux estimates. Fast-response *in situ* atmospheric $^{13}CH_4$ and $^{12}CH_4$ measurements can robustly quantify the distributions of $\delta^{13}C_{CH_{4source}}$ from various CH_4 sources and characterize seasonal changes in these distributions. They can also therefore provide additional constraint for modeling efforts that use atmospheric $\delta^{13}C_{CH_4}$ data to quantify emission sources in global inventories [*Allan et al.*, 2001; *Lassey et al.*, 2007].

Modeling efforts to date have shown limited improvements from using both $\delta^{13}C_{CH_4}$ and CH_4 data, as opposed to CH_4 data alone, largely because GG-C-IRMS instrumentation limitations make $\delta^{13}C_{CH_4}$ data very scarce [*Fletcher et al*. 2004a; 2004b; *Bousquet et al*., 2006].

Longer time series of EC or flux chamber $^{12}CH_4$ and $^{13}CH_4$ measurements may elucidate the seasonal dependence of processes affecting CH_4 fluxes, particularly in regions such as the arctic [*Dlugokencky et al*., 2009, 2011] which have diverse CH_4 sources potentially susceptible to large scale environmental changes. In this study of a *Sphagnum*-dominated fen in New Hampshire, we used a week of automatic flux chamber measurements to characterize the bulk isotopic composition of late-August CH_4 emissions. We observed $\delta^{13}C_{CH_4}$ enrichment of ebullitive fluxes at night, which may be related to changes in oxygen status near plant roots. Continuous data, including $\delta^{13}C_{CH_4}$, over a year from autochambers can potentially identify the biogeochemical drivers of changes in both CH_4 fluxes and their isotopic composition at various timescales.

Acknowledgements

Parts of this reasearch were supported by the Department of Energy, Small Business Innovation Research Award DE-FG02-07ER84889 and the National Science Foundation Graduate Research Fellowship Program. The authors acknowledge Sean Sylva at the Woods Hole Oceanographic Institute for isotopic analysis of our calibration cylinders. We would also like to thank Jack Dibb, Nicola Blake, and Sallie Whitlow, and for all their help at the fen. We thank Ryan McGovern, Daniel Glenn, Stanley Huang, Scott Herndon, Ezra Woods, and Bob Prescott of Aerodyne, and Bill Munger, Bruce Daube, Josh McLaren, Rodrigo Jimenez, and Elaine Gottlieb of Harvard University. Lastly, we acknowledge the contributions of John B. Miller and two additional anonymous reviewers.

References

Allan, W., M. R. Manning, K. R. Lassey, D. C. Lowe, and A. J. Gomez (2001), Modeling the variation of delta C-13 in atmospheric methane: Phase ellipses and the kinetic isotope effect, *Global Biogeochemical Cycles*, *15*(2), 467-481.

Baldocchi, D. D., and D. R. Bowling (2003), Modelling the discrimination of (CO_2)-C-13 above and within a temperate broad-leaved forest canopy on hourly to seasonal time scales, *Plant Cell and Environment*, *26*(2), 231-244.

Bousquet, P., et al. (2006), Contribution of anthropogenic and natural sources to atmospheric methane variability, *Nature*, *443*(7110), 439-443.

Bousquet, P., B. Ringeval, I. Pison, E. J. Dlugokencky, E.-G. Brunke, C. Carouge, F. Chevallier, A. Fortems-Cheiney, C. Frankenberg, D. A. Hauglustaine, P. B. Krummel, R. L. Langenfelds, M. Ramonet,M. Schmidt, L. P. Steele, S. Szopa, C. Yver, N. Viovy, and P. Ciais (2011), Source attribution of the changes in atmospheric methane for 2006–2008, *Atmospheric Chemistry and Physics*, 11, 3689-3700.

Bowling, D. R., D. E. Pataki, and J. R. Ehleringer (2003), Critical evaluation of micrometeorological methods for measuring ecosystem-atmosphere isotopic exchange of CO_2, *Agricultural and Forest Meteorology*, *116*(3-4), 159-179.

Bubier, J., P. Crill, A. Mosedale, S. Frolking, and E. Linder (2003), Peatland responses to varying interannual moisture conditions as measured by automatic CO_2 chambers, *Global Biogeochemical Cycles*, *17*(2) 1066, doi:10.1029/2002GB001946.

Carroll, P., and P. Crill (1997), Carbon balance of a temperate poor fen, *Global Biogeochemical Cycles*, *11*(3), 349-356.

Cerling, T. E., D. K. Solomon, J. Quade, and J. R. Bowman (1991), On the isotopic composition of carbon in soil carbon dioxide, *Geochimica et Cosmochimica Acta*, 55, 3403-3405.

Chanton, J. P., G. J. Whiting, N. E. Blair, C. W. Lindau, and P. K. Bollich (1997), Methane emission from rice: Stable isotopes, diurnal variations, and CO_2 exchange, *Global Biogeochemical Cycles*, 11(1), 15-27.

Chasar, L. S., J. P. Chanton, P. H. Glaser, and D. I. Siegel (2000), Methane concentration and stable isotope distribution as evidence of rhizospheric processes: Comparison of a fen and bog in the Glacial Lake Agassiz Peatland complex, *Ann Bot-London*, *86*(3), 655-663.

Crosson, E. R., K. N. Ricci, B. A. Richman, F. C. Chilese, T. G. Owano, R. A. Provencal, M. W. Todd, J. Glasser, A. A. Kachanov, B. A. Paldus, T. G. Spence, R. N. Zare (2002), Stable isotope ratios using cavity ring-down spectroscopy: Determination of C-13/C-12 for carbon dioxide in human breath, *Analytical Chemistry*, 74(9), 2003-2007.

Dawson, T. E., S. Mambelli, A. H. Plamboeck, P. H. Templer, and K. P. Tu (2002), Stable isotopes in plant ecology, *Annual Review of Ecology and Systematics*, *33*, 507-559.

De Bievre, P., N. E. Holden, and I. L. Barnes (1984) Isotopic Abundances and Atomic Weights of the Elements, *Journal of Physical and Chemical Reference Data*, 13, 809-891.

Dlugokencky, E. J., S. Houweling, L. Bruhwiler, K. A. Masarie, P. M. Lang, J. B. Miller, and P. P. Tans (2003), Atmospheric methane levels off: Temporary pause or a new steady-state?, *Geophysical Research Letters*, *30*(19), 4.

Dlugokencky, E. J., L. Bruhwiler, J. W. C. White, L. K. Emmons, P. C. Novelli, S. A. Montzka, K. A. Masarie, P. M. Lang, A. M. Crotwell, J. B. Miller, and L. V. Gatti (2009), Observational constraints on recent increases in the atmospheric CH_4 burden, *Geophysical Research Letters*, 36, L18803, doi:10.1029/2009GL039780.

Dlugokencky E. J., E. G. Nisbet, R. Fisher, and D. Lowry (2011), Global atmospheric methane: budget, changes and dangers. *Philosophical Transactions of the Royal Society of London Series A: Mathematical, Physical and Engineering Sciences*, 369, 2058-2072.

Faist, J., F. Capasso, D. L. Sivco, C. Sirtori, A. L. Hutchinson, and A. Y. Cho (1994), Quantum Cascade Laser, *Science*, *264*(5158), 553-556.

Fletcher, S. E. M., P. P. Tans, L. M. Bruhwiler, J. B. Miller, and M. Heimann (2004a), CH_4 sources estimated from atmospheric observations of CH_4 and its C-13/C-12 isotopic ratios: 1. Inverse modeling of source processes, *Global Biogeochemical Cycles*, *18*(4).

Fletcher, S. E. M., P. P. Tans, L. M. Bruhwiler, J. B. Miller, and M. Heimann (2004b), CH_4 sources estimated from atmospheric observations of CH_4 and its C-13/C-12 isotopic ratios: 2. Inverse modeling of CH4 fluxes from geographical regions, *Global Biogeochemical Cycles*, *18*(4).

Frolking, S., and P. Crill (1994), Climate controls on temporal variability of methane flux from a poor fen in southeastern New Hampshire – measurement and modeling, *Global Biogeochemical Cycles*, *8*(4), 385-397.

Gierczak, T., R. K. Talukdar, S. C. Herndon, G. L. Vaghjiani, and A. R. Ravishankara (1997), Rate coefficients for the reactions of hydroxyl radicals with methane and deuterated methanes, *Journal of Physical Chemistry A*, *101*(17), 3125-3134.

Goodrich, J. P., R. K. Varner, S. Frolking, B. N. Duncan, and P. M. Crill (2011), High-frequency measurements of methane ebullition over a growing season at a temperate peatland site, *Geophyscial Research Letters*, 38, L07404.

Griffis, T. J., S. D. Sargent, J. M. Baker, X. Lee, B. D. Tanner, J. Greene, E. Swiatek, and K. Billmark (2008), Direct measurement of biosphere-atmosphere isotopic CO_2 exchange using the eddy covariance technique, *J Geophys Res-Atmos*, *113*(D8).

Gupta, P., D. Noone, J. Galewsky, C. Sweeney, and B. H. Vaughn (2009), Demonstration of high-precision continuous measurements of water vapor isotopologues in laboratory and remote field deployments using wavelength-scanned cavity ring-down spectroscopy (WS-CRDS) technology, *Rapid Communications in Mass Spectrometry*, *23*(16), 2534-2542.

Hendriks, D. M. D., A. J. Dolman, M. K. van der Molen, and J. van Huissteden (2008), A compact and stable eddy covariance set-up for methane measurements using off-axis integrated cavity output spectroscopy, *Atmospheric Chemistry and Physics*, *8*(2), 431-443.

Ibrom, A., E. Dellwik, S. E. Larsen, and K. Pilegaard (2007a), On the use of the Webb-Pearman-Leuning theory for closed-path eddy correlation measurements, *Tellus Series B-Chemical and Physical Meteorology*, *59*(5), 937-946.

Ibrom, A., E. Dellwik, H. Flyvbjerg, N. O. Jensen, and K. Pilegaard (2007b), Strong low-pass filtering effects on water vapour flux measurements with closed-path eddy correlation systems, *Agricultural and Forest Meteorology*, *147*(3-4), 140-156.

Kaimal, J. C. and J. J. Finnigan (1994), *Atmospheric boundary layer flows: their structure and measurement*, Oxford University Press, US.

Knohl, A., and N. Buchmann (2005), Partitioning the net CO_2 flux of a deciduous forest into respiration and assimilation using stable carbon isotopes, *Global Biogeochemical Cycles*, *19,* GB4008, doi:10.1029/2004GB002301.

Kormann, R. and F. X. Meixner (2000), An analytical footprint model for non-neutral stratification, *Boundary-Layer Meteorology*, (99), 207-224.

Kormann, R., H. Muller, and P. Werle (2001), Eddy flux measurements of methane over the fen "Murnauer Moos", 11 degrees 11 ' E, 47 degrees 39 ' N, using a fast tunable diode laser spectrometer, *Atmospheric Environment*, *35*(14), 2533-2544.

Kosterev, A. A., R. F. Curl, F. K. Tittel, C. Gmachl, F. Capasso, D. L. Sivco, J. N. Baillargeon, A. L. Hutchinson, and A. Y. Cho (1999), Methane concentration and isotopic composition measurements with a mid-infrared quantum-cascade laser, *Optics Letters*, *24*(23), 1762-1764.

Kroon, P. S., A. Hensen, H. J. J. Jonker, M. S. Zahniser, W. H. van 't Veen, and A. T. Vermeulen (2007), Suitability of quantum cascade laser spectroscopy for CH_4 and N_2O eddy covariance flux measurements, *Biogeosciences*, *4*(5), 715-728.

Lassey, K. R., D. C. Lowe, and M. R. Manning (2000) The trend in atmospheric methane δ13C and implications for isotopic constraints on the global methane budget, *Global Biogeochemical Cycles*, 14(1), 41-49.

Lassey, K. R., D. M. Etheridge, D. C. Lowe, A. M. Smith, and D. F. Ferretti (2007), Centennial evolution of the atmospheric methane budget: what do the carbon isotopes tell us?, *Atmospheric Chemistry and Physics*, *7*(8), 2119-2139.

Lee, X., W. Massman, and B. Law (2004), Handbook of micrometeorology: a guide for surface flux measurement and analysis, Kluwer Academic Publishers, Dordrecht, The Netherlands.

Lee, X. H., T. J. Griffis, J. M. Baker, K. A. Billmark, K. Kim, and L. R. Welp (2009), Canopy-scale kinetic fractionation of atmospheric carbon dioxide and water vapor isotopes, *Global Biogeochemical Cycles*, *23*.

Lelieveld, J., P. J. Crutzen, and F. J. Dentener (1998), Changing concentration, lifetime and climate forcing of atmospheric methane, *Tellus Series B-Chemical and Physical Meteorology*, *50*(2), 128-150.

Lowe, D. C., C. A. M. Brenninkmeijer, S. C. Tyler, and E. J. Dlugkencky (1991), Determination of the isotopic composition of atmospheric methane and its application in the antarctic, *Journal of Geophysical Research-Atmospheres*, *96*(D8), 15455-15467.

McManus, J. B., P. L. Kebabian, and W. S. Zahniser (1995), Astigmatic mirror multipass absorption cells for long-path-length-spectroscopy, *Applied Optics*, *34*(18), 3336-3348.

McManus, J. B., D. D. Nelson, J. H. Shorter, R. Jimenez, S. Herndon, S. Saleska, and M. Zahniser (2005), A high precision pulsed quantum cascade laser spectrometer for measurements of stable isotopes of carbon dioxide, *Journal of Modern Optics*, 52(16), 2309-2321.

McManus, J. B., D. D. Nelson, and M. S. Zahniser (2010), Long-term continuous sampling of $^{12}CO_2$, $^{13}CO_2$ and $^{12}C^{18}O^{16}O$ in ambient air with a quantum cascade laser spectrometer, *Isotopes in Environmental and Health Studies*, *46*(1), 49-63.

McManus, J. B., M. S. Zahniser, D. D. Nelson (2011), Dual quantum cascade laser trace gas instrument with astigmatic Herriott cell at high pass number, *Applied Optics*, 50(4), A74-A85.

Melloh, R. A., and P. M. Crill (1996), Winter methane dynamics in a temperate peatland, *Global Biogeochemical Cycles*, *10*(2), 247-254.

Miller, J. B., K. A. Mack, R. Dissly, J. W. C. White, E. J. Dlugokencky, and P. P. Tans (2002), Development of analytical methods and measurements of C-13/C-12 in atmospheric CH_4 from the NOAA Climate Monitoring and Diagnostics Laboratory global air sampling network, *Journal of Geophysical Research-Atmospheres*, *107*(D13).

Montzka, S. A., M. Krol, E. Dlugokencky, B. Hall, P. Jöckel, and J. Lelieveld (2011), Small Interannual Variability of Global Atmospheric Hydroxyl, *Science*, 331, 67-69.

Mohn J., C. Guggenheim, B. Tuzson, M. K. Vollmer, S. Toyoda, N. Yoshida, and L. Emmenegger (2010), A liquid nitrogen-free preconcentration unit for measurements of ambient

N_2O isotopomers by QCLAS, *Atmospheric Measurement Techniques*, 3 (3) 609-618.

Nelson, D. D., J. H. Shorter, J. B. McManus, and M. S. Zahniser (2001), Sub-part-per-billion detection of nitric oxide in air using a thermoelectrically cooled mid-infrared quantum cascade laser spectrometer, *Applied Physics B: Lasers and Optics*, 75, 343-350.

Nelson, D. D., B. McManus, S. Urbanski, S. Herndon, and M. S. Zahniser (2004), High precision measurements of atmospheric nitrous oxide and methane using thermoelectrically cooled mid-infrared quantum cascade lasers and detectors. *Spectrochimica Act Part A-Molecular and Biomolecular Spectroscopy*, 60(14), 3325-3335.

Pataki, D. E., J. R. Ehleringer, L. B. Flanagan, D. Yakir, D. R. Bowling, C. J. Still, N. Buchmann, J. O. Kaplan, and J. A. Berry (2003), The application and interpretation of Keeling plots in terrestrial carbon cycle research, *Global Biogeochemical Cycles*, *17*(1), doi:10.1029/2001GB001850.

Popp, T. J., J. P. Chanton, G. J. Whiting, and N. Grant (1999), Methane stable isotope distribution at a Carex dominated fen in north central Alberta, *Global Biogeochemical Cycles*, *13*(4), 1063-1077.

Popp, T. J., J. P. Chanton, G. J. Whiting, and N. Grant (2000), Evaluation of methane oxidation in the rhizosphere of a Carex dominated fen in north central Alberta, Canada, *Biogeochemistry*, *51*(3), 259-281.

Press, W.H., S.A. Teukolsky, W.T. Vetterling, and B.P. Flannery (1992), *Numerical Recipes in C: The Art of Scientific Computing*, Second Edition, Cambridge University Press, New York, USA.

Quay, P., J. Stutsman, D. Wilbur, A. Snover, E. Dlugokencky, and T. Brown (1999), The isotopic composition of atmospheric methane, *Global Biogeochemical Cycles*, *13*(2), 445-461.

Rigby, M., R. G. Prinn, P. J. Fraser, P.G. Simmonds, R. L. Langenfelds, J. Huang, D. M. Cunnold, L. P. Steele, P. B. Krummel, R. F. Weiss, S. O'Doherty, P. K. Salameh, H. J. Wang, C. M. Harth, J. Muehle, and L. W. Porter (2008), Renewed growth of atmospheric methane, *Geophysical Research Letters*, *35*(22), L22805.

Rinne, J., T. Riutta, M. Pihlatie, M. Aurela, S. Haapanala, J. P. Tuovinen, E. S. Tuittila, and T. Vesala (2007), Annual cycle of methane emission from a boreal fen measured by the eddy covariance technique, *Tellus Series B-Chemical and Physical Meteorology*, *59*(3), 449-457.

Saleska, S. R., J. H. Shorter, S. Herndon, R. Jimenez, B. McManus, J. W. Munger, D. D. Nelson, and M. S. Zahniser (2006), What are the instrumentation requirements for measuring the isotopic composition of net ecosystem exchange of CO_2 using eddy covariance methods? *Isotopes in Environmental and Health Studies*, 42(2), 115-133.

Saueressig, G., J. N. Crowley, P. Bergamaschi, C. Bruhl, C. A. M. Brenninkmeijer, and H. Fischer (2001), Carbon 13 and D kinetic isotope effects in the reactions of CH_4 with O(D-1) and OH: New laboratory measurements and their implications for the isotopic composition of stratospheric methane, *Journal of Geophysical Research-Atmospheres*, *106*(D19), 23127-23138.

Schuepp, P. H., M. Y. Leclerc, J. I. Macpherson, and R. L. Desjardins (1990), Footprint prediction of scalar fluxes from analytical solutions of the diffusion equation, *Boundary-Layer Meteorology*, *50*(1-4), 353-373.

Shannon, R. D., J. R. White, J. E. Lawson, and B. S. Gilmour (1996), Methane efflux from emergent vegetation in peatlands, *J Ecol*, *84*(2), 239-246.

Shoemaker, J. K. and D. P. Schrag (2011), Subsurface characterization of methane production and oxidation from a New Hampshire wetland, *Geobiology*, 8, 234-243

Smeets, C. J., R. Holzinger, I. Vigano, A. H. Goldstein, and T. Rockmann (2009), Eddy covariance methane measurements at a Ponderosa pine plantation in California, *Atmospheric Chemistry and Physics*, 9 (21), 8365-8375.

Treat, C. C., J. L. Bubier, R. K. Varner, and P. M. Crill (2007), Timescale dependence of environmental and plant-mediated controls on CH_4 flux in a temperate fen, *Journal of Geophysical Research-Biogeosciences*, *112*(G1), G01014.

Tuzson, B., J. Mohn, M. J. Zeeman, R. A. Werner, W. Eugster, M. S. Zahniser, D. D. Nelson, J. B. McManus, and L. Emmenegger (2008), High precision and continuous field measurements of delta C-13 and delta O-18 in carbon dioxide with a cryogen-free QCLAS, *Applied Physics B-Lasers and Optics*, *92*(3), 451-458.

Tuzcon, B. J., R. V. Hiller, K. Zeyer, W. Eugster, A. Neftel, C. Ammann, and L. Emmenegger (2010), Field intercomparison of two optical analyzers for CH_4 eddy covariance flux measurements, *Atmospheric Measurement Techniques*, 3, 1519-1531.

Verma, S. B., F. G. Ullman, D. Billesbach, R. J. Clement, J. Kim, and E. S. Verry (1992), Eddy-correlation measurements of methane flux in a northern peatland ecosystem, *Boundary-Layer Meteorology*, *58*(3), 289-304.

Waechter, H., J. Mohn, B. Tuzson, L. Emmenegger, and M. W. Sigrist (2008), Determination of N_2O isotopomers with quantum cascade laser based absorption spectroscopy, *Optics Express*, *16*(12), 9239-9244.

Webb, E. K., G. I. Pearman, and R. Leuning (1980), Correction of flux measurements for denstiy effects due to heat and water-vapor transfer, *Quarterly Journal of the Royal Meteorological Society*, *106*(447), 85-100.

Whiticar, M. J. (1999), Carbon and hydrogen isotope systematics of bacterial formation and oxidation of methane, *Chem. Geol.*, *161*(1-3), 291-314.

Wienhold, F. G., H. Frahm, and G. W. Harris (1994), Measurements of N_2O fluxes from fertilized grassland using a fast response tunable diode laser spectrometer, *Journal of Geophysical Research*, 99(D8), 16557-16567.

Wille, C., L. Kutzbach, T. Sachs, D. Wagner, and E. M. Pfeiffer (2008), Methane emission from Siberian arctic polygonal tundra: eddy covariance measurements and modeling, *Global Change Biology*, *14*(6), 1395-1408.

Witinski, M., D. S. Sayres, and J. G. Anderson (2010), High precision methane isotopologue ratio measurements at ambient mixing ratios using integrated cavity output spectroscopy, *Applied Physics B-Lasers and Optics*, 102(2), 375-380.

Zahniser, M. S., D. D. Nelson, J. B. McManus, and P. L. Kebabian (1995), Measurement of trace gas fluxes using tunable diode-laser spectroscopy, *Philosophical Transactions of the Royal Society of London Series A: Mathematical, Physical and Engineering Sciences*, *351*(1696), 371-381.

Zahniser, M. S., D. D. Nelson, J. B. McManus, S. C. Herndon, E. C. Wood, J. H. Shorter, B. H. Lee, G. W. Santoni, R. Jimenez, B. C. Daube, S. Park, E. A. Kort, and S. C. Wofsy (2009), Infrared QC laser applications to field measurements of atmospheric trace gas sources and sinks in environmental research: enhanced capabilities using continuous wave QCLs, *SPIE*, *7222,* doi: 10.1117/12.815172.

Chapter 3:

Aircraft Emissions of Methane and Nitrous Oxide during the Alternative Aviation Fuel Experiment[2]

Abstract

Given the predicted growth of aviation and the recent developments of alternative aviation fuels, quantifying methane (CH_4) and nitrous oxide (N_2O) emission ratios for various aircraft engines and fuels can help constrain projected impacts of aviation on the Earth's radiative balance. Fuel-based emission indices for CH_4 and N_2O were quantified from CFM56-2C1 engines aboard the NASA DC-8 aircraft during the first Alternative Aviation Fuel Experiment (AAFEX-I) in 2009. The measurements of JP-8 fuel combustion products indicate that at low thrust engine states (idle and taxi, or 4% and 7% maximum rated thrusts, respectively) the engines emit both CH_4 and N_2O at a mean ± 1σ rate of 170 ± 160 mg CH_4 (kg Fuel)$^{-1}$ and 110 ± 50 mg N_2O (kg Fuel)$^{-1}$, respectively. At higher thrust levels corresponding to greater fuel flow and higher engine temperatures, CH_4 concentrations in engine exhaust were lower than ambient concentrations. Average emission indices for JP-8 fuel combusted at engine thrusts between 30% and 100% of maximum rating were -54 ± 33 mg CH_4 (kg Fuel)$^{-1}$ and 32 ± 18 mg N_2O (kg Fuel)$^{-1}$, where the negative sign indicates consumption of atmospheric CH_4 in the engine. Emission factors for the synthetic Fischer-Tropsch fuels were statistically indistinguishable from those for JP-8.

[2] Santoni, G. W., B. H. Lee, E. C. Wood, S. C. Herndon, R. C. Miake-Lye, S. C. Wofsy, J. Barry McManus, D. D. Nelson, M. S. Zahniser (2011), *Environ. Sci. & Technol.*, **45**, 7075-7082, doi:10.1021/es200897h.

3.1. Introduction

Methane (CH_4) is a radiatively active gas in Earth's emission spectrum, roughly 25 times more effective on a per-molecule level than CO_2 in terms of its integrated greenhouse effect at hundred-year timescales (1). Nitrous oxide (N_2O) has an even larger per-molecule global warming potential, roughly 300 times higher than CO_2 on these timescales. This is partly because its atmospheric lifetime is ~120 years, compared to the ~9 year methane lifetime (2). The concentration of these two species in the atmosphere is determined primarily by a balance between surface sources and atmospheric losses. Atmospheric destruction of CH_4 occurs largely via reaction with the hydroxyl radical (OH) while loss of atmospheric N_2O mainly proceeds via stratospheric photodissociation (3, 4). Since 1750, when atmospheric CH_4 concentrations hovered around 700 nmol/mol, anthropogenic activities have increased CH_4 abundances to ~1850 nmol/mol (2). CH_4 growth rates leveled off in the mid-1980s and early part of the 21st century (5), but recent studies have shown renewed growth (6,7). In that same time-period, the atmospheric abundance of N_2O has increased from 270 nmol/mol to its present value of ~320 nmol/mol (8).

Given their radiative importance and long atmospheric lifetimes, quantifying the impact of the airline industry on climate change must include accurate accounting of CH_4, N_2O, and CO_2. Many studies have measured CO_2 emissions from aircraft engines (9), but fewer have examined CH_4 and N_2O emissions. Direct aircraft emissions of these species have the potential to affect global budgets, particularly given the growth of the aviation industry in the recent decades. Nitrogen oxide emissions also indirectly decrease the lifetime of CH_4 in the atmosphere via chemical feedbacks involving ozone (O_3) and OH (10). A competing effect exists with carbon monoxide (CO) emissions, as feedbacks with CO and OH can increase the atmospheric lifetime

of CH_4 (10). Aircraft emissions are also noteworthy in that most of the emissions occur at altitude.

Previous studies have highlighted the large variability of CH_4 concentrations seen at the exit of engines operating at different conditions. Spicer et al. (11,12) were among the first to give detailed aircraft exhaust emission concentrations for a variety of organic species in military and commercial aircraft engines. Wiesen et al. (13) examined CH_4 and N_2O emissions from different commercial jet engines using different fuels during the AERONOx campaign. The main finding emphasized in these studies was the consumption of atmospheric CH_4 at high engine thrust conditions, the production of CH_4 at low-power conditions, and the production of N_2O irrespective of engine mode. This suggested that aircraft emissions had negligible impacts on the global CH_4 budget. They also found that N_2O emissions were smaller than those of lower-temperature combustion power plants (14) and concluded that aircraft emissions of N_2O had a negligible impact on the global N_2O budget.

CH_4 emissions at idle and taxi conditions, however, varied by 500%, dependent on engines used and fuels consumed. Spicer et al. (12) showed enhancements of upwards of 9 μmol/mol in undiluted exhaust, roughly 5 times ambient concentrations, whereas Spicer et al. (11) measured CH_4 concentrations of 1.8 μmol/mol in the exhaust, most of which was likely from the ambient air flushed through the turbine engines. The ambient CH_4 concentration is currently 1.85 μmol/mol, though it was closer to 1.7 μmol/mol in 1992 (15). While there has been a consensus on the overall trends, quantitative assessments of CH_4 emissions as a function of engine thrust remain poorly constrained.

AAFEX provided a means to quantify non-CO_2 greenhouse gas emission data for a variety of fuels, ambient conditions, and modes of engine operation. Preliminary results from AAFEX

were presented in the NASA AAFEX report (16, Appendix E for the present study) and analysis of the AAFEX dataset is intended to guide the aviation industry in addressing the most important emission issues associated with alternative fuels.

3.2. Experimental Section

Rising concerns regarding air quality and continued dependence on foreign oil have generated interest in the development of alternative aviation fuels. AAFEX provided a means of comprehensive testing of the effects of different fuels on engine operation and exhaust composition. The tests were performed on the ground in Palmdale, CA on the same CFM56-2C1 engine studied during APEX-1 (20) and were intended to simulate the engine operating conditions during flight. AAFEX included three chemically distinct fuels: JP-8, representative of the Jet-A fuels currently used throughout the world, a Fischer-Tropsch (FT-1) fuel derived from a natural gas feedstock and synthesized by Shell, and a second Fischer-Tropsch (FT-2) fuel derived from a gasified coal feedstock and synthesized by Sasol. The fuels were analysed for content and material properties by the Air Force Research Lab (16). In addition to the pure fuels, 50/50-by-volume blends of the fuels were tested. During all tests, engines 2 and 3 (the two engines closest to the fuselage) were active and were sampled at 1 m and 30 m probes. Engine 2 (inboard left engine) served as a reference as it burned JP-8 for the entire test duration while engine 3 (inboard right engine) burned either JP-8 or the synthetic fuel depending on the test day. Both trace gas and particulate measurements were made at multiple distances from the inlet to characterize aging of the various emissions. Gas phase measurements included CO_2, CO, NO_x, SO_2, CH_4, N_2O, HONO, total and speciated hydrocarbons, and hazardous air pollutants while particle measurements included number density, size distribution, mass, aerosol chemical composition, and black carbon composition (16). Advected plume emissions presented in this

study were sampled downwind of the plane at the 145 m probe (see TOC art). The daily AAFEX test activities are summarized in Table 3.1.

The majority of instrumentation at AAFEX was located on the starboard side of the plane. The downwind trailers housed instrumentation to measure CH_4, CO_2, O_3, NO_x, HONO, N_2O, and particulates, and were positioned 145 m away from the engine output in the direction of the predominant wind and 1.3 m above the ground. This positioning was critical to measure advected plumes of engine exhaust at low power conditions, when exit velocities of engine emissions did not have sufficient momentum to reach the downwind trailer inlet. The inlet was designed to eliminate the need of filters which would corrupt the HONO measurement, but still remove particulates by inertial separation, thereby eliminating potential degradation of the sampling cell mirrors.

Advances in laser and detector technology have allowed for greater sensitivity in high-resolution absorption spectroscopy (17). Zahniser et al. (18) and Lee et al. (19), provide a description of the spectrometers used at AAFEX to measure CH_4 and N_2O with in-field 1-Hz precisions of 0.6 nmol/mol and 0.3 nmol/mol, respectively. Briefly summarizing, the CH_4 spectrometer consists of a mid-infrared continuous-wave Quantum Cascade Laser (QCL – Alpes Lasers) that is tuned across an absorption line for CH_4 in the 1294-1295 cm^{-1} region. Light from the QCL is directed into an astigmatic multi-pass sampling cell operated at low pressure (< 50 torr) and detected by a thermoelectrically cooled 8 μm detector. To achieve this precision on the CH_4 line, two mirrors spaced 88.23 cm apart are housed in a 5 L sample cell such that 238 passes between the astigmatic mirrors result in an effective optical path length of 210 m. A flow rate of 11 slpm, corresponding to a cell time constant of 1.05 seconds, was achieved during AAFEX measurements using a 600 l/min scroll pump. The N_2O measurement was made using a second

Table 3.1: Fuel used, average ambient temperature, and relative humidity for each experiment during AAFEX. When two fuels are listed, these represent 50/50-by-volume blends. Ambient temperature and relative humidity were found to have no significant effect on either CH_4 or N_2O emission indices.

Date (2009)	Experiment	Fuel	Start	End	Temp(°C)	RH (%)
1/26	JP-8 initial test	JP-8	16:00	19:20	5	60
1/27	JP-8 warm	JP-8	12:40	15:30	10	30
1/28	JP-8 cold	JP-8	06:00	09:30	-3	30
1/28	FT1 warm	FT1	12:30	15:40	10	30
1/29	FT1 cold	FT1	05:40	08:30	0	60
1/30	FT1 blend	JP-8/FT1	06:15	09:40	2	55
1/30	FT2 warm	FT2	10:50	13:40	14	25
1/31	FT2 cold	FT2	05:45	07:00	0	75
1/31	FT2 blend	JP-8/FT2	08:30	10:40	14	30
1/31	JP-8 warm	JP-8	12:40	15:30	17	20
2/1	DAY OFF					
2/2	JP-8 cold	JP-8	07:11	09:00	2	60

very similar instrument. Simultaneous measurements of CO_2 were made using a commercially available Licor LI-6262 infrared gas analyzer. By making highly time-resolved measurements of CH_4 and CO_2, the concentrations of each are quantified in both the exhaust plume and in the background air unaffected by the exhaust.

3.3. Results and Discussion

Figure 3.1 shows time series data from January 26, 2009 showing the different correlations between CH_4, N_2O and CO_2 concentrations. During idle conditions, CH_4 plumes of 30 nmol/mol correspond to 70 μmol/mol CO_2 plumes. At 30% thrust conditions, this relation changes noticeably, with larger 200 μmol/mol CO_2 plumes corresponding to CH_4 depletions of 10 nmol/mol below the background atmospheric mixing ratio. Fuel-based emission ratios in units of nmolCH_4/μmolCO_2 can be calculated by regressing CH_4 against CO_2 in individual plumes, as shown in Figure 3.1. Fuel-based emission indices are calculated according to Herndon et al. (21):

$$EI_{CH_4} = F_c \cdot \frac{M_{CH_4}}{M_{CO_2}} \cdot \frac{\Delta CH_4}{\Delta CO_2} \tag{3.1}$$

where M represents the molecular mass and F_c represents the stoichiometric calculation of CO_2 produced per kilogram of fuel consumed (with units g CO_2 (kg Fuel)$^{-1}$) assuming complete combustion and given a particular hydrogen to carbon ratio. The hydrogen contents by mass for JP-8, FT1, and FT2 are 13.6%, 15.5%, and 15.1% hydrogen, respectively, corresponding to F_c values of 3160, 3090, and 3110 g CO_2 (kg Fuel)$^{-1}$ (16, 22). Identical emission index calculations are carried out for N_2O by accounting for the molecular mass differences. These emission indices of CH_4 and N_2O were calculated for 1480 plumes at various engine thrust modes, of which only the plumes with a variance on the regression smaller than 0.2 were used (n = 1103) in subsequent analysis.

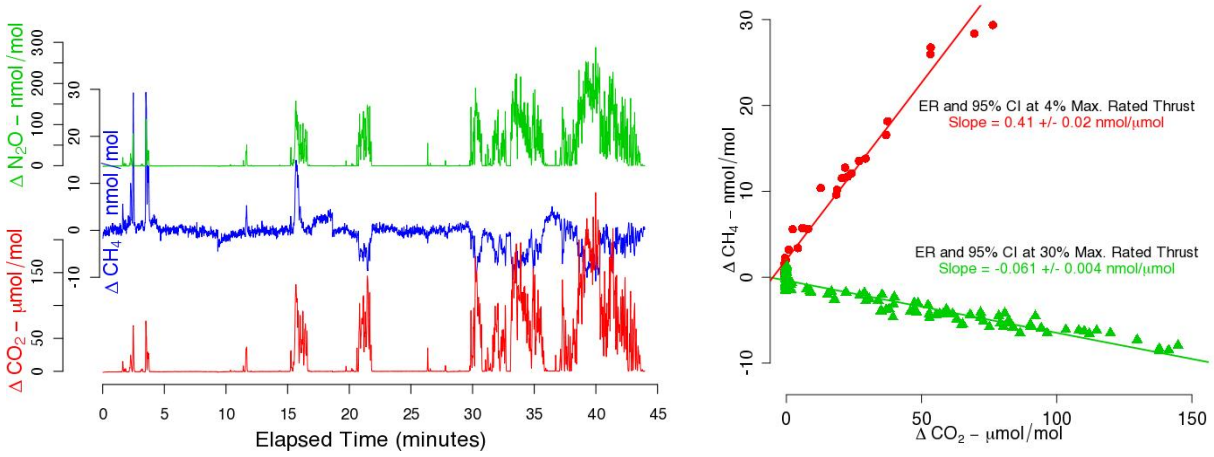

Figure 3.1: (left) Time series (January 26th, 2009, 2pm local time) of the enhancement above background values (ΔCH_4, ΔN_2O, ΔCO_2) of ambient plume AAFEX data illustrating positive correlation between CH_4 and CO_2 at idle conditions (before minute 20), and negative correlation at higher thrusts (after minute 20). N_2O is positively correlated with CO_2 at all thrust conditions. **(right)** Two examples of emission ratio (ER) regressions at 4% (idle) and 30% (approach) maximum rated thrust using CH_4 and CO_2 data from the left panel.

The number of plumes observed at low power conditions is typically fewer than those at higher engine thrusts because advection of the plumes of engine exhaust was facilitated by the wind velocities generated by higher thrusts. The figure also illustrates the broader distributions observed at idle (4%) and taxi (7%) conditions in comparison with those at higher engine thrusts, with the latter constrained by the limited amount of atmospheric CH_4 available to combust. Figure 3.2 and Table 3.2 summarize CH_4 and N_2O emission indices as well as undiluted carbon dioxide concentrations observed at the engine exhaust plane (EEP) (23). Two sample T-tests were performed between each fuel (JP-8 vs. FT-1, JP-8 vs. FT-2, and FT1 vs. FT2) at each of the 7 engine thrust conditions shown in Table 3.2. Of the 21 population comparisons for CH_4, 5 were significant at the p=0.05 level, but the mean p-value was 0.30. For N_2O, 10 of the 21 tests had p-values below 0.05, but the mean p-value was 0.15, also suggesting that the emission indices of the different fuels were statistically indistinguishable. We note that N_2O emission indices for FT-1 are consistently higher than JP-8 while those of FT-2 are consistently lower. Table 3.2 also shows emission rates for N_2O and CH_4 calculated using median fuel flow rates recorded in the cockpit during each test.

To validate ambient plume measurements and explain the discrepancies between studies at both high and low engine thrust conditions, two subsamples (one at 4-7% and one at 100% thrust) of core flow aircraft exhaust were taken from the 1-m inlet during each simulated flight and analyzed with the same instrumentation while the aircraft engines were off. The subsamples were introduced into evacuated 2-L steel canisters and then diluted down with ultra-high purity helium to pressurize the canisters. These subsamples were then overblown across the 145-m inlet of the spectrometers to validate the emission ratios calculated from the advected plume data. Only two samples were done for each simulated flight because of the limited time

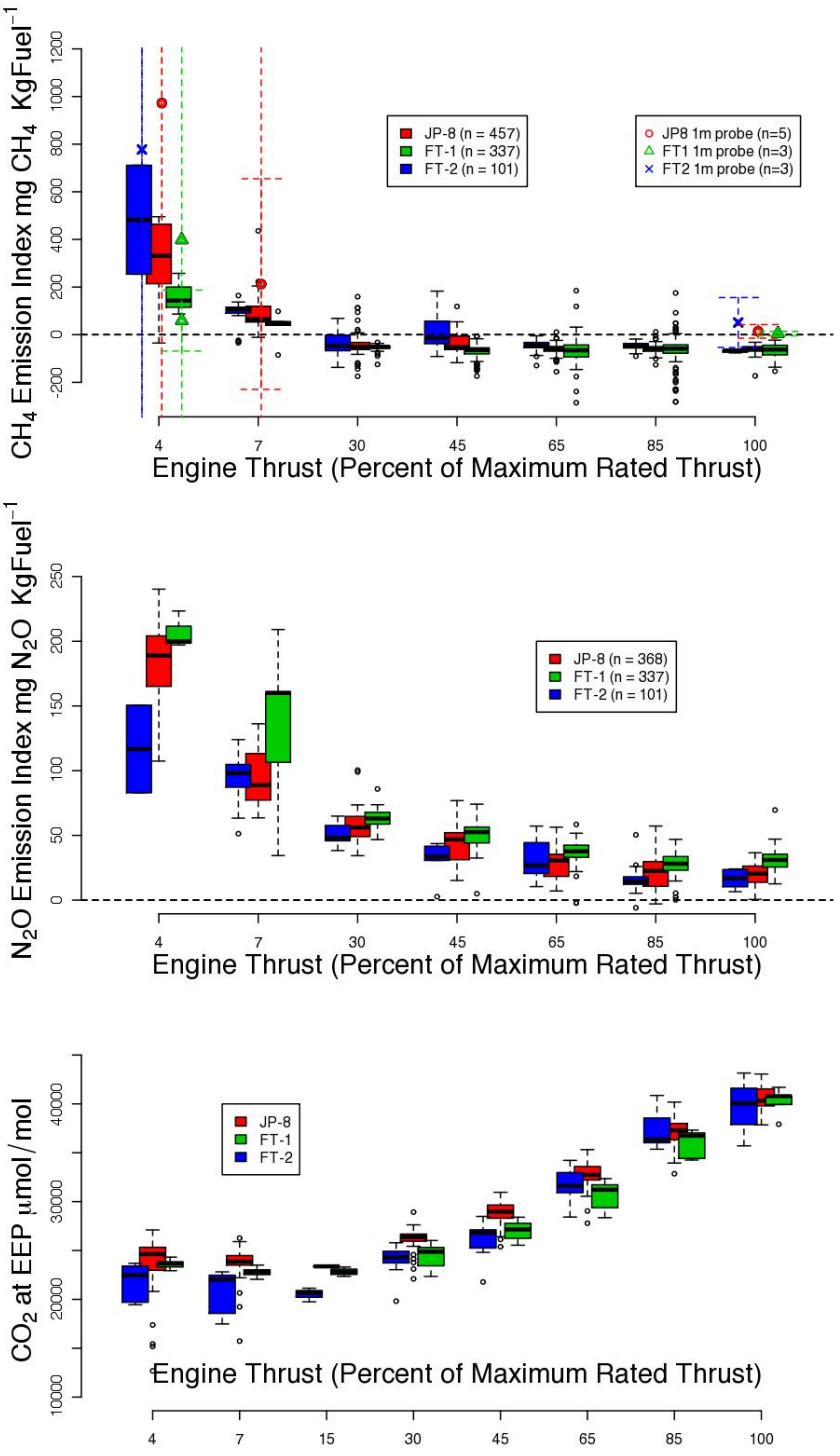

Figure 3.2: CH_4 emission indices **(top)**, N_2O emission indices **(middle)**, and CO_2 concentration at the Engine Exhaust Plane (**bottom**, courtesy of Changlie Wey) binned by fuel and percent maximum rated engine thrust. The latter is used to calculate plume dilution of canister samples taken from the 1-m probe which are shown superimposed on the CH_4 EI plot (**top**). Black bars represent the median, boxes extend from the first to the third quartile, and whiskers represent 1.5 inter-quartile ranges. Outliers are shown as black circles.

Table 3.2: Calculated emission indices for CH_4 and N_2O according to percentage maximum rated engine thrust condition and fuel type. Median values ± 1σ are given and the 95% confidence intervals are shown in parentheses. Emission rates for CH_4 and N_2O are calculated by multiplying median fuel flows by emission indices. Errors can also be calculated using this scaling. The emission rate for CO_2 is derived from each fuel's percent hydrogen by mass (and consequently the carbon content) as well as the median fuel flow rate.

Percent Thrust (LTO Cycle)	Fuel	Fuel Flow (kg/hr)	CH_4 EI mg/(kgFuel)	CH_4 Rate (g/hr)	N_2O EI mg/(kgFuel)	N_2O Rate (g/hr)	CO_2 Rate (kg/hr)
4% (Idle)	JP-8	428	331±165 (±87)	142	189±41 (±24)	81	1350
	FT-1		143±87 (±98)	61	200±14 (±16)	86	1320
	FT-2		483±323 (±448)	207	117±48 (±66)	50	1330
7% (Taxi)	JP-8	456	66±84 (±30)	30	89±21 (±8)	40	1440
	FT-1		46±69 (±60)	21	160±67 (±58)	73	1410
	FT-2		107±59 (±28)	49	98±19 (±9)	45	1420
30% (Approach)	JP-8	1134	-51±54 (±13)	-57	56±13 (±3)	64	3580
	FT-1		-51±17 (±6)	-58	63±8 (±3)	71	3500
	FT-2		-47±68 (±50)	-53	48±9 (±7)	55	3530
45% (Approach)	JP-8	1545	-52±44 (±11)	-81	47±14 (±4)	72	4880
	FT-1		-64±34 (±7)	-100	53±13 (±3)	81	4770
	FT-2		-14±106 (±93)	-21	34±16 (±14)	52	4800
65% (Cruise)	JP-8	2200	-60±19 (±3)	-132	31±11 (±2)	68	6950
	FT-1		-66±59 (±13)	-144	38±10 (±2)	83	6800
	FT-2		-45±23 (±7)	-98	27±14 (±4)	59	6840
85% (Climb-out)	JP-8	2934	-58±18 (±3)	-170	23±13 (±3)	66	9270
	FT-1		-59±68 (±13)	-172	28±8 (±2)	83	9070
	FT-2		-49±17 (±7)	-145	14±10 (±4)	42	9130
100% (Take-off)	JP-8	3320	-59±26 (±10)	-195	20±10 (±4)	68	10500
	FT-1		-62±31 (±11)	-207	31±10 (±4)	103	10300
	FT-2		-67±6 (±4)	-221	17±7 (±6)	56	10300

available between fuel experiments to evacuate, pressurize, and sample the canisters. Corrections for the dilution were made by multiplying the CH_4 values with the ratio of CO_2 values observed at the EEP (Figure 3.2) to the equilibrated concentration measured while sampling the canister. Corresponding CH_4 emission indices are shown in Figure 2 for 11 canisters collected in this way. It should be noted that emission indices at 100% thrust calculated from subsamples in this way can never be less than zero, as the subsamples at 100% thrust contain no CH_4 and the values recorded by the spectrometer were within the detection limit of the CH_4 measurement. The emission indices derived from plume regressions are negative at high thrusts only because the engine is consuming atmospheric CH_4. In the absence of background atmospheric CH_4, these plume measurements would also be zero. The canister measurements depend on the accuracy, as opposed to the precision, of both the CH_4 and CO_2 measurements, and therefore have much larger error bars. Nevertheless, they validate the finding of CH_4 production at low engine power settings and CH_4 consumption at high engine power settings.

The canister data also demonstrate the importance of engine history on CH_4 emissions. Two subsamples taken from the same inlet at 7% engine thrusts - the first being sampled while the engine was starting from a cold state, and the latter sampled after the engine had operated for 40 minutes at higher thrusts – show vastly differing CH_4 emission indices. The former is off the range of Figure 2 while the latter is indistinguishable from zero. This partially explains the variability seen in advected plume derived emission indices as the timing of the change in engine thrust condition is not coincident with the detection of the plume at the 145-m inlet.

The total amount of CH_4 and N_2O emitted or consumed during a hypothetical landing take-off cycle or a simulated hour of cruising can be calculated by multiplying the above emission rates by the time-in-mode for each segment of a flight. Table 3.3 shows this calculation using the

time-in-modes for a standard International Civil Aviation Organization (ICAO) landing take-off (LTO) cycle as well as one hour of cruising (65% maximum rated thrust) engine power. The calculation indicates that there are slight net CH_4 emissions during this hypothetical LTO cycle, but that even just 1 hour of cruise conditions (65% thrust) leads to far more atmospheric CH_4 destruction. N_2O emissions, in contrast, are positive throughout the LTO cycle, but represent a negligible global N_2O source to the atmosphere. Scaling up the emission rate of N_2O from the ~20 billion gallons of fuel consumed by the airline industry annually results in a yearly N_2O flux of ~4 Gg N_2O yr^{-1}, or roughly .025 % of the total source term of 17.7 Tg N yr^{-1} (2). Aircraft CH_4 emissions, in contrast to N_2O, represent a net atmospheric sink term, consuming roughly 3.5 Gg CH_4 yr^{-1}, completely negligible in terms of the global source and sink terms, each on the order of 580 Tg CH_4 yr^{-1} (2).

A discussion of this work in the context of previous studies is helpful. Wiesen et al. (13) and Heland and Schafer (24) are the only studies, to our knowledge, that present N_2O emissions data. The results of past studies and the present AAFEX work are presented as mean engine exhaust concentrations of N_2O in Figure 3.3. Wiesen et al. (13) measured N_2O offline from exhaust filled cylinders and reported a mean ± 1σ N_2O emission index of 0.11 ± 0.0098 g N_2O (kg Fuel)$^{-1}$ across all thrust settings. This was not corrected for ambient N_2O concentrations, which, if accounted for, would decrease the average emission index by ~30% to a value closer to .077 g N_2O (kg fuel)$^{-1}$, still slightly higher than the average value across all thrust settings of 0.066 ± 0.0018 g N_2O (kg Fuel)$^{-1}$ in this study. The trend of increasing N_2O emissions with increasing thrust is the reverse of the trend at AAFEX. A potential explanation of this trend is that nitrogen oxides (NO_x) can convert to N_2O in these engine plumes, especially in the presence of acid

Table 3.3: Estimates of total CH_4, N_2O, and CO_2 emissions for a simulated Landing-Take-Off (LTO) cycle and a simulated 1-hour flight at cruise thrust using JP-8 fuel. CH_4 and N_2O are also presented as CO_2(e) for ease of comparison of radiative forcing changes attributed to the emissions relative to CO_2.

Mode	**CH_4 rate (g/hr)**	**N_2O rate (g/hr)**	**CO_2 rate (kg/hr)**	**Time in mode (hrs)**	**Total CH_4 emitted (g) (CO_2(e) (g))**	**Total N_2O emitted (g) (CO_2(e) (g))**	**Total CO_2 emitted (g)**
Approach	-57	+64	+3580	0.067	-3.8 (-95)	+4.3 (1300)	$2.4 \cdot 10^5$
Taxi (7%)	+30	+40	+1440	0.433	+13 (320)	+17 (5100)	$6.2 \cdot 10^5$
Take-off	-195	+68	+10500	0.012	-2.3 (-60)	+0.8 (240)	$1.3 \cdot 10^5$
Climb-out	-170	+66	+9300	0.037	-6.3 (160)	+2.4 (720)	$3.4 \cdot 10^5$
Total for					+0.6 (3)	+25 (7500)	$1.3 \cdot 10^6$
Cruise (65%)	-132	+68	+7000	1	-132 (-3300)	+68 ($2.0 \cdot 10^4$)	$7.0 \cdot 10^6$
Flight Total					-131 (-3280)	+93 ($2.7 \cdot 10^4$)	$8.3 \cdot 10^6$

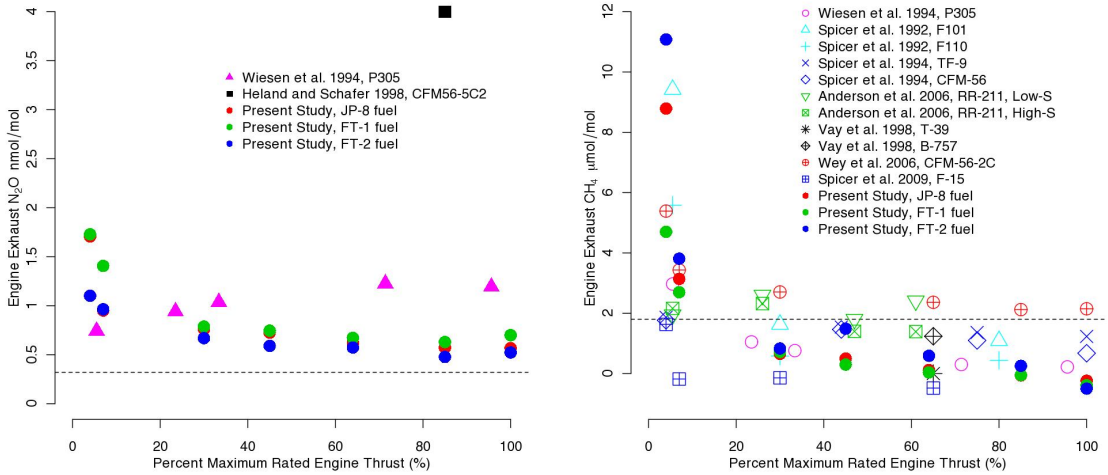

Figure 3.3: Mean engine exhaust concentrations of CH_4 and N_2O for various aircraft emission studies compared to the present AAFEX study. Atmospheric mixing ratios of CH_4 and N_2O are shown as dashed lines for reference.

aerosols (13). Such a mechanism could explain the differences at lower thrusts seen during AAFEX, as these plumes had longer lifetimes than those sampled at higher powers where advection was aided by larger engine exit velocities. The gross agreement with Wiesen et al. (13), however, suggests that this effect is small. Heland and Schafer (24) measured N_2O emissions of aircraft exhaust using a passive FTIR spectrometer. This technique relies heavily on good spectroscopic parameters for the various absorbers present and good background spectra to normalize out the absorption due to molecules present in the instrument aperture but not in the plume. They reported an emission index for higher-thrust levels of 1.3 g N_2O (kg Fuel)$^{-1}$, a full order of magnitude greater than those of Wiesen et al. (13) and this study, but also state that N_2O mixing ratios were below the detection limit at idle power conditions. The engine probed in Heland and Schafer (24) is the same as that of AAFEX. The large discrepancy between the emission ratios reported and the lack of data at idle conditions when N_2O emissions have been shown not significantly different from other power conditions call into question the instrument precisions of N_2O possible with a passive spectrometer.

Other studies mention N_2O aircraft emissions but do not report data. Vay et al. (22), for instance, measured contrail plumes behind a T-39 and a B-757 aircraft but did not report the N_2O data, finding that it was not an important exhaust constituent. During the Airbone Arctic Stratospheric Expedition, Zheng et al. (25) examined 20 plumes of NO_y, 5 of which correlated to CO_2 enhancements. Of those 5 plumes, they found no significant increases for either N_2O or CH_4, and argue that a CH_4 depletion would not have been persistent long enough in the atmosphere to be observed. These findings are consistent with our results.

In addition to the present work, seven other studies have characterized aircraft CH_4 emission data, and the results of these experiments are presented as mean pure engine CH_4 exhaust

concentrations in Figure 3.3. Pure exhaust concentrations are calculated by multiplying emission ratios of Equation 3.1 by the difference between CO_2 values at the EEP and ambient values and adding ambient concentrations. Spicer et al. (11) were among the first to report detailed organic species as well as CO, CO_2, and nitrogen oxides for aircraft engine emissions. The 1992 study (11) published data using JP-4 fuel in F-101 and F-110 engines, used primarily on the B1-B and F-16 airplanes, respectively. The 1994 paper (12) focused on engines used in more commercial transport aircraft such as the Boeing 737, the CFM-56 and TF-39. Interestingly, the core engine of the CFM-56 is the same as that of the F-101 engine used in the 1992 study. Nevertheless, the two engines seemingly produced very different CH_4 emission indices particularly at idle. Wiesen et al. (13) report positive CH_4 emission indices at all powers but also present exhaust concentrations which are always influenced by ambient atmospheric CH_4. Their emission indices are positive at high thrusts only because CH_4 is present in the air used in the aircraft engines. Given their extractive sampling technique, removing the influence of background atmospheric CH4 abundance was not possible, but their emission indices are misleading because background air samples were not characterized. Only the exhaust concentrations are used when comparing across studies in Figure 3.

During the NASA Experiment to Characterize Aircraft Volatile Aerosol and Trace-species Emissions (EXCAVATE), Anderson et al. (26) measured CH_4 with a 1-Hz precision of 1 nmol/mol on the Rolls Royce RB211-535E4 engine using two different JP-5 fuels and reported CH_4 emission concentrations as well as upper limits of emission indices. They chose not to report possibly negative emission indices, as these represent consumption of CH_4, but present exhaust concentrations of CH_4 that are similar to ambient values around 1.8 μmol/mol. Their emission indices are dependent on the instrumental accuracy, which they report as 1% (as

opposed to a precision of .1%) meaning that nearly all of their reported exhaust CH_4 concentrations are within 20 nmol/mol of ambient CH_4 concentrations. In contrast with direct exhaust canister sampling, the advected plume method employed in this study relies only on the instrument precision, as it is the relative changes in CH_4 that determine emission indices. Our instrument precision is .03%. The emission indices of JP-8 fuel during low power during the AAFEX mission were higher by an order of magnitude than during the EXCAVATE mission, most likely attributable to the different engine, fuel, and engine history before sampling. EXCAVATE low power results most closely resemble those of Spicer et al. (11), while AAFEX low power results are more similar to those of Spicer et al. (12).

One research question that persists in many of these simulated flight engine emission studies is whether the results are representative of actual flight conditions. Vay et al. (22) sought to answer this during the SUCCESS (Subsonic Aircraft: Contrail and Cloud Effects Special Study) campaign by sampling CO, CH_4 (with reported 1-sec precision of 1 nmol/mol), N_2O, and H_2O from inlets aboard the NASA DC-8 (the same plane used as the emission source in AAFEX) flying behind a T-39 and B-757 aircraft. They reported that 81% of the plume crossings exhibited a negative correlation between CH_4 and CO_2, illustrating consumption of atmospheric CH_4. Their reported emission indices ranged from -1.6 to 1.2 g CH_4 $(kg\ Fuel)^{-1}$, with the positive values attributed to transient engine conditions (i.e. changing from 65% to 85% maximum rated thrust). The range of values observed at AAFEX were much smaller in magnitude than the -1.6 value, though we note that only 12 plumes were quantified during SUCCESS. Their findings further validate previous ground-based simulated flight CH_4 exhaust emission studies. Furthermore, Wiesen et al. (13) showed that CH_4 depletion at high power was observed from aircraft both at a ground-level test facility and at a special altitude-simulation test cell.

It is important to note that aircraft NO_x emissions at altitude have a greater potential to impact global CH_4 budgets than the levels of CH_4 emissions quantified in these various studies, whether positive or negative (2). Stevenson and Derwent (27), for instance, used a global lagrangian chemistry transport model to calculate that aircraft NO_x emissions amounting to an integrated pulse of 1 Tg NO_2 at altitude resulted in an eventual removal of 2.5 Tg CH_4 from the system, or less than 0.5% of total CH_4 sink terms. Because high thrust (>30% maximum rated thrust) NO_x emission indices are a factor of ~200 greater than the equivalent magnitude of CH_4 emission indices, the indirect CH_4 consumption due to chemical cycling through NO_x, O_3, OH, etc. affects CH_4 distributions more than the direct CH_4 consumption in the engine (28).

Two studies differ markedly from the aforementioned experiments and the present AAFEX results. Measurements during the Aircraft Particle Emissions eXperiment (APEX) reported positive CH_4 emission indices at higher engine power (Wey et al. 2006). CH_4 was measured with a multi-gas analyzer. Due to its relatively broad spectroscopic resolution, this instrument does not have the specificity to CH_4 that other measurement techniques have, and may have been subject to interference from other species present in the exhaust. Spicer et al. (29) also present CH_4 emission indices for both a C-130 aircraft and a F-15 aircraft. The corrigendum to the study (30) noted an error in the algorithm used to calculate emission factors which decreased the CH_4 emission factors by ~15% for the C-130 and changed the sign on the F-15 factors. Only the F-15 emission indices are presented in Figure 3 as the emission factors for the C-130 aircraft are so high that corresponding CH_4 exhaust concentrations at all power settings would be on the order of 20-30 μmol/mol, well beyond the range of the figure. We also note that their equation for determining emission factors effectively removes the CO_2 concentrations measured from the emission factor calculation by assuming that all of the fuel carbon is converted to either CO_2, CO

or other hydrocarbons. Because the equation then depends on the emission factors of other chemical species, many of which have much lower measurement precisions, these values are not directly comparable to other CH_4 emission indices, which may be an additional reason why the C-130 values are beyond the range of expected emission indices and exhaust concentrations.

Although low power emissions of CH_4 seem to vary by almost an order of magnitude, these studies agree, with the exception of Spicer et al. (30), on the general trend of CH_4 consumption at power conditions greater than idle and taxi, the predominate mode of engine operation. Data presented here further confirms CH_4 emission results from previous aircraft exhaust studies and demonstrates that the adoption of alternative fuels by the airline industry will have negligible end-use effects on these long-lived greenhouse gases. Increased use of fertilizer to produce Fischer-Tropsch feedstock, however, may increase the N_2O emissions associated with the total life-cycle emissions from FT fuels.

This AAFEX study, in conjunction with previous CH_4 and N_2O exhaust studies, provides another robust constraint on long-lived greenhouse gas emissions of commercial aircraft engines in operation today. Furthermore, CH_4 emissions are essential to understanding the speciation of total hydrocarbons, a variable more commonly measured during engine certification. Accounting for speciation of organic emissions including CH_4, particularly at low power settings, helps constrain the correct proportions of individual compounds that contribute the most risk to human health and welfare. The measurement precisions of both CH_4 and N_2O presented in this study are the best to date, more than a factor of two times better than previous studies. By considering a representative flight LTO cycle, the net contributions to global CH_4 from aviation due to direct CH_4 emissions are negative, indicating a net CH_4 consumption. NO_x emissions at

altitude, however, have a greater impact on the global CH_4 budget than direct CH_4 emissions, whether positive or negative.

Acknowledgements

Parts of this reasearch are supported by the Department of Energy, Small Business Innovation Research Award DE-FG02-07ER84889, the PARTNER Center of Excellence (jointly sponsored by the FAA, NASA and Transport Canada) via Missouri University of Science and Technology, and the National Science Foundation Graduate Research Fellowship Program. The authors also greatly acknowledge W. Berk Knighton of Montana State University, Michael T. Timko and Zhenhong Yu of Aerodyne Research Inc., and Changlie Wey of ASRC Aerospace Corp. They would also like to thank Bruce Anderson, Robert Howard, Dan Bulzan, Frank Cutler, Mike Bereda, members of the Air Force Research Lab, and the entire DC-8 crew that made these measurements possible. They are also grateful for the comments and suggestions of the reviewers.

References

1. Lelieveld, J., P. J. Crutzen, and F. J. Dentener. Changing concentration, lifetime and climate forcing of atmospheric methane. *Tellus Series B-Chemical and Physical Meteorology*. **1998**, 50, 128–150.

2. Denman, K., G. Brasseur, A. Chidthaisong, P. Ciais, P. Cox, R. Dickinson, D. Hauglustaine, C. Heinze, E. Holland, D. Jacob, U. Lohmann, S. Ramachandran, P. da Silva Dias, S. Wofsy, and X. Zhang. Couplings Between Changes in the Climate System and Biogeochemistry. In *Climate Change 2007: The Physical Science Basis*. In *Contribution of Working Group I to the Fourth Assessment Report of the Intergovernmental Panel on Climate Change*. Cambridge University Press: Cambridge, United Kingdom and New York, NY, USA: 2007.

3. Quay, P., J. Stutsman, D. Wilbur, A. Snover, E. Dlugokencky, and T. Brown. The isotopic composition of atmospheric methane. *Global Biogeochemical Cycles*. **1999**, 13, 445–461.

4. Prather, M. J. Time scales in atmospheric chemistry: Coupled perturbations to N_2O, NO_y, and O_3. *Science*. **1998**, 279, 1339–1341.

5. Lassey, K. R., D. M. Etheridge, D. C. Lowe, A. M. Smith, and D. F. Ferretti. Centennial evolution of the atmospheric methane budget: what do the carbon isotopes tell us? *Atmospheric Chemistry and Physics*. **2007**, 7, 2119–2139.

6. Dlugokencky, E. J., L. Bruhwiler, J. W. C. White, L. K. Emmons, P. C. Novelli, S. A. Montzka, K. A. Masarie, P. M. Lang, A. M. Crotwell, J. B. Miller, and L. V. Gatti. Observational constraints on recent increases in the atmospheric CH_4 burden. *Geophysical Research Letters*. **2009**, 36, L18803.

7. Rigby, M., R. G. Prinn, P. J. Fraser, P. G. Simmonds, R. L. Langenfelds, J. Huang, D. M. Cunnold, L. P. Steele, P. B. Krummel, R. F. Weiss, S. O'Doherty, P. K. Salameh, H. J. Wang, C. M. Harth, J. Muhle, and L. W. Porter. Renewed growth of atmospheric methane. *Geophysical Research Letters*. **2008**, 35, 6.

8. Kroeze, C., A. Mosier, and L. Bouwman. Closing the global N_2O budget: A retrospective analysis 1500-1994. *Global Biogeochemical Cycles*. **1999**, 13, 1-8.

9. Brasseur, G. P., R. A. Cox, D. Hauglustaine, I. Isaksen, J. Lelieveld, D. H. Lister, R. Sausen, U. Schumann, A. Wahner, and P. Wiesen. European scientific assessment of the atmospheric effects of aircraft emissions. *Atmospheric Environment*. **1998**, 32, 2329–2418.

10. Prather, M. J. and J. Hsu. Coupling of Nitrous Oxide and Methane by Global Atmospheric Chemistry. *Science*. **2010**, 330, 952–954.

11. Spicer, C., M. Holdren, D. Smith, D. Hughes, and M. Smith. Chemical composition of exhaust from aircraft turbine engines. *Journal of Engineering for Gas Turbines and Power*. **1992**, 114, 111–117.

12. Spicer, C., M. Holdren, R. Riggin, and T. Lyon. Chemical composition and photochemical reactivity of exhaust from aircraft turbine engines. *Annales Geophysicae*. **1994**, 12, 944–955.

13. Wiesen, P. J., J. Kleffmann, R. Kurtenbach, and K. Becker. Nitrous oxide and methane emissions from aero engines. *Geophysical Research Letters*. **1994**, 21, 2027–2030.

14. Laird, C. K. and S. A. Sloan. Nitrous-oxide emissions from U.K. power-stations. *Atmospheric Environment Part A-General Topics*. **1993**, 27, 1453–1457.

15. Dlugokencky, E. J., K. A. Masarie, P. M. Lang, and P. P. Tans. Continuing decline in the growth rate of the atmospheric methane burden. *Nature*. **1998**, 393, 447–450.

16. B. E. Anderson et al. Alternative Aviation Fuel Experiment (AAFEX). **2011**, NASA TM-2011-217059.

17. Tuzson, B., J. Mohn, M. J. Zeeman, R. A. Werner, W. Eugster, M. S. Zahniser, D. D. Nelson, J. B. McManus, and L. Emmenegger. High precision and continuous field measurements of delta C-13 and delta O-18 in carbon dioxide with a cryogen-free QCLAS. *Applied Physics B-Lasers and Optics*. **2008**, 92, 451–458.

18. Zahniser, M. S., D. D. Nelson, J. B. McManus, S. C. Herdon, E. C. Wood, J. H. Shorter, B. H. Lee, G. W. Santoni, R. Jimnez, B. C. Daube, S. Park, E. A. Kort, and S. C. Wofsy. Infrared qc laser applications to field measurements of atmospheric trace gas sources and sinks in environmental research: enhanced capabilities using continuous wave QCLS. *SPIE*. **2009**, 7222; DOI 10.1117/12.815172.

19. Lee, B.H, E.C. Wood, M. S. Zahniser, J. B. McManus, D. D. Nelson, S. C. Herdon, G. W. Santoni, S. C. Wofsy, and J. W. Munger. Simultaneous measurements of atmospheric HONO and NO_2 via absorption spectroscopy using tunable mid-infrared continous-wave quantum cascade lasers. *Applied Physics B-Lasers and Optics*. **2010**, 102, 417-423.

20. Wey, C. C., B. E. Anderson, C. Hudgins, C. Wey, X. Li-Jones, E. Winstead, L. K. Thornhill, P. Lobo, D. Hagen, P. Whitefield, P. E. Yelvington, S. C. Herndon, T. B. Onasch, R. C. Miake-Lye, J. W. Wormhoudt, B. Knighton, R. Howard, D. Bryant, E. Corporan, C. Moses, D. Holve, and W. Dodds. Aircraft particle emissions experiment (APEX). *NASA/TM-2006-214382*. 2006.

21. Herndon, S., J. Shorter, M. Zahniser, D. Nelson, J. Jayne, R. Brown, R. C. Miake-Lye, I. Waitz, P. Silva, T. Lanni, K. Demerjian, and C. Kolb. NO and NO_2 emission ratios measured from in-use commercial aircraft during taxi and takeoff. *Environ. Sci. Technol*. **2004**, 38, 6078–6084.

22. Vay, S., B. Anderson, G. W. Sachse, J. E. Collins, J. R. Podolske, C. H. Twohy, B. Gandrud, K. R. Chan, S. L. Baughcum, and H. A. Wallio. DC-8-based observations of aircraft CO, CH_4, N_2O, and H_2O(g) emission indices during SUCCESS. *Geophysical Research Letters*. **1998**, 25, 1717–1720.

23. Yelvington, P. E., S. C. Herndon, J. C. Wormhoudt, J. T. Jayne, R. C. Miake-Lye, W. B. Knighton, and C. Wey. Chemical speciation of hydrocarbon emissions from a commercial aircraft engine. *Journal of Propulsion and Power*. **2007**, 23, 912–918.

24. Heland, J. and K. Schafer. Determination of major combustion products in aircraft exhausts by FTIR emission spectroscopy. *Atmospheric Environment*. **1998**, 32, 3067–3072.

25. Zheng, J., A. J. Weinheimer, B. A. Ridley, S. C. Liu, G. W. Sachse, B. E. Anderson, and J. E. Collins. An analysis of aircraft exhaust plumes from accidental encounters. *Geophysical Research Letters*. **1994**, 21, 2579–2582.

26. Anderson, B., G. Chen, and D. Blake. Hydrocarbon emissions from a modern commercial airliner. *Atmospheric Environment*. **2006**, 40, 3601–3612.

27. Stevenson, D.S. and R.G. Derwent. Does the location of aircraft nitrogen oxide emissions affect their climate impact? *Geophysical Research Letters*. **2009**, 36, L17810.

28. Stevenson, D. S., R. M. Doherty, M. G. Sanderson, W. J. Collins, C. E. Johnson, and R. G. Derwent. Radiative forcing from aircraft NOx emissions: Mechanisms and seasonal dependence. *Journal of Geophysical Research-Atmospheres*. **2004**, 109, D17.

29. Spicer, C. W., M. W. Holdren, K. A. Cowen, D. W. Joseph, J. Satola, B. Goodwin, H. Mayfield, A. Laskin, M. L. Alexander, J. V. Ortega, M. Newburn, R. Kagann, and R. Hashmonay. Rapid measurement of emissions from military aircraft turbine engines by downstream extractive sampling of aircraft on the ground: Results for C-130 and F-15 aircraft. *Atmospheric Environment*. **2009**, 43, 2612–2622.

30. Spicer, C. W., M. W. Holdren, K. A. Cowen, D. W. Joseph, J. Satola, B. Goodwin, H. Mayfield, A. Laskin, M. L. Alexander, J. V. Ortega, M. Newburn, R. Kagann, and R. Hashmonay. Corrigendum to: Rapid measurement of emissions from military aircraft turbine engines by downstream extractive sampling of aircraft on the ground: Results for C-130 and F-15 aircraft. *Atmospheric Environment*. **2009**, 43, 6120–6120.

Chapter 4:

Intercomparison of the Airborne Quantum Cascade Laser Spectrometer (QCLS) Measurements of the Greenhouse Gas suite – CO_2, CH_4, N_2O, and CO – during the CalNex and HIPPO campaigns

Abstract

We present a comparison of aircraft observations of the suite of long-lived greenhouse gases (CO_2, CH_4, N_2O, and CO) using a direct-absorption pulsed quantum cascade laser spectrometer (QCLS) operated during the HIPPO and CalNex airborne experiments. The QCLS measurements are compared to two vacuum ultraviolet (VUV) CO instruments (CalNex and HIPPO), a cavity ring-down spectrometer (CRDS) measuring CO_2 and CH_4 (CalNex), two broadband non-dispersive infrared spectrometers (NDIR) measuring CO_2 (HIPPO), two onboard gas chromatographs measuring a variety of chemical species including CH_4, N_2O, and CO (HIPPO), and various flask-based measurements of all four species. QCLS measurements are tied to NOAA standards using an in-flight calibration system. The details of the end-to-end calibration procedures and the data quality-assurance and quality-control (QA/QC) are presented. Specifically, we discuss best practices for the traceability of standards given uncertainties in calibration cylinders, isotopic and surface effects for the suite of long-lived greenhouse gas tracers, interpolation techniques for in-flight calibration additions, and the effects of instrument linearity on retrieved mixing ratios.

4.1. Introduction

Growing interest in understanding the drivers of climate change has sparked innovation in instrumentation to measure the suite of long-lived greenhouse gases and associated chemical tracers (Fried et al. 2009, Nelson et al. 2004, Zare et al. 2009). The increase in measurements has not, however, been accompanied by a standardization of calibration techniques. Many sensors rely on the accuracy of spectroscopic parameters (e.g. linestrengths and their pressure and temperature dependencies) to derive *in-situ* 'spectroscopically-calibrated' mixing ratios from raw spectra (Rothman et al. 2009, Zahniser et al. 1995). The use of this raw data is often appropriate, particularly if: 1) a sensor is linear with respect to the range of observed concentrations, and 2) the quantity of interest is the relative enhancement of one chemical tracer versus another or versus background values measured on the same sensor. More and more studies, however, are incorporating data from different sensors (Gerbig et al. 2003, Zhao et al. 2009, Xiang et al. 2012, Miller et al. 2008). It is in this context that spectroscopically-calibrated mixing ratios are insufficient, as small differences in sensor accuracies can have large effects on inversion results (Santoni et al. 2013).

Here we discuss best practices for the traceability of airborne spectrometer measurements. We present an overview of the quantum cascade laser spectrometer (QCLS) sensor used on two airborne campaigns - the HIAPER Gulfstream-V Pole-to-Pole Observations (HIPPO, Wofsy et al. 2011) and the California Research at the Nexus of Air Quality and Climate Change (CalNex, Ryerson et al. 2012) experiment – and present measurement intercomparisons with other onboard sensors. We describe operations of the QCLS and the calibrations of the long-lived greenhouse-gas suite measurements of CO_2, CH_4, N_2O, and CO. We evaluate the traceability of calibration standards from NOAA values to the in-flight standards as well as long-term sensor

stability. We then characterize the in-flight drift through standard-addition interpolations and discuss how this affects our overall accuracy. In the context of traceability and sensor accuracy, we discuss sample conditioning, surface equilibration effects, and isotopic effects on calibration standards.

4.2. Quantum Cascade Laser Spectrometer

4.2.2. QCLS hardware

This work focuses on data collected using the Harvard/Aerodyne-Research-Inc. quantum cascade laser spectrometer (QCLS). To the extent they are needed in explaining the traceablility of our measurements, we briefly describe the instrument characteristics, noting that more details of the spectrometer are available in Jimenez et al. (2005) and Jimenez et al. (2006). The QCLS uses three pulsed quantum cascade lasers to measure CO_2, CH_4, N_2O, and CO by absorption spectroscopy. One laser (QCL1) is used as a light source for a differential absorption measurement of CO_2 by recording an absorption spectrum relative to a known standard flowing through a separate measurement cell. The remaining two lasers are tuned across absorption lines for CH_4 and N_2O in one scan (QCL2), and CO in another (QCL3), making use of a multi-pass astigmatic sample cell to increase the effective optical path length (McManus et al., 1995). The light pulses from the 3 QCLs are detected using photovoltaic detectors housed and cooled in two liquid nitrogen (LN_2) dewars: one for CO_2/QCL1, and the other for both CH_4/N_2O/QCL2 and CO/QCL3. The optical table, QCL1, two 10-cm path length sampling cells, and a dewar housing InSb detectors for the CO_2 portion of the QCLS are enclosed in a pressure vessel flushed with ultra-high-purity nitrogen to remove the effects of absorption external to the sampling cells. QCL2 and QCL3, an astigmatic multi-pass sampling cell with an effective 76 m path length, and a dewar housing the HgCdTe detectors are mounted on a second optical table surrounded by a

temperature regulated enclosure. The pulses from QCL2 and QCL3 are temporally multiplexed on the same detector.

The spectra acquired from the two optical tables are controlled and analyzed by the same computer. TDL Wintel® software controls the laser temperature (and overall output frequency), tuning ramp rate (the wavelength frequency resolution over which the laser is tuned) and the detector multiplexing (for QCL2 and QCL3 which share a common detector). The temperature regulation of the QCLs is achieved by means of peltier modules coupled to a closed-circuit recirculating fluid kept at fixed temperature within ± 0.1 K. With the exception of the chiller fluid, electronics and computer, the CO_2 measurement (QCLS-CO2) can be considered independent from the CH_4, N_2O, and CO measurements (QCLS-DUAL) and we refer to those two sensors as such.

The instrument is fully-autonomous and sampling, calibration, temperature regulation, and pressure control are controlled by a data-logger (CR10X, Campbell Scientific). It logs control variables and periodically dumps them via a serial connection to the computer running TDL Wintel® for storage on a solid state hard drive. Because the sampling and control strategy is controlled by the data-logger and the spectral analysis is performed by the TDL Wintel® software running on the computer, in-flight spectra are acquired using a fixed nominal cell pressure and cell temperature. Raw spectra are later reanalyzed with the logged CR10 cell pressure and cell temperature measurements to generate spectroscopically-calibrated mixing ratios. Figure 4.1 shows the raw spectra and the Levenberg-Marquardt fits to the spectra for the three QCLs. The CO_2 spectrum appears inverted because this particular air sample has less CO_2 than the calibration air flowing through the reference cell.

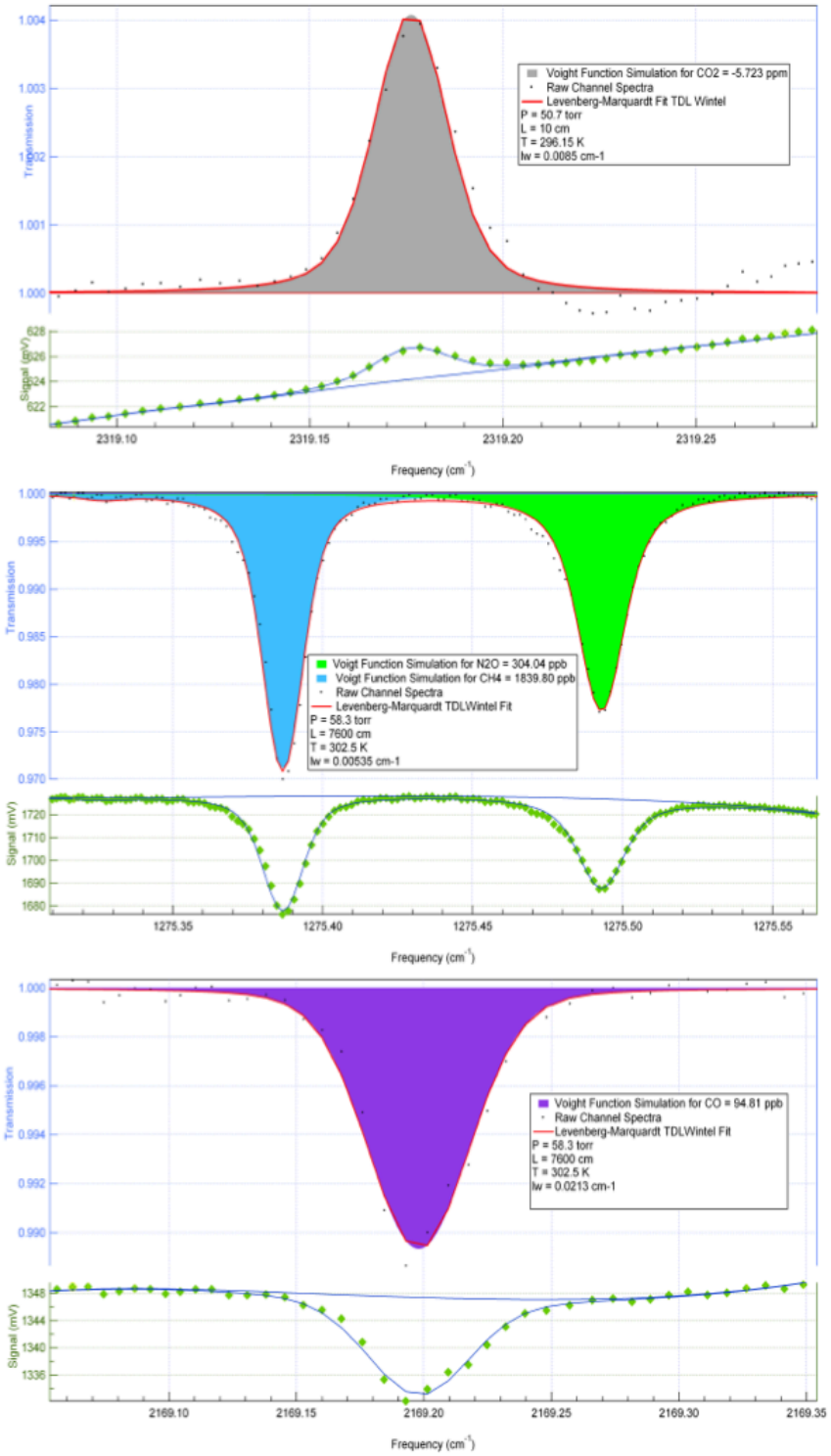

Figure 4.1: The absorption spectra for the 3 quantum cascade lasers. QCL1 (a) is a differential measurement of $^{12}CO_2$ and therefore appears inverted because this sample has a lower concentration of CO_2 than the reference gas. QCL2 (b) shows the spectrum for CH_4 and N_2O and QCL3 (c) shows the spectrum for CO.

Optical-based measurements are particularly sensitive to fluctuations in temperature and pressure (Zahniser et al. 1995) and careful controls must be implemented, particularly during flight where large dynamic ranges in both variables are observed (Fried et al. 2008). Because pressure and temperature regulation can never be perfect, in-flight calibrations at regular intervals from cylinders are used to track sensor drift. As long as the inter-calibration time interval is shorter than the long-term drift, calibrations can offset inaccuracies due to pressure and temperature fluctuations. The Allan variance, a measure of the precision of a sensor as a function of averaging time, can be used to quantify both the short and long-term precision of a sensor as well as the drift. Figure 4.2 shows the in-flight Allan variance for the CO_2, CH_4, N_2O, and CO measurements from the QCLS with 1-second RMS precisions of 20, 0.5, 0.08, and 0.15 ppb, respectively. The measurements shown in Figure 4.2 were taken during a section of HIPPO that sampled a relatively constant air mass. This is the same section of data presented in the supplementary material section of Kort et al. (2011). Table 4.1 summarizes the Allan precisions at 1, 10, and 100 seconds for the 4 species. Between 1 and 10 seconds, the Allan precision decreases for all species, but only continues to decrease between 10 and 100 seconds for N_2O. This is largely because atmospheric variability in CO_2, CH_4, and CO is larger relative to N_2O as the atmospheric lifetime of N_2O in the troposphere is long and the sources are weaker than the other species. Because of this, Table 4.1 also includes the Allan precision from laboratory tests that sampled air continuously flowing from calibration cylinders with near-ambient atmospheric concentrations.

The instrument schematic for QCLS-CO2 is shown in Figure 4.3 and is very similar to the flow schematic for QCLS-DUAL. QCLS-CO2 and QCLS-DUAL have independent inlets. On the HIAPER-GV, both inlets extend out from the QCLS rack to a dedicated NCAR HIAPER

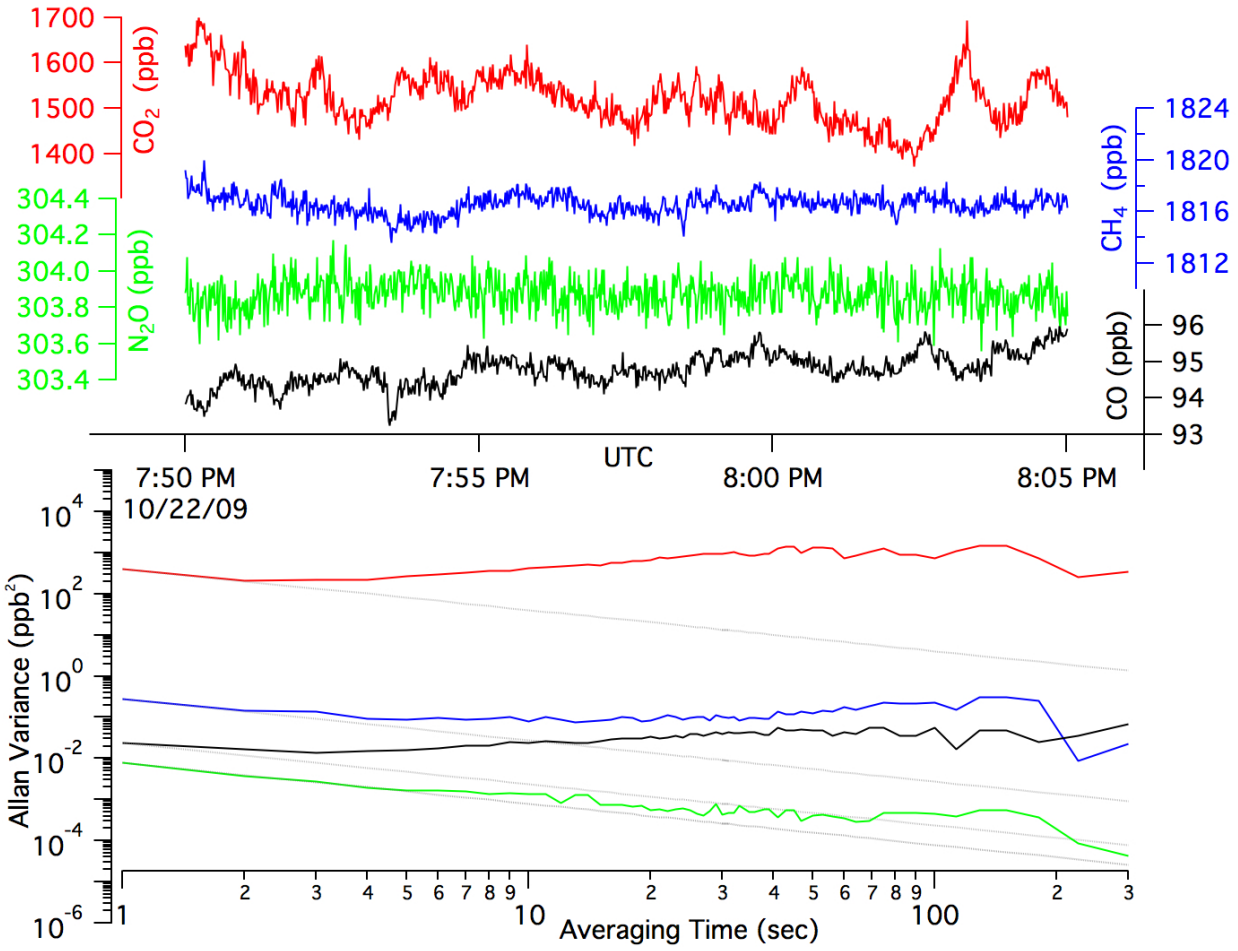

Figure 4.2: Time series for the 4 QCLS species during 20 minutes of in-flight sampling over the Pacific during HIPPO II (top) and the Allan variance as a function of averaging time for the data shown (bottom). Table 4.1 summarizes these data and also provides corresponding values for sampling from a calibration cylinder in the laboratory.

Table 4.1: Allan precision as a function of averaging time for the 4 QCLS species measured during the in-flight sampling of a relatively constant air mass on HIPPO II, October 22nd, 2009 ('flight') and during laboratory testing sampling continuously from a secondary calibration cylinder ('lab'). Accuracy estimates are based on the accuracy of the NOAA primary cylinders.

	1σ Allan Precision (ppb)						
	1 sec		**10 sec**		**100 sec**		
Species	flight	lab	flight	lab	flight	lab	**Accuracy (ppb)**
CO_2	20.	13	20.	2.3	27	1.7	100
CH_4	0.52	0.50	0.28	0.18	0.47	0.09	1
N_2O	0.089	0.080	0.037	0.038	0.021	0.024	0.2
CO	0.15	0.15	0.15	0.041	0.24	0.018	3.5

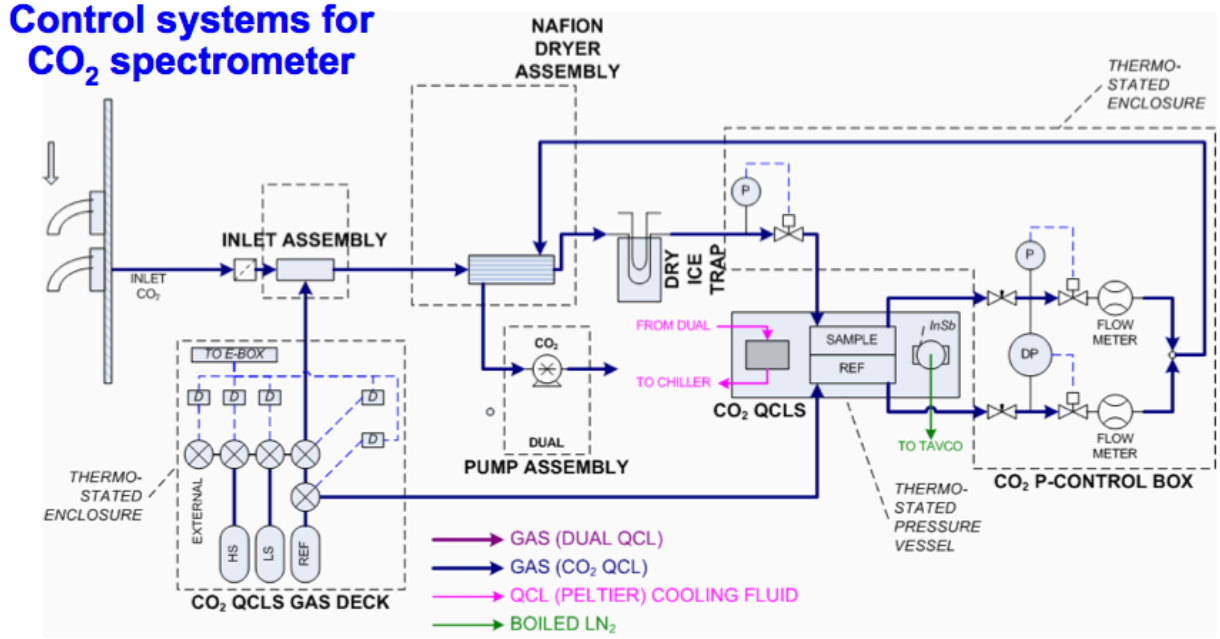

Figure 4.3: Schematic of the QCLS-CO2 sampling system.

Modular Inlet (HIMIL) mounted to the edge of the aircraft. The HIMIL extends the inlet 19 cm from the body of the aircraft (NCAR 2005) and the two QCLS inlets sample from within the center flow path, oriented away from the direction of flow. This orientation minimizes large particle entrainment and protects the sampling system from liquid water and ice. For the NOAA P-3 aircraft, the inlets both consist of stainless steel 1/2' OD tubing bent at 90 degrees and oriented at -135 degrees relative to the horizontal direction of flight. Once the sample enters the body of both aircrafts, the two sample lines consist of ~1.5 m of Dekoron™ tubing (¼' OD for QCLS-CO2 and ½' OD for QCLS-DUAL) and each sample streams reaches a 2 μm filter mounted in an aluminum filter holder (Gelman Sciences, Inc., Rossdorf, Germany). Calibration gases are added downstream of the filter using a combination of 2-way and 3-way solenoid valves. When activated, the solenoid valves allow air from two sets of calibration gas decks which each include 3 cylinders (1.1 L for QCLS-CO2 and 2.0 L for QCLS-DUAL) to over-blow the inlet. The regulators for the calibration cylinders are set on the ground to achieve an excess flow >100 sccm (QCLS-CO2) or >200 sccm (QCLS-DUAL) which flows via the filters and inlets out the aircraft. From this point, the sample (or calibration air) travels through a 1-tube (QCLS-CO2, see Daube et al. 2002 for an explanation of this choice) or 50-tube (QCLS-DUAL) Nafion™ membrane dryer to remove the bulk of the water vapor. Then air passes through a Teflon dry-ice trap to further reduce the dewpoint to below -70 °C. A stainless steel filter at the outlet of the dry-ice trap ensures that particles cannot thaw, evaporate, and contaminate the measurement cell mirrors. From the dry ice-trap, air enters the sampling cells, the pressures of which are controlled both upstream and downstream of the cell using a pressure controller and valve (MKS 722, 100 torr). For QCLS-CO2, the sample and reference cells are controlled to 70 ± 0.1 hPa using another pressure controller and value measuring the differential pressure

between the sample and reference cells. For QCLS-DUAL, the 0.5 L cell is controlled to 70 ± 0.1 hPa. After the pressure control element downstream of the sampling cells, the flows are routed back through the outer tube enclosing the Nafion membrane tubes to create the necessary H_2O gradient across the membrane. The flows are then combined into a 4-stage diaphragm pump (KNF Neuberger, Inc.) fitted with Teflon-lined diaphragms. Two of the heads are connected in parallel and the remaining two in series to compensate throughput and power. For the HIAPER-GV, the exhaust is then dumped to a dedicated exhaust manifold in the aircraft. For CalNex, the exhaust is dumped through a third stainless steel port downstream of the inlet.

Overall instrument response time is largely controlled by the sampling cell volume, pressure, and flow rate. Additional lags associated with mixing within the different sampling volumes are second order effects, but are minimized by using ¼ OD and ½ OD Dekaron™ for QCLS-CO2 and QCLS-DUAL respectively. The larger diameter tubing is needed for QCLS-DUAL because of the larger sample cell volume. The flow rate through QCLS-CO2 and QCLS-DUAL is 0.1 and 1.5 slpm, which correspond to cell flushing times of ~1 sec for both sensors, assuming plug flow.

4.2.2. QCLS hardware

In-flight calibrations are made using sample-additions from compressed gas cylinders in two 'gas decks' mounted on the QCLS flight rack (see Figure 4.3). The QCLS-CO2 gas deck contains three 1.1 L carbon-fiber wrapped aluminum compressed air cylinders and the QCLS-DUAL gas deck has three 2.0 L cylinders. The QCLS-CO2 gas deck is filled with three whole-air standards containing CO_2 concentrations in the ~370-410 ppm range, two of which are used as 'spans' (a low-span at ~375 ppm and a high-span at ~405 ppm) and the other as the 'reference' (at roughly ambient concentrations of ~390 ppm). The QCLS-DUAL gas deck also

contains two spans and a 'zero,' which is ultra-pure whole air. The gas decks are filled using air from size AL compressed air cylinders ordered from Scott-Marrin gases. The AL cylinders used to fill the QCLS-CO2 gas deck are calibrated on the historic Harvard Licor-based ground calibration unit discussed in Daube et al. (2002). The AL cylinders used to fill the QCLS-DUAL gas deck are calibrated using the QCLS itself and a set of 'primary' size ALM cylinders filled and calibrated by NOAA. We refer to the AL cylinders used to fill gas-decks as 'secondary' calibration cylinders. Secondary cylinders are typically initially pressurized to ~ 2100 psi and the gas decks are filled to as high a pressure as possible, usually >1800 psi. Gas-decks are sampled until the pressure drops to 500 psi, well before drifts in concentration become apparent (Daube et al. 2002). Table 4.2a summarizes the two calibrations of the primary cylinders used in HIPPO and CalNex and Table 4.2b summarizes the calibration obtained for the secondary cylinders used to fill the QCLS-DUAL gas deck.

For QCLS-DUAL, secondary cylinders are calibrated against the NOAA primary tanks. Figure 4.4 shows the calibration procedure used to calibrate a secondary cylinder in the lab. We turn on the QCLS and allow it to equilibrate while it is sampling zero-air from an AL cylinder for at least 2 hours. Three primary tanks and a secondary 'target' tank are plumbed into a external bank of solenoid valves connected to the QCLS-DUAL via an external port on the gas deck. The QCLS is operated in exactly the same mode as in-flight sample-addition, where the calibration solenoid is actuated and excess calibration air (>100sccm and >200 sccm for QCLS-CO2 and QCLS-DUAL, respectively) flows out through the QCLS inlet. The primary and secondary tanks are plumbed into the external solenoid bank and the QCLS via 1/8' OD stainless steel tubing. After equilibration, we sample zero-air for 5 minutes, then sequentially flow air from three primaries in order of lowest to highest concentration for 3 minutes each. After this

Table 4.2a: Summary of the primary calibration cylinders used during the CalNex and HIPPO campaigns for QCLS-DUAL. The primary cylinders were made and calibrated at NOAA in 2005, then recalibrated again after CalNex and before HIPPO IV in 2011. The difference between the two calibrations is shown for each tank and each species.

			CH_4 (ppb)		N_2O (ppb)		CO (ppb)	
Name	**Cylinder ID**	**Cal Date**	**M.R.**	**1σ**	**M.R.**	**1σ**	**M.R.**	**1σ**
Primary 1	ND24119	7/6/2005	991.8	0.3	154.6	0.2	45.1	0.6
Primary 1	ND24119	6/30/2011	995.2	0.3	155.0	0.2	50.4	0.2
			Δ= -3.4		Δ= -0.4		Δ= -5.3	
Primary 2	ND24116	7/6/2005	1361.2	0.2	326.92	0.13	102.2	0.4
Primary 2	ND24116	8/16/2011	1363.3	0.5	326.92	0.10	103.5	0.7
			Δ= -2.1		Δ= 0		Δ= -1.3	
Primary 3	ND24117	7/11/2005	1801.1	0.3	339.2	0.15	352.6	2
Primary 3	ND24117	6/20/2011	1801.1	0.2	339.43	0.15	352.9	0.5
			Δ= 0		Δ=-0.23		Δ= -0.3	
Primary 4	ND24118	5/5/2005	2470.9	0.3	356.39	0.15	980.1	10
Primary 4	ND24118	8/16/2011	2466.5	1	357.03	0.16	982.4	6.7
			Δ= 4.4		Δ=-0.64		Δ= -2.3	
Primary 5	ND29403	8/30/2007	490.5	2.4	248.12	0.10	21.5	0.1
Primary 5	ND29403	6/21/2011	486.8	0.2	247.85	0.11	22.7	0.4
			Δ= 3.7		Δ= 0.27		Δ= -1.2	

Table 4.2b: Summary of the secondary calibration cylinders used to fill the gas deck during the CalNex and HIPPO campaigns for QCLS-DUAL. Tanks that were used for multiple deployments (different shadings) were recalibrated prior to each use.

Name	Cylinder ID	Date	CH_4 (ppb)	N_2O (ppb)	CO (ppb)
H1/H2 LS	CC12362	11/20/2008	1504.94	255.11	34.76
H1/H2 HS	CC81179	11/20/2008	1929.76	338.52	201.69
H1/H2/CN LS	CC37815	01/29/2010	1672.87	301.55	58.32
H1/H2/H3 HS	CC62384	01/29/2010	2210.91	354.11	328.84
H3/H4/H5 LS	CC89589	01/29/2010	1666.70	298.43	43.75
H3/CN HS	CC113530	01/29/2010	2200.46	358.14	326.22
H3 REF	CC73108	02/01/2010	1924.41	336.22	199.90
H1/H2/H3 HS	CC62384	01/12/2011	2210.50	353.96	328.91
H3/CN HS	CC113530	01/12/2011	2201.21	358.33	327.02
CN LS	CC37840	01/13/2011	1684.78	308.85	48.17
CN HS	CC83782	01/13/2011	2195.21	356.93	339.56
H1/H2/CN LS	CC37815	01/14/2011	1672.87	301.29	58.57
H4/H5 REF	CC56519	01/14/2011	1803.68	331.65	146.47
H3/H4/H5 LS	CC89589	01/14/2011	1667.08	297.72	45.69
H4/H5 REF	CC56519	02/10/2012	1803.53	331.63	140.47
H3/H4/H5 LS	CC89589	02/10/2012	1666.97	297.63	46.43

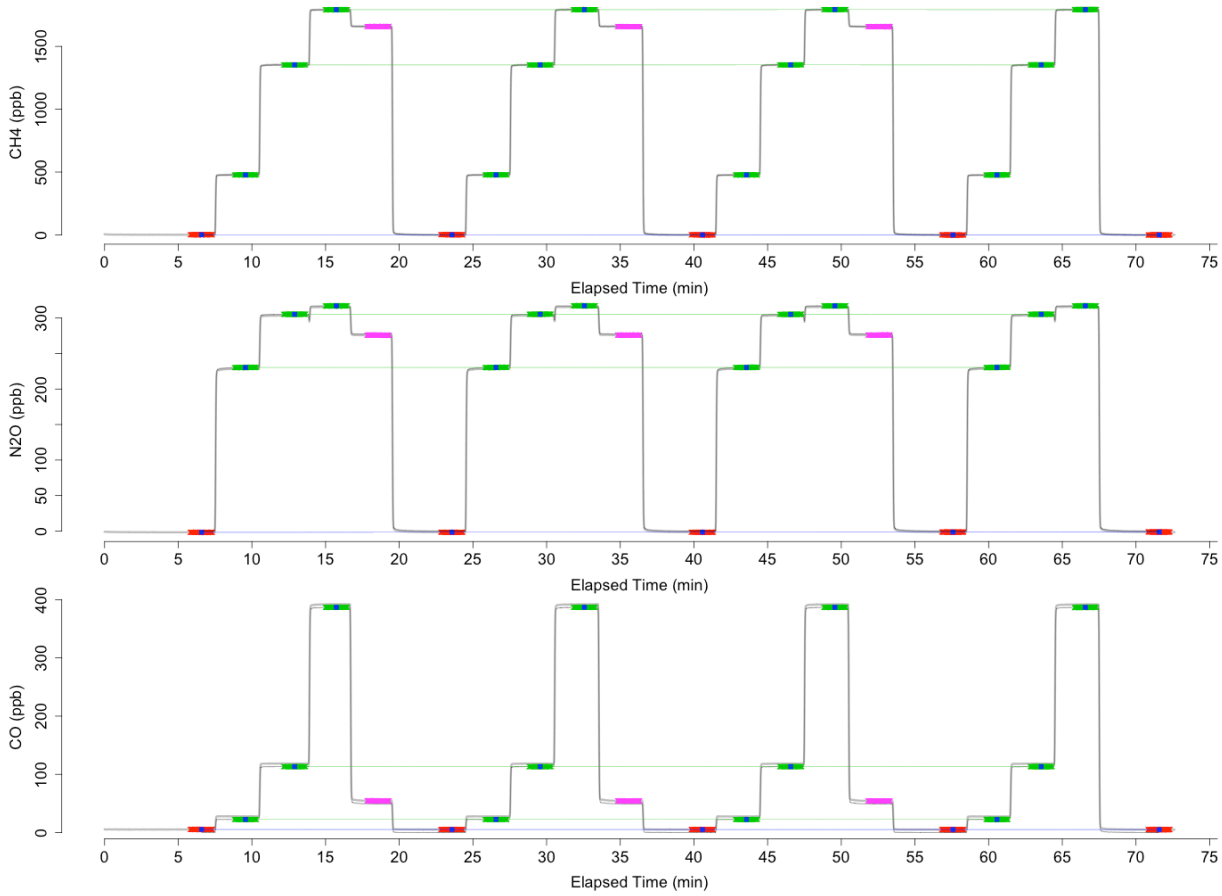

Figure 4.4: The sampling sequence used to calibrate a secondary cylinder (Table 4.2b) using 3 primary cylinders (Table 4.2a). Zero air (red) is sampled for 5 minutes, the primary cylinders are then each sampled for 3 minutes (green) in order of increasing concentration and then the target secondary cylinder (pink) is sampled for 3 minutes. The pink points are interpolated to the two primaries that bracket the secondary concentration and that data is shown in Figure 4.5.

sequence, we sample the target secondary tank, also for three minutes. We then repeat this cycle an additional 3 times, as shown in Figure 4.4, not sampling the target secondary on the last iteration. We use the last 90 seconds of a given 5 minute zero air sample (red x's) to calculate 5 zero-air values. These 5 values are linearly interpolated to the sampling times and subtract this trace (the blue line) to the raw mixing ratios (grey trace). The last 90 seconds (green x's) of the 'zero-subtracted' data (black trace = grey trace – blue trace) are then averaged to generate a value for each of the 4 primary sampling intervals (blue square). Those 4 values are then linearly interpolated to the QCLS sampling times (green lines). The last 90 seconds of the target sampling window (pink x's) are then interpolated to the green interpolation lines. Figure 4.5 shows the data corresponding to the 270 pink x's, concatenated together for each of the QCLS-DUAL species during three independent sets of calibrations in 2010-2012 for the same tank, CC89589 (Table 4.2b). We calculate linearly interpolated (using the two closest) and quadratically interpolated (using all three) values that correspond to the mean of the three 90 second sampling segments. The average of those values is reported as the calibrated secondary values (Table 4.2b), where values more than 2σ from the mean, if they exist, are excluded in the calculation.

We test for filling errors by filling the gas decks with secondary tanks and then performing a similar calibration of the gas deck itself. For gas deck calibration, we sample the low-span and high-span 'targets' simultaneously and use all four primary cylinders. Because use of the primary cylinders with QCLS required the instrument to be in a laboratory setting, we were able to perform gas-deck calibrations only before or after a given deployment. When the small cylinders in the gas decks reached 500 psi, they were flushed (3X) and filled

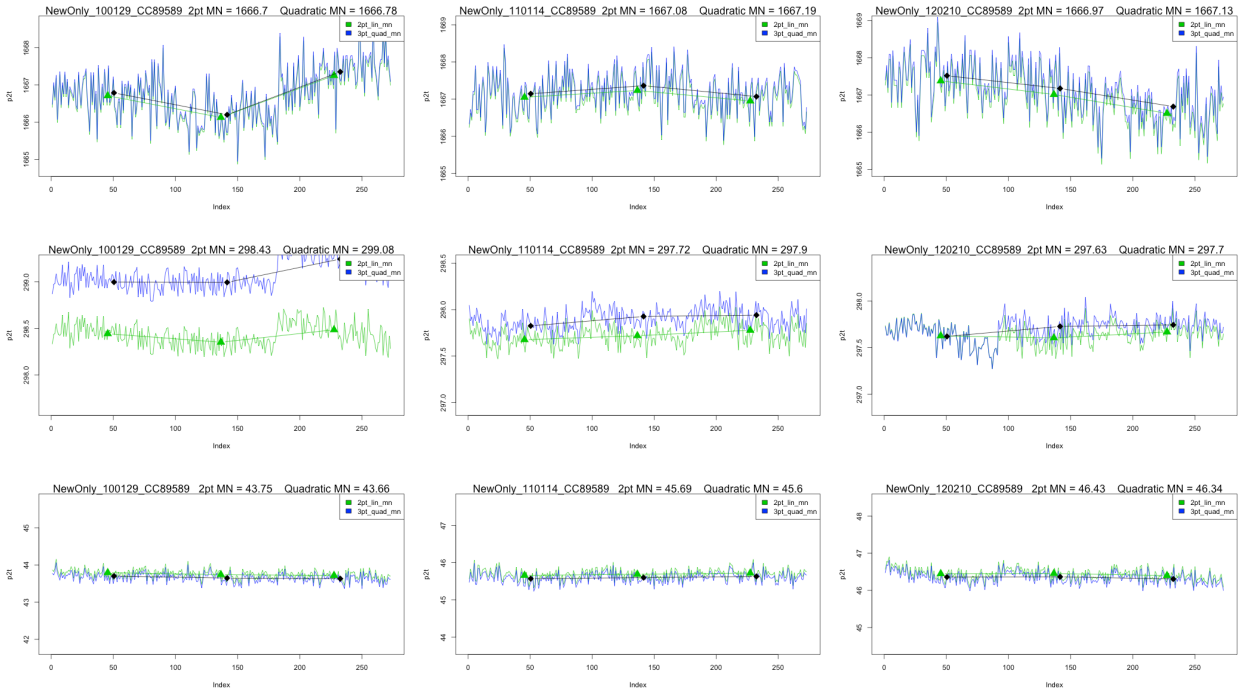

Figure 4.5: The concatenated target secondary cylinder interpolated values (i.e. the pink points in Figure 4.4). The three panels represent a calibration of the secondary cylinder CC89589 in 2010, 2011, and 2012, that was used to fill the gas deck for HIPPO III, IV, and V, illustrating the stability of the tank over time. Also plotted in blue is the quadratic fit to all3 primary cylinders used in the calibration of this tank.

with calibration air from AL secondary cylinders. For HIPPO, the refills would take place in Christchurch NZ, using a different set of secondary cylinders than the secondary cylinders used to fill the gas decks on the southbound HIPPO flights. We would therefore calibrate the gas deck after filling it but before using in on the southbound flights, and after both filling it and using it on the northbound flights. Because of these logistics, the calibration values calculated during gas-deck calibrations were only used as a check against filling error, ensuring that the gas-deck values fell within 3σ of the uncertainty attributed to the secondary tank calibration (Figure 4.5) from the NOAA primary cylinders. For consistency, the calibration values assigned to the air in the gas decks were always the value from the secondary cylinder calibration shown in Figure 4.5. Figure 4.5 shows that, within uncertainty, there is no evidence of drift in the secondary cylinders from 2010 to 2012.

In flight data is then tied to the NOAA scale by periodic standard additions from the gas decks. The sampling structure is shown in Figure 4.6. Within a given 60 minutes, the calibration sequences is as follows: minutes 7-9, 22-24, 37-39, 52-54 sampled zero/reference, minutes 9-10 and 39-40 sampled low-span, minutes 10-11 and 40-41 sampled high-span, and minutes 41-42 sampled a check-span. Because of differential equilibration times for the different species, we changed the order of the LS and HS additions to occur before the zero-air additions (see below). The zero was sampled most frequently at 15-minute intervals to track QCLS drift. The low and high-spans were sampled at 30-minute intervals, and the reference-span was sampled every hour for one minute. For a given hour of flight, the effective sampling duty cycle was therefore less than ~78% (47 minutes of sampling per hour). The calibrations for QCLS-DUAL and QCLS-CO2 occur on the same interval. Instead of sampling zero-air like QCLS-DUAL, however, the QCLS-CO2 samples the reference gas in both the sample and reference cell

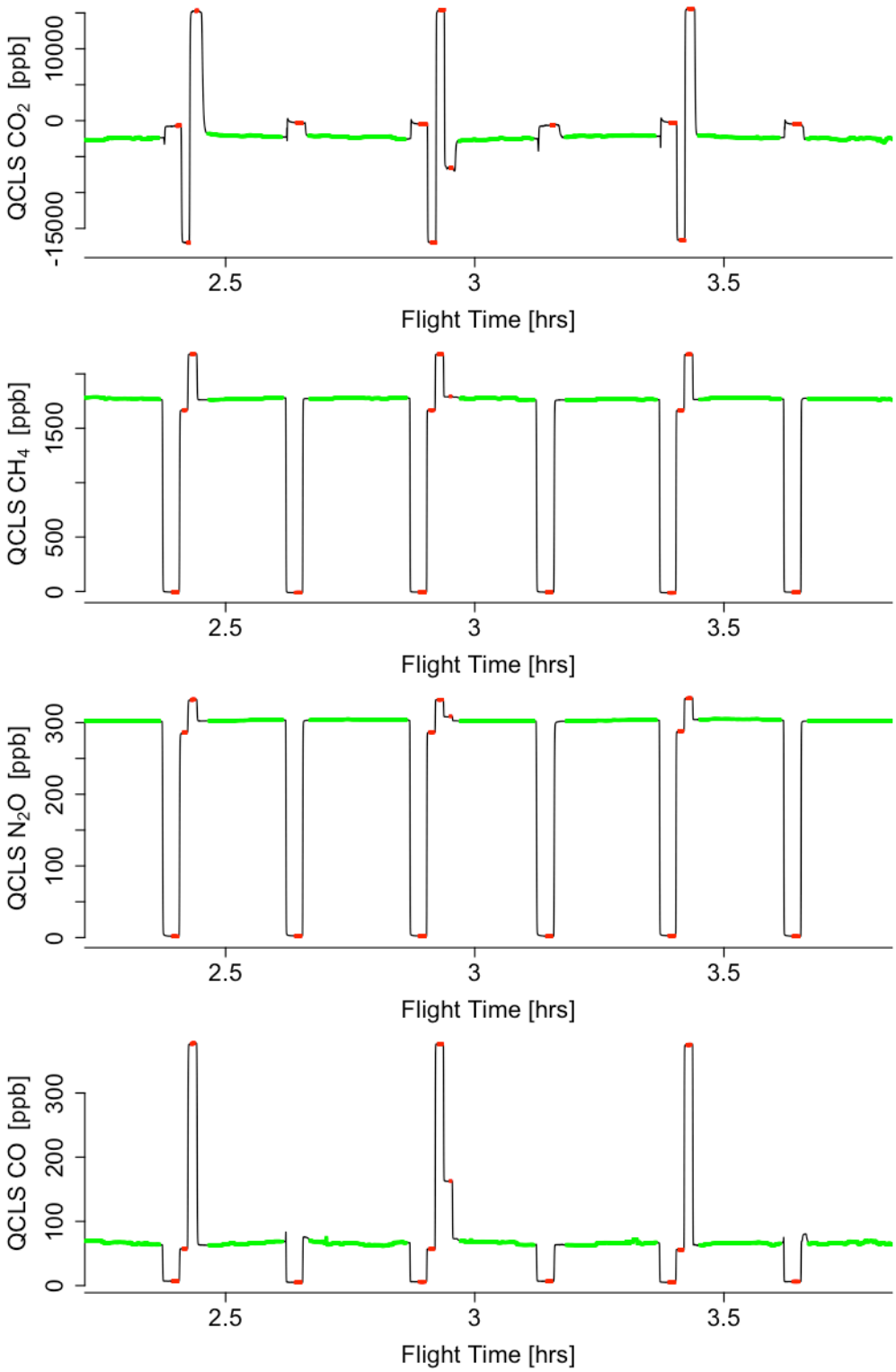

Figure 4.6: Calibration sequence of in-flight measurements. The reference gas (QCLS-CO2) and zero gas (QCLS-DUAL) are sampled every 15 minutes, a low-span and a high span every 30 minutes, and a check-span every two hours. The sample data (green) are interpolated to the mean values of each group of the calibration spans (red).

in order to obtain a relatively flat spectrum. The zero/reference is sampled for 2 minutes for two main reasons: 1) the zero/reference is the most frequently sampled calibration standard and therefore tracks the environmental temperature and pressure variability which cause drift, and 2) the equilibration of the N_2O trace is slower than the other species. Because the gas deck reference/zero-air additions are used to track drift and to interpolate the measurement to standard values, equilibration of the gas-deck standard additions is essential.

We ran a number of tests to characterize the slow equilibration in N_2O observed in the zero-air additions. Figure 4.7 shows a concatenated time series of various sampling intervals in which we repeatedly sampled between a zero-air cylinder and a span cylinder for 3-minute intervals. The different colors indicate different combinations of elements upstream of the sampling cell that came into contact with the sample. The tests included instances in which the air went straight from the cylinders to the sampling cell (through a nominal 0.5 m of Dekaron that was unavoidable). Various other upstream elements were added between the cylinder and the sampling cell, including different lengths of Dekaron, stainless steel tubing, PFA, and Nafion™. Figure 4.7 shows this data superimposed upon one another (with the zero-air value assigned from the mean value of 145-165 seconds of the 180 second sampling window) and the y-axis range normalized by the secondary cylinder calibrated value (N_2O = 319.3 ppb, CH_4 = 1919.6 ppb, CO = 223.4 ppb) and multiplied by a constant factor of 500 to expand the axes. Both CH_4 and CO are largely unaffected by the different sampling materials, likely because of their lower boiling points (-164 °C and -192 °C, respectively) relative to N_2O (-88 °C). Stainless steel was the only sampling material that was not affected by absorption/desorption for N_2O. The importance of this effect scaled with the surface area of the Dekaron or PFA encountered. Using stainless steel is impractical in many instances, so this effect is often unavoidable, but is important to consider

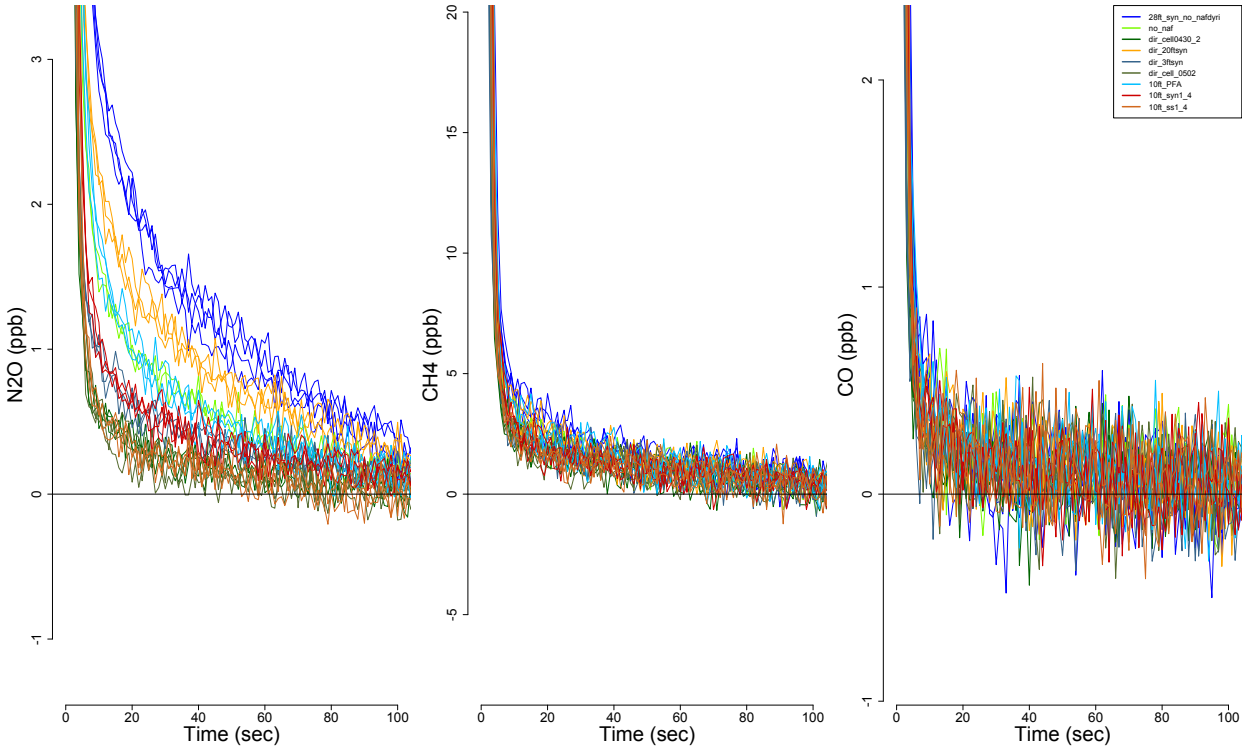

Figure 4.7: A series of square-wave tests, alternatively sampling from a check-span secondary tank with ambient concentration and a zero-air tank every 5 minutes, superimposed upon one-another to illustrate the slow sample equilibration time for N_2O. A decrease in the surface area of PFA or Dekaron™ results in a faster equilibration time. Both CH_4 and CO do not exhibit this behavior.

in the context of measurement traceability. We reached a compromise by sampling the zero-air for 2 minutes, sampling the LS and HS before sampling the zero-air, and using a smaller sampling window to calculate the zero-air spectroscopically-calibrated mixing ratios of N_2O, as seen in Figure 4.6.

Using a reference calibration cylinder (one with near-ambient atmospheric concentrations, e.g. CC56519 in Table 4.2b) instead of a zero to track instrument stability would minimize the effect of this problem. Because this tank is used so frequently to track drift, however, it would have been impractical to use, particularly on HIPPO where opportunities to ship calibration tanks and refill the gas decks are limited. We tested this assumption on one flight during HIPPO V (RF14, Sept 9, 2011) and showed that using a 1-minute equilibration time for a reference tank at ambient concentrations gave nearly equivalent results as using a 2-minute zero-air tank.

It should be noted that the boiling point of CO_2 (-57 C) is even higher than that of N_2O, so this effect is equally important for CO_2, and can be observed in Figure 4.6. Because QCLS-CO2 is a differential measurement, however, it matters to a much smaller extent as the Dekoron™ is always in contact with air that is very close to ambient.

To calculate sampling and calibration windows, we use an empirical relationship that is a function of ambient pressure, and tubing length. These differ for HIPPO and CalNex because of the hardware configurations, notably the use of the HIMIL on HIPPO. HIPPO spanned a larger pressure and temperature range because of the HIAPER GV capabilities compared to CalNex, which saw higher concentrations above a strong source region and experienced more turbulent flights. For HIPPO and QCLS-DUAL, we calculate experimental delay times from the HIMIL to the calibration-addition point just downstream of the inlet filter (Figure 4.3) as a linear function of ambient pressure in the HIMIL. We also calculate a time delay corresponding to the

equilibration time from that point to the measurement cell as a quadratic function of ambient pressure in the HIMIL. These have the functional form:

$$t_{delay} = 1.6201 \cdot P_{amb} \quad (4.1)$$

$$t_{equil} = 0.02763 \cdot {P_{amb}}^2 + 0.14993 \cdot P_{amb} + 3.75488 \quad (4.2)$$

The dynamic range of ambient pressure is much smaller in CalNex and does not include a HIMIL, so the equilibration time for CalNex is treated as a constant value derived from plume comparisons between QCLS and a fast-response black-carbon measurement (Schwarz et al. 2010) that was available for both HIPPO and CalNex. Equations for QCLS-CO2 have different coefficients but the same form. The equations were calculated empirically during several test flights on each campaign (Table 4.3) and then held constant throughout each campaign.

The HIMIL port, while complicating the instrument equilibration time, had the effect of dampening the input pressure variability of the sample. For CalNex, however, the variability in the sample pressure was occasionally not adequately controlled by the pressure control elements. Certain fluctuations in pressure were able to propagate to the sampling cell and affect the measurements. The effect of this cell 'ringing' was most apparent in the N_2O measurement which occasionally showed high-frequency (1 Hz) positive and negative excursions of >1-2 ppb for N_2O, a trace that should only see negative excursions in stratospheric air. We apply a filter to the measurements in which the 1Hz rate change of pressure is greater than 3 standard deviations of the mean (σ =0.16 hPa/sec). This resulted in an effective duty cycle that was 3% lower than without the pressure filter, but removed spurious spikes in the data.

Calibration time intervals were determined using these functions and the solenoid valve actuation time and a mean mixing ratio for each sample addition was calculated in a given window. The zero-air values measured every 15 minutes were then fit using a penalized Akima

Table 4.3: Summary of the HIPPO and CalNex flight dates, duration, and locations.

	HIPPO I			HIPPO II			HIPPO III			HIPPO IV			HIPPO V			CalNex		
Flight	YYMMDD	Hours	Location	YYMMDD	Hours	Location	YYMMDD	Hours	Location	YYMMDD	Hours	Location	YYMMDD	Hours	Location	YYMMDD	Hours	Location
TF01	81213	1.8	CO<>SD	91020	2.5	CO<>OK	100316	2.4	around CO	110607	1.9	CO<>4cor	-	-	(see RF01)	100430	5.4	DEN -> ONT
TF02	81217	4.6	CO<>IO,OK	91022	4.4	CO<>WLEF	100318	3.6	CO<>OK	110609	6.1	CO<>TX	-	-	(see RF02)	-	-	-
TF03	90106	1.5	CO<>SD	-	-	-	-	-	-	-	-	-	-	-	-	-	-	-
RF01	90108	1.1	CO->MT	91031	6.3	CO->AK	100324	6	CO->AK	110614	5.8	CO->AK	110809	5.1	CO<>WLEF	100504	4.8	SoCAB
RF02	90109	7.7	MT->AK	91102	7.3	AK<>NP	100326	8.2	AK<>NP	110616	8.9	AK<>NP	110811	6.8	CO<>TX	100507	6.9	SJV
RF03	90112	6.9	AK<>NP	91104	7.8	AK->HI	100329	8.4	AK->HI	110618	8.6	AK->HI	110816	6.1	CO->AK	100508	7.1	SoCAB
RF04	90114	8.4	AK->HI	91107	8.2	HI->CI	100331	6.3	HI->AS	110622	8.3	HI->CI	110818	4.2	AK<>NP	100511	7.2	SAC
RF05	90116	6.8	HI->AS	91109	7	CI->NZ	100402	5.9	AS->NZ	110625	6.8	CI->NZ	110819	8.6	AK<>NP	100512	7.8	SJV
RF06	90118	6	AS->NZ	91111	7.7	NZ<>SP	100405	7.8	NZ<>SP	110628	7.3	NZ->SP->HO	110822	7.8	AK->HI	100514	6.2	SoCAB
RF07	90120	8.6	NZ<>SP	91114	7.9	NZ->SI	100408	5.7	NZ->AS	110701	6.8	HO->DA	110824	8.4	HI->CI	100516	7.8	SoCAB
RF08	90123	7.2	NZ->TA	91116	8.6	SI->HI	100410	6.2	AS->HI	110704	6	DA>SA	110827	7.2	CI->NZ	100519	6.7	SoCAB
RF09	90126	6.6	TA->EI	91119	7.7	HI->AK	100413	8.3	HI->AK	110706	6.4	SA->MI	110829	8.9	NZ<>SP	100521	3	SoCAB
RF10	90128	7.9	EI->CR	91121	7.4	AK<>NP	100415	7.8	AK<>NP	110707	6.2	MI<>AK	110901	6.1	NZ->CI	100524	6.3	SJV - N
RF11	90130	6.1	CR->CO	91122	4.8	AK->CO	100416	5	AK->CO	110710	8.3	AK<>NP	110903	8.6	CI->HI	100530	5.8	SoCAB - N
RF12	-	-	-	-	-	-	-	-	-	110711	6.5	AK->CO	110906	8.1	HI->AK	100531	5.9	SoCAB - N
RF13	-	-	-	-	-	-	-	-	-	-	-	-	110908	8.5	AK<>NP	100602	6.2	SoCAB - N
RF14	-	-	-	-	-	-	-	-	-	-	-	-	110909	4.8	AK->CO	100603	6.7	SoCAB - N
RF15	-	-	-	-	-	-	-	-	-	-	-	-	-	-	-	100614	7.3	SAC
RF16	-	-	-	-	-	-	-	-	-	-	-	-	-	-	-	100616	6.9	SJV
RF17	-	-	-	-	-	-	-	-	-	-	-	-	-	-	-	100618	7.1	SJV
RF18	-	-	-	-	-	-	-	-	-	-	-	-	-	-	-	100620	7.1	SoCAB
Total Flight Hours		**81.1**			**87.6**			**81.6**			**93.9**			**99.2**			**122.2**	
Total Flights		**14**			**13**			**13**			**14**			**14**			**19**	

spline interpolation technique (Akima, 1970) to evaluate the drift of the instrumentation. Other smoothers, such as loess, splines, interpolators occasionally cause severe curvature in the interpolation, particularly near the beginning of flight where sensors may not be fully equilibrated. This zero-air-akima-spline is evaluated at all the 1 Hz sampling times and subtracted from the entire dataset. Using the zero-air-aspline-subtracted data ($CH_{4,Zraw}$), the mean values of each low-span and high-span window are interpolated using the same akima-spline to the measurement times. $CH_{4,Zraw}$ is then linearly interpolated to the low-span-akima-spline and high-span-akima-spline (CH_{4,Z_ALS} and CH_{4,Z_AHS}, respectively) according to:

$$CH_{4,cal} = \left(\frac{CH_{4,Zraw} - CH_{4,Z\_ALS}}{CH_{4,Z\_AHS} - CH_{4,Z\_ALS}}\right) \cdot \left(CH_{4,HS_{VAL}} - CH_{4,LS_{VAL}}\right) + CH_{4,LS_{VAL}} \quad (4.3)$$

where $CH_{4,LS_{VAL}}$ and $CH_{4,HS_{VAL}}$ are the two constant values of the low-span and high-span secondary AL calibration cylinders used to fill the gas-deck (Table 4.2b). The equations for N_2O and CO are equivalent. Figure 4.8 shows the different akima-splines for an arbitrary flight during HIPPO 5, along with the ambient pressure for the 4 species. The axes are all scaled such that the different tracers – zero-air, low-span, high-span, and reference air – from the gas decks have equivalent ordinate ranges. The CO_2 trace in Figure 4.8 is in units of ppb relative to the reference, meaning that a value of -17500, corresponds to the low-span that is 17.5 ppm lower than the near-ambient reference. Figure 4.8 is a standard output product of the batch processing and is purposely scaled to emphasize the fluctuations of calibration standards over the course of a given flight. Because of the linear interpolation between the zero-subtracted low-span and high-span, the relative fluctuation of those two tracers has the largest effect on the effective calibrated measurements.

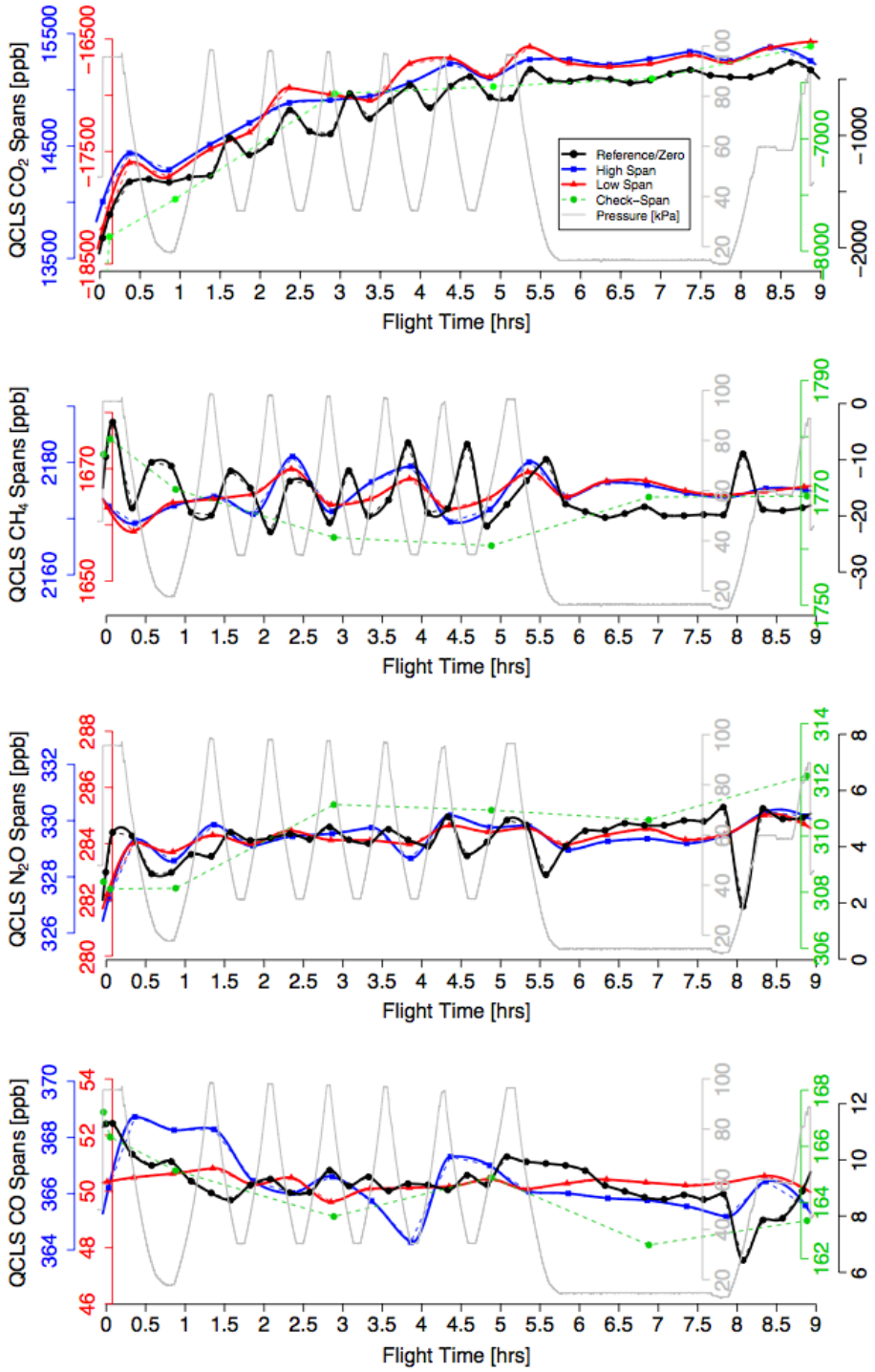

Figure 4.8: The gas-deck in-flight calibration addition stability over the course of one flight on HIPPO V. Each point represents the average of the group of red points in Figure 4.6 and the axes for each QCLS species are equivalent in range. The lines represent the Akima spline interpolations to the different spans and are used to relate the spectroscopically-calibrated mixing ratios to the NOAA scale. QCLS-CO2 and QCLS-DUAL use different interpolation techniques as discussed in the text. The HIMIL inlet pressure is also shown in grey.

The CO_2 calibration additions shown in Figure 4.8 are treated slightly different than the QCLS-DUAL species. Because QCLS-CO2 is a differential measurement and the range of observations are the largest of any species (in terms of concentration changes measured over the course of a flight), the CO_2 interpolation is not calculated linearly. Instead, we take the median of the low-span, reference, and high-span values calculated over the course of any particular flight and fit a quadratic function to those median values. The reference-subtracted measurements are then quadratically interpolated to this fixed function. We experimented with different methods to calibrate the CO_2 measurements and found that using a method similar to QCLS-DUAL resulted in spurious wave generation in the measurements that were not physical. Because the reference/zero calibration is sampled at 2X the frequency of the spans, the reference trace is able to best compensate for the measurement drift. Physically, we expect that the response of QCLS-CO2 over the range of concentrations sampled should not change dramatically, and this is confirmed in the flight-to-flight variability of the quadratic interpolation function (see below). For this reason, we fix the quadratic function and make it follow the more frequent reference calibration trace.

Figure 4.9 shows the variability of the quadratic function for QCLS-CO2 (during CalNex) and the linearity of QCLS-DUAL (in lab). The 4 sets of panels show the 1:1 plot of the raw spectroscopically-calibrated QCLS mixing ratios versus the NOAA-calibrated primary cylinder values. The linear fits to QCLS-DUAL are calculated using a type II regression with prescribed errors in the abscissa and ordinate (York, 2004). For the x-axis, the uncertainties are prescribed by the NOAA calibrations and for the y-axis, errors are given by the standard deviation of the mean spectroscopically-calibrated QCLS measurements. The bottom panel shows the residual values for the different tanks. For CO_2, the fit is not linear, as described above, and the residuals

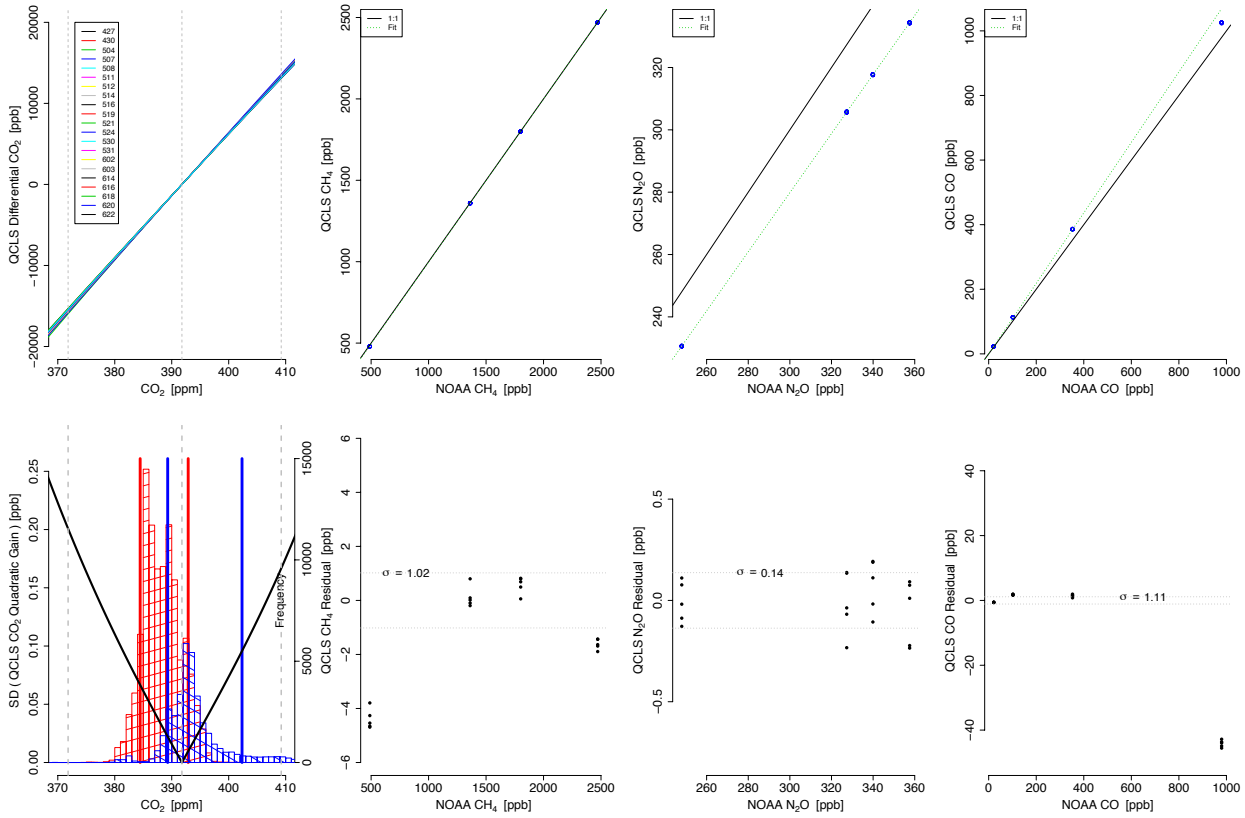

Figure 4.9: An estimate of the calibration linearity (top) and uncertainty (bottom) for the 4 QCLS species. For QCLS-CO2, the quadratic interpolation function for each research flight in CalNex (which is more variable that in the HIPPO) is shown. The standard deviation across the 21 flights as a function of calibrated mixing ratio is shown in the bottom panel, reaching a minimum at the value of the reference gas deck calibration cylinder. The histograms of the CalNex (blue) and HIPPO (data) are shown and the 10% and 90% quantiles are plotted as vertical lines for each, indicating that the variability in the quadratic interpolation function typically contributes no more than 0.1 ppm. For QCLS-DUAL, the 1:1 correspondence of the spectroscopically-calibrated QCLS mixing ratio is plotted against 4 known primary cylinders and regressions are calculated using the error uncertainties from the primary cylinders shown in Table 4.2a. The bottom plot shows the standard deviation of the residual uncertainty, where we exclude the very low CH_4 primary (~500 ppb) and the very high CO (~1000 ppb) from the uncertainty estimate.

shown are flight-to-flight differences in the quadratic fit function over the course of the CalNex mission, which showed greater variance in the quadratic fit coefficients compared to HIPPO. The residual values shown for CO_2 correspond to the standard deviation of the quadratic fit function over the mission, and can be considered an estimate of the sensor accuracy as a function of concentration. To put these estimates of errors in context, the histogram distributions of the HIPPO and CalNex CO_2 measurements are shown along with their 10-90% quantile ranges (solid blue and red lines) to show that this is a very minor error effects for the majority of the measurements.

For QCLS-CO2, secondary cylinders are calibrated against NOAA standards using the Harvard Ground Support Equipment (GSE), described in detail in Daube et al. (2002). The GSE is a Licor model 6251 NDIR analyzer, which measures molecular absorption of CO_2 in a sample stream relative to a reference stream of air. Because it is a nondispersive analyzer, the measurement is sensitive to different parts of the molecular absorption band of CO_2. Tohjima et al. (2009) characterized the sensitivity of 3 Licors (two 6252 and one 6262) to each of the isotopologues of CO_2. They use a Relative Molar Response (RMR) value for each isotopologue to calculate the effective change in concentration determined for each isotopologue (see their Table 4.4). Given a hypothetical CO_2 mixing ratio of 400 ppm, the isotopic abundances in HITRAN (Rothman et al. 2007) can be used to approximate the individual mixing ratios of the three dominant isotopologue – $^{16}O^{12}C^{16}O$, $^{16}O^{13}C^{16}O$, and $^{16}O^{12}C^{18}O$ – as 393.68160, 4.42296 and 1.57883 ppm, respectively. The sum of these three concentrations is less than 400 (399.68339) as other minor isotopes contribute to the total concentration. Atmospheric CO_2 has an approximate isotopic composition of $\delta^{13}C = -10$ ‰ and $\delta^{18}O = 40$ ‰, where these quantities are calculated according to:

Table 4.4: Biases between QCLS and CCG flask measurements at the reported mean concentrations of each species for the five HIPPO campaigns.

Mission	CO_2 bias (ppm)	CO_2 (ppm)	CH_4 bias (ppb)	CH_4 (ppb)	N_2O bias (ppb)	N_2O (ppb)	CO bias (ppb)	CO (ppb)
HIPPO 1	0.14	385.9	1.2	1788.1	0.61	321.0	-3.71	77.3
HIPPO 2	-0.06	386.7	0.75	1801.2	1.18	320.9	-1.52	84.0
HIPPO 3	-0.09	389.9	0.44	1795.0	1.15	320.0	-1.59	95.3
HIPPO 4	-0.25	390.6	1.04	1800.0	1.23	322.8	-1.14	72.2
HIPPO 5	-0.3	387.5	0.79	1813.7	1.18	322.4	-1.72	74.5
Mean	-0.11		0.85		1.07		-1.94	

$$\delta^{13}C_{CO_2} = \left[\frac{R13_{sam}}{R13_{vpdb}} - 1\right] \cdot 1000 \quad (4.4)$$

$$\delta^{18}O_{CO_2} = \left[\frac{R18_{sam}}{R18_{vsmow}} - 1\right] \cdot 1000 \quad (4.5)$$

and R13 represents the ratio of ^{13}C to ^{12}C in a sample of CO_2 or in the standard Veinna Pee Dee Belemnite (vpbd = 0.011180) and R18 represents the ratio of ^{18}O to ^{16}O in CO_2 or in Standard Mean Ocean Water (vsmow = 0.0020052). Using these equations, we can calculate atmospheric values for R13 and R18 of 0.0110682 and 0.002085408, respectively. The abundance of the dominant isotopologue ($^{12}C^{16}O^{16}O$) must therefore be 1 minus the R13 and twice the R18 abundances, or 0.984761, which corresponds to a concentration of 393.592606. Because QCLS-CO2 only scans across one absorption line for the dominant isotopologue (mass 44), calibration additions using cylinders with non-atmospheric isotopic composition can therefore result in biases in the measurements. A hypothetical tank that has a total CO_2 concentration of 400 ppm and isotopic composition of $\delta^{13}C$ = -35 ‰ and $\delta^{18}O$ = 10 ‰ (typical of a Scott Marrin cylinder) will have dominant isotopologue $^{16}O^{12}C^{16}O$, $^{16}O^{13}C^{16}O$, and $^{16}O^{12}C^{18}O$ concentrations of 393.752405, 4.312064 and 1.618919 ppm, the sum of which is still 399.68339. But the concentration of the $^{12}C^{16}O_2$ isotopologue is higher by 0.1598 ppm compared to the concentration with near-atmospheric isotopic composition. This must be accounted for in relating calibration cylinder values to sample concentrations.

The mean RMR corrections for the three dominant isotopologues from the two Licor-6252 are mean(1.0073,1.0040), mean(0.21,0.45),mean(1.26,1.43), which are multiplied by the difference in isotopologue concentrations between the 400 ppm cylinder and the 400 ppm atmospheric sample. When summed, the mean value is -0.059 ppm with a range over the two

instrument of -0.041 to -0.077 ppm. Chen et al. (2010) calculated a similar value of using specific isotopic composition of the tanks of -0.09 ppm.

To account for the combined effect on the QCLS-CO2 calibration, the -0.059 ppm and the 0.1598 values must be added to the retrieved sample mixing ratio. The -0.059 ppm puts the calibration cylinder values calculated using the GSE onto the same isotopic scale as the NOAA primaries (i.e. atmospheric isotopic composition). The 0.1598 value accounts for the fact that QCLS-CO2 derives a total mixing ratio using the absorption spectrum of the dominant $^{12}C^{16}O_2$ isotopologue and the HITRAN abundance, which differs from the atmospheric abundance as shown above. These effects partially offset, but result in a ~0.1 ppm bias term, which is important considering that atmospheric concentration gradients are often not much larger than this. The particular isotopic values used in the various calibration cylinders used (Table 4.2b) are used to calculate the exact corrections for the tanks. The NOAA primary tanks had near-atmospheric ^{13}C isotopic composition of around -10 to -15 ‰, Scott Specialty tanks usually fell in the -45 to -50 ‰ range, and Scott-Marrin usually fell in the -30 to -40 ‰ range.

The error for CH_4 due to differing isotopic composition between the atmosphere (-47 ‰) and calibration cylinders (typically -30 ‰) was calculated to be a ~0.3 ppb effect, smaller than the 1 Hz precision. The effects for N_2O and CO were proportionally smaller and these effects are therefore ignored for QCLS-DUAL.

4.3. Missions and Other Instrumentation

The QCLS was operated in the same configuration in both CalNex and HIPPO with only minor changes due to the aircraft-specific issues already discussed. We now present comparisons with other coincident instruments.

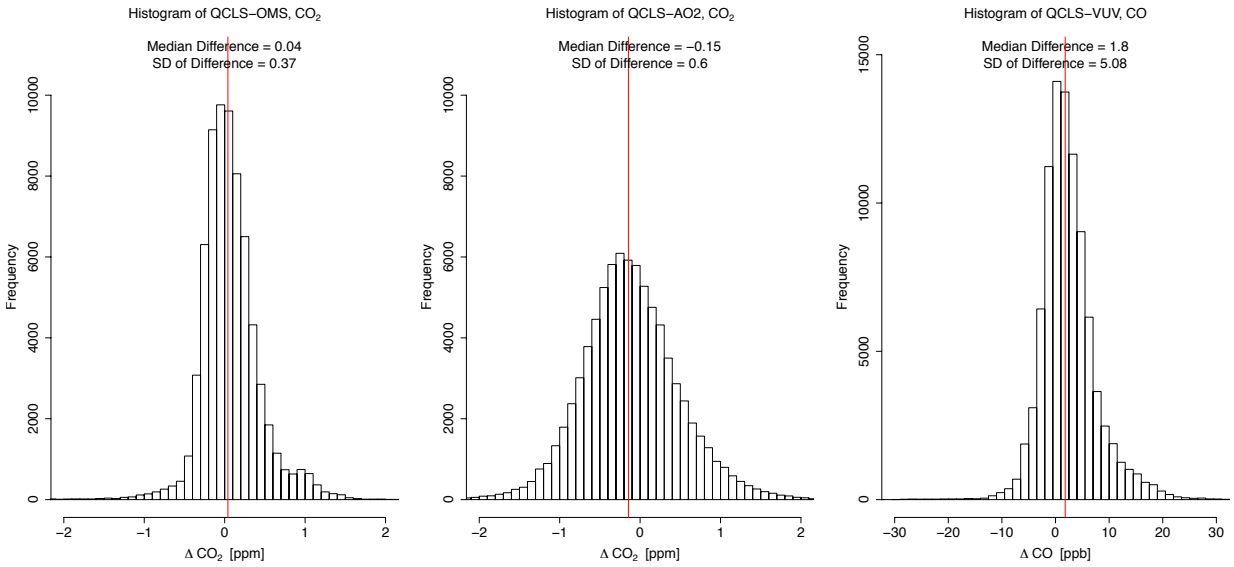

Figure 4.10: The 1 Hz HIPPO I-V data comparison for QCLS-CO2 with OMS (left) and AO2 (middle) as well as the QCLS-DUAL CO comparison with the RAF VUV-CO.

For HIPPO, two additional fast-response (>1Hz) CO_2 sensors were available for comparison: the OMS sensor (Daube et al. 2002), and the AO2 sensor, another NDIR Licor-based instrument (Stephens et al. 2000). Figure 4.10 shows the 1 Hz measurement difference distribution for QCLS against OMS and AO2 for all HIPPO flights. QCLS-CO2 and OMS agree to better than 0.05 ppm, with a standard deviation of the difference of 0.37, owing in part to the slower cell response time of OMS. Assuming the sensors have no covariance, the 1Hz OMS precision of 0.1 ppm and the 1Hz QCLS precision of 0.02 ppm would sum in quadrature for an expected precision of 0.1 ppm. The actual distribution is 0.37 ppm, roughly a factor of 4 higher. QCLS-CO2 and AO2 agree to within 0.15 ppm and have an even larger variance on the distribution of the measurement differences. The Research Aviation Facility (RAF) vacuum ultraviolet (VUV) CO sensor is the only other fast-response instrument measuring one of the QCLS species. That comparison, also shown in Figure 4.10, shows a bias of 1.8 ppb over the HIPPO mission.

Two onboard gas chromatographs - the Unmanned Aircraft Systems (UAS) Chromatograph for Atmospheric Trace Species (UCATS, Hintsa et al. 2000) and the PAN and other Trace Hydrohalocarbon ExpeRiment (PANTHER, Moore et al. 2003) - measured a variety of chemical species including CH_4, N_2O, and CO. Figure 4.11 shows the one-to-one comparison of the QCLS to UCATS (top) and PANTHER (bottom) after applying the averaging kernel of each GC to the 1 Hz QCLS data. In addition to the *in situ* data, sparser NOAA flask measurements from the Whole Air Sampler (WAS) are compared in Figure 4.12. The axes ranges on Figures 11 and 12 are the same, with the exception of N_2O, which has large variability from the GC-based measurements. Table 4.4 summarizes the biases for each of the QCLS species at the mean concentration measured on each of the 5 HIPPO transects. The type II regressions (York, 2004) in these figures use uncertainty values of 200, 2, 0.2, and 1 ppb for the QCLS measurements of

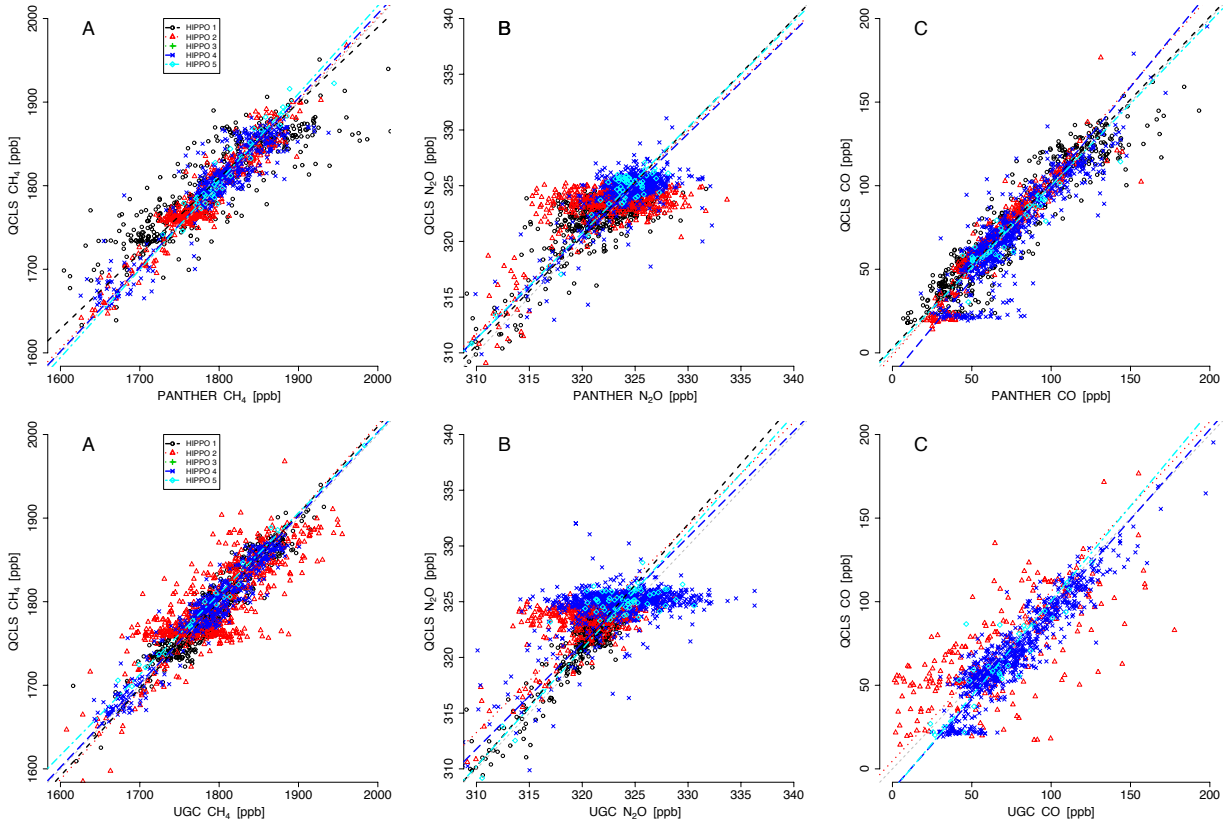

Figure 4.11: QCLS-DUAL comparisons to the onboard gas chromatographs PANTHER (top) and UCATS (bottom) for CH_4 (A), N_2O (B), and CO (C).

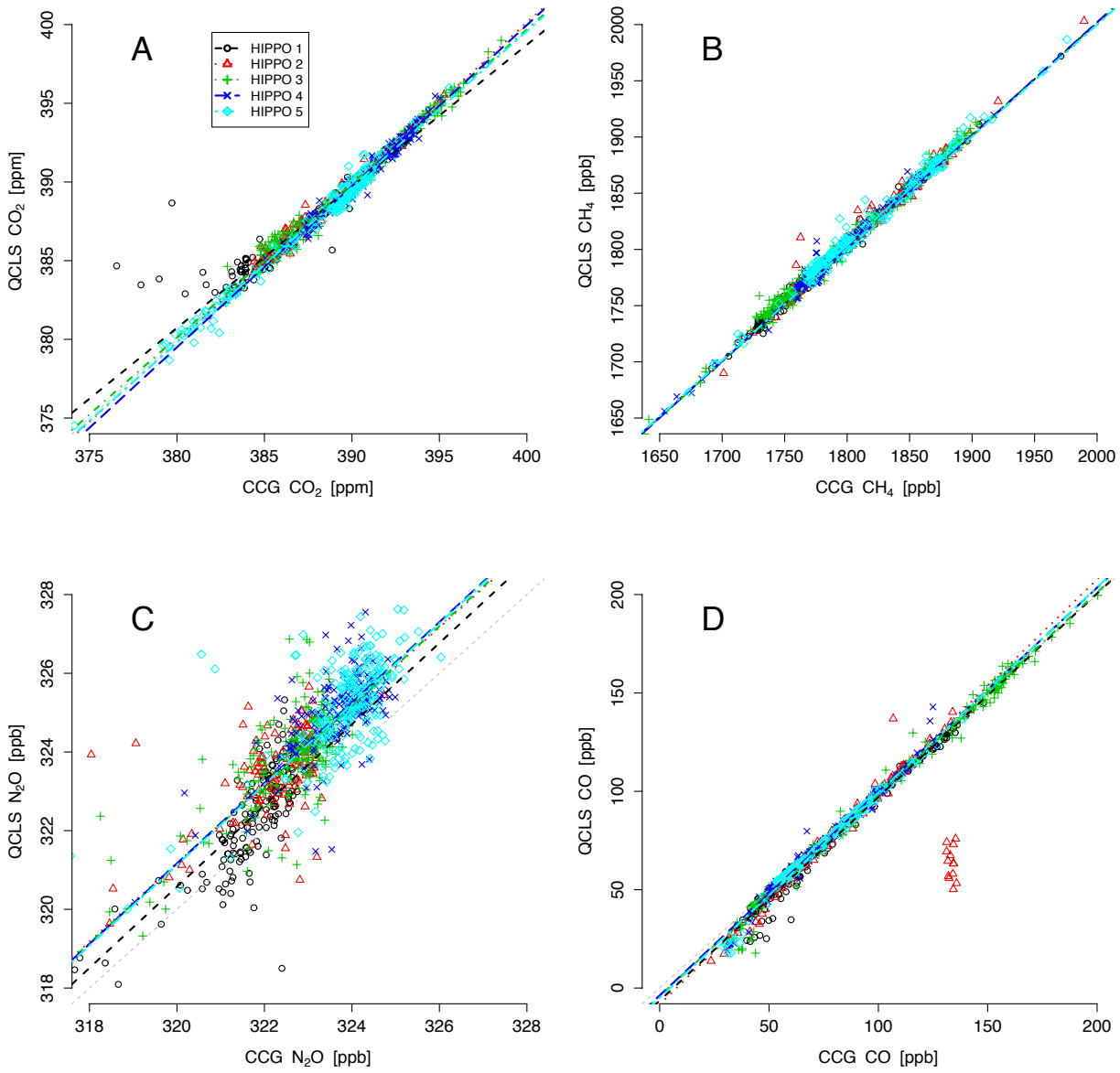

Figure 4.12: QCLS comparisons to NOAA flask data during HIPPO I-V for CO_2 (A), CH_4 (B), N_2O (C), and CO (D). With the exception of N_2O which has a much tighter correlation with the flask measurements, the axes are all scaled to the same ranges as Figure 4.11. The biases for each fit are reported in Table 4.4.

CO_2, CH_4, N_2O, and CO, respectively, corresponding to the calibration uncertainties shown in Table 4.2a, and half of those values for the NOAA CCG flask values (Zhao and Tans 2006, Dlugokencky et al. 2005, Hall et al., 2007, Novelli et al., 1994). Mean biases calculated over the course of HIPPO are -112, 0.85, 1.07, and -1.94 ppb for the 4 species. Only N_2O falls outside of the estimated uncertainties in the measurements. This is in part due to the recalibration of primary cylinder 4 (Table 4.2a) that changed by more than 4σ the NOAA calibration uncertainty. This cylinder falls on the high range of the NOAA N_2O calibration standards and is only bracketed by one NOAA standard with higher concentration (Hall et al. 2007).

For CalNex, the payload of the NOAA P-3 aircraft included simultaneous 1 Hz measurements of CO using another VUV spectrometer and CO_2 and CH_4 using the NOAA/Picarro Cavity Ring-Down Spectrometer (CRDS). The comparisons for all three species are shown in Figure 4.13. No additional sensors measured N_2O during CalNex. The CRDS made 1-Hz measurements of CO_2 and CH_4 with 1-second RMS precisions of 100 and 1.5 ppb, respectively [*Peischl et al.*, 2012]. Both sets of measurements were independently calibrated to NOAA standards during flight, accounting for roughly 20% of the sampling duty cycle for each instrument. The QCLS and CRDS CO_2 data agreed well with one another, with a mean bias term of 0.05 ppm and standard deviation of 0.51 over 130 flight hours of sampling, similar to the QCLS and OMS comparison on HIPPO. The bias in CH_4 was 4.5 ppb, more than our estimated uncertainty, with a standard deviation of 5.1 ppb. The cause of the bias between the CH_4 measurements has remained a mystery, but may be due to variability in the O_2/N_2 ratio of the air used in the calibration of CRDS-based measurements (Chen et al. 2009). These biases correspond to errors of 0.01% and 0.25 % for CO_2 and CH_4, respectively, using background concentrations of 390 ppm and 1800 ppb.

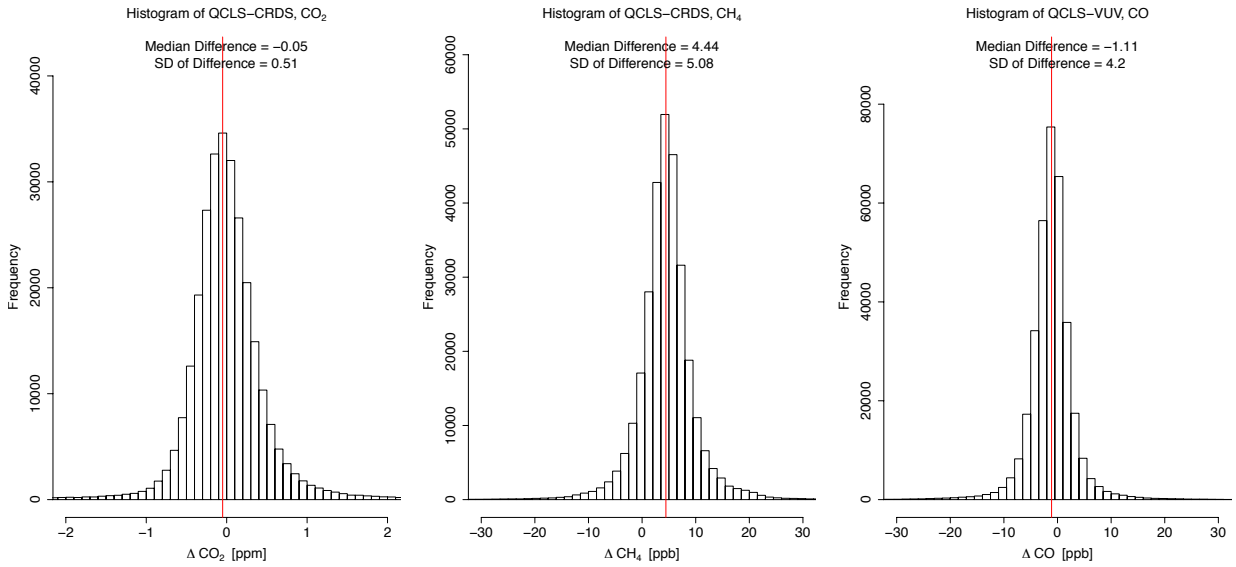

Figure 4.13: The 1 Hz CalNex data comparison for QCLS with the NOAA/Picarro CRDS for CO_2 (left) and CH_4 (middle) as well as the comparison with the NOAA VUV sensor for CO (right).

To minimize data gaps in the 1 Hz flight data over the missions, we fit a a loess curve with a 1000 second span window to calculate the time-evolution of the QCLS minus OMS/CRDS/VUV concentration bias. The more-precise QCLS data is used as the primary data, and calibration-gaps are filled using the sum of the OMS/CRDS/VUV data and the loess bias curve. This resulted in an overall mission data retrieval duty cycle of over 95% for HIPPO and 97% for CalNex, a significant improvement over the ~78% duty cycle from QCLS alone. These merge products are denoted CO2.X, CH4.X, and CO.X. A merge product for N_2O was not created because no other fast-response N_2O sensors were available for either mission.

4.4. Conclusions

Airborne observation of the long-lived greenhouse gas suite of CO_2, CH_4, N_2O, and CO can be accurate to better than 0.03%, 0.05%, 0.01%, and 2% relative to background concentrations of 390 ppm, 1850 ppb, 325 ppb, and 100 ppb respectively, given adequate pressure and temperature regulation and robust in-flight calibration procedures that improve upon spectroscopically-calibrated measurements. We report long-term accuracy for CO_2, CH_4, N_2O, and CO from nearly 450 flight hours of 100, 1, 1.1, and 2 ppb, respectively. The datasets generated using the QCLS for HIPPO and CalNex have provided extensive global (HIPPO) and regional (CalNex) coverage and have been useful in many studies to date (Wunch et al. 2010, Kort et al. 2011, Wecht et al. 2012, Kort et al. 2012, Xiang et al., 2012, Peischl et al., 2012). We emphasize the importance of in-flight calibrations traceable to NOAA standards, essential in studies that combine measurements from independent sensors, and present best practices for their implementation.

Acknowledgements

We would like to thank all the pilots, aircraft technicians, and support staff of the NCAR HIAPER-GV and NOAA P-3 and the as well as many NOAA and NCAR collaborators that made the CalNex and HIPPO measurements possible. This work was supported by the following grants to Harvard University: NASA NNX09AJ94G, NNX11AG47G, and NNX09AU40G, NSF ATM-083091-2, NOAA NA09OAR4310122, and NA11OAR4310158. GWS acknowledges support from the NSF Graduated Research Fellowship Program and the EPA Science to Achieve Results Fellowship.

References

Chen, H., J. Winderlich, C. Gerbig, A. Hoeferl, C. W. Rella, E. R. Crosson, A. V. Pelt, J. Steinbach, O. Kolle, V. Beck, B. C. Daube, E. W. Gottlieb, V. Y. Chow, G. W. Santoni, and S. C. Wofsy (2010), High-accuracy continuous airborne measurements of greenhouse gases (CO2 and CH4) using the cavity ring-down spectroscopy (CRDS) technique, Atmospheric Measurement Techniques, 3(2), 375-386.

Daube B. C., K. A. Boering, A. E. Andrews, S. C. Wofsy (2002) A high-precision fast-response airborne CO2 analyzer for in situ sampling from the surface to the middle stratosphere. J. Atmos. Oceanic Technol. 19, 10, 1532-1543.

Dlugokencky, E. J., R. C. Myers, P. M. Lang, K. A. Masarie, A. M. Crotwell, K. W. Thoning, B. D. Hall, J. W. Elkins and L. P. Steele (2005), Conversion of NOAA atmospheric dry air CH4 mole fractions to a gravimetrically prepared standard scale, JGR-Atmospheres, 110, D18, doi:10.1029/2005JD006035

Fried, A., G. Diskin, P. Weibring, D. Richter, J.G. Walega, G. Sachse, T. Slate, M. Rana and J. Podolske, Tunable infrared laser instruments for airborne atmospheric studies, Applied Physics B: Lasers 92, 409-417, 2009.

Gerbig, C., J. C. Lin, S. C. Wofsy, B. C. Daube, A. E. Andrews, B. B. Stephens, P. S. Bakwin, and C. A. Grainger (2003), Toward constraining regional-scale fluxes of CO2 with atmospheric observations over a continent: 2. Analysis of COBRA data using a receptor-oriented framework, J. Geophys. Res., 108(D24), 4757, doi:10.1029/ 2003JD003770.

Hall, B. D., G. S. Dutton and J. W. Elkins, (2007), The NOAA nitrous oxide standard scale for atmospheric observations, Journal of Geophysical Research-Atmospheres, 112, doi:10.1029/2006JD007954

Jiménez et al (2005) Atmospheric trace gas measurements using a dual quantum-cascade laser mid-infrared absorption spectrometer, Proceedings of SPIE, 5738, doi:10.1117/12.597130.

Jiménez et al. (2006) A New Quantum-Cascade Laser Based Spectrometer for High-Precision Airborne CO2 Measurements, WMO/GAW Reports, 168, 100-105.

Kort, E. A., P. K. Patra, K. Ishijima, B. C. Daube, R. Jiménez, J. Elkins, D. Hurst, F. L. Moore, C. Sweeney, and S. C. Wofsy (2011) Tropospheric distribution and variability of N2O: Evidence for strong tropical emissions, Geophysical Research Letters, 38, L15806, doi:10.1029/2011GL047612.

Kort, E. A., S. C. Wofsy, B. C. Daube, M. Diao, J. W. Elkins, R. S. Gao, E. J. Hintsa, D. F. Hurst, R. Jiménez, F. L. Moore, J. R. Spackman, and M. A. Zondlo (2012) Atmospheric observations of Arctic Ocean methane emissions up to 82° north. Nature Geosci, 5, 318-321, doi:10.1038/ngeo1452.

McManus, J. B., P. L. Kebabian, and W. S. Zahniser (1995), Astigmatic mirror multipass absorption cells for long-path-length-spectroscopy, Appl. Opt., 34(18), 3336–3348, doi:10.1364/AO.34.003336.

Miller, S.M., Matross, D. M., Andrews, A. E., Millet, D. B., Longo, M. , Gottlieb, E. W., Hirsch, A. I., Gerbig, C. , Lin, J. C. , Daube, B. C. , Hudman, R. C. , Dias, P. L. S. , Chow, V. Y., and Wofsy S. C. (2008) Sources of carbon monoxide and formaldehyde in North America determined from high-resolution atmospheric data, Atmos. Chem. Phys. 8 (24), 7673.

Moore, F. L., J. W. Elkins, E. A. Ray, G. S. Dutton, R. E. Dunn, D. W. Fahey, R. J. McLaughlin, T. L. Thompson, P. A. Romashkin, D. F. Hurst, and P. R. Wamsley (2003) Balloonborne in situ gas chromatograph for measurements in the troposphere and stratosphere, Journal Of Geophysical Research, 108 (D5), 8330, doi:10.1029/2001JD000891.

NCAR, UCAR, RAF (2005) NCAR HIAPER Modular Inlet – HIMIL http://www.eol.ucar.edu/~dcrogers/HIAPER/Inlets/HIMIL/.
Nelson, D.D., J.B. McManus, S. Urbanski, S. Herndon, and M.S. Zahniser. High precision measurements of atmospheric nitrous oxide and methane using thermoelectrically cooled mid-infrared quantum cascade lasers and detectors. Spectrochimica Acta A 60: 3325-3335, 2004.

Novelli, P. C., J.E. J.. Collins, R. C. Myers, G.W. Sachse and H.E. Scheel, (1994), Reevaluation of the NOAA/CMDL carbon monoxide reference scale and comparisons with CO reference gases at NASA-Langley and the Fraunhofer Institute, Journal of Geophysical Research-Atmospheres, 99, D6, 12833-12839, JD00314.

Rothman, L. S. et al. (2009) The HITRAN 2008 molecular spectroscopic database, Journal of Quantitative Spectroscopy & Radiative Transfer,110 (9-10),533-572.

Ryerson et al. (2012), The 2010 California Research at the Nexus of Air Quality and Climate Change (CalNex) field study, Journal of Geophysical Research, doi:10.1002/jgrd.50331.

Santoni, G. W., B. Xiang , E. A. Kort , B. C. Daube , A. E. Andrews , C. Sweeney , K. J. Wecht , J. Peischl , T. B. Ryerson , W. M. Angevine , M. Trainer , T. Nehrkorn , J. Eluszkiewicz , S. Jeong , M. L. Fischer , R. A. Ferrare , S. C. Wofsy (2013) California's Methane Budget derived from CalNex P-3 Aircraft Observations and a Lagrangian Transport Model, Journal of Geophysical Reasearch, submitted.

Schwarz, J. P., J. R. Spackman, R. S. Gao, L. A. Watts, P. Stier, M. Schulz, S. M. Davis, S. C. Wofsy, and D. W. Fahey (2010), Global‐scale black carbon profiles observed in the remote atmosphere and compared to models, Geophysical Research Letter, 37, L18812, doi:10.1029/2010GL044372.

Wecht, K. J., D. J. Jacob, S. C. Wofsy, E. A. Kort, J. R. Worden, S. S. Kulawik, D. K. Henze, M. Kopacz, and V. H. Payne (2012) Validation of TES methane with HIPPO aircraft observations: implications for inverse modeling of methane sources. Atmos. Chem. Phys., 12, 1823-1832, doi:10.5194/acp-12-1823-2012.

Wunch, D., G. C. Toon, P. O. Wennberg, S. C. Wofsy, B. B. Stephens, et al. (2010) Calibration

of the Total Carbon Column Observing Network using aircraft profile data. Atmos. Meas. Tech., 3, 1351-1362, doi:10.5194/amt-3-1351-2010.

Wofsy, S. C., et al. (2011) HIAPER Pole-to-Pole Observations (HIPPO): Fine grained, global scale measurements for determining rates for transport, surface emissions, and removal of climatically important atmospheric gases and aerosols*, Phil. Trans. of the Royal Society A,* 369(1943), 2073-2086.

Xiang B., S. M. Miller, E. A. Kort, G. W. Santoni, B.C. Daube, R. Commane, W. M. Angevine, T.B. Ryerson, M. K. Trainer, A. E. Andrews, T. Nehrkorn, H. Tian and S. C. Wofsy (2013) Nitrous oxide (N2O) emissions from California based on 2010 CalNex airborne measurements, J. Geophys. Res. Atmos. 118, doi: 10.1029/2012JD018244.

York, D., N. M. Evensen, M. L. Martinez, and J. D. B. Delgado (2004) Unified equations for the slope, intercept, and standard errors of the best straight line, *Am. J. Phys.,* 3, DOI: 10.1119/1.1632486.

Zahniser, M. S., D. D. Nelson, J. B. McManus, S. C. Herndon, E. C. Wood, J. H. Shorter, B. H. Lee, G. W. Santoni, R. Jimenez, B. C. Daube, S. Park, E. A. Kort, and S. C. Wofsy (2009), Infrared QC laser applications to field measurements of atmospheric trace gas sources and sinks in environmental research: enhanced capabilities using continuous wave QCLs, Proceedings of SPIE - The International Society for Optical Engineering, 7222, doi: 10.1117/12.815172.

Zahniser, M. S., Nelson, D. D., McManus, J. B., et al.: Measurement of Trace Gas Fluxes Using Tunable Diode-Laser Spectroscopy, Philosophical Transactions of the Royal Society of London Series a-Mathematical Physical and Engineering Sciences, 351(1696), 371–381, 1995.

Zare, R. N. D. S. Kuramoto, C. Haase, S. M. Tan, E. R. Crosson, N. M. R. Saad (2009) High-precision optical measurements of 13C/12C isotope ratios in organic compounds at natural abundance, Proceedings of the National Academy of Sciences, 106 (27) 10928-10932.

Zhao, C., A. E. Andrews, L. Bianco, J. Eluszkiewicz, A. Hirsch, C. MacDonald, T. Nehrkorn, and M. L. Fischer, Atmospheric inverse estimates of methane emissions from Central California, J. Geophys. Res., 114, D16302, doi:10.1029/2008JD011671, 2009.

Zhao, C. L. and P. P. Tans (2006), Estimating uncertainty of the WMO mole fraction scale for carbon dioxide in air, Journal of Geophysical Research-Atmospheres, 111, D8, doi:10.1029/2005JD006003

Chapter 5:

California's Methane Budget derived from CalNex P-3 Aircraft Observations and a Lagrangian Transport Model[3]

Abstract

We present top-down estimates of California emission inventories for methane (CH_4) using atmospheric observations from eleven NOAA P-3 flights during the CalNex 2010 campaign. Measurements were made using a quantum cascade laser spectrometer (QCLS) and a cavity ring-down spectrometer (CRDS), each calibrated to NOAA standards in-flight. Six daytime flights sampled above the northern and southern central valley, and an additional five daytime flights probed the south coast air basin around Los Angeles. The data show large (>100 ppb) CH_4 enhancements associated with point and area sources such as livestock, landfills, wastewater treatment plants, natural gas production and distribution infrastructure, and rice agriculture. We compare aircraft observations to modeled CH_4 distributions by accounting for a) transport using the Stochastic Time-Inverted Lagrangian Transport (STILT) model driven by Weather Research and Forecasting (WRF) meteorology, b) emissions from various inventories gridded to 0.1° x 0.1° resolution, and c) boundary conditions imposed at the edge of the WRF model domain. Using a Bayesian inversion to the flight data and accounting for errors associated with transport, planetary boundary layer height, boundary conditions, seasonality of emissions, and the spatial resolution of surface emissions, we estimate California's CH_4 budget to be 2.4 ± 0.52 (95% C.I.) $TgCH_4$/yr, or 1.6 ± 0.34 times the California Air Resources Board (CARB) CH_4 budget (1.52 $TgCH_4$/yr). Annual emissions from livestock, landfills, rice, natural gas infrastructure, and

[3] Santoni, G. W., B. Xiang, E. A. Kort, B. C. Daube, A. E. Andrews, C. Sweeney, K. J. Wecht, J. Peischl, T. B. Ryerson, W. M. Angevine, M. Trainer, T. Nehrkorn, J. Eluszkiewicz, S. Jeong, M. L. Fischer, R. A. Ferrare, and S. C. Wofsy[1] (2013), *Journal of Geophysical Research Atmospheres*, submitted.

wastewater account for 1.47 ± 0.35, 0.41 ± 0.15, 0.09 ± 0.05, 0.28 ± 0.09, and 0.11 ± 0.02 $TgCH_4$/yr of the total, respectively, representing 171%, 121%, 320%, 191%, and 125% (weighted mean = 160%) of CARB's current estimates for these sources.

5.1. Introduction

Changes in atmospheric greenhouse gas (GHG) concentrations have perturbed the climate system and led to radiative forcing differences of 2.77 W m^{-2} since preindustrial times (1750), with methane (CH_4) accounting for nearly 30% of this change [*Montzka et al*., 2011]. In 2006, the state of California passed Assembly Bill 32 (AB-32, the California Global Warming Solutions Act) requiring the state to reduce its GHG emissions to 1990 levels by 2020, roughly 15% below present values. The California Air Resources Board (CARB) estimates that current annual GHG emissions in California amount to 530 MMT $CO_{2,eq}$ (2009 value), of which CH_4 accounts for 7% or 32 MMT $CO_{2,eq}$, equivalent to 1.52 Tg CH_4 using a 100-year Global Warming Potential (GWP) for CH_4 of 21 [*CARB*, 2011]. Climate-change mitigation strategies will likely identify CH_4 sources such as landfills, wastewater treatment plants, natural gas infrastructure, and agricultural sources as low-cost targets in emissions reductions strategies [*van Vuuren et al.*, 2006, 2010]. Uncertainties in emission inventories, however, present a significant challenge for CARB both in enforcing AB-32 and tracking the progress of GHG emissions reduction strategies. Few data sources have historically been available to quantitatively assess the accuracy of bottom-up emission databases or to track changes over time.

Atmospheric CH_4 measurements can be used to constrain surface emissions, but these techniques are typically limited by insufficient spatial coverage and/or temporal resolution. On the scale of an eddy-flux tower (2-30 m above ground), temporal changes in fluxes can be accurately measured and errors are typically an order of magnitude smaller than the fluxes

themselves, but these measurements are representative of small source areas, typically with length scales on the order of 10^1–10^3 m [*Lee et al*., 2004]. Tall towers or aircraft measurements can help to resolve regional or state-wide emissions with length scales of 10^3–10^5 m [*Gourdji et al.*, 2012; *Miller et al*., 2012]. Tall towers sample a limited domain but produce consistent time series able to resolve the seasonality of emissions, especially in the near-field [*Jeong et al.*, 2012]. In contrast, aircraft measurements are sensitive to upwind sources at larger spatial scales and are thus able to constrain emissions from entire states or regions, limited in time to the measurement period [*Kort et al.*, 2008; *Xiang et al.*, 2013].

We sought to overcome some of the limitations of previous studies by using intensive flight-based measurements of CH_4 during the California Research at the Nexus of Air Quality and Climate Change (CalNex 2010) campaign. The CalNex flight paths were chosen to repeatedly sample over the majority of California's surface area, before and after the onset of the growing season. The spatial coverage of these measurements over California is unprecedented. In this paper, we use various CalNex data products to validate meteorological variables and assess inaccuracies in the modeled boundary conditions, two of the dominant sources of error in regional-scale Lagrangian particle dispersion model inversions. Then we constrain surface fluxes of CH_4 in California by means of a Bayesian inversion framework that makes use of high-resolution (0.1° x 0.1°) prior emission flux distributions from the best available global and regional emission inventories. The optimized emission inventories specific to California represent significant improvements in the spatial distribution of sources compared to global products. Below we present the measurements of CH_4 taken aboard the NOAA P-3 during CalNex as well as the modeling framework results for a variety of inversions and discuss the implications for state climate policy decisions.

5.2. Measurements

The NOAA P-3 aircraft payload included instrumentation to measure a diverse set of atmospheric tracers in both the gas and aerosol phases during CalNex. This work focuses primarily on CH_4 data collected using two sensors: the Harvard/Aerodyne-Research-Inc. quantum cascade laser spectrometer (QCLS) and the NOAA/Picarro wavelength-scanned cavity ring-down spectrometer (CRDS). The QCLS used three pulsed quantum cascade lasers to measure CO_2, CH_4, N_2O, and CO by direct absorption spectroscopy with 1-second RMS precisions of 20, 0.5, 0.08, and 0.15 ppb, respectively [*Kort et al.*, 2012]. The CRDS made 1-Hz measurements of CO_2 and CH_4 with 1-second RMS precisions of 100 and 1.5 ppb, respectively [*Peischl et al.*, 2012]. Both sets of CH_4 measurements were independently calibrated to NOAA standards during flight, accounting for roughly 15% of the sampling duty cycle for each instrument. The QCLS and CRDS data agreed well with one another, with a mean bias term of 4.5 ppb over 130 flight hours and a variance in the bias of 1.5 ppb over the 20 flights. This bias corresponds to an error of 0.25 % relative to the background CH_4 concentration of 1800 ppb. To minimize data gaps in the flight data, a loess curve fit with a 1000 second span window was used to calculate the time-evolution of the QCLS – CRDS CH_4 concentration bias. The more precise QCLS data are used as the primary data, and calibration gaps are filled using the sum of the CRDS data and the loess bias curve. This resulted in an overall mission data retrieval duty cycle of over 97%.

We averaged the data to avoid autocorrelation and to minimize model computation. Averaging resulted in an effective measurement integration window of ~10-20 seconds, depending on altitude (Supplementary Material Section 1). Figure 5.1 shows flight path of the P-3 for 6 flights over the central valley and the mean locations of continuous vertical profiles of

CH_4 where the P-3 sampled over a >1300 m vertical extent (left) that correspond to the CH_4 vertical profiles (right). We note that the May 24th central valley flight sampled at night and was therefore excluded from the analysis as the plane rarely sampled air from the planetary boundary layer. Figure 5.2 shows the corresponding data for the 5 flights in and around the South Coast Air Basin (SoCAB) where night flights were also excluded.

Because our model (described in section 3) uses height above ground level for coordinates, and the P-3 radar altitude system is only accurate for roll angles near zero, we use the reliable GPS position from the P-3 and calculate the aircraft height above the ground using the Shuttle Radar Topography Mission (SRTM) Digital Elevation Map (DEM), which has resolution of 1 km x 1 km, finer than the spatial resolution of the inner-most domain of WRF [*Farr et al.*, 2007].

5.3. Model

The Stochastic Time-Inverted Lagrangian Transport model is a Lagrangian Particle Dispersion Model (LPDM) that can be run in time-reversed fashion in order to estimate the integrated-in-time upwind emissions that contribute to the concentration observed at a particular measurement location (receptor). By combining high-resolution transport and numerous realizations of stochastically altered wind-velocities, STILT generates an ensemble of trajectories that can be aggregated into a "footprint." This footprint represents the transfer function giving spatially and temporally resolved increments of tracer mixing ratio in response to unit surface emission fluxes along the space/time trajectories [*Lin et al.,* 2003]. Several studies have highlighted the model's capabilities as a tool for trace-gas source attribution: *Gerbig et al.* [2003], *Kort et al.* [2008], and *Xiang et al.* [2012] used flight-measurement-based STILT inversions, and *Zhao et al.* [2009], *Miller et al.* [2012], and *Jeong et al.* [2012] used tower-

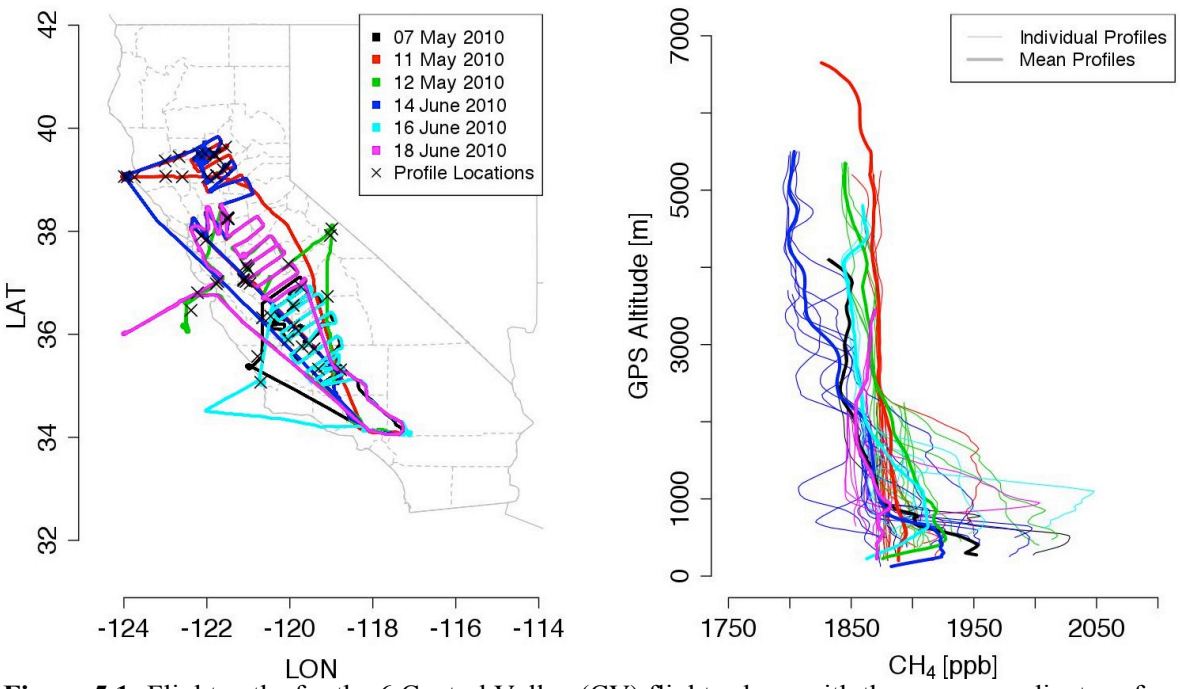

Figure 5.1: Flight paths for the 6 Central Valley (CV) flights along with the mean coordinates of vertical profile locations with ranges > 1300 m and the corresponding CH_4 profiles (with a 150 m smoothing window) at those locations averaged over each day.

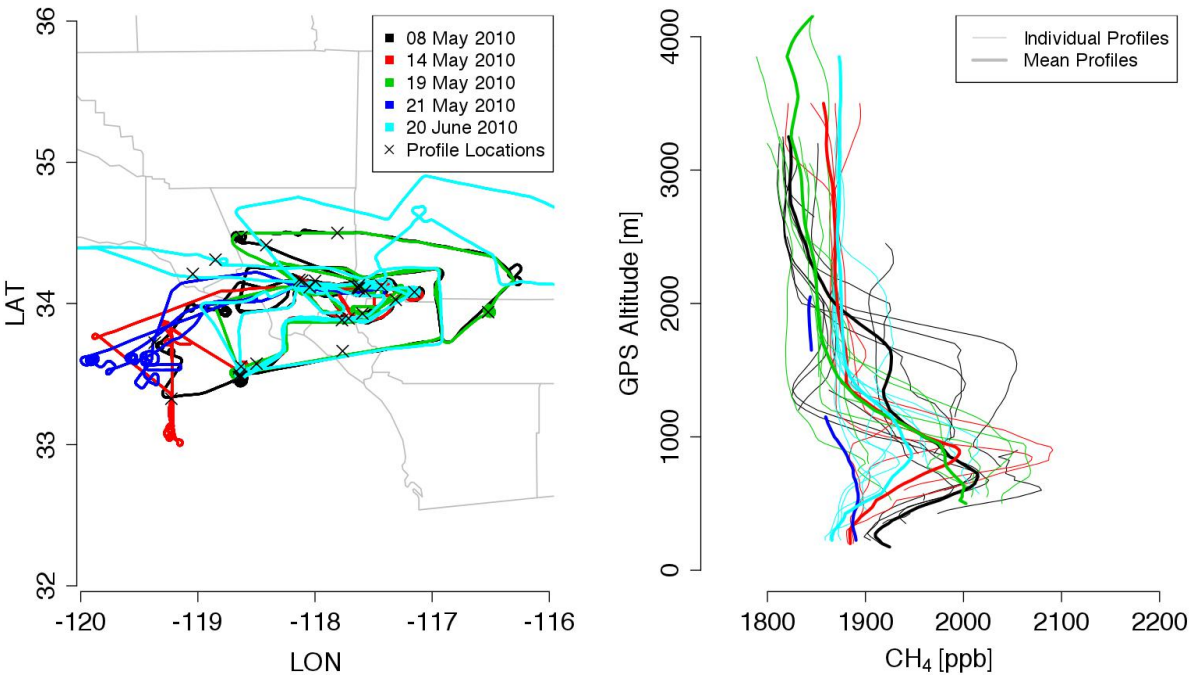

Figure 5.2: Flight paths for the 5 South Coast Air Basin (SoCAB) flights along with the mean coordinates of vertical profile locations with ranges > 1300 m and the corresponding CH_4 profiles (with a 150 m smoothing window) at those locations and averaged over each day.

measurement-based STILT inversions, all with the goal of constraining regional fluxes of CO_2, CH_4, or N_2O.

In the following sections, we discuss: 3.1) the WRF-STILT model, 3.2) emission inventories of CH_4, 3.3) upwind boundary conditions, and 3.4) inversion methods used to optimize the emission prior estimates.

5.3.1 WRF-STILT

STILT is driven with meteorological fields from the Weather Research and Forecasting (WRF) model version 3 [*Skamarock et al.*, 2008] customized for transport modeling [*Nehrkorn et al.*, 2010] and the configurations and evaluation of the model runs for the CalNex 2010 measurement period are discussed in detail in *Angevine et al.* [2012]. For this study, we present results using both the GM4 and the EM4N model configurations [*Angevine et al.* 2012] and summarize only the details relevant to these implementations. For the GM4 configuration, WRF version 3.2.1 was initialized with Global Forecast System (GFS) analyses and run on one-way nested grids of 36 (d01), 12 (d02), and 4 (d03) km spacing with 40 vertical levels, 14 of which were below 1 km, using the Mellor-Yamada-Janjic Planetary Boundary Layer (PBL) scheme and a five-layer thermal diffusion land surface model ('slab') with the U.S. Geological Survey land-use data. For the EM4N configuration, WRF version 3.3 was initialized with European Centre for Medium-Range Weather Forecasts (ECMWF) Re-Analysis-Interim (ERA-Interim) initialization and run on two-way nested grids of 36 (d01), 12 (d02), and 4 (d03) km spacing with 60 vertical levels, 19 of which were below 1 km, using the Mellor-Yamada-Janjic Planetary Boundary Layer (PBL) scheme and the Noah land surface model with Moderate Resolution Imaging Spectroradiometer (MODIS) land-use and land-cover data. Each domain is skewed and the corners of d02 are located at (lat,lon) coordinates of (28.28,-123.64), (46.44, -131.72),

(31.50, -101.80), and (50.78,-103.38) (Supplementary Material Section 2). Time-averaged mass-coupled winds were output from WRF and used to drive STILT, significantly improving mass conservation [*Nehrkorn et al.*, 2010]. We use the latest version of STILT (www.stilt-model.org version 640) that includes the multinest capability (i.e., each particle is allowed to utilize its own highest-resolution grid), a feature essential for a faithful representation of dispersion in nested runs [*McKain et al.*, 2012].

For each receptor (averaged measurement location), an ensemble of 500 STILT particles was run backwards in time for 5 days using the GM4 and EM4N WRF fields. The footprint for each receptor is calculated in each WRF grid-box in units of ppb/(*n*mol m^{-1} s^{-1}) by counting the number of particles residing in the mixed-layer, the height of which is defined here as ½ of the WRF-derived PBLH [*Lin et al.*, 2003, 2004]. The modeled concentration of CH_4 at the receptor is then obtained by multiplying each STILT footprint over the 5 days with spatially and temporally explicit surface fluxes to obtain the enhancement of CH_4 due to surface emissions in the WRF domain. This enhancement is added to the background value of CH_4 at the location of the particle at the end of its trajectory to derive the modeled CH_4 concentration.

5.3.2 Emission Inventories

The California Air Resources Board (CARB) estimates California's CH_4 budget to be 1.52 $TgCH_4$/yr (Table 5.1). We use both global and regional databases as initial estimates of surface fluxes of CH_4 in California. The Emission Database for Global Atmospheric Research (EDGAR) has periodically updated its past and present day anthropogenic emissions of GHGs by country and by spatial grid. We use EDGAR version 3.2 Fast Track 2000 (EDGARv32FT200) at 1° x 1° grid resolution [*Olivier et al.*, 2005] and EDGAR version 4.2

Table 5.1: California CH_4 emission prior estimates from CARB, EDGAR, EDGAR-Substituted, and CalGEM inventories.

	Prior Estimates of Methane Emission Inventories					
CARB Category	**Subcategory CARB** (non-gridded)	**Flux** $TgCH_4/yr$	**Subcategory** Gridded to 0.1° x 0.1°	**Flux** $TgCH_4/yr$	**Subcategory** Gridded to 0.1° x 0.1°	**Flux** $TgCH_4/yr$
Agriculture & Forestry	Ag Energy Use	0.000	EDGAR 4.2 Fossil Fuel Fires	0.000		
	Ag Residue Burning	0.001	EDGAR 4.2 Agricultural waste burning	0.001		
	Enteric Fermentation	0.443	EDGAR 4.2 Enteric Fermentation	0.345		
	Forest and Range Management	0.008	USDA Other Cattle by County	0.258	CALGEM Non-Dairy Cows	0.314
			USDA Beef Cows by County	0.050		
			USDA Milk Cows by County	0.173		
			CARB Dairy Locations and Milk Cows	0.185	CALGEM Diary Cows	0.232
	Manure Management	0.418	EDGAR 4.2 Manure management	0.112		
	Rice Cultivation	0.027	EDGAR 4.2 Agricultural soils	0.032	CALGEM Crop Agriculture Annual	0.064
			USDA Rice Planted by County May (x 12)	0.042	CALGEM Crop Agriculture May (x12)	0.053
			USDA Rice Planted by County June (x 12)	0.249	CALGEM Crop Agriculture June (x 12)	0.170
			EDGAR 4.2 Large scale biomass burning	0.001	CALGEM Wetlands	0.038
			GFED Fire CH4	0.000		
	Other	0.000	EDGAR 4.2 Fugitive from Solid	0.000		
			Sector Total EDGAR 4.2	**0.491**	**Sector Total CALGEM**	**0.610**
	Sector Total	**0.898**	**with CARB/USDA substitutes**	**0.693**		
Commercial	Various Sectors	0.002				
	Sector Total	**0.002**				
Electricity Generation	Imports	0.001				
	In state	0.004				
	Sector Total	**0.005**				
Industrial	CHP: Industrial	0.001				
	Landfills	0.319	EDGAR 4.2 Solid waste disposal	0.601		
	Solid Waste Treatment	0.022	CARB Landfills	0.300	CALGEM Landfills	0.304
	Manufacturing	0.004	EDGAR 4.2 Industrial process and product use	0.005		
	Mining	0.000				
	Not Specified	0.025	EDGAR 4.2 Energy manufacturing transformation	0.020		
	Oil & Gas Extraction	0.038			CALGEM Natural Gas	0.093
	Petroleum Marketing	0.000				
	Petroleum Refining	0.003	EDGAR 4.2 Oil production and refineries	0.026		
	Pipelines	0.093	EDGAR 4.2 Gas production and distribution	0.483		
	Wastewater Treatment	0.090	EDGAR 4.2 Waste water	0.153	CALGEM Wastewater	0.063
			Sector Total EDGAR 4.2	**1.288**	**Sector Total CALGEM**	**0.459**
	Sector Total	**0.595**	**with CARB substitutes**	**0.987**		
Residential	Household Use	0.010	EDGAR 4.2 Residential	0.026		
	Sector Total	**0.010**	**Sector Total EDGAR 4.2**	**0.026**		
Transportation	Aviation	0.000				
	Not Specified	0.000	EDGAR 4.2 Non-road transportation	0.000		
	On Road	0.013	EDGAR 4.2 Road transportation	0.014	CALGEM Petroleum	0.054
	Rail	0.000				
	Water-borne	0.000				
	Sector Total	**0.013**	**Sector Total EDGAR 4.2**	**0.014**	**Sector Total CalGEM**	**0.054**
State Totals	**CARB Non-Gridded**	**1.523**	**EDGAR 4.2 Total Anthropogenic**	**1.819**	**CALGEM (not including wetlands)**	**1.124**
			EDGAR 32FT 2000 Total Anthropogenic	**2.317**		
			EDGAR 4.2 with cow,rice,landfill substitutes	**1.719**		

(EDGARv42) at 0.1° x 0.1° grid resolution [*EC-JRC/PBL*, 2011]. Monthly fire emissions of CH_4 from the Global Fire Emissions Database version 3 (GFED3) for May and June 2010 at 0.5° x 0.5° were averaged and included as an additional database [*van der Werf et al.*, 2010]. Table 5.2a lists the sector-specific EDGAR 4.2 emissions that were optimized.

To improve upon the spatial distributions of these global gridded CH_4 emission inventories, California-specific CH_4 emission inventories for landfills, cattle, and rice were constructed using state and county databases. The California Department of Resources Recycling and Recovery (CalRecycle) maintains a database of solid-waste facilities in California in which the location and acreage used for disposal is tabulated [*SWIS*, 2011]. Using the findings from *Goldsmith et al.* [2012], we take an average value for California landfill emissions of 11.29 g CH_4 m^{-2} day^{-1} and use the total disposal acreage given for each solid waste facility in the database to calculate the total CH_4 flux. We note that landfill emissions can vary by soil cover, soil thickness, anoxic conditions, temperature, wind speed, etc. and this heterogeneity is difficult to capture in our modeling framework. This flux is then distributed into the same 0.1° x 0.1° grid spacing as the EDGAR 4.2 database. An equivalent method is used for constructing a California-specific emissions database of dairy-cow emissions, where an emission rate of 11.36 g CH_4 hr^{-1} per cow [*Mitloehner et al.*, 2009] is combined with dairy locations and cow populations at those dairies (data available at http://www.esrl.noaa.gov/csd/projects/calnex/ [*Salas et al.*, 2008]).

Because the locations of other types of cattle are not specified, agricultural census data by county are used to construct county-specific CH_4 emissions inventories for all cattle: dairy cows, beef cattle, and other unclassified cattle such as calves, steers, bulls, dairy and beef replacements, etc. Of the 7.55 million head of cattle in California, 1.75 million are milk/dairy cows, another 0.6 million are beef cows, and the remainder (5.2 million) are other forms of cattle (data

available from http://www.nass.usda.gov/Quick_Stats/). Beef and dairy cows produce comparable emissions of CH_4 [*Boadi and Wittenberg*, 2001], and other cattle typically produce less because of size, efficiency, and gross energy intake [*Johnson and Johnson*, 1995], though variations in per-head CH_4 emissions can range from ~ 2–20 g CH_4 hr^{-1} [*Westberg et al.*, 2001]. We use the same emissions rate for dairy and beef cows and a factor of 2 smaller for other cattle, noting that in this inversion framework the spatial distributions of the cattle are more important than the actual magnitudes of the prior.

Emissions from rice cultivation are also constructed using county-specific acreage planted (data available at http://www.nass.usda.gov/Quick_Stats/) and an emission rate of 50 and 300 mg CH_4 m^{-2} day^{-1} in May and June, respectively, corresponding to the onset of methanogenesis in rice paddies [*McMillan et al.*, 2007]. With the exception of rice, most of the sources in the central valley near Walnut Grove, CA have minimal seasonality in their emissions [*Jeong et al.*, 2012]. For the seasonally varying rice emissions, we calculate scaling factors on the inversions using the May and June rice emission rates and apply the optimized scaling factors to the annual budget reported in *McMillan et al.* [2007] of 37 g CH_4 m^{-2} yr^{-1}, which is the mean of the annual budget estimates calculated from three different methods. When this is multiplied by the USDA planted rice acreage, the total annual prior estimate of the flux is 0.087 $TgCH_4/yr$. Table 5.2b lists the emission categories in grey that have been used in the EDGAR-substituted emissions inventory, where the 4 EDGAR categories shown in white are the categories that were replaced with inventories constructed from CalRecycle/CARB/USDA data.

We also use prior emission estimates from the California Greenhouse Gas Emissions Measurement (CalGEM) Project (data from http://calgem.lbl.gov/prior_emission.html). Details of the CalGEM emission prior are discussed in *Jeong et al.* [2012], but we note several important

aspects of the inventory that were modified for the purposes of this study. Of the 8 categories included in the database and listed in Table 5.2c, the crop/rice emissions from the DNDC model are temporally resolved at monthly intervals and we use the May and June emissions as prior model enhancements for the flights in each of those respective months. Similarly to the EDGAR-substituted inversions, we apply the scaling factors to the annual prior budget of 0.064 $TgCH_4$/yr and do not scale the DNDC crop/rice emissions to the CARB estimate shown in Table 5.1. We also do not scale the dairy cow and non-dairy-cattle emissions to the CARB estimates, preserving the per-head-of-cow emission factor of 0.39 kgC/dairycow/day (=21.7 g CH_4 hr^{-1}) for a typical mix of lactating and non-lactating dairy cows [*Salas et al.*, 2008] and 0.27 kgC/nondairycow/day (=15 g CH_4 hr^{-1}) for average beef cows (US-EPA, 2012), with minor contributions from other animals. One reason these values are higher than those used in the EDGAR-substituted inventory is that the CalGEM estimates represent values corresponding to 'whole farm models' [*Ellis et al.*, 2010] whereas the EDGAR and EDGAR-substituted inventories explicitly estimate the manure management term.

Wetland emissions are not included in CARB's anthropogenic CH_4 emission budget, so we subtract their modeled enhancements from the measured mixing ratios using the CalGEM wetland emission estimates which are based on the Carnegie-Ames-Standford Approach (CASA) CH_4 model [*Potter et al.*, 2006]. Median enhancements for the May and June flights due to wetland emissions were 0.15 ppb (95% quantile = 2.2 ppb) as wetland emissions have seasonal maxima later in the growing season. As an additional check, we also calculate wetland enhancements using the 'JK' wetland inventory described by *Bergamaschi et al.* [2007], indexed for each month on a coarser 1/2° by 1/2° grid and report that these calculated enhancements are consistently lower that those from CalGEM wetland estimates, largely because of the grid

Table 5.2a: EDGAR 4.2 CH_4 inventory sources (left), inversion results for the CV (middle) and SoCAB (right).

Prior Estimates of CH4 Emissions Inventories

EDGAR 4.2 Subcategory 0.1° x 0.1°	Total Flux Prior $TgCH_4/yr$	Flux Prior CV $TgCH_4/yr$	Flux Prior SCB $TgCH_4/yr$	Fraction SoCAB
EDGAR 4.2 Energy manufacturing transformation	0.020	0.010	0.010	51%
EDGAR 4.2 Non-road transportation	0.000	0.000	0.000	30%
EDGAR 4.2 Road transportation	0.014	0.007	0.008	54%
EDGAR 4.2 Residential	0.026	0.018	0.007	29%
EDGAR 4.2 Fugitive from Solid	0.000	0.000	0.000	0%
EDGAR 4.2 Oil production and refineries	0.026	0.015	0.011	44%
EDGAR 4.2 Gas production and distribution	0.483	0.255	0.228	47%
EDGAR 4.2 Industrial process and product use	0.005	0.002	0.003	58%
EDGAR 4.2 Enteric Fermentation	0.345	0.338	0.007	2%
EDGAR 4.2 Manure management	0.112	0.108	0.004	3%
EDGAR 4.2 Agricultural soils	0.032	0.032	0.000	0%
EDGAR 4.2 Agricultural waste burning	0.001	0.001	0.000	2%
EDGAR 4.2 Large scale biomass burning	0.001	0.001	0.000	4%
EDGAR 4.2 Solid waste disposal	0.601	0.327	0.274	46%
EDGAR 4.2 Waste water	0.153	0.068	0.085	55%
EDGAR 4.2 Fossil Fuel Fires	0.000	0.000	0.000	0%
Totals	**1.819**	**1.182**	**0.636**	**35%**

	CV	SoCAB	Fraction SoCAB
Effective Scaling NOAA B.C. (unitless scaling)	1.986	0.546	
Effective Scaling GEOS-Chem B.C. (unitless scaling)	1.765	0.579	
Posterior Total GM4 NOAA B.C.(TgCH4/yr)	**2.349**	**0.348**	13%
Posterior Total GM4 GEOS-Chem B.C. (TgCH4/yr)	**2.087**	**0.368**	15%
Posterior Total EM4N NOAA B.C.(TgCH4/yr)	**2.539**	**0.317**	11%
Posterior Total EM4N GEOS-Chem B.C. (TgCH4/yr)	**2.236**	**0.325**	13%

Total CA Budget (NOAA B.C. & GM4)	**2.696 ± 0.408**	$TgCH_4/yr$
Total CA Budget (GEOS-Chem B.C. & GM4)	**2.456 ± 0.567**	$TgCH_4/yr$
Total CA Budget (NOAA B.C. & EM4N)	**2.856 ± 0.533**	$TgCH_4/yr$
Total CA Budget (GEOS-Chem B.C. & EM4N)	**2.561 ± 0.714**	$TgCH_4/yr$
MEAN	**2.642 ± 0.555**	$TgCH_4/yr$

EDGAR 4.2 CV Inversions

Optimized Independently	Colinearity Factor	Scaling GM4/NOAA	Fluxes $TgCH_4/yr$	Scaling EM4N/NOAA	Fluxes $TgCH_4/yr$	Scaling GM4/GEOS	Fluxes $TgCH_4/yr$	Scaling EM4N/GEOS	Fluxes $TgCH_4/yr$
C	5.15	1.83	0.019	2.212	0.022	1.53	0.015	1.893	0.019
C	5.15	1.83	0.000	2.212	0.000	1.53	0.000	1.893	0.000
C	5.15	1.83	0.012	2.212	0.015	1.53	0.010	1.893	0.012
C	5.15	1.83	0.033	2.212	0.040	1.53	0.028	1.893	0.034
C	5.15	1.83	0.000	2.212	0.000	1.53	0.000	1.893	0.000
C	5.15	1.83	0.027	2.212	0.032	1.53	0.022	1.893	0.028
B	4.07	1.03	0.263	1.198	0.306	0.73	0.186	0.890	0.227
C	5.15	1.83	0.004	2.212	0.004	1.53	0.003	1.893	0.004
A	1.67	3.41	1.152	3.518	1.189	3.32	1.124	3.352	1.133
A	1.67	3.41	0.369	3.518	0.380	3.32	0.360	3.352	0.362
C	5.15	1.83	0.059	2.212	0.072	1.53	0.050	1.893	0.061
C	5.15	1.83	0.002	2.212	0.002	1.53	0.001	1.893	0.002
C	5.15	1.83	0.001	2.212	0.002	1.53	0.001	1.893	0.001
B	4.07	1.03	0.338	1.198	0.392	0.73	0.238	0.890	0.291
B	4.07	1.03	0.071	1.198	0.082	0.73	0.050	0.890	0.061
C	5.15	1.83	0.000	2.212	0.000	1.53	0.000	1.893	0.000
		Prior Total	1.182		1.182		1.182		1.182
		INVERSION TOTAL	**2.349**		**2.539**		**2.087**		**2.236**

Scaling Factors		Mean	Sdev	Mean	Sdev	Mean	Sdev	Mean	Sdev
Cows/Manure	A	3.408	0.330	3.518	0.332	3.324	0.363	3.352	0.420
Oil&Gas/Lndfl/WW	B	1.032	0.171	1.198	0.191	0.727	0.215	0.890	0.242
Rest	C	1.830	0.156	2.212	0.209	1.528	0.239	1.893	0.297

Fluxes	Prior	Posterior	CI = 2 sigma	Posterior	CI	Posterior	CI	Posterior	CI
Cows/Manure	0.446	1.521	0.295	1.569	0.296	1.483	0.324	1.495	0.375
Oil&Gas/Lndfl/WW	0.651	0.671	0.223	0.780	0.249	0.473	0.279	0.579	0.315
Rest	0.086	0.157	0.027	0.189	0.036	0.131	0.041	0.162	0.051
Total	1.182	**2.349**	0.365	**2.539**	0.491	**2.087**	0.520	**2.236**	0.671

EDGAR 4.2 SoCAB Inversions

Optimized Independently	Colinearity Factor	Scaling GM4/NOAA	Fluxes $TgCH_4/yr$	Scaling EM4N/NOAA	Fluxes $TgCH_4/yr$	Scaling GM4/GEOS	Fluxes $TgCH_4/yr$	Scaling EM4N/GEOS	Fluxes $TgCH_4/yr$
B	1.04	0.52	0.005	0.476	0.005	0.55	0.006	0.487	0.005
B	1.04	0.52	0.000	0.476	0.000	0.55	0.000	0.487	0.000
B	1.04	0.52	0.004	0.476	0.004	0.55	0.004	0.487	0.004
B	1.04	0.52	0.004	0.476	0.004	0.55	0.004	0.487	0.004
B	1.04	0.52	0.000	0.476	0.000	0.55	0.000	0.487	0.000
B	1.04	0.52	0.006	0.476	0.005	0.55	0.006	0.487	0.006
B	1.04	0.52	0.119	0.476	0.108	0.55	0.126	0.487	0.111
B	1.04	0.52	0.001	0.476	0.001	0.55	0.001	0.487	0.001
A	1.04	1.86	0.013	1.811	0.013	2.04	0.014	1.873	0.013
A	1.04	1.86	0.007	1.811	0.006	2.04	0.007	1.873	0.007
B	1.04	0.52	0.000	0.476	0.000	0.55	0.000	0.487	0.000
B	1.04	0.52	0.000	0.476	0.000	0.55	0.000	0.487	0.000
B	1.04	0.52	0.000	0.476	0.000	0.55	0.000	0.487	0.000
B	1.04	0.52	0.144	0.476	0.130	0.55	0.152	0.487	0.133
B	1.04	0.52	0.044	0.476	0.040	0.55	0.047	0.487	0.041
B	1.04	0.52	0.000	0.476	0.000	0.55	0.000	0.487	0.000
		Prior Total	0.636		0.636		0.636		0.636
		INVERSION TOTAL	**0.348**		**0.317**		**0.368**		**0.325**

Scaling Factors		Mean	Sdev	Mean	Sdev	Mean	Sdev	Mean	Sdev
Cows/Manure	A	1.860	0.144	1.811	0.161	2.037	0.177	1.873	0.194
Oil&Gas/Lndfl/WW/Rest	B	0.524	0.032	0.476	0.031	0.554	0.035	0.487	0.032

Fluxes	Prior	Posterior	CI = 2 sigma	Posterior	CI	Posterior	CI	Posterior	CI
Cows/Manure	0.011	0.020	0.003	0.019	0.003	0.021	0.004	0.020	0.004
Oil/Gas/Waste/Rest	0.626	0.328	0.040	0.298	0.039	0.347	0.044	0.305	0.040
Total	0.636	**0.348**	0.043	**0.317**	0.042	**0.368**	0.047	**0.325**	0.043

Table 5.2b: EDGAR-Substituted CH_4 inventory sources (left), inversion results for the CV (middle) and SoCAB (right).

Prior Estimates of CH4 Emissions Inventories EDGAR-Substituted Subcategory 0.1° x 0.1°	Total Flux Prior $TgCH_4/yr$	Flux Prior CV $TgCH_4/yr$	Flux Prior SCB $TgCH_4/yr$	Fraction SoCAB
EDGAR 4.2 Energy manufacturing transformation	0.020	0.010	0.010	51%
EDGAR 4.2 Non-road transportation	0.000	0.000	0.000	30%
EDGAR 4.2 Road transportation	0.014	0.007	0.008	54%
EDGAR 4.2 Residential	0.026	0.018	0.007	29%
EDGAR 4.2 Fugitive from Solid	0.000	0.000	0.000	0%
EDGAR 4.2 Oil production and refineries	0.026	0.015	0.011	44%
EDGAR 4.2 Gas production and distribution	0.483	0.255	0.228	47%
EDGAR 4.2 Industrial process and product use	0.005	0.002	0.003	58%
EDGAR 4.2 Enteric Fermentation	0.345	0.338	0.007	2%
USDA Other Cattle by County	0.258	0.256	0.002	1%
USDA Beef Cows by County	0.050	0.050	0.000	0%
USDA Milk Cows by County	0.173	0.170	0.002	1%
CARB Milk Cows by Dairy Location	0.185	0.161	0.024	13%
EDGAR 4.2 Manure management	0.112	0.108	0.004	3%
EDGAR 4.2 Agricultural soils	0.032	0.032	0.000	0%
USDA Rice Planted by County May (x 12)	0.042	0.042	0.000	0%
USDA Rice Planted by County June (x 12)	0.249	0.249	0.000	0%
EDGAR 4.2 Agricultural waste burning	0.001	0.001	0.000	2%
EDGAR 4.2 Large scale biomass burning	0.001	0.001	0.000	4%
GFED Fire CH4	0.000	0.000	0.000	0%
EDGAR 4.2 Solid waste disposal	0.601	0.327	0.274	46%
CARB Landfills	0.300	0.219	0.080	27%
EDGAR 4.2 Waste water	0.153	0.068	0.085	55%
EDGAR 4.2 Fossil Fuel Fires	0.000	0.000	0.000	0%
Totals	**1.719**	**1.257**	**0.462**	**27%**

	CV	SoCAB	Fraction SoCAB
Effective Scaling NOAA B.C. (unitless scaling)	1.635	0.785	
Effective Scaling GEOS-Chem B.C. (unitless scaling)	1.500	0.835	
Posterior Total GM4 NOAA B.C.($TgCH_4/yr$)	**2.055**	**0.363**	15%
Posterior Total GM4 GEOS-Chem B.C. ($TgCH_4/yr$)	**1.886**	**0.386**	17%
Posterior Total EM4N NOAA B.C.($TgCH_4/yr$)	**2.175**	**0.343**	14%
Posterior Total EM4N GEOS-Chem B.C. ($TgCH_4/yr$)	**1.987**	**0.359**	15%

Total CA Budget (NOAA B.C. & GM4)	**2.418 ± 0.393**	$TgCH_4/yr$
Total CA Budget (GEOS-Chem B.C. & GM4)	**2.271 ± 0.510**	$TgCH_4/yr$
Total CA Budget (NOAA B.C. & EM4N)	**2.518 ± 0.529**	$TgCH_4/yr$
Total CA Budget (GEOS-Chem B.C. & EM4N)	**2.345 ± 0.667**	$TgCH_4/yr$
MEAN	**2.388 ± 0.525**	$TgCH_4/yr$

EDGAR-Substituted CV Inversions

Optimized Independently	Colinearity Factor	Scaling GM4/NOAA	Fluxes $TgCH_4/yr$	Scaling EM4N/NOAA	Fluxes $TgCH_4/yr$	Scaling GM4/GEOS	Fluxes $TgCH_4/yr$	Scaling EM4N/GEOS	Fluxes $TgCH_4/yr$
E	6.32	1.392	0.014	1.674	0.017	1.096	0.011	1.339	0.014
E	6.32	1.392	0.000	1.674	0.000	1.096	0.000	1.339	0.000
E	6.32	1.392	0.009	1.674	0.011	1.096	0.007	1.339	0.009
E	6.32	1.392	0.025	1.674	0.030	1.096	0.020	1.339	0.024
E	6.32	1.392	0.000	1.674	0.000	1.096	0.000	1.339	0.000
E	6.32	1.392	0.020	1.674	0.024	1.096	0.016	1.339	0.020
C	4.03	1.049	0.268	1.372	0.350	0.735	0.188	0.989	0.252
E	6.32	1.392	0.003	1.674	0.003	1.096	0.002	1.339	0.003
A	1.92	2.093	0.536	2.150	0.551	2.144	0.549	2.181	0.559
A	1.92	2.093	0.104	2.150	0.107	2.144	0.107	2.181	0.109
A	1.92	2.093	0.337	2.150	0.346	2.144	0.345	2.181	0.351
A	1.92	2.093	0.226	2.150	0.233	2.144	0.232	2.181	0.236
D	1.74	0.872	0.036	1.030	0.043	0.560	0.023	0.650	0.027
D	1.74	0.872	0.217	1.030	0.257	0.560	0.140	0.650	0.162
E	6.32	1.392	0.001	1.674	0.001	1.096	0.001	1.339	0.001
E	4.03	1.392	0.001	1.674	0.001	1.096	0.000	1.339	0.001
B	2.37	1.657	0.363	1.444	0.317	1.410	0.309	1.303	0.286
C	4.03	1.049	0.072	1.372	0.094	0.735	0.050	0.989	0.068
E	6.32	1.392	0.000	1.674	0.000	1.096	0.000	1.339	0.000
		Prior Total	1.257		1.257		1.257		1.257
		INVERSION TOTAL	**2.055**		**2.175**		**1.886**		**1.987**

Scaling Factors		Mean	Sdev	Mean	Sdev	Mean	Sdev	Mean	Sdev
Dairy/NDai/Manure	A	2.093	0.223	2.150	0.255	2.144	0.278	2.181	0.327
Landfill	B	1.657	0.154	1.444	0.185	1.410	0.168	1.303	0.245
Oil&Gas/WW	C	1.049	0.183	1.372	0.253	0.735	0.239	0.989	0.286
Rice	D	0.872	0.220	1.030	0.257	0.560	0.274	0.650	0.326
Rest	E	1.392	0.168	1.674	0.220	1.096	0.235	1.339	0.276

Fluxes	Prior	Posterior	CI = 2 sigma	Posterior	CI	Posterior	CI	Posterior	CI
Dairy/NDai/Manure	0.575	1.203	0.256	1.236	0.294	1.233	0.319	1.254	0.376
Landfill	0.219	0.363	0.067	0.317	0.081	0.309	0.074	0.286	0.107
Oil&Gas/WW	0.324	0.340	0.119	0.444	0.163	0.238	0.155	0.320	0.185
Rice	0.087	0.076	0.038	0.089	0.044	0.049	0.047	0.056	0.057
Rest	0.053	0.073	0.018	0.088	0.023	0.058	0.025	0.071	0.029
Total	1.257	**2.055**	0.348	**2.175**	0.486	**1.886**	0.463	**1.987**	0.620

EDGAR-Substituted SoCAB Inversions

Optimized Independently	Colinearity Factor	Scaling GM4/NOAA	Fluxes $TgCH_4/yr$	Scaling EM4N/NOAA	Fluxes $TgCH_4/yr$	Scaling GM4/GEOS	Fluxes $TgCH_4/yr$	Scaling EM4N/GEOS	Fluxes $TgCH_4/yr$
C	2.681	0.662	0.007	0.645	0.007	0.699	0.007	0.632	0.007
C	2.681	0.662	0.000	0.645	0.000	0.699	0.000	0.632	0.000
C	2.681	0.662	0.005	0.645	0.005	0.699	0.005	0.632	0.005
C	2.681	0.662	0.005	0.645	0.005	0.699	0.005	0.632	0.005
C	2.681	0.662	0.000	0.645	0.000	0.699	0.000	0.632	0.000
C	2.681	0.662	0.007	0.645	0.007	0.699	0.008	0.632	0.007
C	2.681	0.662	0.151	0.645	0.147	0.699	0.159	0.632	0.144
C	2.681	0.662	0.002	0.645	0.002	0.699	0.002	0.632	0.002
					0.000				0.000
A	1.172	1.647	0.004	1.737	0.004	1.757	0.004	1.784	0.004
A	1.172	1.647	0.000	1.737	0.000	1.757	0.000	1.784	0.000
					0.000				0.000
A	1.172	1.647	0.039	1.737	0.041	1.757	0.042	1.784	0.042
A	1.172	1.647	0.006	1.737	0.006	1.757	0.006	1.784	0.006
					0.000				0.000
					0.000				0.000
					0.000				0.000
C	2.681	0.662	0.000	0.645	0.000	0.699	0.000	0.632	0.000
					0.000				0.000
C	2.681	0.662	0.000	0.645	0.000	0.699	0.000	0.632	0.000
					0.000				0.000
B	2.885	1.002	0.081	0.809	0.065	1.087	0.087	1.038	0.084
C	2.681	0.662	0.056	0.645	0.055	0.699	0.059	0.632	0.053
C	2.681	0.662	0.000	0.645	0.000	0.699	0.000	0.632	0.000
		Prior Total	0.462		0.462		0.462		0.462
		INVERSION TOTAL	**0.363**		**0.343**		**0.386**		**0.359**

Scaling Factors		Mean	Sdev	Mean	Sdev	Mean	Sdev	Mean	Sdev
Dairy/NDai/Manure	A	1.647	0.186	1.737	0.208	1.757	0.185	1.784	0.227
Landfill	B	1.002	0.084	0.809	0.081	1.087	0.088	1.038	0.118
Oil&Gas/WW/Rest	C	0.662	0.036	0.645	0.044	0.699	0.038	0.632	0.038

Fluxes	Prior	Posterior	CI = 2 sigma	Posterior	CI	Posterior	CI	Posterior	CI
Dairy/NDai/Manure	0.030	0.049	0.011	0.051	0.012	0.052	0.011	0.053	0.013
Landfill	0.080	0.081	0.013	0.065	0.013	0.087	0.014	0.084	0.019
WW/Gas/Rest	0.352	0.233	0.025	0.227	0.031	0.246	0.026	0.222	0.027
Total	0.462	**0.363**	0.046	**0.343**	0.043	**0.386**	0.047	**0.359**	0.047

Table 5.2c: CalGEM CH_4 inventory sources (left), inversion results for the CV (middle) and SoCAB (right).

Prior Estimates of CH4 Emissions Inventories

CALGEM Subcategory 0.1° x 0.1°	Total Flux Prior $TgCH_4/yr$	Flux Prior CV $TgCH_4/yr$	Flux Prior SCB $TgCH_4/yr$	Fraction SoCAB
CG_lndf	0.304	0.147	0.1568	52%
CG_dair	0.232	0.200	0.0316	14%
CG_ndai	0.314	0.311	0.0032	1%
CG_ngas	0.093	0.059	0.0335	36%
CG_petr	0.054	0.047	0.0070	13%
CG_wetl	0.038	0.037	0.0009	2%
CG_crop	0.064	0.064	0.0000	0%
CG_wwtr	0.063	0.008	0.0549	87%
Totals	**1.161**	**0.873**	**0.288**	**26%**

	CV	SoCAB	Fraction SoCAB
Effective Scaling NOAA B.C. (unitless scaling)	2.214	1.075	
Effective Scaling GEOS-Chem B.C. (unitless scaling)	2.028	1.132	
Posterior Total GM4 NOAA B.C.(TgCH4/yr)	**1.933**	**0.310**	14%
Posterior Total GM4 GEOS-Chem B.C. (TgCH4/yr)	**1.770**	**0.326**	16%
Posterior Total EM4N NOAA B.C.(TgCH4/yr)	**2.221**	**0.282**	11%
Posterior Total EM4N GEOS-Chem B.C. (TgCH4/yr)	**2.012**	**0.291**	13%

Total CA Budget (NOAA B.C. & GM4)	**2.242 ± 0.339**	$TgCH_4/yr$
Total CA Budget (GEOS-Chem B.C. & GM4)	**2.096 ± 0.451**	$TgCH_4/yr$
Total CA Budget (NOAA B.C. & EM4N)	**2.502 ± 0.483**	$TgCH_4/yr$
Total CA Budget (GEOS-Chem B.C. & EM4N)	**2.303 ± 0.632**	$TgCH_4/yr$
MEAN	**2.286 ± 0.476**	$TgCH_4/yr$

CALGEM CV Inversions

Optimized Independently	Colinearity Factor	Scaling GM4/NOAA	Fluxes $TgCH_4/yr$	Scaling EM4N/NOAA	Fluxes $TgCH_4/yr$	Scaling GM4/GEOS	Fluxes $TgCH_4/yr$	Scaling EM4N/GEOS	Fluxes $TgCH_4/yr$
A	1.860	1.859	0.273	2.267	0.333	1.472	0.216	1.819	0.267
B	1.338	2.450	0.491	2.833	0.567	2.416	0.484	2.737	0.548
B	1.338	2.450	0.762	2.833	0.882	2.416	0.752	2.737	0.852
C	3.455	2.383	0.141	2.653	0.157	1.875	0.111	2.096	0.124
C	3.455	2.383	0.112	2.653	0.124	1.875	0.088	2.096	0.098
X		1.000	0.037	1.000	0.037	1.000	0.037	1.000	0.037
D	1.904	1.593	0.102	1.623	0.104	1.089	0.070	1.114	0.071
E	1.453	1.904	0.015	2.124	0.017	1.656	0.013	1.796	0.014
		Prior Total	0.873		0.873		0.873		0.873
		INVERSION TOTAL	**1.933**		**2.221**		**1.770**		**2.012**

Scaling Factors		Mean	Sdev	Mean	Sdev	Mean	Sdev	Mean	Sdev
Landfills	A	1.86	0.29	2.27	0.37	1.47	0.38	1.82	0.49
Cows(D&ND)	B	2.45	0.20	2.83	0.28	2.42	0.26	2.74	0.37
NatGas&Pet	C	2.38	0.30	2.65	0.35	1.88	0.40	2.10	0.45
Crop(Rice)	D	1.59	0.30	1.62	0.31	1.09	0.39	1.11	0.40
Wastewater	E	1.90	0.24	2.12	0.35	1.66	0.35	1.80	0.44

Fluxes	Prior	Posterior	CI = 2 sigma	Posterior	CI	Posterior	CI	Posterior	CI
Landfills	0.147	0.273	0.085	0.333	0.108	0.216	0.111	0.267	0.145
Cows(D&ND)	0.511	1.253	0.210	1.449	0.290	1.236	0.267	1.400	0.380
NatGas&Pet	0.106	0.253	0.063	0.281	0.075	0.199	0.086	0.222	0.096
Crop(Rice)	0.064	0.102	0.038	0.104	0.040	0.070	0.050	0.071	0.051
Wastewater	0.008	0.015	0.004	0.017	0.006	0.013	0.006	0.014	0.007
Total	0.836	**1.896**	0.299	**2.184**	0.441	**1.734**	0.411	**1.975**	0.591

CALGEM SoCAB Inversions

Optimized Independently	Colinearity Factor	Scaling GM4/NOAA	Fluxes $TgCH_4/yr$	Scaling EM4N/NOAA	Fluxes $TgCH_4/yr$	Scaling GM4/GEOS	Fluxes $TgCH_4/yr$	Scaling EM4N/GEOS	Fluxes $TgCH_4/yr$
A	1.515	0.825	0.129	0.700	0.110	0.887	0.139	0.732	0.115
B	1.238	1.441	0.046	1.367	0.043	1.520	0.048	1.348	0.043
B	1.238	1.441	0.005	1.367	0.004	1.520	0.005	1.348	0.004
A	1.515	0.825	0.028	0.700	0.023	0.887	0.030	0.732	0.025
A	1.515	0.825	0.006	0.700	0.005	0.887	0.006	0.732	0.005
X		1.000	0.001	1.000	0.001	1.000	0.001	1.000	0.001
X		1.000	0.000	1.000	0.000	1.000	0.000	1.000	0.000
C	1.504	1.745	0.096	1.732	0.095	1.771	0.097	1.801	0.099
		Prior Total	0.288		0.288		0.288		0.288
		INVERSION TOTAL	**0.310**		**0.282**		**0.326**		**0.291**

Scaling Factors		Mean	Sdev	Mean	Sdev	Mean	Sdev	Mean	Sdev
Lndfl&NGas&Pet	A	0.82	0.07	0.70	0.07	0.89	0.07	0.73	0.06
Cows(D&ND)	B	1.44	0.21	1.37	0.19	1.52	0.20	1.35	0.19
Wastewater	C	1.74	0.10	1.73	0.09	1.77	0.12	1.80	0.11

Fluxes	Prior	Posterior	CI = 2 sigma	Posterior	CI	Posterior	CI	Posterior	CI
Lndfl&NGas&Pet	0.197	0.163	0.028	0.138	0.028	0.175	0.027	0.144	0.025
Cows(D&ND)	0.035	0.050	0.015	0.048	0.013	0.053	0.014	0.047	0.013
Wastewater	0.055	0.096	0.011	0.095	0.010	0.097	0.013	0.099	0.012
Total	0.287	**0.309**	0.040	**0.281**	0.042	**0.325**	0.040	**0.290**	0.041

resolution. We therefore chose to use CalGEM wetland emission enhancements to remove the influence of wetlands in all the inversions shown.

Figure 5.3 shows the spatial distributions of EDGAR and CalGEM prior anthropogenic CH_4 flux maps plotted logarithmically and gridded to 0.1° x 0.1° resolution. From these maps, total CH_4 emissions by category are tabulated in Table 5.1 and compared with the CARB state-wide estimates. The EDGAR-substituted emission prior is not explicitly plotted in Figure 5.3 but has the same spatial features as the CALGEM agricultural since it is derived from the same geospatial datasets.

Based on the work of *Jeong et al.* [2012], we estimate uncertainty due to seasonal variation from the standard deviation of the seasonal scaling factors obtained from the southern portion of the Central Valley (R08 in *Jeong et al.* [2012]), a region with large CH_4 sources but minimal seasonally varying crop/rice emissions. This estimate suggests that the seasonality adds an additional error of 26% to our inversion results due to extrapolation to an annual cycle.

5.3.3 Boundary Conditions

Because STILT models only CH_4 enhancements due to surface emissions in the near-field regions that have non-zero footprints, the far-field upwind concentration of CH_4 must be accounted for when comparing modeled receptor results to measurements. This is done by assigning a CH_4 concentration to each of the 500 particle trajectories per receptor at the location and time that each particle reaches the edge of the WRF d02 domain. We compare two methods for assigning these boundary conditions: 1) a 'NOAA-curtain' specified at 1° latitude, 1000 m altitude, and daily time resolution in the remote Pacific constructed from flights by the

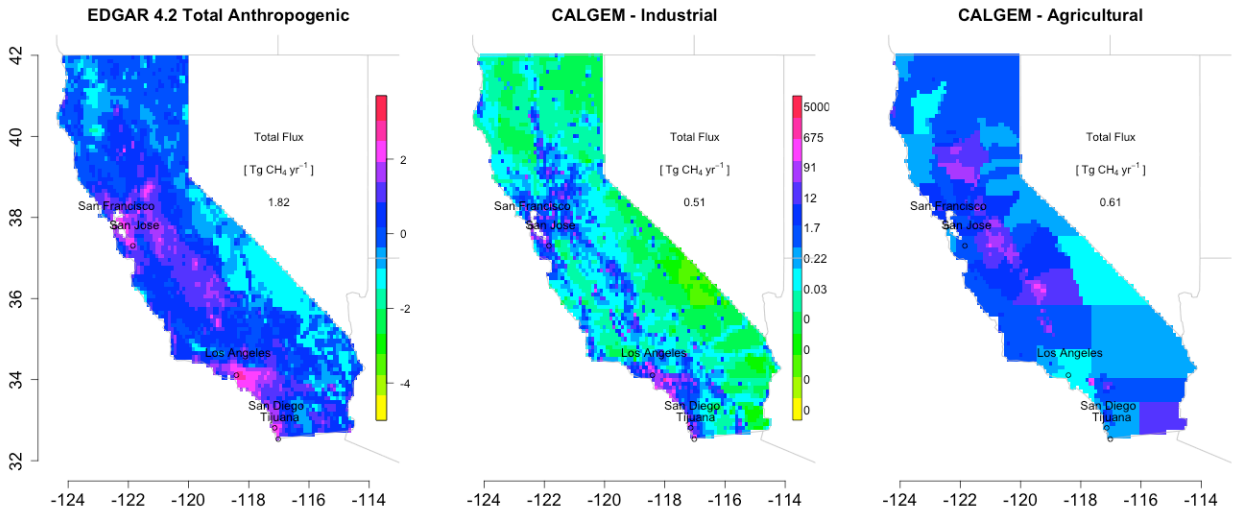

Figure 5.3: Spatial distributions of the surface logarithmic CH_4 emission prior estimates from EDGAR and CalGEM at 0.1° x 0.1° resolution. The two color-scales are the same for all plots, with the left scale in units of log(ppb) and the right scale in units of (ppb).

NOAA/ESRL Carbon Cycle Group Aircraft Program and flask samples that have been collected for more than 10 years in Hawaii, Trinidad Head, CA and Estevan Point, BC [*Andrews et al.*, 2013], and 2) a GEOS-Chem model simulation of CH_4 at a 1/2° latitude, 2/3° longitude, and various vertical resolutions typically on the order of ~100 m in the troposphere [*Pickett-Heaps et al.,* 2011]. To estimate the uncertainty and bias introduced by each of these boundary conditions, we compare both to data taken using the QCLS during the HIAPER Gulfstream-V Pole-to-Pole Observation (HIPPO) program which flew 9 longitudinal transects from ~67°S to ~80°N over the Pacific making measurements from the surface (500 ft) to ~14 km and captured different weekly segments of the seasonal cycle between 2009 and 2011 [*Wofsy et al.*, 2011]. Because these different data existed in various spatial distributions, a loess two-dimesional filter (latitude and altitude) was applied to each data set and the residual differences were plotted for the 30°N-50°N curtain corresponding to where 100 % of the STILT receptors exited the WRF domain (see Supplementary Material Section 3 and discussion below).

5.3.4 Inversion Methods

We optimize emission inventories using Bayesian inversions on the data. This approach scales independent source types separately and accounts for error associated with the emission inventories' prior estimates, WRF meteorology, and boundary conditions. In the inversion, optimized *a posteriori* scaling factors, $\underline{\hat{\lambda}}$ (n x 1), for the n source categories (which range from n=2 to n=5 depending on the inversion) are calculated analytically according to:

$$\underline{\hat{\lambda}} = \underline{\underline{\widehat{S_\lambda}}} \left(\underline{\underline{K}}^T \underline{\underline{S_\varepsilon}}^{-1} \underline{y} + \underline{\underline{S}}_{prior}^{-1} \underline{\lambda}_{prior} \right) \tag{5.1}$$

where $\underline{\underline{\widehat{S_\lambda}}}$ (n x n) is the *a posteriori* error matrix for $\underline{\lambda}$ and is calculated according to:

$$\underline{\underline{\widehat{S_\lambda}}} = \left(\underline{\underline{K}}^T \underline{\underline{S_\varepsilon}}^{-1} \underline{\underline{K}} + \underline{\underline{S}}_{prior}^{-1} \right)^{-1} \tag{5.2}$$

where $\underline{\underline{K}}$ (m x n) is a matrix representing the modeled CH_4 enhancement of the n categories at the m receptors, $\underline{\lambda}_{prior}$ (n x *1*) is the *a priori* scaling factors (a vector of ones), $\underline{y}$ (m x *1*) is the background-subtracted CH_4 measurement at the m receptors (i.e. the enhancements), $\underline{\underline{S}}_{\varepsilon}$ (m x m) is the model-data mismatch error covariance matrix, and $\underline{\underline{S}}_{prior}$ (n x n) is the *a priori* error matrix for $\underline{\lambda}$. We use the correlation matrix (Table 5.3) of the enhancement time series as an estimate of the *a priori* error-covariance matrix, scaled to an uncertainty of 30% in the prior estimates, and test the effect of different uncertainty scalings using L-curve theory [*Hansen*, 2001; *Brioude et al.*, 2011]. The correlation matrix accounts for the manifestation of the spatial colinearity of the different emission categories in the observed concentration enhancements. We compare inversions using both the correlation matrix scaled to 30% uncertainty and a diagonal matrix with 30% uncertainty in the emission prior estimates, corresponding to an assumption of no covariance between the different sources.

Following similar conventions as *Zhao et al.* [2009], the error covariance matrix $\underline{\underline{S}}_{\varepsilon}$ is constructed according to:

$$\underline{\underline{S}}_{\epsilon} = \underline{\underline{S}}_{inst} + \underline{\underline{S}}_{eddy} + \underline{\underline{S}}_{tran} + \underline{\underline{S}}_{part} + \underline{\underline{S}}_{boun} + \underline{\underline{S}}_{aggr} \quad (5.3)$$

where each of the terms represent error contributions to total model error and are assumed to be uncorrelated (i.e. zero covariance). $\underline{\underline{S}}_{inst}$ is the error due to the accuracy of the instruments (CRDS and QCLS) and is set to 2 *ppb*. $\underline{\underline{S}}_{eddy}$ is the error due to the turbulent fluctuations in CH_4 concentration due to atmospheric eddies. This is estimated as the variance in the concentration averaged into each receptor (see Supplementary Material Section 1) and typically ranges from 0.2–10 ppb (5^{th} and 95^{th} quartile), with higher values corresponding to measurements taken within the PBL.

Table 5.3: $\underline{\underline{S}}_{prior}$ correlation matrices for the CVand the SoCAB for the CalGEM inventory.

	Central Valley Flights				
	CG_lndf	CG_da_nd	CG_ng_pt	CG_crop	CG_wwtr
CG_lndf	1				
CG_da_nd	0.31	1			
CG_ng_pt	0.64	0.45	1		
CG_crop	0.28	0.09	0.61	1	
CG_wwtr	0.47	0.26	0.44	0.04	1

	South Coast Air Basin Flights		
	CG_ld_ng_pt	CG_da_nd	CG_wwtr
CG_ld_ng_pt	1		
CG_da_nd	0.39	1	
CG_wwtr	0.55	0.38	1

$\underline{S}_{tran}$ accounts for the various forms of error introduced by the WRF meteorological fields, notably wind velocities and uncertainties in PBLH. *Angevine et al.* [2012] compared WRF wind velocities with profilers at LAX and Chowchilla and show that both GM4 and EM4N have stronger winds, with mean biases/standard-deviations of ~0.6/2.7 m/s and ~1.0/2.8 m/s, respectively. *Lin and Gerbig* [2005] quantified the error associated with wind speed and demonstrated that inversions done without an extra error term for the wind were often too precise. We use the value of ~10% of the average predicted CH_4 enhancement from *Jeong et al.* [2012], noting that the standard deviations of the wind speeds in this study are comparable. Errors in PBLH were determined by multiplying the relative error of the PBLH by the mean CH_4 enhancement within the PBL (<1000 m). The PBLH error was calculated by comparing WRF modeled PBLH to estimates of PBLH from 2 sources: 1) vertical profiles of potential temperature (θ) and water vapor from the P-3 and 2) data from the High Spectral Resolution Lidar (HSRL) airborne aerosol backscatter instrument aboard the NASA LaRC B200 King Air during the CalNex & CARES (Carbonaceous Aerosol and Radiative Effects Study) deployments in May and June of 2010 [*Fast et al.*, 2012; *Scarino et al.*, submitted 2013]. Similar to *Liu and Liang* [2010], the PBLH is assumed to be the height at which $\frac{d\theta}{dz}$ is maximized, or $\frac{d\mathrm{H_2O}}{dz}$ is minimized, where the data is averaged into 100 m vertical bins, or roughly the vertical resolution of WRF and height of the steepest vertical gradient of both quantities, normalized by the total range of θ and H_2O in the profile, is selected as the observed PBLH. Because the P3 never reaches into the surface layer, methods of deriving PBLH are limited. A total of 61 vertical P-3 profiles were available for PBLH validation and the comparison revealed a larger bias in the GM4 than the EM4N runs. The HSRL data allowed for a more comprehensive evaluation of the PBLH bias and variance, revealing a bias of 85 m and -5 m at 1000 m altitude for the GM4 and

EM4N PBLH estimates, respectively, in the Central Valley. This is consistent with the results of *Angevine et al.*, [2012] who also found a low PBLH bias at Chowchilla in the GM4 implementation of WRF. Biases in the South Coast Air Basin at 1000 m altitude were 85 m and 155 m for the GM4 and EM4N PBLH, respectively, also consistent with *Angevine et al.*, [2012] who reported slight degradation in Los Angeles basin with WRF runs using the Noah land surface model. Uncertainty in the HSRL measurements due to possible aerosol layers above the boundary layer makes it difficult to determine whether there is a bias in the WRF PBLH over the LA Basin. Attempts to filter out affected data resulted in too few remaining points to conclusively determine whether the bias was statistically different than zero. The biases are not explicitly used in the inversion error estimates, but are presented as a measure of accuracy in PBLH estimates. The standard deviation of the HSRL-WRF differences was ~400 m (40%) for both GM4 and EM4N configurations, of which 23% and 33% are attributable to errors in WRF and the HSRL retrievals, respectively. Average flight profiles show a mean enhancement of 47 ppb below 1000 m compared to above 1000 m altitude. We therefore use an error of 16 ppb for $\underline{\underline{S}}_{tran}$ (23% of 47ppb ≈ 11 ppb for the PBLH error and 10% of 47 ppb ≈ 5 ppb for the wind errors, respectively). Supplementary Material Section 4 presents the details of the PBLH comparisons.

$\underline{\underline{S}}_{part}$ accounts for the error attributed to using a finite number of particles for each receptor. By comparing CH_4 enhancements modeled for a range of 50–1000 particles released from each receptor, we observed that using 500 particles resulted in a 2.2% (95% C.I.) error on the enhancement, corresponding to an error of 1 ppb for $\underline{\underline{S}}_{part}$.

We approximate the error introduced by the boundary condition from the variance on the distribution of the 500 CH_4 values assigned at the last position (Lat/Alt/Time for the NOAA

curtain, and Lat/Lon/Alt/Time for GEOS-Chem boundary condition). The mean value of this term is 4 ppb for the NOAA-curtain and 8 ppb for GEOS-Chem. The latter term is larger because GEOS-Chem values are assigned explicitly for the Lat/Lon/Alt location while the NOAA-curtain values are assigned only along the ending Lat/Alt location on the curtain. We add this in quadrature to the variance of each distribution compared with HIPPO 3 data, which is 11 ppb and 7.8 ppb for NOAA and GEOS-Chem, respectively. The total $\underline{\underline{S}}_{boun}$ error is then ~12 ppb.

The two remaining sources of error, $\underline{\underline{S}}_{aggr}$ and $\underline{\underline{S}}_{foot}$, both result from having finite grid resolution of both the WRF model (4 km x 4 km) and the emission inventories (0.1° x 0.1° or worse in the case of county-specific emissions). We approximate $\underline{\underline{S}}_{aggr}$ by examining the difference in the dairy cow enhancements that are gridded at county scales and by dairy lat/lon locations. The residual variance of these two distributions for all receptors is 6 ppb.

Data aggregation (see Supplementary Material Section 1) was done in a way to minimize the correlated errors between neighboring receptors, and we therefore approximate off-diagonal elements as zero. When summed in quadrature, the total error is estimated as 23 ppb for each receptor, larger than the summertime model-data mismatch error of 15-20 ppb of *Jeong et al.* [2012]. The model-data mismatches range from 27 to 32 ppb, depending on the sub-selection, consistent with the estimates from individual error terms. We present inversion results using the model-data mismatch errors to populate $\underline{\underline{S}}_{\varepsilon}$ (e.g. we use 31 ppb for the CalGEM central valley inversion, which corresponds to an error of 1.7% using a background CH_4 concentration of 1800 ppb), noting that L-curve theory optimizes the *a priori* error relative to the model-data mismatch error (Supplementary Material Section 5).

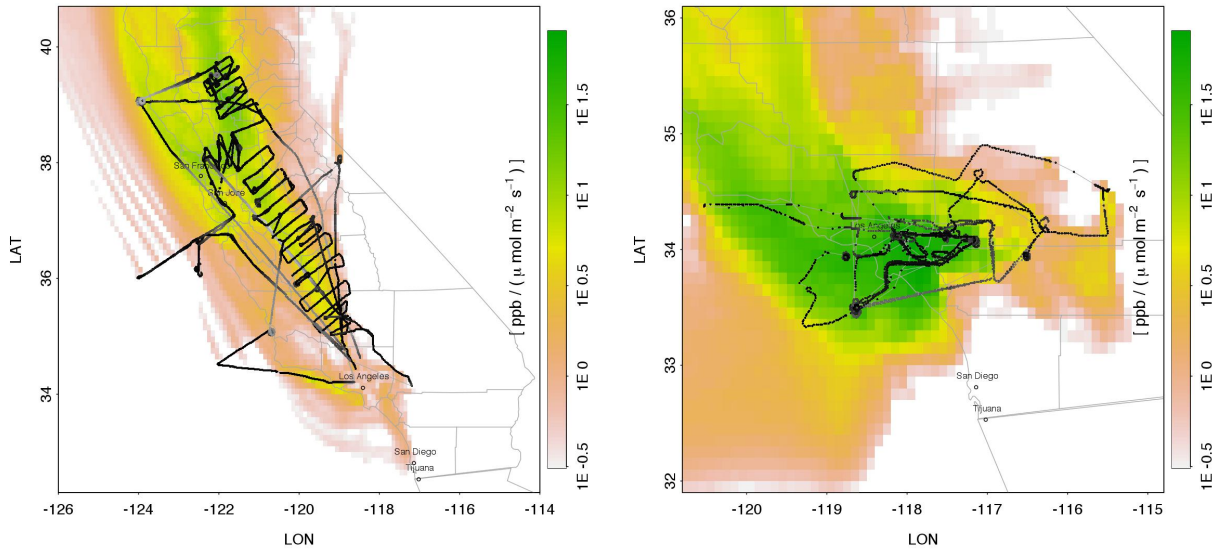

Figure 5.4: Cumulative footprints for the CV (left) and SoCAB (right) receptors.

5.4. Results and Discussion

Figure 5.4 show the cumulative footprints corresponding to the 6 Central Valley (CV) flights and 5 South Coast Air Basin (SoCAB) flights shown in Figures 5.1 and 5.2, respectively. The footprints shown represent the total modeled CH_4 enhancement in ppb that would be observed at the flight receptor locations assuming a uniform unit flux at the surface of 1000 *n*mol m^{-2} s^{-1}. Tabulating grid cells in which average modeled enhancements from a uniform unit flux over the 6 flights are 3 times the RMS of the NOAA curtain boundary condition over the measurements campaign (or > 51 ppb), we calculate that we are able to constrain 74 % of the surface area of the state, and 91 % of the total emissions when those 74% of grid cells are weighted by EDGAR 4.2 emissions. The SoCAB flights are sensitive to 100% of the SoCAB area and emissions alike.

Figure 5.5 shows the time series of the CH_4 measurements and model results for the CV and SoCAB flights, respectively, using the EM4N meteorology and the CalGEM emissions inventory. Figure 5.6 show the corresponding results plotted as vertical profiles. For each flight, we remove the first and last 100 receptors, corresponding to ~20 minutes of measurements taken during take off and landing, respectively. These zones are flight landing and takeoff zones and therefore cannot be faithfully modeled. Using footprints from STILT and the *a priori* emissions distributions from Figure 5.3 and Table 5.2a,b,c, we calculate modeled enhancement time series for each category of emissions. We then calculate variance inflation factors (VIFs), a measure of the co-linearity of the *a priori* emission distributions, combining terms that are highly correlated until the VIFs of each combined enhancement time series is < 5 and the different source contributions are deemed independent [*Jackson et al*., 2009]. Tables 5.2a, b, and c show the VIFs for the combinations of terms in the *a priori* emission inventories grouped by letter (A, B,

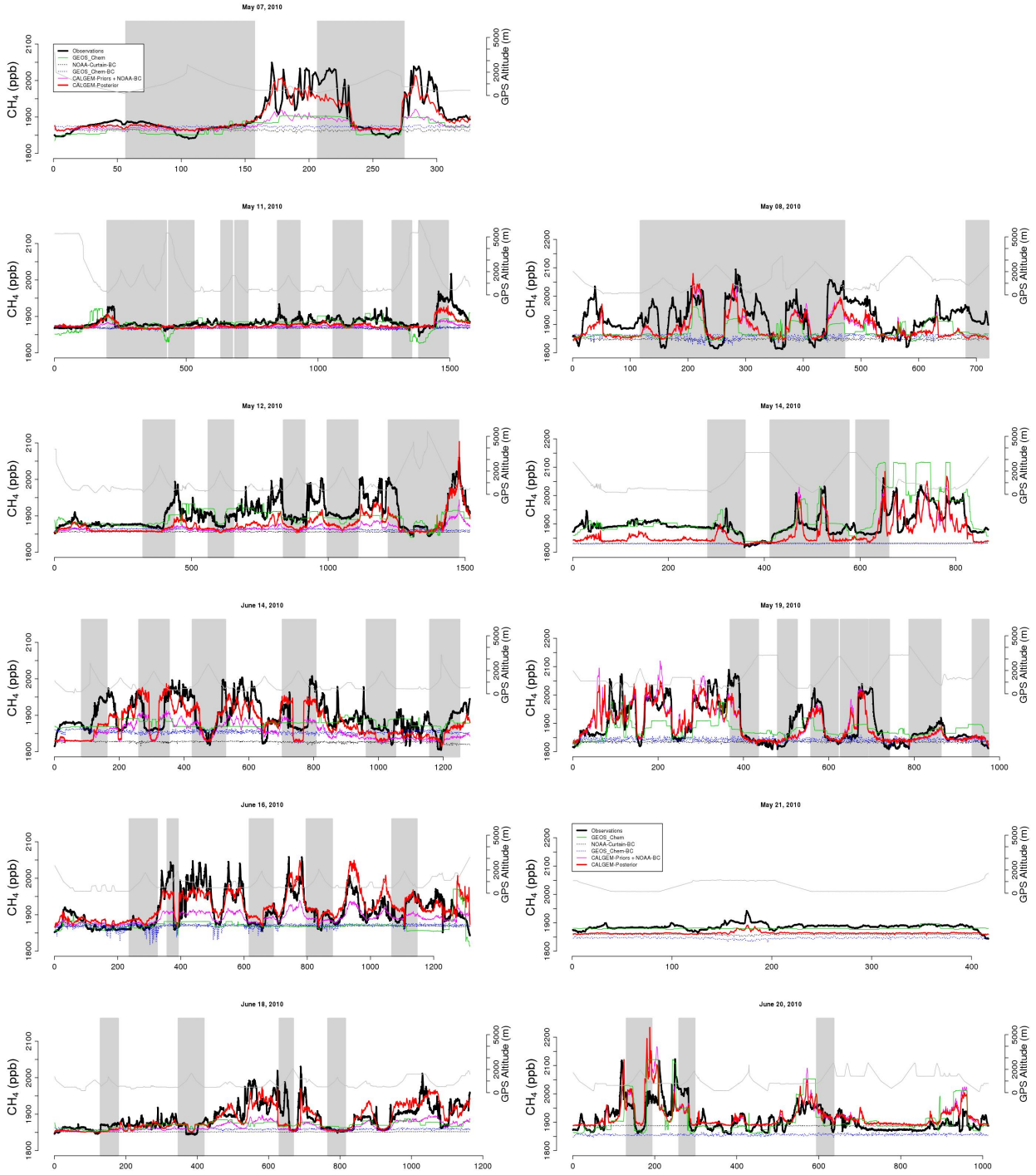

Figure 5.5: Time series of CH_4 for the 6 CV (left) and 5 SoCAB (right) flights along with the altitude trace. Modeled concentrations are shown in colors pre and post inversions. Only the NOAA curtain boundary condition based inversions are shown, but the GEOS-Chem boundary condition is shown (dotted black) to compare to the NOAA curtain boundary condition (dotted blue). The EDGAR-substituted inversions are not shown but represent a hybrid between the EDGAR and CalGEM inversions. GEOS-Chem modeled CH_4 concentrations at the receptors are shown in green and the locations of flight profiling have grey backing and correspond to the locations of the X's in Figures 5.1 and 5.2.

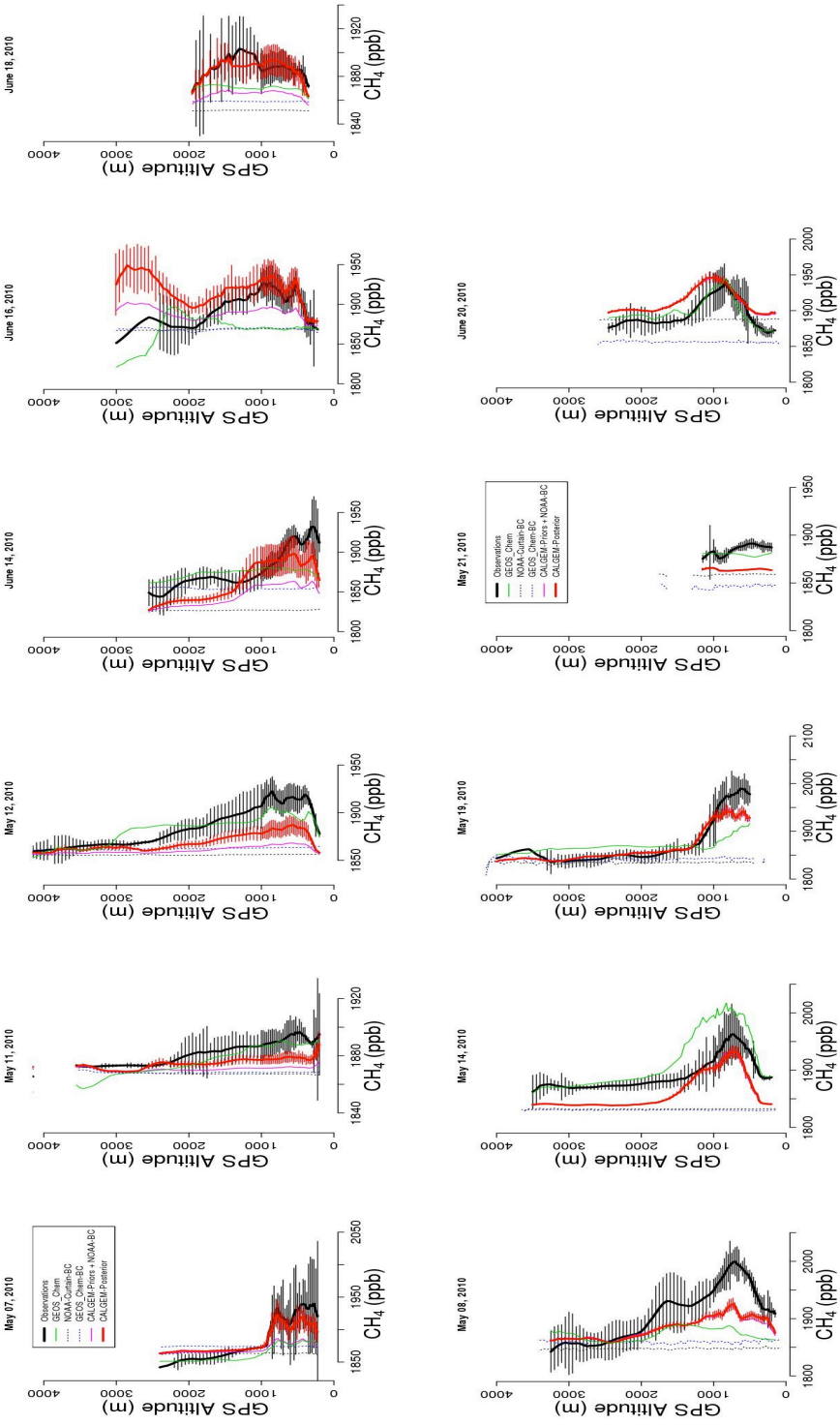

Figure 5.6: Mean vertical profiles for the CV (left) and SoCAB (right) flights using the same data from Figure 5.5. Error bars represent 2 standard deviations for the observations and the 95% confidence interval for the inversions.

C, etc.). Many emission categories, particularly those in EDGAR, have similar spatial distribution because they are constructed from emission factors that are population distribution dependent [*EC-JRC/PBL*, 2011; *Wunch et al.*, 2009]. Inversions done with all of these categories treated as independent basis-functions often result in negative (i.e. non-physical) scaling factors for certain categories to best match observations. In comparing Tables 5.2a,b,c, the number of combined enhancement terms (denoted A, B, C, etc. representing the n scaling factors in $\underline{\hat{\lambda}}$) is 3 for the EDGAR inversions and 5 for both the EDGAR-substituted and CalGEM inversions in the central valley. We note that for the EDGAR inversions we allow the VIFs of the weak emission sources (denoted "Rest") to exceed 5. In the South Coast Air Basin, the emission sources tend to be more collocated and therefore fewer source terms can be optimized independently (n=2 for the EDGAR inversions and n=3 for both the EDGAR-substituted and CalGEM inversions). Each of the 3 *a priori* emission inventory inversions (Table 5.2a,b,c) is done 16 times for the various combinations of GM4 and EM4N meteorology, GEOS-Chem and NOAA-curtain boundary conditions, and CV and SoCAB flights. Flight data is used to correct the biases in the boundary conditions (see below) but residual differences in the boundary conditions persist and are notable for some of the flights shown in Figures 5.5 and 5.6. Supplementary Material Section 6 includes figures corresponding to Figures 5.5 and 5.6 for the EDGAR and EDGAR-Substituted emission inventories.

The inversions that make use of the GEOS-Chem boundary condition result in scaling factors that correspond to posterior annual fluxes that are ~0.1-0.2 $TgCH_4$/yr lower than the inversions that use the NOAA-curtain boundary condition, or 7-13% of the 1.52 $TgCH_4$/yr CARB estimate. Without applying bias corrections to individual flights, the difference between the GEOS-Chem and NOAA-curtain boundary conditions inversions is ~0.5 $TgCH_4$/ yr, or almost 33% of the

budget. This stresses the importance of accurate boundary conditions in this type of inverse modeling. We assess the validity of each boundary condition by comparing the interpolated distributions of CH_4 along the HIPPO flight tracks on the latitudinal-altitudinal curtain at -145° W between 30° and 50° N and 500 to 7500 m altitude. GEOS-Chem is sampled at the grid-box of the flight track location and the NOAA curtain is loosely derived for -145° W. Applying the same 2-D (Lat/Alt) loess filter to each of the data sets, we compare the distributions of the residual differences between 1) GEOS-Chem and HIPPO and 2) NOAA-curtain and HIPPO for all 9 HIPPO transects which spanned the 2009-2011 time period to resolve any seasonal dependence on boundary condition biases (Supplementary Material Section 3). The distributions highlight the effect of transient synoptic-scale variability in CH_4 concentrations that both GEOS-Chem and the NOAA curtain have difficulty resolving. In aggregate, both (1) and (2) tend to be biased low by 8.6 and 7.6 ppb, respectively and the standard deviation of these distributions average 10 ppb.

Because the boundary condition differences are largely driven by synoptic events, we adjust for the bias of each boundary condition for a given day by filtering the CalNex CH_4 data to calculate free-tropospheric upwind CH_4 concentrations. We categorize the following receptors from the 11 CalNex flights analyzed as being representative of free-tropospheric upwind background conditions: measurements from altitudes > 2000 m with negligible surface footprints, defined as the set of receptors with modeled CH_4 enhancements < 0.1 ppb from a uniform unit flux of 1000 *n*mol m^{-2} s^{-1}, a flux that is much larger than any of the *a priori* flux estimates anywhere in California as seen in Figure 5.3. The mean of this *in situ* data (CH4.X in Table 5.4) is compared to the assigned boundary condition values for the *n* data receptors in each flight from the NOAA-curtain and GEOS-Chem boundary conditions showing the flight-to-flight

Table 5.4: Boundary condition offsets for different flights compared to measurements that did not see the surface.

	Flight Date	mean(CH4.X)	sd(CH4.x)	NOAA_Curtain B.C.	GEOS_Chem B.C.	NOAA offset	GEOS offset	SD(NOAA offset)	SD(GEOS-offset)	n	Mean Exit LAT	Mean Exit LON
Central Valley	507	1839.27	9.46	1835.13	1846.45	5.52	-3.01	8.92	9.48	248	39.04	-126.91
	511	1857.93	20.14	1847.68	1873.81	13.43	-9.97	19.44	19.87	226	43.76	-127.49
	512	1848.87	6.82	1848.25	1862.96	0.22	-13.21	7.37	8.04	108	47.27	-120.95
	614	1813.29	16.62	1838.01	1820.19	-26.14	-7.36	14.33	18.80	582	40.66	-127.93
	616	1857.61	8.29	1839.79	1853.97	16.90	-0.87	9.07	18.68	200	46.62	-128.58
	618	1832.75	30.45	1835.98	1833.47	0.32	-5.07	23.23	24.65	208	37.87	-127.04
Los Angeles	508	1825.01	14.10	1830.20	1837.16	-8.84	-13.74	12.08	12.75	326	35.11	-125.77
	514	1827.07	6.46	1847.11	1867.24	-21.31	-40.81	6.85	6.64	38	42.94	-120.73
	519	1814.83	17.86	1833.37	1828.89	-20.71	-12.59	17.20	15.92	213	37.02	-126.18
	521	1848.17	4.97	1844.02	1877.84	3.65	-31.47	6.38	9.54	10	38.66	-126.31
	620	1871.43	2.48	1831.47	1875.43	39.17	-8.54	5.74	12.82	106	35.77	-126.25
	Mean:	1839.66	12.51	**1839.18**	**1852.49**	**0.20**	**-13.33**	**11.87**	**14.29**	206	40.43	-125.83
	SD:	18.86		**6.66**	**20.46**	**19.20**	**12.19**			156	4.19	2.60

discrepancies between the two boundary conditions and the measurements representative of air parcels that have not been influenced by surface emissions. On average, the NOAA-curtain is less biased (0.2 vs. -13 ppb for GEOS-Chem) and has higher flight-to-flight variability (σ = 19 vs. 12 ppb). We perform the inversions after adding the individual flight-biases for each boundary condition from Table 5.4 to the measured enhancements (y in Equation 5.1) and filtering outliers in a similar manner to *Bergamaschi et al.* [2005] and *Jeong et al.* [2012].

Outliers are removed when the difference between the measured and predicted mixing ratios is > 123 ppb, or 3 times the standard deviation of the model-data mismatch using all the data (41 ppb). We do this because very fresh emissions associated with high concentrations are not well mixed in an atmospheric column are therefore not explicitly modeled by WRF-STILT. Because our goal is to invert for emission scaling factors, we also filter out data that is representative of the boundary condition, using the same < 0.1 ppb surface enhancement from the uniform flux over California used to identify the boundary condition biases. Of the 14658 receptors modeled over the 11 flights presented in Figures 5.5 and 5.6, 9892 and 4766 represent CV and SoCAB data, respectively. Filtering receptors whose footprints show little surface influence in our areas of interest removes ~25% of the receptors and filtering for model-data mismatches >123 ppb removes an additional 2% of the receptors so that the total filtered CV and SoCAB receptors number 6988 and 3743 for the inversions.

We present the results of the EDGAR 4.2, EDGAR-substituted, and CalGEM inversions in Tables 5.2a,b, and c, respectively, with errors in $\underline{\underline{S}}_{prior}$ corresponding to 15%, the optimized *a priori* error estimate from L-curve theory (Supplementary Material Section 5). Figure 5.7 compares the prior and posterior results corresponding to the CalGEM inversions in Table 5.2c. Confidence Intervals (C.I.'s) on the scaling factors are calculated as follows: 1) For each receptor

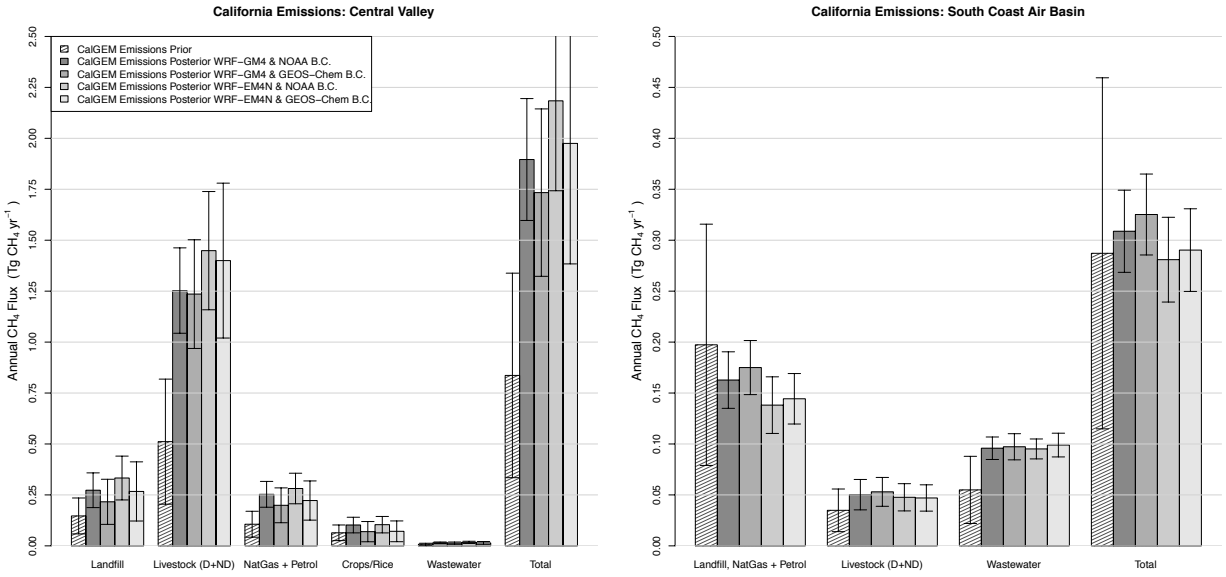

Figure 5.7: Optimized California CH_4 emissions for the CV and SoCAB using the CalGEM inventory. Corresponding total emissions are shown in Table 5.2c.

and each emission source, we bootstrap the enhancement for that particular source for the 500 trajectories and calculate the mean of the 500 resampled (with replacement) distributions and the standard deviation of those means, 2) For each set of inversions, we resample 1000 times with replacement both the background-subtracted measurements ($\underline{y}$) and the emission source enhancements ($\underline{\underline{K}}$), 3) For each flight and each of the 1000 resampled values of $\underline{y}$, we add random terms (6 terms for the CV and 5 terms for the SoCAB) of mean zero and standard deviation corresponding to the 'SD(NOAA-offset)' or 'SD(GEOS-offset)' in Table 5.4 to the ($\underline{y}$) values corresponding to each of the 5 or 6 flights, 4) For each element in each of the 1000 resampled values of $\underline{\underline{K}}$ we add a random term with mean zero and standard deviation of the bootstrapped enhancement distribution for a given emission source. The 95% C.I.'s on each source category is then represented as 2 times the standard deviation of the 1000 resampled inversion estimates. We note that had we omitted the error term corresponding to the boundary condition uncertainty in the inversion (step 3), C.I.'s are 30-60% lower than those reported alone, implying that uncertainty in the boundary condition leads to significant uncertainty in the inversion.

We redo all inversions for errors in $\underline{\underline{S}}_{prior}$ corresponding to 10%, 15%, 25%, 50%, and 75% uncertainties in the prior emissions distributions and present only those corresponding to 15% uncertainty in Table 5.2. The different prior uncertainties have minimal effects on the results and those differences are discussed in Supplementary Material Section 5. The C.I.'s on the fluxes reported in Table 5.2 represent an estimate of the precision of the modeled inversions, not the accuracy. The accuracy depends on any biases in the modeling introduced by seasonality and errors in PBLH, which we estimate to be 26% and 0-15% (depending on the meteorology), respectively, or 26-30% when summed in quadrature. We present confidence intervals in Table

5.2 based on the precision of the modeling techniques, but the budgets themselves have inaccuracies that are an additional 30%.

Several features of the different inversions merit discussion. The EDGAR 4.2 inversion results estimate California emissions at 2.4-2.8 ± 0.4-0.7 $TgCH_4$/yr depending on the meteorology and boundary condition chosen. As discussed by *Wunch et al.* [2009], many of the EDGAR emission categories are constructed based on population densities and emission factors. This explains why 'Gas Production and Distribution,' 'Waste Water,' and 'Solid Waste Disposal,' which wouldn't be expected to have the same source distribution patterns, are all strongly correlated with a mean VIF of 69. Because of this we are only able to invert for 3 scaling factors and the trace of the averaging kernel (a measure of the information content of the observing system) for this inversion is 1.7 in the CV and 1.1 in the SoCAB. Confidence intervals are especially large for the cattle-related and population-derived emission terms, each on the order of 0.3-0.4 $TgCH_4$/yr.

By replacing certain EDGAR 4.2 categories of emissions with California-specific inventories for cattle, rice, and landfill data, these terms become more spatially independent and a greater number of individual emissions categories can be optimized. For the EDGAR-substituted inversion in Table 5.2b, cattle terms (A), landfill emissions (B), and crop/rice emissions (D), are all optimized individually with VIFs all below 3 and the trace of the averaging kernel for this inversion is 2.9 in the CV and 1.9 in the SoCAB. Gas production and wastewater emissions (term C) do not in reality have similar spatial distributions, but are both EDGAR population-based categories and have a VIF of 4. We note that for this inversion, dairy cow emissions are distributed according to dairy locations, but other cattle and beef cow emissions are at county-scales. The inversion generates a scaling factor on these emissions of 2.0-2.2, resulting in a

posterior emission of ~1.2 ± 0.3 $TgCH_4$/yr in the CV. The allocation of these 1.2 $TgCH_4$/yr into the different sub-categories of cattle-related emissions requires finer spatial distributions of the other cattle, beef cows, and manure distributions. California dairy cows have been extensively studied [*Mitloehner et al.*, 2009], notably because they are corralled, but it should be stressed that only 1.75 of the 7.55 million head of cattle in California are dairy cows, and the emissions of other cattle are less well known. Likewise, the CH_4 emissions associated with manure management practices are poorly quantified and dependent on manure management practices, moisture, and other environmental variables [*Sommer et al.*, 2004].

Emissions from rice based on the work of *McMillan et al.*, [2007] have optimized uncertainties that are the largest as a percentage of the emissions magnitudes themselves, compared with other sources. The June 14th flight, which sampled above the northern CV in the early part of the growing season [*Peischl et al.*, 2012] where the majority of the rice agriculture is located, show that the prior fluxes in the middle of the flight match the observations better than the optimized results. The inclusion of other flights in the CV inversions is the reason that the rice emissions for the state using the CV data are estimated as 0.05-0.09 ± 0.04-0.06 $TgCH_4$/yr, slightly lower on average than the a priori estimate of 0.087 $TgCH_4$/yr. Individual inversions for that flight result in a scaling factor of 1.03, suggesting that the prior estimate constructed from planted rice acreage from the USDA is a reasonable emissions model. Day-to-day variability in CH_4 fluxes (such as those induced by water table depth in the case of rice or wetland emissions), however, is not a factor in these emission inventories and therefore more flight measurements over many days provides the necessary statistics for representative inversions at these scales.

The CalGEM inversions make use of the most spatially explicit distribution of CH_4 fluxes in California. Landfills (A), dairy and non-dairy cattle emissions (B), natural gas and petroleum

(C), crop/rice emissions (D), and wastewater emissions (E) are optimized individually and represent 0.41 ± 0.15, 1.47 ± 0.35, 0.28 ± 0.09, 0.09 ± 0.05, and 0.11 ± 0.02 $TgCH_4$/yr sources, respectively, according to the EM4N meteorology and the mean of the NOAA-curtain and GEOS-Chem boundary conditions. These represent 121%, 171%, 191%, 320%, and 125% (weighted mean = 160%) of CARB's current estimates for those sources, respectively. The C.I.'s for the CalGEM inversions are the lowest on average of any of the prior emission estimates, especially for the crop/rice, natural gas, and wastewater emissions, demonstrating the utility of improved spatial emission distributions in such modeling frameworks. The trace of the averaging kernel is 2.7 in the CV and 2.4 in the SoCAB. CalGEM represents an improvement in the spatial distributions of the different CH_4 sources when compared to the EDGAR-substituted inventory, itself representing an improvement over EDGAR.

The CalGEM inversion results in a total California CH_4 budget of 2.4 ± 0.52 (95% C.I.) $TgCH_4$/yr, or 1.6 ± 0.34 (95% C.I.) times the California Air Resources Board budget estimate of 1.52 $TgCH_4$/yr. Biases due to inaccuracies in meteorology and extrapolation to the full seasonal cycle add 30% to the reported 95% C.I. inversion precisions, making the total inversion accuracy estimate 2.4 ± 0.90 $TgCH_4$/yr (= 2*sqrt(2.4^2*.15^2 + 1^2*.26^2 + .26^2*.15^2)). CARB's current estimate of 1.52 $TgCH_4$/yr is therefore underestimated by a factor of 1.6 ± 0.34 (95% C.I. precision) and 1.6 ± 0.60 (95% C.I. accuracy).

Figure 5.8 compares the prior (left) and posterior (right) modeled enhancements for the CV and the SoCAB to the measurements showing the flight-by-flight (colors) and total (grey) fits using a type II regression. Errors in the abscissa are represented by the standard deviation of the 1 Hz CH_4 measurements averaged to each receptor point and errors in the ordinate are given by a combination of all the errors discussed in Section 3.4 for each modeled receptor [*York et al.*,

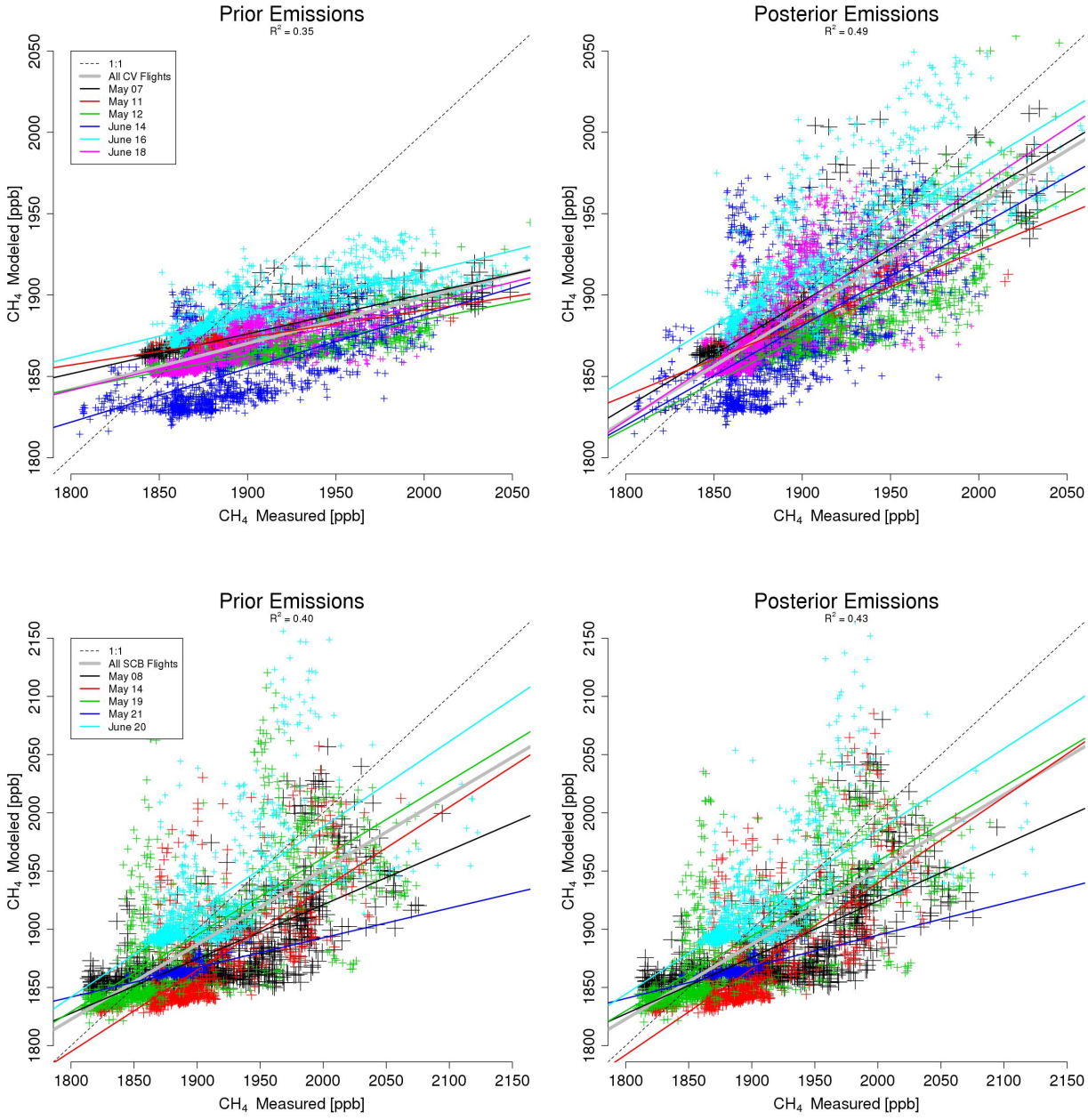

Figure 5.8: Measured and modeled concentrations for the CV (top) and SoCAB (bottom) flights pre (left) and post (right) optimization using the CalGEM emission inventories.

2004]. Figure 5.8 further highlights the need for numerous flights in constraining surface fluxes, as the day-to-day variability in the slope (colored lines) is almost 100% of the average (grey). Because of the improved spatial distributions of the *a priori* emissions estimates (compared to the EDGAR and EDGAR-Substituted emission inventories), the inversions improve the R^2 of the fit from 0.35 to 0.49 in the CV and show marginal improvement in the SoCAB.

As population demographics continue to shift towards cities, quantifying megacity carbon emissions have become interesting from a scientific and regulatory viewpoint. *Hsu et al.* [2008], *Wunch et al.* [2009], *Wennberg et al.* [2012], and, most recently, *Peischl et al.* [2013] have tried to quantify the CH_4 emissions from the LA Megacity. They arrived at emissions estimates of 0.38 ± 0.1 (value from *Wennberg et al.* [2012] using adjusted CO emissions for 2007/8), 0.6 ± 0.1, 0.44 ± 0.1, and 0.41 ± 0.1 $TgCH_4$/yr respectively. In comparison, we derive SoCAB budgets of 0.32 ± 0.04, 0.35 ± 0.05 and 0.29 ± 0.04 using the EDGAR, EDGAR-substituted and CalGEM emission priors, respectively, and the EM4N meteorology. These results agree within error, falling on the lower end of the reported ranges. The inversion results that use the GM4 meteorology are on average 0.03 $TgCH_4$/yr higher, consistent with slightly lower PBLH values in EM4N relative to GM4 (Supplementary Material Section 4).

Previous estimates were derived from measuring the ratio of CH_4 to CO and relying on the accuracy of the CO inventory, inherently convolving errors from both the CO emissions inventory and the assumption that the sources are well mixed and have similar spatial structures into the estimate. We note that CO emissions, which are largely driven by emissions from the on-road gasoline fleet, are dependent on the efficiency of the fleet of vehicles on the road [*Harley et al.*, 2001]. Continuing changes in CO emissions (e.g. Parrish et al., [2006]) that are not reflected in inventories can explain some of the discrepancy between emissions inventories

such as EDGAR and CARB [*Wunch et al.*, 2009]. In contrast, WRF-STILT simulates the CH_4 observations independent of CO inventories, as seen in Figures 5.5 and 5.6. Though data from certain areas offshore point to atmospheric dynamics in the model that are not present in the real atmosphere (see e.g. the modeled enhancements offshore on May 14 that do not exist in the data), the model simulates the observations reasonably well with an $R^2 = 0.40$ (Figure 5.8), which improves to 0.43 after the inversion.

The EDGAR inversions show that EDGAR CH_4 emissions are overestimated by nearly a factor of 2 for the SoCAB (Supplementary Material Section 6). When the EDGAR-substituted and CalGEM inventories are used, we are able to quantify the relative contribution of specific CH_4 sources. Cattle emissions appear to be underestimated by a factor of 1.3-2.0, consistent with the cattle emission scaling factors in the rest of the state. Both the EDGAR-substituted and CalGEM inversions generate consistent estimates of the cattle emissions in the SoCAB of ~0.05 $TgCH_4$/yr. The comparisons between the estimates of other source sectors, however, are less consistent. The EDGAR-substituted inversions attribute ~0.08 $TgCH_4$/yr to landfill emissions, while the CalGEM inversions estimate them as ~0.12 $TgCH_4$/yr, using the weighting of the prior flux estimates to scale the optimized category (i.e. $0.12 = 0.155 \times (0.157 / 0.197)$ from Table 5.1). Natural gas emissions have even greater disagreement, with the EDGAR-substituted inversions estimating emissions as ~0.15 $TgCH_4$/yr compared to ~0.03 $TgCH_4$/yr for the CalGEM inversions. Wastewater emissions are ~0.06 and ~0.10 for the EDGAR-substituted and CalGEM inversions, respectively. Because of the collinearity of many sources in the SoCAB, inverting for independent sources such as NG leaks is difficult. While individual sources are hard to distinguish, the different inversions constrain SoCAB emissions of CH_4 to range from

0.28 – 0.39 $TgCH_4$/yr, roughly 10-25% lower than the central values given in previous work, but consistent within errors.

5.5. Conclusion

We estimate California's CH_4 budget to be 2.4 ± 0.90 (95% C.I.) $TgCH_4$/yr after accounting for both errors associated with the precision of our inversions (± 0.52 $TgCH_4$/yr) and errors associated with extrapolating 11 days of measurements to the annual cycle (± 0.72 $TgCH_4$/yr). This is likely a conservative estimate of the overall error. CARB's current CH_4 budget is 1.52 $TgCH_4$/yr, indistinguishable from, but falling on the edge of, our 95% confidence interval. Our estimate suggests that CARB's budget should be scaled up by a factor of 1.6 ± 0.60 (95% C.I.). The underestimate in the CARB inventory is associated with cattle and manure (68% of the total underestimate) and natural gas (15%). Rice emissions, while underestimated by more than a factor of 3 by CARB, account for only 7% of the total underestimate.

In order to fulfill the goals set forth in AB-32, better *a priori* emission estimates, with accurate spatial distributions (of at least 0.1 x 0.1, if not better) of CH_4 sources and their seasonality, need to be developed and tracked by CARB. Continued measurements are also needed. We emphasize the importance of aircraft measurements at altitudes >2000 m and upwind in the marine boundary layer and free troposphere to constrain the boundary conditions for air entering California and to characterize uncertainties associated with meteorological transport. The precision of our inversion estimate is very robust, largely because these comprehensive measurements were made concurrently during CalNex. The largest contributor to our annual budget error is the uncertainty associated with extrapolation to a full seasonal cycle. A network of towers making continuous measurements of CH_4 would provide much tighter constraints than those given here. We demonstrate that the CalNex flights resulted in

measurement footprints that were sensitive to nearly 91% of California's emissions and 100% of the South Coast Air Basin emissions. Supplemented with a network of towers, to better capture seasonality of emissions, repeated flights every few years over a larger seasonal window would allow accurate tracking of the progress towards AB 32.

Acknowledgements: We would like to thank all the pilots and aircraft technicians of the NOAA P-3 (CalNex) and the NCAR GV (HIPPO) as well as many NOAA collaborators that made the CalNex measurements possible. We acknowledge the NOAA/ESRL Carbon Cycle Group Aircraft Network which provided critical information on background CH_4 mole fractions for this study. This work was supported by the following grants to Harvard University: NASA NNX09AJ94G, NNX11AG47G, and NNX09AU40G, NSF ATM-083091-2, NOAA NA09OAR4310122, and NA11OAR4310158. We thank the NASA Advanced Supercomputing Division for their generous computing support. GWS acknowledges support from the NSF Graduated Research Fellowship Program and the EPA Science to Achieve Results Fellowship. EAK thanks the W. M. Keck Institute for Space Studies for support and notes that portions of this work were performed at the Jet Propulsion Laboratory, California Institute of Technology, under contract with NASA. MLF and SJ acknowledge support from the California Energy Commission (CEC) Public Interest Environmental Research, the California Air Resources Board, and the LBNL Laboratory Directed Research programs through the US Dept. of Energy under contract No. DE-AC02-05CH11231. The WRF-STILT development at AER has been funded by the NSF Atmospheric Chemistry Program (grant ATM-0836153). HSRL operations were supported by the NASA Science Mission Directorate, the Department of Energy Atmospheric Systems Research program (Interagency Agreement DE-AI02-05ER63985), the Office of Science, Office of Biological and Environmental Research (OBER), and the NASA CALIPSO project. The authors would also like to thank the NASA Langley King Air B-200 flight crew for their outstanding work supporting these flights and measurements.

References

A. E. Andrews, J. D. Kofler, M. E. Trudeau, J. C. Williams, D. H. Neff, K. A. Masarie, D. Y. Chao, D. R. Kitzis, P. C. Novelli , C. L. Zhao, E. J. Dlugokencky, P. M. Lang, M. J. Crotwell, M. L. Fischer, M. J. Parker, J. T. Lee, D. D Buamann, A. R. Desai, C. O. Stanier, S. F. J. de Wekker, D. E. Wolfe, J. W. Munger, and P. P. Tans (2013) CO_2, CO and CH_4 measurements from the NOAA Earth System Research Laboratory's Tall Tower Greenhouse Gas Observing Network: instrumentation, uncertainty analysis and recommendations for future high-accuracy greenhouse gas monitoring efforts, *Atmospheric Measurement Techniques*, 6, 1461-1553, doi:10.5194/amtd-6-1461-2013.

Angevine, W.M., Eddington, L., Durkee, K., Fairall, C., Bianco, L., Brioude, J. (2012) Meteorological model evaluation for CalNex 2010, Monthly Weather Review, 140, 3885–3906, doi:10.1175/MWR-D-12-00042.1.

ARB (2011) California's 2000-2009 Greenhouse Gas Emissions Inventory Technical Support Document, Planning and Technical Support Division. http://www.arb.ca.gov/app/ghg/2000_2009/ghg_sector.php, http://www.arb.ca.gov/cc/inventory/pubs/reports/ghg_inventory_00-09_report.pdf

Assembly Bill 32 (AB32) California Global Warming Solutions Act (2006) http://www.leginfo.ca.gov/pub/05-06/bill/asm/ab_0001-0050/ab_32_bill_20060927_chaptered.pdf

Bergamaschi, P., M. Krol, F. Dentener, A. Vermeulen, F. Meinhardt, R. Graul, M. Ramonet, W. Peters, and E. J. Dlugokencky (2005), Inverse modelling of national and European CH4 emissions using the atmospheric zoom model TM5, *Atmos. Chem. Phys.,* **5,** 2431–2460.

P. Bergamaschi, C. Frankenberg, J. F. Meirink, M. Krol, F. Dentener, T. Wagner, U. Platt, J. O. Kaplan, S. Körner, M. Heimann, E. J. Dlugokencky, and A. Goede (2007), Satellite chartography of atmospheric methane from SCIAMACHY on board ENVISAT: 2. Evaluation based on inverse model simulations, J. Geophys. Res., 112, D02304, doi:10.1029/2006JD007268.

Boadi, D. A. and K. M. Wittenberg (2001), Methane production from dairy and beef heifers fed forages differing in nutrient density using the sulphur hexafluoride (SF6) tracer gas technique. *Canadian Journal of Animal Science,* 201-206.

Brioude, J., S.-W. Kim, W. M. Angevine, G. J. Frost, S.-H. Lee, S. A. McKeen, M. Trainer, F. C. Fehsenfeld, J. S. Holloway, T. B. Ryerson, E. J. Williams, G. Petron, and J. D. Fast (2011), Top-down estimate of anthropogenic emission inventories and their interannual variability in Houston using a mesoscale inverse modeling technique, *J. Geophys. Res.*, 116, D20305, doi:10.1029/2011JD016215.

CARB (California Air Resources Board): AB 32 fact sheet: California Global Warming Solutions Act of 2006, 25 Sept 2006, http://www.arb.ca.gov/cc/factsheets/ab32factsheet.pdf.

CARB (California Air Resources Board): Implementation timeline , California Global Warming Solutions Act of 2006, 7 April 2009, http://www.arb.ca.gov/cc/factsheets/ab32timeline.pdf.

Ellis, J. L., A. Bannink, J. Frange, E. Kebreab, and J. Dijkstra (2010) Evaluation of enteric methane prediction equations for dairy cows used in whole farm models, *Global Change Biology*, 16, 3246–3256, doi: 10.1111/j.1365-2486.2010.02188.x.

European Commission (EC), Joint Research Centre (JRC)/Netherlands Environmental Assessment Agency (PBL). Emission Database for Global Atmospheric Research (EDGAR), release version 4.2. http://edgar.jrc.ec.europa.eu, 2011.

Farr, T. G., et al. (2007), The Shuttle Radar Topography Mission, *Rev. Geophys*., 45, RG2004, doi:10.1029/2005RG000183.

Fast, J. D., W. I. Gustafson, L. K. Berg, W. J. Shaw, M. Pekour, M. Shrivastava, J. C. Barnard, R. A. Ferrare, C. A. Hostetler, J. A. Hair, M. Erickson, B. T. Jobson, B. Flowers, M. K. Dubey, S. Springston, R. B. Pierce, L. Dolislager, J. Pederson, and R. A. Zaveri (2012) Transport and mixing patterns over Central California during the carbonaceous aerosol and radiative effects study [CARES]. *Atmos. Chem. Phys*., 12, 1759-1783.

Gerbig, C., J. C. Lin, S. C. Wofsy, B. C. Daube, A. E. Andrews, B. B. Stephens, P. S. Bakwin, and C. A. Grainger (2003), Toward constraining regional-scale fluxes of CO2 with atmospheric observations over a continent: 2. Analysis of COBRA data using a receptor-oriented framework, *J. Geophys. Res.,* 108(D24), 4757, doi:10.1029/ 2003JD003770.

Gourdji, S. M., K. L. Mueller, V. Yadav, D. N. Huntzinger, A. E. Andrews, M. Trudeau, G. Petron, T. Nehrkorn, J. Eluszkiewicz, J. Henderson, D. Wen, J. Lin, M. Fischer, C. Sweeney, and A. M. Michalak (2012), North American CO2 exchange: inter-comparison of modeled estimates with results from a fine-scale atmospheric inversion. *Biogeosciences*, 9, 458-475.

Goldsmith, C. D., J. Chanton, T. Abichou, N. Swan, R. Green, and G. Hater (2012) Methane emissions from 20 landfills across the United States using vertical radial plume mapping, *Journal of the Air & Waste Management Association*, 62 (2), 183-197.

Hansen, P. C. (2001), The L-curve and its use in the numerical treatment of inverse problems, in *Computational Inverse Problems in Electrocardiology*, edited by P. Johnston, pp. 119–142, WIT Press, Southampton, U. K.

Harley, R.A., McKeen, S.A., Pearson, J., Rodgers, M.O., Lonneman, W.A. (2001) Analysis of motor vehicle emissions during the Nashville/Middle Tennessee ozone study, *Journal of Geophysical Research*, 106 (D4), 3559–3567.

Hsu, Y.K., T. VanCuren, S. Park, C. Jakober, J. Herner, M. FitzGibbon, D. R. Blake, D. D. Parrish (2010) Methane emissions inventory verification in sourthern California, *Atmospheric Environment*, 44, 1-7.

Jackson, L. S., N. Carslaw, D. C. Carslaw, and K. M. Emmerson (2009) Modelling trends in OH radical concentrations using generalized additive models, *Atmospheric Chemistry and Physics*, 9, 2021-2033.

Jeong, S., C. Zhao, A. E. Andrews, L. Bianco, J. M. Wilczak, and M. L. Fischer (2012) Seasonal variation of CH4 emissions from central California, *Journal of Geophysical Research*, 117, D11306, doi:10.1029/2011JD016896.

Johnson, K. A. and D. E. Johnson (1995) Methane emissions from cattle, *Journal of Animal Science*, 73, 2483-2492.

Kitanidis, P. K (1997) Introduction to Geostatistics, Cambridge University Press.

Kort, E. A., J. Eluszkiewicz, B. B. Stephens, J. B. Miller, C. Gerbig, T. Nehrkorn, B. C. Daube, J. O. Kaplan, S. Houweling, and S. C. Wofsy (2008), Emissions of CH4 and N2O over the United States and Canada based on a receptor-oriented modeling framework and COBRA-NA atmospheric observations, *Geophy. Res. Lett.,* **35,** L18808, doi:10.1029/2008GL034031.

Kort, E. A., S. C. Wofsy, B. C. Daube, M. Diao, J. W. Elkins, R. S. Gao, E. J. Hintsa, D. F. Hurst, R. Jimenez, F. L. Moore, J. R. Spackman, and M. A. Zondlo (2012) Atmospheric observations of Arctic Ocean methane emissions up to 82° north, *Nature Geoscience*, 5, doi:10.1038/NGEO1452.

Lin, J. C., C. Gerbig, S. C. Wofsy, A. E. Andrews, B. C. Daube, K. J. Davis, and C. A. Grainger (2003) A near-field tool for simulating the upstream influence of atmospheric observations: The Stochastic Time-Inverted Lagrangian Transport (STILT) model, *J. Geophys. Res.,* 108(D16), 4493, doi:10.1029/2002JD003161.

Lin, J. C., C. Gerbig, S. C. Wofsy, A. E. Andrews, B. C. Daube, C. A. Grainger, B. B. Stephens, P. S. Bakwin, and D. Y. Hollinger (2004), Measuring fluxes of trace gases at regional scales by Lagrangian observations: Application to the CO2 Budget and Rectification Airborne (COBRA) study, J. Geophys. Res., 109, D15304, doi:10.1029/2004JD004754.

Lin, J. C. and C. Gerbig (2005) Accounting for the effect of transport errors on tracer inversions, *Geophys. Research Letters,* 32, L01802, doi:10.1029/2004GL021127.

Liu, S., and X. Liang (2010) Observed Diurnal Cycle Climatology of Planetary Boundary Layer Height, *Journal of Climate*, 23, doi: 10.1175/2010JCLI3552.1.

McMillan, A. M. S., M. L. Goulden, and S. C. Tyler (2007) Stoichiometry of CH4 and CO2 flux in a California rice paddy, *J. Geophys. Res.,* 112, G01008, doi:10.1029/2006JG000198.

Miller, S. M., E. A. Kort, A. I. Hirsch, E. J. Dlugokencky, A. E. Andrews, X. Xu, H. Tian, T. Nehrkorn, J. Eluszkiewicz, A. M. Michalak, and S. C. Wofsy (2012) Regional sources of nitrous oxide over the United States: Seasonal variation and spatial distribution, *Journal of Geophysical Research*, 117, D06310, doi:10.1029/2011JD016951.

Miller, S.M., Matross, D. M., Andrews, A. E., Millet, D. B., Longo, M. , Gottlieb, E. W., Hirsch, A. I., Gerbig, C. , Lin, J. C. , Daube, B. C. , Hudman, R. C. , Dias, P. L. S. , Chow, V. Y., and Wofsy S. C. (2008) Sources of carbon monoxide and formaldehyde in North America determined from high-resolution atmospheric data, *Atmos. Chem. Phys.*, 8 (24), 7673.

Mitloehner, F. M., H. Sun, and J. F. Karlik (2009) Direct measurements improve estimates of dairy greenhouse-gas emissions. *California Agriculture* 63(2):79-83. DOI: 10.3733/ca.v063n02p79.

Montzka, S. A., E. J. Dlugokencky, J. H. Butler (2011) Non-CO2 greenhouse gases and climate change. *Nature,* doi 10.1038/nature10322.

Nehrkorn, T., J. Eluszkiewicz, S. C. Wofsy, J. C. Lin, C. Gerbig, M. Longo, S. Freitas (2010) Coupled weather research and forecasting–stochastic time-inverted lagrangian transport (WRF–STILT) model, *Meteorol Atmos Phys*, 107:51–64 doi10.1007/s00703-010-0068-x.

NOAA, California Air Resources Board, California Energy Commission: 2010 CalNex White Paper, 9 Jan 2008, http://www.esrl.noaa.gov/csd/calnex/whitepaper.pdf, 2008.

Olivier, J. G. J., J. A. Van Aardenne, F. Dentener, L. Ganzeveld, and J. A. H. W. Peters, Recent trends in global greenhouse gas emissions: Regional trends and spatial distribution of key sources, in Non-CO_2 Greenhouse Gases (NGGG-4), pp. 325, 330, Mill press, Rotterdam, Netherlands, 2005.
http://edgar.jrc.ec.europa.eu/Main_differences_between_EDGARv42_and_v41.pdf

Peischl, J. T. B. Ryerson, J. S. Holloway, M. Trainer, A. E. Andrews, E. L. Atlas, D. R. Blake, B. C. Daube, E. J. Dlugokencky, M. L. Fischer, A. H. Goldstein, A. Guha, T. Karl, J. Kofler, E. Kosciuch, P. K. Misztal, A. E. Perring, I. B. Pollack, G. W. Santoni, J. P. Schwarz, J. R. Spackman, S. C. Wofsy, and D. D. Parrish (2012) Airborne observations of methane emissions from rice cultivation in the Sacramento Valley of California, *Journal of Geophysical Research*, 117, D00V25, doi:10.1029/2012JD017994.

Peischl, J., T. B. Ryerson, K. C. Aikin, A. E. Andrews, E. Atlas, D. Blake, J. Brioude, B. C. Daube, J. A. de Gouw, E. Dlugokencky, G. J. Frost, D. R. Gentner, J. B. Gilman, A. H. Goldstein, R. A. Harley, J. S. Holloway, J. Kofler, W. C. Kuster, P. M. Lang, P. C. Novelli, G. W. Santoni, M. Trainer, S. C. Wofsy, and D. D. Parrish (2013) Quantifying sources of methane using light alkanes in the Los Angeles Basin, California, *submitted*.

Pickett-Heaps, C. A., D. J. Jacob, K. J. Wecht, E. A. Kort, S. C. Wofsy, G. S. Diskin, D. E. J. Worthy, J. O. Kaplan, I. Bey, and J. Drevet: Magnitude and seasonality of wetland methane emissions from the Hudson Bay Lowlands (Canada), *Atmos. Chem. Phys.,* 11, 3773-3779, doi:10.5194/acp-11-3773-2011, 2011.

Potter, C., S. Klooster, S. Hiatt, M. Fladeland, V. Genovese, and P. Gross (2006), Methane emissions from natural wetlands in the United States: Satellite-derived estimation based on ecosystem carbon cycling, *Earth Interact.*, 10, 1–12, doi:10.1175/EI200.1.

Salas, W., C. Li, F. Mitloehner, and J. Pisano (2008), Developing and applying process based models for estimating greenhouse gas and air emission from California dairies, PIER Energy Relat. Environ. Res. Rep. CEC-500-2008-093, Calif. Energy Comm., Sacramento.

Scarino, M. D. Obland, J. D. Fast, S. P. Burton, R.A. Ferrare, C. A. Hostetler, L. K. Berg, B. Lefer, C. Haman, J. W. Hair, R. R. Rogers, C. Butler, A. L. Cook, D. B. Harper, Comparison of

Mixed Layer Heights from Airborne High Spectral Resolution Lidar, Ground-based Measurements, and the WRF-Chem Model during CalNex and CARES, *to be submitted to ACP*, 2013.

Skamarock, W. C., J. B. Klemp, J. Dudhia, D. O. Gill, D. M. Barker, M. G. Duda, X. Huang, W. Wang, and J. G. Powers (2008), A description of the advanced research WRF version 3, Technical Note 475+STR, 133 pp, National Center for Atmospheric Research, Boulder, Colorado.

Solid Waste Information System (SWIS) of CalRecycle (2011) http://www.calrecycle.ca.gov/SWFacilities/Directory/

Sommer, S. G., S. O. Petersen, and H. B. Moller (2004) Algorithms for calculating methane and nitrous oxide emissions from manure management, *Nutrient Cycling in Agroecosystems,* 69, 143-154.

United States Department of Agriculture (USDA) National Agricultural Statistics Service (NASS) Quick Statistics (2012) http://www.nass.usda.gov/Quick_Stats/.

United States Environmental Protection Agency (US-EPA). Inventory of U.S. Greenhouse Gas Emissions and Sinks: 1990-2010-Annexes (2012) http://www.epa.gov/climatechange/Downloads/ghgemissions/US-GHG-Inventory-2012-Annexes.pdf

van der Werf, G. R., Randerson, J. T., Giglio, L., Collatz, G. J., Mu, M., Kasibhatla, P. S., Morton, D. C., DeFries, R. S., Jin, Y., and van Leeuwen, T. T.: (2010) Global fire emissions and the contribution of deforestation, savanna, forest, agricultural, and peat fires (1997–2009), *Atmos. Chem. Phys.,* 10, 11707-11735, doi:10.5194/acp-10-11707-2010.

van Vuuren, D. P., J. Weyant, F. de la Chesnaye (2006) Multi-gas scenarios to stabilize radiative forcing, *Energy Economics*, 28, 102-120, doi:10.1016/j.eneco.2005.10.003.

van Vuuren, D. P., E. Stehfest, M. G. J. den Elzen, J. van Vliet, M. Isaac (2010) Exploring IMAGE model scenarios that keep greenhouse gas radiative forcing below 3 W/m2 in 2100, *Energy Economics*, 32, 1105-1120, doi:10.1016/j.eneco.2010.03.001.

Wennberg, P. O. W. Mui, D. Wunch, E. A. Kort, D. R. Blake, E. L. Atlas, G. W. Santoni, S. C. Wofsy, G. S. Diskin, S. Jeong, and M. L. Fischer (2012) On the Sources of Methane to the Los Angeles Atmosphere, *Environmental Science and Technology,* 46, 9282−9289.

Westberg, H., B. Lamb, K. A. Johnson, and M. Huyler (2001) Inventory of methane emissions from U. S. cattle. *Journal of Geophysical Research-Atmospheres* 106(D12): 12633-12642.

Wofsy, S. C., et al. (2011) HIAPER Pole-to-Pole Observations (HIPPO): Fine grained, global scale measurements for determining rates for transport, surface emissions, and removal of climatically important atmospheric gases and aerosols*, Phil. Trans. of the Royal Society A,* 369(1943), 2073-2086.

Wunch, D., P. O. Wennberg, G. C. Toon, G. Keppe-Aleks, and Y. G. Yavin (2009) Emissions of greenhouse gases from a North American megacity, *Geophysical Research Letters* 36 L L15810, doi:10.1029/2009GL039825.

Xiang B., S. M. Miller, E. A. Kort, G. W. Santoni, B. C. Daube, R. Commane, W. M. Angevine, T. B. Ryerson, M. K. Trainer, A. E. Andrews, T. Nehrkorn, H. Tian and S. C. Wofsy (2013) Nitrous oxide (N2O) emissions from California based on 2010 CalNex airborne measurements, *J. Geophys. Res. Atmos*. 118, doi: 10.1029/2012JD018244.

York, D., N. M. Evensen, M. L. Martinez, and J. D. B. Delgado (2004) Unified equations for the slope, intercept, and standard errors of the best straight line, *Am. J. Phys.,* 3, DOI: 10.1119/1.1632486.

Zhao, C., A. E. Andrews, L. Bianco, J. Eluszkiewicz, A. Hirsch, C. MacDonald, T. Nehrkorn, and M. L. Fischer (2009) Atmospheric inverse estimates of methane emissions from Central California, *J. Geophys. Res.,* 114, D16302, doi:10.1029/2008JD011671.

Appendix

S1. Data-averaging:

Flights averaged 6-8 hours in duration. Because atmospheric variability of long-lived trace gases such as CH_4 is relatively low in many parts of the atmosphere, 1-Hz data is autocorrelated, especially in the absence of nearby sources. We fit spherical and exponential semi-variograms to the 1-Hz CH_4 data in two dimensions: the lat-lon plane and altitude [Kitanidis 1997]. A total of 133 vertical profiles, defined as sustained increases or decreases in altitude over a minimum vertical extent of 1300 meters, were captured over the 6 flights in the Central Valley. The median semi-variogram model range using the 1-Hz CH_4 data was 160 ± 90 m. We chose to average data to 1/3 of this lengthscale. Because a significant relationship existed between the semi-variogram range and the mean altitude of the profile, we aggregated profile data under two regimes: data below 1000 m was averaged in 25 m vertical bins and data above 1000 m was averaged in 50 m bins. Data not included in vertical profiles was broken into 20 minute intervals over which the lat-lon semi-variogram model was fit to the data, resulting in a median horizontal range of 22 ± 10 km. Average aircraft speed during the flights was ~100 m/s, suggesting that to cover 7 km (1/3 of the lengthscale) would require ~70 seconds of flight. Averaging non-profile data into 70 second bins arbitrarily gave more weight to profile data in modeling applications, so we averaged level-flight data to 20 seconds instead, preserving the proportion of profile and level-flight that existed in the 1 Hz data. This averaging resulted in a ~17 fold decrease in the number of data points (receptors) that were modeled in the analysis.

S.2 Nested WRF domains

Supplementary Figure S1 shows the locations of the d02 (left) and d03 (right) WRF grids used in both the GM4 and EM4N runs. PBLH values on June 16th, 2010 at UTC 18:00 are

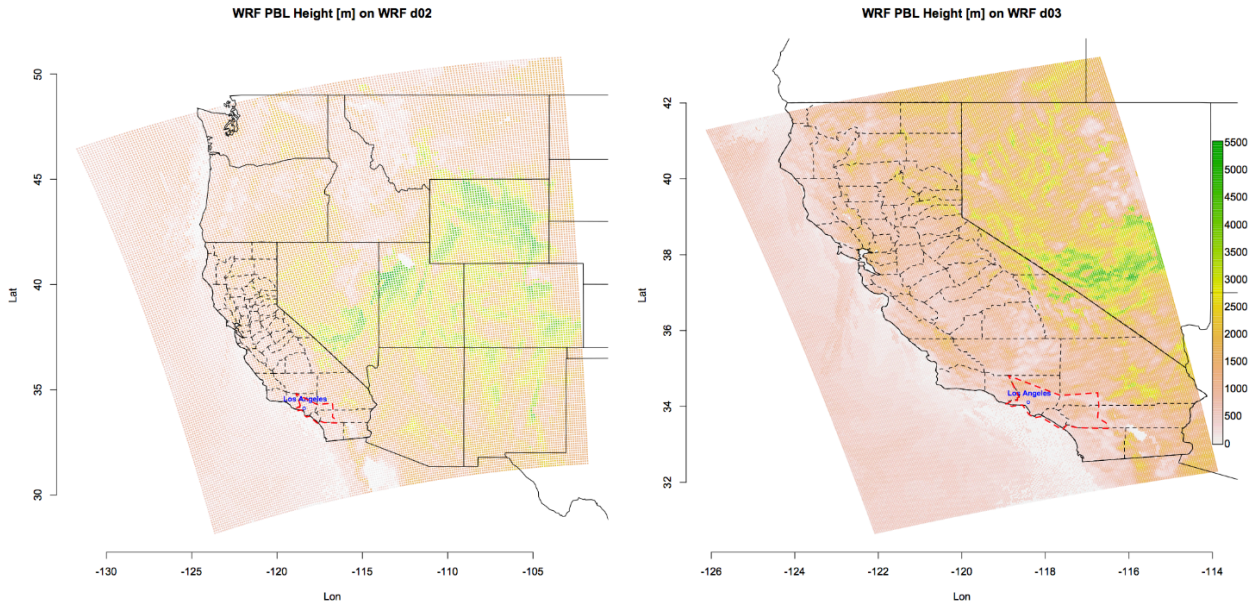

Figure S1: WRF nested domains.

plotted with the same character expansion to illustrate the model resolution of 12 km and 4 km for the d02 and d03, respectively.

S3. Boundary condition comparisons with HIPPO data.

Inaccuracies in the boundary conditions are a major source of error in a Lagrangian meso-scale modeling frameworks. This work provides a detailed comparison of boundary condition biases and errors using the HIPPO flight campaign [*Wofsy et al.*, 2011]. Supplementary Figure S2 shows 9 rows of plots corresponding to the flight paths of the 9 HIPPO transects over the Pacific. The first column shows the flight path for each HIPPO, with the southbound legs shown in green, and the northbound legs shown in red. The second column shows a loess smoothed Altitudinal/Latitudinal curtain constructed from the QCLS data along the flight tracks shown in dotted white. We sample the GEOS-Chem model output along the same flight track and show the loess smoothed Altitudinal/Latitudinal curtain in the third column. The fourth column shows the locations of the NOAA-curtain remote Pacific boundary condition constructed from flights by the NOAA/ESRL Carbon Cycle Group Aircraft Program as white dots. The same loess filter is applied to the data. Column 5 shows the difference between column 1 and column 2 over the 30°-50° domain, where all of the receptor STILT trajectories exit the WRF model domain. Column 6 shows a histogram of the points shown in column 5, where the vertical resolution is 50 m and the horizontal resolution is 0.1°. Columns 7 and 8 show the corresponding comparisons for the NOAA-curtain.

S4. Planetary Boundary Layer Height:

The other dominant source of error in these methods is inaccuracy in modeled planetary boundary layer height (PBLH). PBLH error was calculated by comparing WRF modeled PBLH to estimates of PBLH from 2 sources: 1) vertical profiles of potential temperature (θ) and water

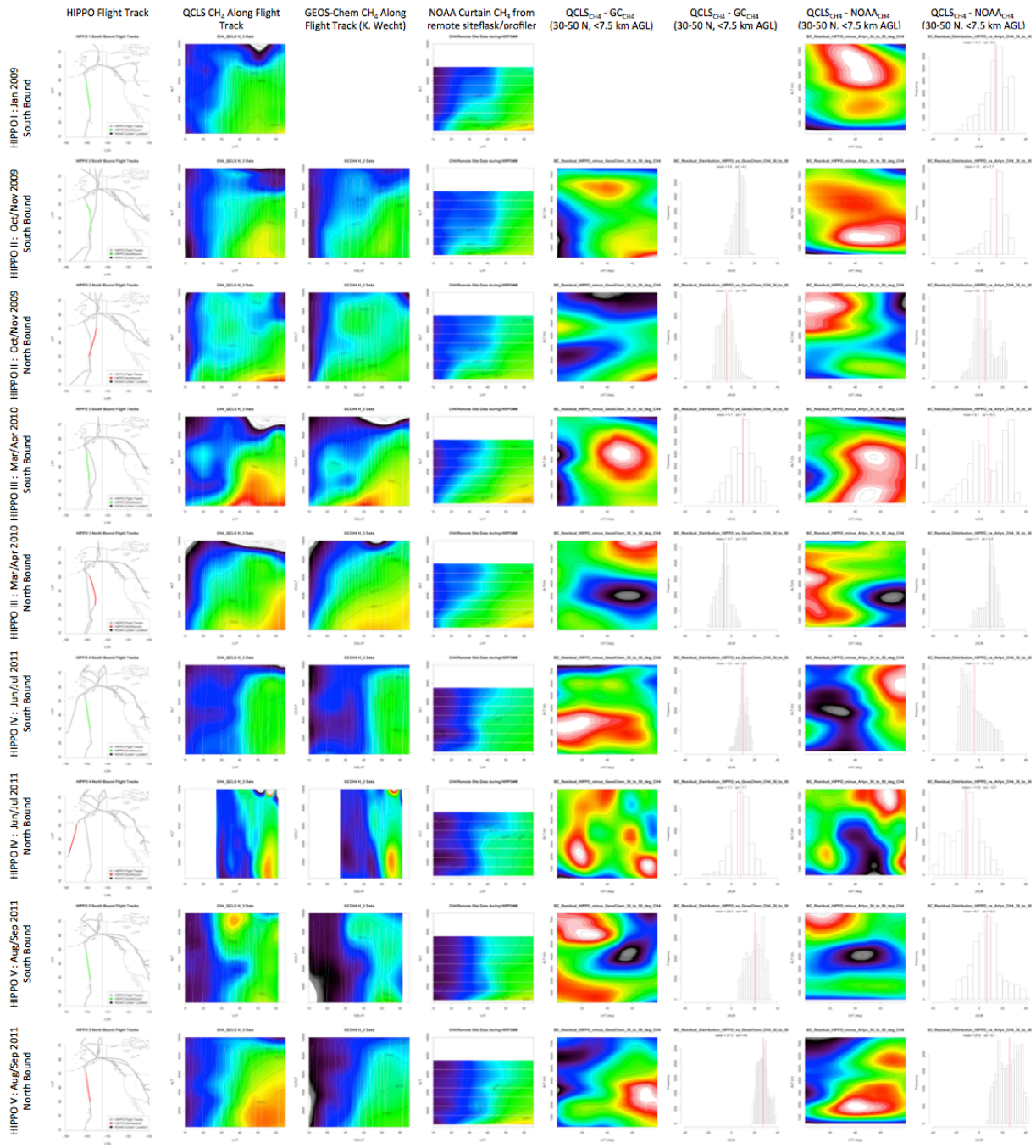

Figure S2: Comparisons of boundary conditions with HIPPO data.

vapor from the P-3 and 2) data from the High Spectral Resolution Lidar (HSRL) airborne aerosol backscatter instrument aboard the NASA LaRC B200 King Air during the CalNex & CARES (Carbonaceous Aerosol and Radiative Effects Study) deployments in May and June of 2010 [*Fast et al.*, 2012; *Scarino et al.*, submitted 2013]. Supplementary Figure S3 shows the location of the vertical profiles (left) used to calculate the PBLH from source (1), the comparison of those PBLH estimates with the GM4 simulated PBLH values (middle), and the same comparison for EM4N (right). Because the P3 never reaches into the surface layer, methods of deriving PBLH are limited. A total of 61 vertical P-3 profiles were available for PBLH validation and the comparison revealed a larger bias in the GM4 than the EM4N runs. Supplementary Figure S4 shows the location of the HSRL sampling (left) and the comparison with the WRF estimates (middle and right). The HSRL data provides much higher resolution in space and time for the PBLH comparison. We filter the HSRL data to only include data for which 1) the absolute value of the difference between the reported 'Best_PBL_Hgt' and 'PBL_Height_AGL' is less than 300, and 2) the rate of change of the underlying terrain ('Ground_Alt') is less than 2 standard deviations of the variability (sdev['Ground_Alt']). Each point represents the mean of the PBLH values in WRF for a given ½ hour (the temporal resolution of WRF) selected in the 0.1° x 0.1° sampling window of the filtered HSRL location. Each point is then assigned an error for a type II regression based on the variance of all the values used in each ½ hour interval [*York et al.*, 2004] where points with a mean difference in PBLH estimate greater than 2 standard deviations of the differenced PBLH estimate are excluded from the fit. Errors assigned to each point in the fit have median values of 350 m for HSRL and 175 m for WRF. If the WRF PBLH sampling window is increased to a 0.5° x 0.5°, the median error is 250 m for WRF, but this has a minimal effect on the regression. Overall, at an altitude of 1000 m in the Central Valley, GM4 and

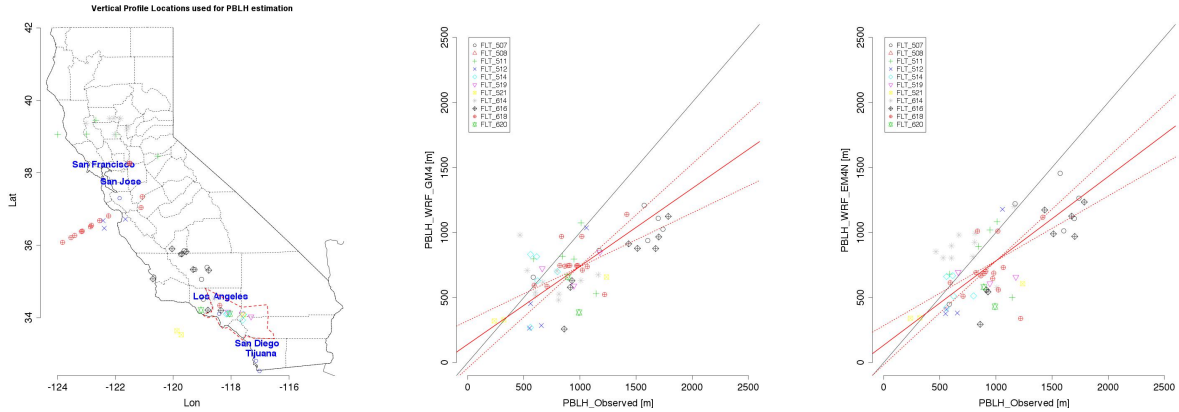

Figure S3: WRF PBLH comparisons with P-3 *in situ* profiling.

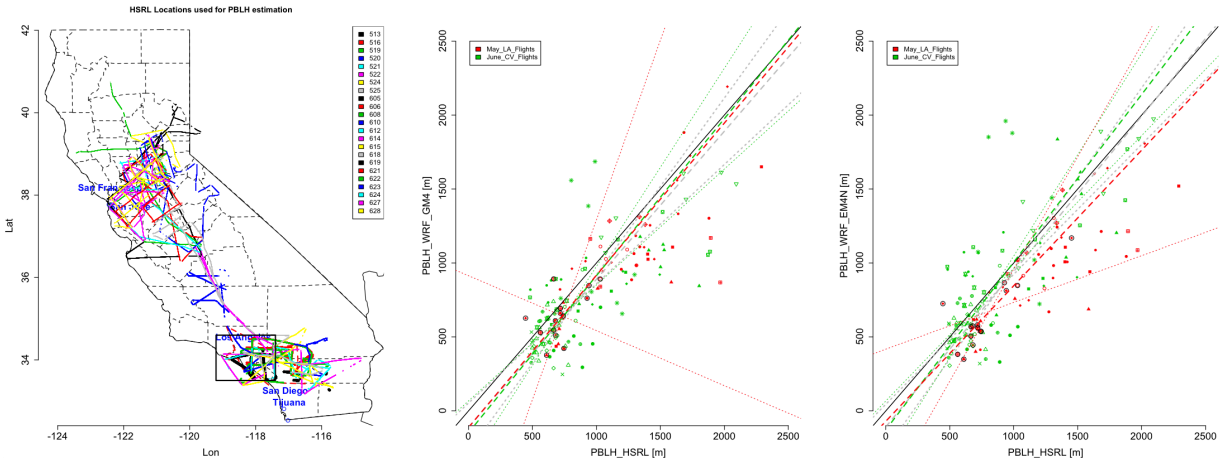

Figure S4: WRF PBLH comparisons with HSRL data.

EM4N PBLH estimates are biased low by 85 m and -5 m, respectively. This is consistent with the results of *Angevine et al.*, [2012] who also found a low PBLH bias at Chowchilla in the GM4 implementation of WRF. Biases in the South Coast Air Basin at 1000 m altitude were 85 m and 155 m for the GM4 and EM4N PBLH, respectively, also consistent with *Angevine et al.*, [2012] who reported slight degradation in the Los Angeles basin with WRF runs using the Noah land surface model. Uncertainty in the HSRL measurements due to the possibility of aerosol layers above the boundary layer makes it difficult to determine whether there is a bias in the WRF PBLH over the LA Basin. We suspect that the bias can be attributed to a high bias in the HSRL data where aerosol layers above the turbulent PBL over mountainous regions surrounding the SoCAB may be indistinguishable from the PBL itself. We therefore further filter the SoCAB data to include only points that lie within the domain used in *Angevine et al.*, [2012] (shown as a black box) and points with underlying terrain <500 m to avoid HSRL data taken in the mountainous regions (points circled in black), but these filters result in too few remaining points to conclusively determine whether the bias is statistically different than zero. The biases are not explicitly used in the inversion error estimates, but are presented as a measure of accuracy in the modeled PBLH estimates.

S5. *A priori* inversion errors

The uncertainties assigned to the *a priori* emission inventories are difficult to estimate. Assigning values of 10%, 15%, 25%, 30%, 50%, and 75% represent different weighting of the observational and *a priori* emission inventory portions of the cost functions in the inversion. Equations 5.1 and 5.2 minimize the cost function:

$$J = J_{\varepsilon} + \alpha J_{pri}$$

$$J = \frac{1}{2}\left(\underline{y} - \underline{\underline{K}}\,\underline{\hat{\lambda}}\right)^{T} \underline{\underline{S_{\varepsilon}^{-1}}} \left(\underline{y} - \underline{\underline{K}}\,\underline{\hat{\lambda}}\right) + \alpha \frac{1}{2}\left(\underline{\hat{\lambda}} - \underline{\lambda_{prior}}\right)^{T} \underline{\underline{S_{prior}^{-1}}} \left(\underline{\hat{\lambda}} - \underline{\lambda_{prior}}\right)$$

where α represents the weighting of the *a priori* emission inventory in the cost function relative to the observational model-data mismatch error. Supplementary Figure S5 (left) shows the inversion scaling factors as a function of log(α), where the far right of the plot represents high values of α such that the *a priori* error dominates and the measurements provide no additional information. The far left of the plot shows the scaling factors when the cost function $J \simeq J_\varepsilon$. Theory suggests that the optimal value for α is given by the location of the corner of the L-curve (middle), where the log of the norm of the error associated with the measurements, log(J_ε), is plotted against the log of the norm of the error associated with the emission distributions, log(J_{pri}), as a function of α [*Hansen,* 2001]. The curvature of the L-curve is plotted as a function of log(α) (right) to locate the maximum value, which corresponds to an error of 14.7%, roughly 10 times the model-data mismatch error. The α values corresponding to *a priori* uncertainties of 10%, 15%, 25%, 30%, 50%, and 75% are shown as vertical grey lines in the left panel, and the optimized α value corresponding to 14.7% is shown as a vertical blue line. As the weighting of prior uncertainties decreases, emissions from landfills decrease and natural gas and wastewater emissions compensate for that decrease. The inversion results for cows and crop/rice emissions, however, are nearly constant over the range of prior uncertainties calculated.

The total fluxes derived from the different inversions using these 6 different prior uncertainties in the emission inventories are shown in Supplementary Figure S6 and are statistically indistinguishable from one another at the p = 0.01 level. The range of total fluxes derived in the CV and SoCAB inversions never exceeds 3% of the total flux, or >0.07 $TgCH_4$/yr in the Central Valley and >0.01 $TgCH_4$/yr in the South Coast Air Basin.

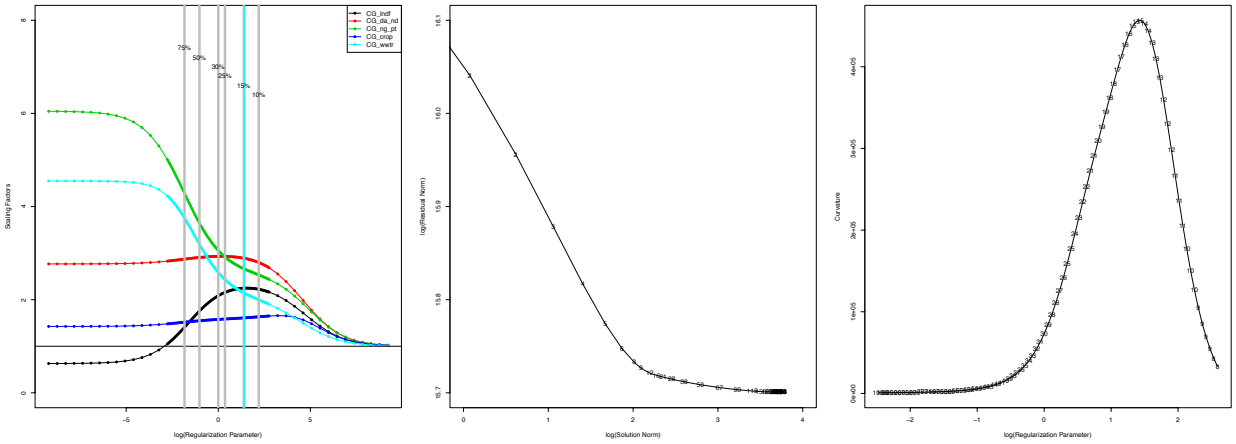

Figure S5: Inversion scaling factors as a function of regularization parameter as well as the L-curve and its curvature.

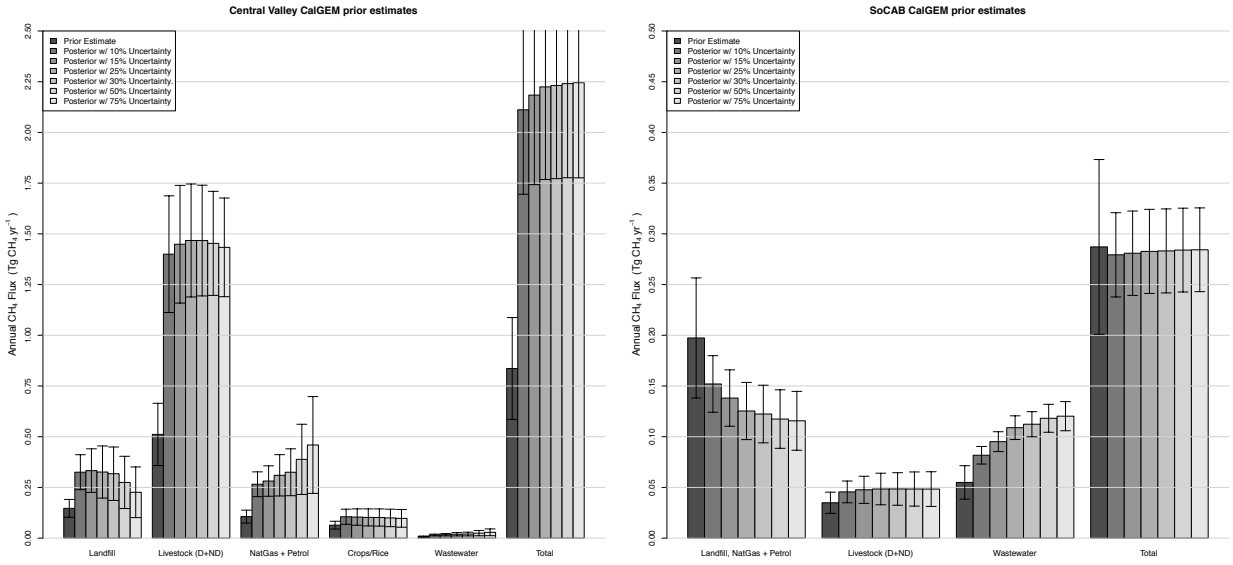

Figure S6: CalGEM inversion results for different uncertainties assigned to the *a priori* emissions.

S6. Inversions with EDGAR and EDGAR-Substituted emission inventories

Supplementary Figures S7 and S8 show the EDGAR and EDGAR-Substituted inversion results plotted as time series and profiles and are equivalent to Figures 5.5 and 5.6 shown in the main text. Most apparent in these figures is the large overestimate of the EDGAR CH_4 emissions in the SoCAB.

S7. Rice Emissions

Supplementary Figure 9 shows the seasonality of the crop/rice emissions in the CalGEM inventory based on the DNDC model. Only the emissions from May and June are included in the CV inversions and the optimized scaling factor is applied to the integrated total annual flux of 0.064 Tg CH_4 yr^{-1}. For the EDGAR-substituted inversion, the emission rates of 50 and 300 mg CH_4 m^{-2} day^{-1} in May and June, respectively, are applied to USDA acreage of rice planted. Consistent with the CalGEM inversions, the scaling factor from the inversion is applied to the annual flux reported in *McMillan et al.* [2007] of 37 g CH_4 m^{-2} yr^{-1}. When this is multiplied by the USDA planted rice acreage, the total annual prior estimate of the flux is 0.087 Tg CH_4 yr^{-1}.

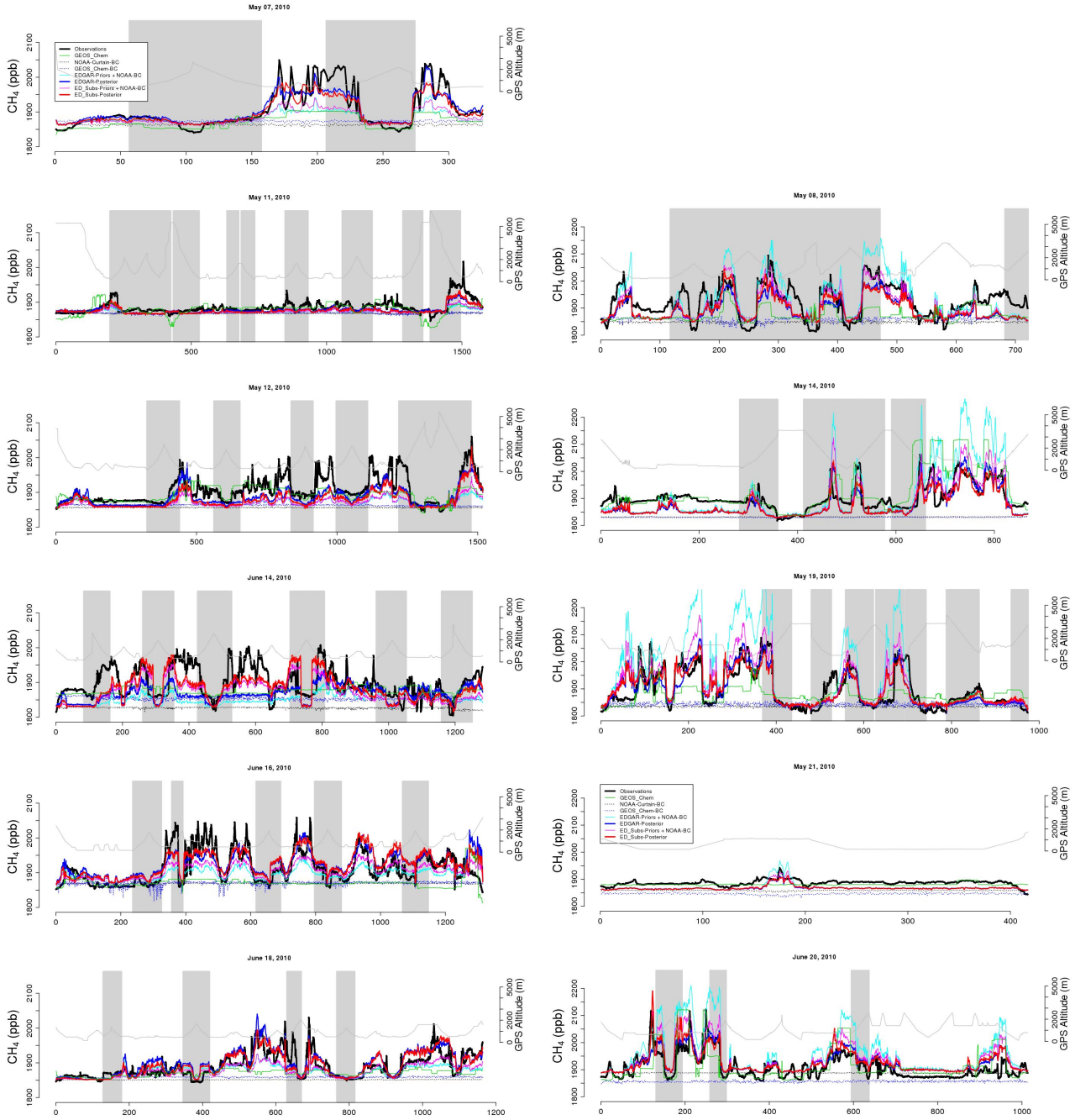

Figure S7: Inversion time series for the EDGAR and EDGAR-Substituted inversions.

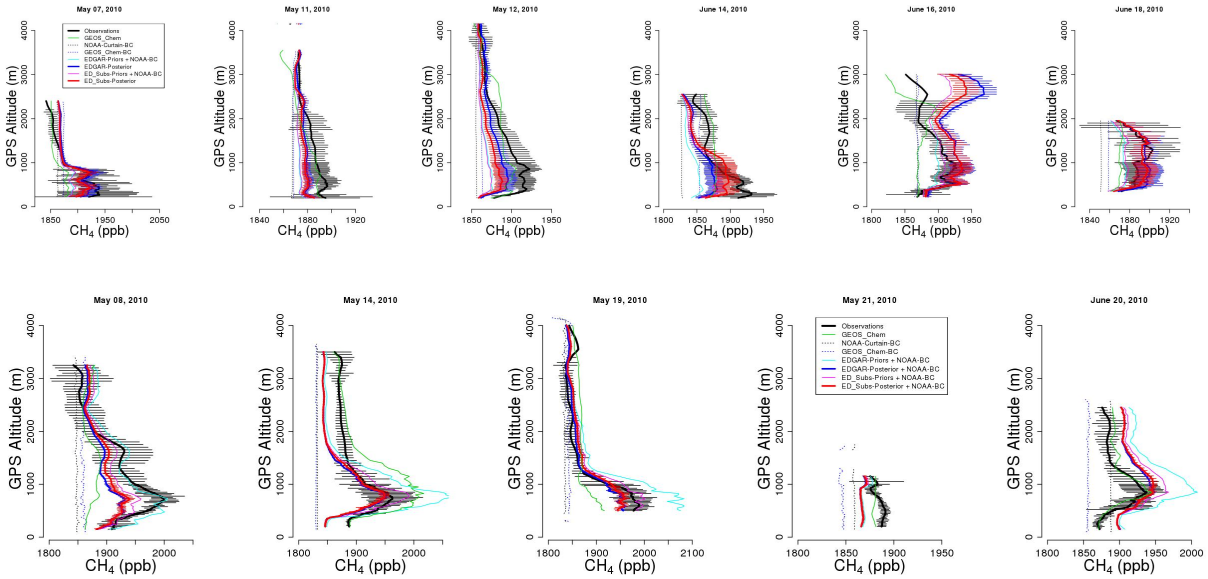

Figure S8: Inversion profiles for the EDGAR and EDGAR-Substituted inversions.

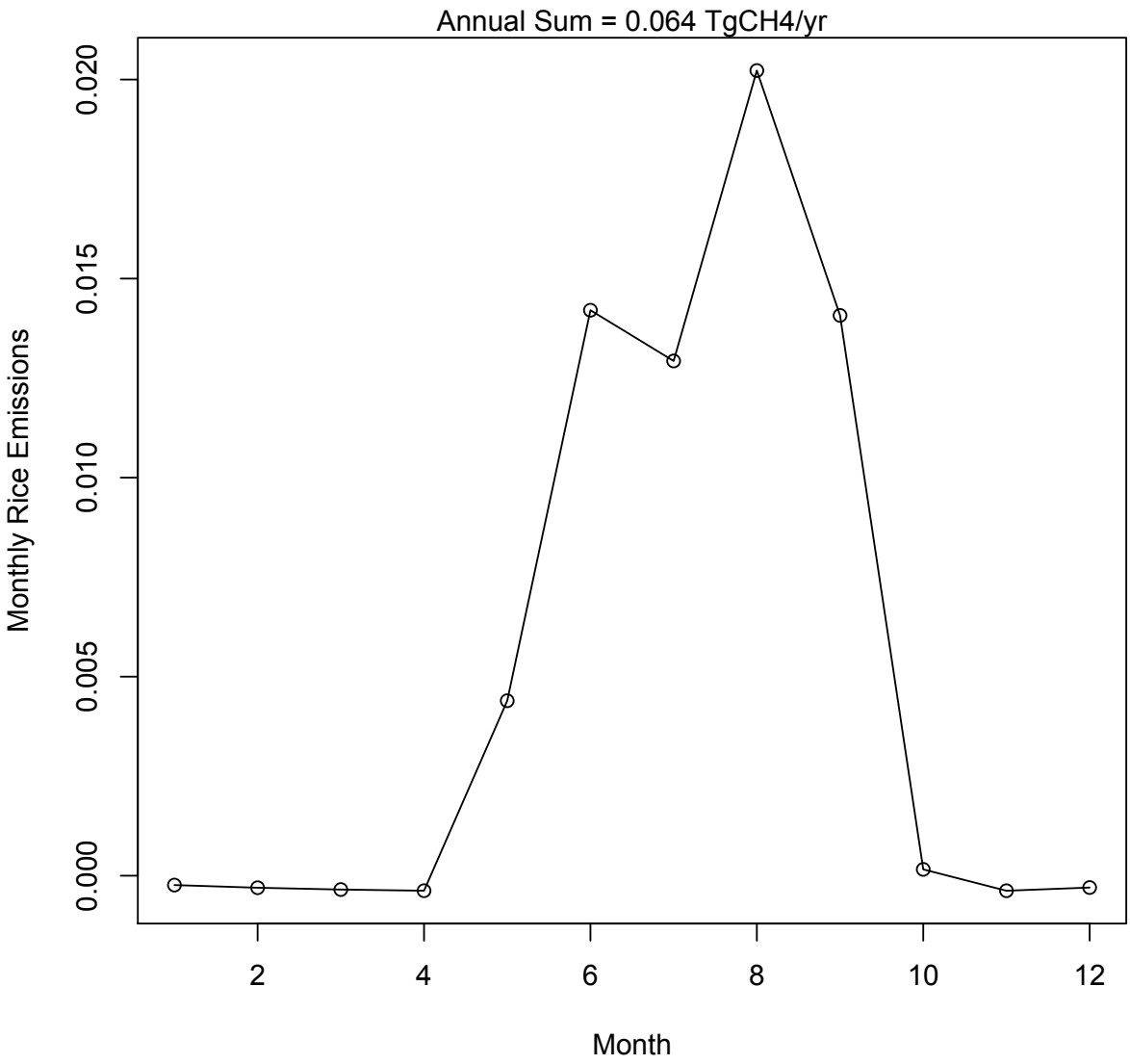

Figure S9: Seasonality of rice emissions in the CalGEM inventory.

S.8 South Coast Air Basin Coordinates

The coordinates of the polygon representing the SoCAB are:

```
SoCAB_lat=c(34.24,34.81,34.29,34.36,34.03,33.7,33.57,33.42,33.44,33.5,
 33.38,33.73,33.7,33.8,34.04,34.00,34.06,34.16,34.16,34.23,34.24)
SoCAB_lon=c(-118.63,-118.88,-117.64,-116.75,-116.72,-116.75,-116.55,-
 116.5,-117.24,-117.5,-117.59,-118.12,-118.28,-118.4,-118.55,-118.8,-
 118.95,-118.78,-118.67,-118.67,-118.62)
```

Wennberg et al. [2012] quantify emissions within the grid box (−119 < Lon < −117 ; 33.4 < Lat < 34.3) that captures the LA Basin. We sum up the different inventories using both polygons. Differences in total Los Angeles emissions are <4% for any of the significant sources. For instance, the difference in total CalGEM LA Basin fluxes between the two polygons is +3%, -1%, +1%, and +1% for landfills, dairies, natural gas, and wastewater, respectively. For non-dairy cows, the difference is 19% but the emissions themselves are less than 1% of the total emissions within the basin. The SCAB-based summations are typically higher due to the inclusion of one or two grid cells to the North of the Wennberg et al. [2012] boundary. The eastern domain is mostly desert and therefore contributes very little to the emissions.

The area of California is set as the polygon from R in the map library:

```
caly = map(database='state',region = 'california',plot= F,fill= T)
CA_lat = caly$y
CA_lon = caly$x;
```